Colloids in confined geometries: hydrodynamics, simulation and rheology

Thesis by

James W. Swan

In Partial Fulfillment of the Requirements

for the Degree of

Doctor of Philosophy

California Institute of Technology

Pasadena, California

2010

(Submitted May 24, 2010)

For Laura.

Acknowledgements

I have been fortunate enough to benefit from the grace and patience of two people during my tenure as a graduate student at caltech. First and most important is my wife Laura who has shown me unwavering support and kindness for more than a decade and throughout this professional interregnum. My achievements are her achievements as well. I would not have grown so much through this process without her confidence in me, and I bear her immeasurable gratitude. Second, I have had exceptional mentorship under John Brady these many years. He allowed me the freedom to explore all my intellectual curiosity and provided the direction I needed to evolve from a student into a scientist. His empathy and forbearance exceed any that were expected or deserved, and I consider myself lucky to have had his pedagogy and guidance.

I have had the chance to collaborate with a number of terrific researchers, and those collaborations have contributed to both the scope and depth of my research experience. These people are Professor Eric Furst and his student Pushkar Lele at the University of Delaware, Aditya Khair who was another of John Brady's graduate students and soon to assume a faculty position and George Petekidis at the University of Crete. The research in this thesis was supported by NSF Nanoscale Initiative Research Teams grant CBET 0506701.

Abstract

The hydrodynamics of colloids in confined geometries is studied hierarchically beginning with the exact solutions for a spherical particle translating, rotating and deforming in the presence of a plane wall at low Reynolds number. The many-bodied hydrodynamic interactions among a collection of spherical particles near a plane wall are computed and used to study the Brownian motion of confined suspensions. The method of reflections is used to describe the motion of a single spherical particle embedded in the fluid constrained by two, parallel plane walls. From this, tables which are independent of the channel width are generated describing the particle's response to various force moments. This same approach is expanded to describe the hydrodynamic interactions among the particles comprising a colloidal dispersion confined in a channel. The simulations arising from this theory depict the short-time self-diffusivity, sedimentation rate and high frequency viscosity of suspensions of varying volume fractions in channels of varying widths. A theory for the scattering of evanescent waves by colloidal dispersions is developed and cast in the form of the diffusivity measured by classical light scattering. A series of simulations is conducted to predict the short-time self-diffusivity and the collective diffusivity measured by evanescent wave dynamic light scattering. The thesis concludes with a discussion of how the developed simulations and theories can be extended to make dynamic measurements as well as a brief consideration of some remaining, open questions.

Contents

List of Tables

List of Figures

Chapter 1

Introduction

The dynamics of micron and sub-micron sized particles suspended in a viscous fluid hold many practical consequences for quotidian living and scientific study. While the honey poured in a cup of tea is Newtonian, the butter lathered on a scone certainly is not. Many paints are dispersions of nano-particles in a suspending medium such as water or latex, while the interiors of cells are suspensions of proteins and other macromolecules which govern the fate of all living organisms. Each and every interaction, no matter the origin, is mediated by the fluid surrounding the suspended particles, and in all these cases: butter spreading, paint running and proteins folding, the dynamics are mediated not just by the interaction of the suspended colloids with each other but also by the interactions of the colloids with the system's boundaries. It is well known that the no-slip condition on surfaces constraining a fluid dramatically affects the dynamics of embedded particles, especially at low Reynolds number. Though even in the simplest geometries, it is quite difficult to calculate the influence of the boundaries on particle motion. These calculations are important, however, to the understanding of the rheology of microstructured fluids [Leighton and Acrivos (1987)], the development of microfluidic devices [Squires and Quake (2005)] and the design and implementation of micro- and nanoscale experiments [Crocker and Grier (1996)] among other applications. Study of the complex hydrodynamics resulting from satisfying boundary conditions on both a particle and the boundary surfaces is nearly a century old, but the efficient calculation of these remains a challenge.

In fact, as dispersive systems of ever smaller dimension (*e.g.* the interior of cells [Daniels, Masi and Wirtz (2006)], microfluidic separators [Ashton, Padala and Kane (2003)], viral packaging [Ali, Marenduzzo and Yeomans (2004)]) are investigated, boundary mediated interactions may become orders of magnitude more important. One role computation can play in these investigations is in determining the degree of influence that the bounding geometry has on the dynamics of particles in suspension. The convergence of colloid science and microfluidics further motivates these calculations. Recent research has been concerned with particle motion in narrow channels via pressure driven flow, electrophoresis, electroosmotic flow and Brownian motion. The additional resistance generated by channel walls plays a role in regulating the kinetics of colloidal scale-assembly processes [Velev and Bhatt (2006)] and also affects the the dynamics and efficacy of electrophoretic separations [Verpoorte (2002)]. Additionally, various biological assays work precisely because of the shape of the microfluidic devices in which they are conducted [see *e.g.* Sia and Whitesides (2003)]. Be it the Brownian motors of Astumian and Hänggi (2002), the deterministic transport of colloids through a varying potential landscape [see *e.g.* Gopinathan and Grier (2004)] or the sorting of biological macromolecules in optical lattices [MacDonald *et al.* (2003)], the fluctuations on which these processes rely are firmly tied to the geometric constraints of the micro-channel in which they take place. Invariably in these studies, a statistical description of a microfluidic process that depends on the intimate hydrodynamic details of the particle motion is generated.

Because of the computational difficulties involved, there are unanswered questions regarding the relationship between the micromechanics of suspensions and a continuum perspective of the same system. What are the boundary conditions between the suspension and any solid boundaries? Surely momentum and mass are conserved across the interface, but what of constitutive relations such as the no-slip condition. Are the appropriate boundary conditions sufficient to model a suspension strictly in terms of its bulk rheology and dynamics? That is, can the suspension be treated as locally unbounded, or is there an inherent "non-locality" for which the bulk treatment cannot account? It will be shown that this is indeed the case. The intricate coupling of suspension structure and hydrodynamic interactions are not strictly separable, and the microstructural details in the bounding geometry are needed to predict material properties. From a higher level perspective, computational simulations of colloidal particles typically study the properties of unbounded suspensions. However, suspensions are often bounded by walls, and a rich assortment of phenomena including templated self-assembly [Aizenburg, Braun and Wiltzius (2000)] and shear-induced resuspension [Leighton and Acrivos (1987)] arise precisely because hydrodynamic flows are intimately coupled to the interactions of particles with boundaries. For colloidal particles in low-Reynolds-number flows, a mobility tensor linearly couples the forces and torques on particles to their velocities and provides a complete characterization of the hydrodynamic interactions among particles. In principle, this tensor includes the effects of a constraining geometry on the hydrodynamics, but including these effects is not trivial. The physics of small particles in a viscous fluid dictate specific properties that must emerge from the hydrodynamic interactions among the embedded particles. Principally, the mobility tensor must be symmetric and positive-definite. While models can be constructed which have neither of these properties, the physics governing the Brownian motion of hydrodynamically interacting particles require that the mobility tensor has orthogonal eigenvectors and strictly positive eigenvalues [Kubo (1966)]. These properties are intrinsic to all the methods discussed herein.

This thesis is organized as follows. In Chapter 2 the model system and corresponding physical simplifications are described. Namely, the results in this thesis apply to physical situations where the Reynolds number describing the relative strength of inertial and viscous forces is small. Under these conditions, the hydrodynamics of systems of rigid, spherical particles near no-slip plane wall boundaries are computed. Subsequently, the Langevin equation governing the stochastic motion of Brownian particles is discussed and from this the so-called “drift” velocity of a colloidal particle is derived. In later chapters, this quantity is computed as it is an important contribution to the mean motion of Brownian particles. Finally, the Stokesian Dynamics method is explained in the most general possible way. The algorithm is independent of the particular technique used to compute the hydrodynamic interactions as well as the particular geometry of the system. For that matter, it is also independent of the method used to invert the various matrices coupling the particle force moments. Each of the next four chapters details the calculation of these matrices for situations where a single or many particles reside near one plane wall or in a channel.

In Chapter 3, the exact solutions for the motion of a single colloidal particle near a plane wall are computed. In particular, translation toward the wall and rotation about the axis normal to the wall are axisymmetric and comprise one class of solution. The transverse motions (*i.e.* translation along the wall, rotation over the wall, and deformation near the wall) comprise a second class. However, bispherical coordinates and separation of variables are used to generate the solutions in both cases. From these, components of the resistance tensor for a single particle near a plane wall are derived. These are compared with the asymptotic approximations valid when the particle is very near the wall. It is shown that computations of the stresslets due to transverse motion are identical to known results with six digit accuracy. These components of the resistance tensor are critical for accurate calculations via the Stokesian Dynamics method when particles are in the presence of macroscopic boundaries. The elements of the resistance tensors depend only on the distance of the particle from the wall and as such, tables of these values distributed logarithmically with respect to this distance are provided.

Chapter 4 develops a simulation technique for accurately modeling the hydrodynamic interactions among many particles near a single plane wall. The method of reflections in conjunction with the boundary integral formulation for Stokes flow is used to describe the fluid velocity field resulting from the motion of many particles with known surface force densities. The *correct* application of a multipole expansion and subsequent use of the well known Faxén formulas describes the motion of the particles in a far-field sense. The Stokesian Dynamics method is used so that both the far-field and the lubrication interactions among the particles and between the particles and the wall are reflected. Key to these results is that the mobility and resistance tensors are symmetric and positive-definite. A discussion about why *several* previous studies failed to meet these metrics ensues, and examples of where this property is critical are presented.

In Chapter 5, a similar approach is used to describe the motion of a single spherical particle in a channel bounded by two plane walls. However, the reflection of the fundamental Stokes flow singularity must be written in terms of its Fourier transformation. The inversion of these expressions can be done with a combination of analytical and numerical methods which the chapter discusses thoroughly. The resulting expressions for the mobility can be written as a linear superposition of inverse powers of the channel width where the coefficients of proportionality depend on the fractional distance of the particle across the channel. These coefficients are tabulated over the entire range of fractional distances (0–1). As a result, simulations can be conducted for any channel width without an intense calculation. Instead, only multiplication of the coefficients by the inverse channel width is necessary. This is a novel result that allows for the rapid simulation of channel flows. The sedimentation rate of a single particle along the channel and normal to the channel walls is computed. Additionally, the drift velocity of a single particle normal to the channel walls is studied. Finally, the shear viscosity of a dilute suspension bound between widely spaced channel walls is compared to an approximation arising from superposition of the hinderance to the channel walls individually.

These tables are applied in Chapter 6 where an algorithm is developed for the rapid simulation of an infinite suspension bound in a channel by parallel plane walls. First, the exact solution for the velocity field resulting from a transversely periodic array of point forces in a fluid confined to a channel is generated. As before, this must be computed in Fourier space because of the more complicated geometry. The force density in the fluid is then divided into two pieces: a global contribution which represents the longest range hydrodynamic interactions, and a local contribution which reflects shorter ranged interactions. This is akin to the Ewald summation method which removes the high frequency components of the force density from the Fourier space solution with a Gaussian filter. These high frequency components are then reconstructed in real space. In this case, since there are no closed form real space solutions when two channel walls are present, the walls are superimposed. That is, the velocity fields resulting from the reconstructed force density in the presence of each wall individually are computed and then simply added together. The advantage here is that since the local velocity field is short ranged, the no-slip condition on each wall can be satisfied to within an exponentially small margin. This approach is then applied to a Stokesian Dynamics simulation with which the short-time self-diffusivity, the sedimentation rate and the high frequency shear viscosity are measured as a function of channel width and volume fraction.

In Chapter 7, a theory for the diffusivity of particles in a suspension measured by evanescent wave dynamic light scattering is developed. This relies on one key simplification. Evanescent waves are like any other laser light except the electric field intensity decays exponentially fast with respect to the distance from its origin. Because the decay is exponential, one can write an effective wave vector describing the scattering, though unlike a typical scattering wave vector this one is complex. The real components correspond to the spatial oscillation of the wave while the imaginary component is the evanescent penetration depth. In this way, the proper application of complex algebra allows one to recast the evanescent wave scattering problem in *exactly* the same form as classical dynamic light scattering. The simulation of a bound suspension is used in a subsequent computation of the short-time self-diffusivity and the collective diffusivity as a function of volume fraction and evanescent wave penetration depth. The thesis concludes with a brief summary of the key results and a discussion of future directions of this work.

Bibliography

[1] J. Aizenberg, P.V. Braun, and P. Wiltzius. Colloidal deposition controlled by electrstatic and capillary forces. *Phys. Rev. Lett.*, 84(13):2997–3000, March 2000.

[2] I. Ali, D. Marenduzzo and J.M. Yeomans Dynamics of polymer packaging. *J. Chem. Phys.*, 121, 8635–8641, 2004.

[3] R. Ashton, C. Padala and R.S. Kane. Microfluidic separation of DNA. *Curr. Opin. in Biotech.*, 14, 497–504, 2003.

[4] R.D. Astumian and P. Hänggi. Brownian motors. *Phys. Today*, 55(11):33–39, November 2002.

[5] J.C. Crocker and D.G. Grier. When like charges attract: The effects of geometrical confinement of long-range colloidal interactions. *Phys. Rev. Lett.*, 77:1897-1900, May 1996.

[6] B.R. Daniels, B.C. Masi and D. Wirtz Probing single-cell micromechanics in vivo: the microrheology of C. elegans developing embryos. *Biophys. J.*, 90(12), 4712–4719, 2006.

[7] A. Gopinathan and D.G. Grier. Statistically locked-in transport through periodic potential landscapes. *Phys. Rev. Lett.*, 92(13), April 2004.

[8] R. Kubo. The fluctuation-dissipation theorem. *Reports on Progress in Physics*, 29(1):255–284, 1966.

[9] D. Leighton and A. Acrivos. Measurement of shear-induced self-diffusion in concentrated suspensions of spheres. *J. Fluid Mech.*, 177:109–131, May 1987.

[10] M.P. MacDonald, G.C. Spalding and K. Dholakia. Microfluidic sorting in an optical lattice. *Nature*, 426:421–424, November 2003.

[11] S.K. Sia and G.M. Whitesides. Microfluidic devices fabricated in poly(dimethylsiloxane) for biological studies. *Electrophoresis*, 24:3563–3576, 2003.

[12] T. Squires and S. Quake. Microfluidics: Fluid physics at the nanoliter scale. *Rev. of Mod. Phys.*, 77:977–1026, July 2005.

[13] O.D. Velev and K.H. Bhatt. On-chip micromanipulation and assembly of colloidal particles by electric fields. *Soft Matter*, 2:738–750, 2006.

[14] E. Verpoorte. Microfluidic chips for clinical and forensic analysis. *Electrophoresis*, 23:677–712, 2002.

Chapter 2

Preliminaries

2.1 Low-Reynolds-number hydrodynamics

2.1.1 A model system from continuum mechanics

The continuum equations governing the velocity ($\mathbf{u}$), density (ρ) and temperature (T) of a Newtonian fluid are

$$\dot{\rho} + \nabla \cdot (\rho \mathbf{u}) = 0, \tag{2.1}$$

$$\rho \left(\dot{\mathbf{u}} + \mathbf{u} \cdot \nabla \mathbf{u} \right) = \nabla \cdot \boldsymbol{\sigma}, \tag{2.2}$$

$$\rho C_p \left(\dot{T} + \mathbf{u} \cdot \nabla T \right) = -\nabla \cdot \mathbf{q} + \mathbf{e} : \boldsymbol{\sigma}, \tag{2.3}$$

where $\boldsymbol{\sigma}$ is the shear stress in the fluid such that

$$\boldsymbol{\sigma} = -p\mathbf{I} + 2\eta \mathbf{e} + \left(\kappa - \frac{1}{3}\eta \right) \nabla \cdot \mathbf{u}, \tag{2.4}$$

with p the thermodynamic pressure and η and κ the Newtonian shear and bulk viscosities. The rate of strain is denoted $\mathbf{e}$. The heat capacity is denoted C_p while $\mathbf{q}$ is the conductive heat flux and often approximated as $-k\nabla T$ where k is the thermal conductivity. Of course an equation of state relates the density, pressure and temperature of the fluid such that $\rho = \rho(p, T)$. Similarly, the material properties (*i.e.* viscosity and conductivity) may depend on the state of the fluid. A reference pressure p_0 will prove useful for scaling the continuum equations as well.

Given a characteristic velocity scale U, characteristic length scale L and temperature scale $\Delta\Theta$ measuring the departure from the characteristic temperature Θ, these equations can be made dimensionless implicitly, *viz.*

$$\dot{\rho} + \nabla \cdot (\rho \mathbf{u}) = 0, \tag{2.5}$$

$$\mathrm{Re}\,(\dot{\mathbf{u}} + \mathbf{u} \cdot \nabla \mathbf{u}) = \nabla \cdot \boldsymbol{\sigma}, \tag{2.6}$$

$$\mathrm{Pe}\left(\dot{T} + \mathbf{u} \cdot \nabla T\right) = -\nabla \cdot \mathbf{q} + \mathrm{Br}\mathbf{e} : \boldsymbol{\sigma}, \tag{2.7}$$

where the characteristic time scale is simply L/U and the characteristic stress is $\eta U/L$. The three dimensionless groups which emerge are:

- $\mathrm{Re} = \rho(\Theta, p_0)UL/\eta(\Theta, p_0)$ – the Reynolds number characterizing the relative importance of inertial and viscous forces.

- $\mathrm{Pe} = \rho(\Theta, p_0)C_p(\Theta, p_0)UL/k(\Theta, p_0)$ – the Peclet number characterizing the relative importance of advective and conductive heat transfer.

- $\mathrm{Br} = \eta(\Theta, p_0)U^2/k(\Theta, p_0)\Delta\Theta$ – the Brinkman number characterizing the relative importance of viscous dissipation and conductive heat transfer.

In the limit that the material is incompressible such that the isothermal compressibility and isobaric expansivity of the fluid are small, the density is effectively constant and the velocity field is divergence free. Similarly, given that $\Delta\Theta$ is small such that departures from the reference temperature Θ are also small, the material properties can be assumed constant. This thesis is concerned with low-Reynold-number flows such that the viscous forces throughout the fluid are significantly stronger than the inertial forces, therefore the limit that $\mathrm{Re} \to 0$ is considered. So that the flow is isothermal, it is also necessary that the Brinkman number be small so that any heat generated by fluid friction is spread quickly throughout the fluid via conduction.

With isothermal boundary conditions and no sources of heat in the fluid, the value of the Peclet number is inconsequential. Summarizing, at low-Reynolds-numbers and for small Brinkman numbers, the governing equations for the motion of an isothermal fluid are,

$$\begin{aligned} \nabla \cdot \mathbf{u} &= 0, \\ \nabla p &= \eta \nabla^2 \mathbf{u}, \end{aligned} \tag{2.8}$$

where the pressure and velocity are dimensional quantities again. These are the Stokes equations.

It is well known that the Stokes equations are not valid everywhere for an arbitrarily small but non-zero Reynolds number. For a sedimenting sphere of radius a (that is $L = a$), an inertial wake in the fluid lies at a distance of roughly $a\mathrm{Re}^{-1}$ from the sphere and alters the sedimentation rate. This is the so-called Whitehead's paradox which arises when attempting a regular expansion of the continuum equations with respect to the Reynolds number. There is an intermediate length scale over which viscous forces and inertial forces have equivalent influence on the fluid dynamics. Still, for small Reynolds numbers, the velocity field surrounding a sedimenting sphere is of magnitude Re over that same length scale. Therefore, these inertial effects on the velocity field are often insignificant. For the present purposes, the Reynolds number over *all* length scales is identically zero.

2.1.2 The Green's function formulation for Stokes flow

Consider a point force of magnitude $\mathbf{F}$ in an unbounded fluid at zero Reynolds number,

$$\nabla \cdot \mathbf{u} = 0, \tag{2.9}$$

$$\nabla p = \eta \nabla^2 \mathbf{u} - \mathbf{F}\delta(\mathbf{x} - \mathbf{x}'), \tag{2.10}$$

where $\mathbf{x}$ is a point within the fluid and $\mathbf{x}'$ is the location of the point force. The solution of these equations via Fourier transformation is straightforward such that

$$\mathbf{u}(\mathbf{x}) = \frac{1}{8\pi\eta r}\left(\mathbf{I} - \hat{\mathbf{r}}\hat{\mathbf{r}}\right)\cdot\mathbf{F}, \tag{2.11}$$

$$p(\mathbf{x}) = \frac{1}{4\pi r^2}\hat{\mathbf{r}}\cdot\mathbf{F}, \tag{2.12}$$

where $\mathbf{r} = \mathbf{x} - \mathbf{x}'$ and $\hat{\mathbf{r}} = \mathbf{r}/r$. The tensorial couple between the force and the velocity is termed the Stokeslet $[\mathbf{J}(\mathbf{x}, \mathbf{x}')]$. This is the fundamental solution for Stokes flow such that, for an arbitrary body force in the fluid denoted $\mathbf{f}(\mathbf{x})$, the resulting flow is

$$\mathbf{u}(\mathbf{x}) = \int_V \mathbf{J}(\mathbf{x}, \mathbf{x}')\cdot\mathbf{f}(\mathbf{x}')d\mathbf{x}', \tag{2.13}$$

where the domain of integration V is the volume containing the fluid. Extending this equation through successive application of the divergence theorem leads to the so-called boundary integral formulation for Stokes flow. As the Stokes equations are elliptic, the solution can always be written in terms of sources at the material boundaries. This can be specialized for the Stokes flow around a set of N, rigid and no-slip particles immersed in an ambient flow denoted $\mathbf{u}^\infty(\mathbf{x})$, *viz.*

$$\begin{aligned}\mathbf{u}(\mathbf{x}) - \mathbf{u}^\infty(\mathbf{x}) = &-\sum_{i=1}^{N}\int_{S_i}\mathbf{G}(\mathbf{x}, \mathbf{x}')\cdot\boldsymbol{\sigma}(\mathbf{x}')\cdot\mathbf{n}'dS_{\mathbf{x}'} \\ &-\int_{S_\infty}\left\{\mathbf{G}(\mathbf{x}, \mathbf{x}')\cdot\boldsymbol{\sigma}(\mathbf{x}')\cdot\mathbf{n}' - [\mathbf{u}(\mathbf{x}') - \mathbf{u}^\infty(\mathbf{x}')]\cdot\boldsymbol{\Sigma}(\mathbf{x}, \mathbf{x}')\cdot\mathbf{n}'\right\}dS_{\mathbf{x}'},\end{aligned} \tag{2.14}$$

where $\boldsymbol{\sigma}(\mathbf{x})$ is the Cauchy stress in the fluid, $\mathbf{n}'$ is the normal to the surface pointing into the fluid, $\mathbf{G}(\mathbf{x}, \mathbf{x}')$ is the Green's function for the velocity field in Stokes flow subject to an arbitrary macroscopic bounding geometry with field point at $\mathbf{x}$ and source at $\mathbf{x}'$ and

$$\Sigma_{ijk}(\mathbf{x}, \mathbf{x}') = -\delta_{ij}P_k(\mathbf{x}, \mathbf{x}') + \eta\left[\partial_{x'_i}G_{jk}(\mathbf{x}, \mathbf{x}') + \partial_{x'_j}G_{ik}(\mathbf{x}, \mathbf{x}')\right]. \tag{2.15}$$

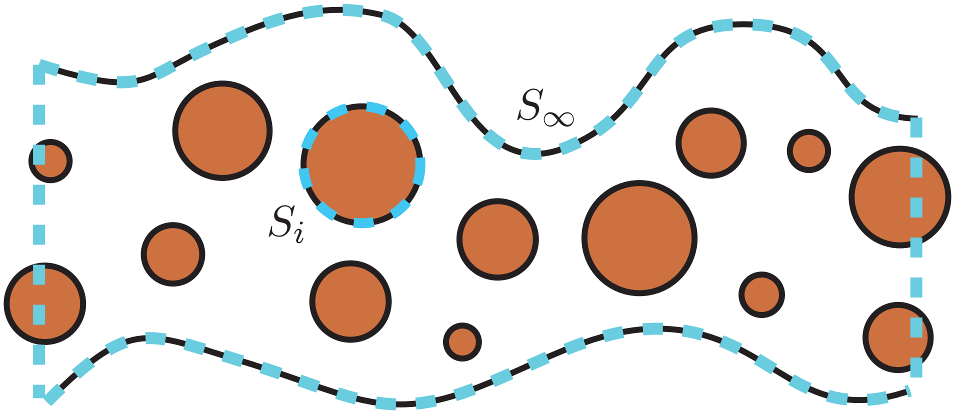

Figure 2.1: Rigid particles and fluid confined by an arbitrary geometry. The surface of the particles and the surface at infinity are indicated as S_i and S_∞. Note that the surface at infinity cuts through both particles and suspension.

Here, $\mathbf{P}(\mathbf{x}, \mathbf{x}')$ is the Green's function for the pressure field in Stokes flow and δ_{ij} is the Kronecker delta function. The S_i's are the surfaces of the particles, while S_∞ is an arbitrary surface which follows the bounding geometry and also contains a finite portion of the suspension. A schematic is shown in figure 2.1.

2.1.3 The grand mobility tensor

Because the Stokes equations are linear, the resulting velocity fields and tractions are linear functions of the boundary data. This has profound consequences on the dynamics of small particles in a viscous fluid. Perhaps the most useful result of this simple fact is the existence of a grand mobility tensor that couples linearly all the moments of the hydrodynamic force density (force, $\mathbf{F}^H$; torque, $\mathbf{L}^H$; stresslet, $\mathbf{S}^H$; *etc.*) on the surface of particles suspended in the fluid to the moments of the particle velocities (translational, $\mathbf{U}$; rotational, $\boldsymbol{\Omega}$; rate of deformation, $\mathbf{E}$; *etc.*) such that

$$\begin{pmatrix} \mathbf{U} - \mathbf{u}^\infty(\mathbf{x}) \\ \boldsymbol{\Omega} - \frac{1}{2}\nabla \times \mathbf{u}^\infty(\mathbf{x}) \\ \mathbf{E} - \mathbf{e}^\infty(\mathbf{x}) \\ \vdots \end{pmatrix} = - \begin{pmatrix} \mathbf{M}_{UF} & \mathbf{M}_{UL} & \mathbf{M}_{US} & \cdots \\ \mathbf{M}_{\Omega F} & \mathbf{M}_{\Omega L} & \mathbf{M}_{\Omega S} & \cdots \\ \mathbf{M}_{EF} & \mathbf{M}_{EL} & \mathbf{M}_{ES} & \cdots \\ \vdots & \vdots & \vdots & \ddots \end{pmatrix} \cdot \begin{pmatrix} \mathbf{F}^H \\ \mathbf{L}^H \\ \mathbf{S}^H \\ \vdots \end{pmatrix} \tag{2.16}$$

where $\mathbf{u}^\infty(\mathbf{x})$ is an ambient velocity field which is present in the absence of the particles and $\mathbf{e}^\infty(\mathbf{x})$ is the rate of deformation of the ambient field. Of course, for rigid particles, $\mathbf{E}$ (the particle rate of strain) is identically zero. Here, the translational velocities of and forces on N particles are represented in terms of $3N$ dimensional velocity and force vectors. The grand mobility tensor, often denoted $\mathcal{M}$, is symmetric and positive-definite. This is an essential aspect of Stokes flow and is a necessary component of any model of Brownian motion. Additionally, as the grand mobility tensor is a linear couple to the boundary data, it can only depend on the geometry of the system under study. This includes not only the configuration of the particles, but also the relative position of any boundaries confining the suspension.

Focus on a single particle n for a moment. The velocity field in the fluid may be expressed as

$$\mathbf{u}(\mathbf{x}) - \mathbf{u}^\infty(\mathbf{x}) = -\int_{S_n} \mathbf{G}(\mathbf{x},\mathbf{x}') \cdot \boldsymbol{\sigma}(\mathbf{x}') \cdot \mathbf{n}' dS_{\mathbf{x}'} + \mathbf{u}'_n(\mathbf{x}), \tag{2.17}$$

where $\mathbf{u}'_n(\mathbf{x})$ is the velocity field generated by the suspension due to the direct forcing of the other particles and the channel walls. Recasting the problem in this form has no effect on the generality of the flow field. By integrating equation (2.17) over the surface of a spherical particle n, one can show that the velocity of particle n is

$$\mathbf{U}_n = -\left(\mathbf{M}_{UF}^{(S)} \cdot \mathbf{F}_n^H + \mathbf{M}_{UL}^{(S)} \cdot \mathbf{L}_n^H + \mathbf{M}_{US}^{(S)} : \mathbf{S}_n^H + \cdots\right) + \left(1 + \frac{a_n^2}{6}\nabla_x^2\right) \left[\mathbf{u}^\infty(\mathbf{x}) + \mathbf{u}'_n(\mathbf{x})\right]\Big|_{\mathbf{x}_n}, \tag{2.18}$$

where the $\mathcal{M}_{UA}^{(S)}$ are elements of the grand mobility tensor for a single particle in the bounding geometry, a_n is the radius of particle n and $\mathbf{x}_n$ denotes its center. The hydrodynamic force, torque and stresslet on particle n are defined as

$$\mathbf{F}_n^H = -\int_{S_n} \boldsymbol{\sigma} \cdot \mathbf{n} dS \tag{2.19}$$

$$\mathbf{L}_n^H = -\int_{S_n} (\mathbf{x} - \mathbf{x}_n) \times \boldsymbol{\sigma} \cdot \mathbf{n} dS \tag{2.20}$$

$$\mathbf{S}_n^H = \frac{1}{2}\int_{S_n} (\mathbf{x} - \mathbf{x}_n)\boldsymbol{\sigma} \cdot \mathbf{n} + \boldsymbol{\sigma} \cdot \mathbf{n}(\mathbf{x} - \mathbf{x}_n) - \eta(\mathbf{u}\mathbf{n} + \mathbf{n}\mathbf{u}) dS. \tag{2.21}$$

Analogous expressions for the torque and rate of deformation arise from integrating the product of the total velocity field and $\mathbf{x}-\mathbf{x}_n$, *viz.*

$$\boldsymbol{\Omega}_n = -\left(\mathbf{M}^{(S)}_{\Omega F}\cdot\mathbf{F}^H_n + \mathbf{M}^{(S)}_{\Omega L}\cdot\mathbf{L}^H_n + \mathbf{M}^{(S)}_{\Omega S}:\mathbf{S}^H_n + \cdots\right) + \frac{1}{2}\nabla\times\left[\mathbf{u}^\infty(\mathbf{x}) + \mathbf{u}'_n(\mathbf{x})\right]\Big|_{\mathbf{x}_n}, \tag{2.22}$$

$$0 = -\left(\mathbf{M}^{(S)}_{EF}\cdot\mathbf{F}^H_n + \mathbf{M}^{(S)}_{EL}\cdot\mathbf{L}^H_n + \mathbf{M}^{(S)}_{ES}:\mathbf{S}^H_n + \cdots\right) + \left(1+\frac{a_\alpha^2}{10}\nabla^2\right)\left[\mathbf{e}^\infty(\mathbf{x}) + \mathbf{e}'_n(\mathbf{x})\right]\Big|_{\mathbf{x}_n}, \tag{2.23}$$

where $\mathbf{e}'_n(\mathbf{x})$ is the rate of strain of the disturbance velocity field. These are the so-called Faxén formulas. It is the combination of $\mathbf{M}^{(S)}_{UF}$ and terms from the disturbance flow and disturbance pressure gradient [$\mathbf{u}'_n(\mathbf{x})$ and $\nabla^2\mathbf{u}'_n(\mathbf{x})$ respectively] proportional to the forces on the particles which comprise $\mathbf{M}_{UF}$. An equivalent statement can be made regarding the other mobility tensors. Additionally, it follows directly from the Stokes equations and the reciprocal theorem that the grand mobility tensor is always symmetric, positive and definite.

The inverse of the grand mobility tensor is termed the grand resistance tensor and denoted

$$\mathcal{R} = \begin{pmatrix} \mathbf{R}_{FU} & \mathbf{R}_{F\Omega} & \mathbf{R}_{FE} & \cdots \\ \mathbf{R}_{LU} & \mathbf{R}_{L\Omega} & \mathbf{R}_{LE} & \cdots \\ \mathbf{R}_{SU} & \mathbf{R}_{S\Omega} & \mathbf{R}_{SE} & \cdots \\ \vdots & \vdots & \vdots & \ddots \end{pmatrix}. \tag{2.24}$$

It often proves useful to switch between the mobility and resistance formulations in the development of numerical algorithms. One must be careful though as $\mathbf{R}^{-1}_{FU} \neq \mathbf{M}_{UF}$. In fact, the calculation of the former quantity is the crux of the computational problem. A strict inversion of this tensor requires $O(N^3)$ operations, while various schemes exist to reduce that operation count to $O(N^2)$ (iterative solution), $O(N\log N)$ (fast fourier transformations) or even $O(N)$ (fast multipole method).

As the force and torque are effectively equivalent dynamically (*i.e.* they are prescribed as opposed to induced moments of the force density on the surfaces of the particles), it is occasionally convenient to bundle them together into a combined force-torque variable designated $\mathbf{F}$. The translation and rotation of the particles are dynamically equivalent as well, and a combined translational-rotational velocity is simply designated $\mathbf{U}$. Throughout the manuscript, this convention is adopted and is easily identifiable by the fact that statements about the torque and rotational velocity are entirely absent. When this occurs, a notation will be made.

2.2 The Langevin equation

In general, the dynamics of particles embedded in a fluid are governed by the Newtonian physics – that is,

$$\mathbf{m} \cdot \dot{\mathbf{U}} = \mathbf{F}^H + \mathbf{F}^P, \tag{2.25}$$

$$\mathbf{i} \cdot \dot{\mathbf{\Omega}} = \mathbf{L}^H + \mathbf{L}^P, \tag{2.26}$$

where $\mathbf{m}$ and $\mathbf{i}$ are the mass and moment of inertia of the particles and $\mathbf{F}^P$ and $\mathbf{L}^P$ are any external force and torque on those particles. When these include stochastic forces due to the random motion of the fluid molecules themselves, this equation is termed the Langevin equation. Integration of the Langevin equation is often straightforward, though accounting properly for the stochastic forces requires some delicacy. For this manuscript, measurements are entirely static. That is, the trajectories of the particles are never computed explicitly, and only the hydrodynamic and thermodynamic properties at equilibrium are probed. However, dynamic measurements of non-equilibrium properties are indeed possible with the methodologies described herein via direct integration of the Langevin equation.

Of course, when $\mathbf{F}^P$ includes Brownian forces, denoted $\mathbf{F}^B$ with statistics,

$$\left\langle \mathbf{F}^B(t) \right\rangle = 0, \tag{2.27}$$

$$\left\langle \mathbf{F}^B(t)\mathbf{F}^B(0) \right\rangle = 2kT\mathbf{R}_{FU}\delta(t), \tag{2.28}$$

where k is the Boltzmann constant, the integration of the Langevin equation is more complicated. The stochastic Brownian forces depend on the position of the particles through the resistance tensor. For a collection of small colloidal particles of negligible Stokes number ($\mathrm{St} = \mathrm{Re}\rho_p/\rho$), where ρ_p is the particles' density, the sum of the forces on the particles are approximately equal to zero, such that

$$\frac{d\mathbf{x}}{dt} = \mathbf{R}_{FU}^{-1} \cdot \mathbf{F}^{B}(t). \tag{2.29}$$

Here, the combined force-torque and translation-rotation convention is adopted. Integration in time to order Δt yields,

$$\mathbf{x}(t+\Delta t) = \mathbf{x}(t) + \mathbf{R}_{FU}^{-1} \cdot \mathbf{F}^{B}(\Delta t)\Delta t + kT\nabla \cdot \mathbf{R}_{FU}^{-1}\Delta t + O(\Delta t). \tag{2.30}$$

The final term reflects the implicit dependence of the Brownian forces on the particle configuration. Computationally, this "deterministic drift" is the result of using a low order integration scheme which does not account for the intermediate particle configurations which must occur as a particle translates over a single time step. A higher order integration scheme (*i.e.* order Δt^2) would eliminate the need to compute and then include this contribution explicitly.

2.3 Stokesian dynamics

Since the Stokes equations governing the fluid physics are linear when the Reynolds number is small, the hydrodynamic force on the particles is coupled linearly to the particle velocities such that $\mathbf{F}^{H} = -\mathbf{R}_{FU} \cdot (\mathbf{U} - \mathbf{u}^{\infty})$, where $\mathbf{R}_{FU}$ is the resistance tensor. The combined force/torque notation is used here again. Clearly, generating and inverting the resistance tensor quickly is the crux of the dynamical problem. To that end, the typical Stokesian Dynamics paradigm is followed and the hydrodynamic force is separated into near-field (or lubrication) and far-field contributions, *viz.*

$$0 = -\mathbf{R}_{FU}^{nf} \cdot (\mathbf{U} - \mathbf{u}^{\infty}) + \mathbf{F}^{H,ff} + \mathbf{F}^{P}, \tag{2.31}$$

and

$$\begin{pmatrix} \mathbf{U} - \mathbf{u}^{\infty} \\ \\ -\mathbf{E}^{\infty} \end{pmatrix} = -\mathcal{M}^{\infty} \cdot \begin{pmatrix} \mathbf{F}^{H,ff} \\ \\ \mathbf{S}^{H,ff} \end{pmatrix}, \tag{2.32}$$

where $\mathbf{R}_{FU}^{nf}$ is the exact two-body lubrication contribution to the resistance tensor less the two body far-field contribution, $\mathbf{F}^{H,ff}$ is the far-field hydrodynamic force, $\mathbf{E}^{\infty}$ is the average rate of strain in the suspension, $\mathcal{M}^{\infty}$ is the far-field mobility tensor, and $\mathbf{S}^{H,ff}$ is the far-field stresslet. With a few algebraic manipulations, this system of equations can be solved for the far-field hydrodynamic force and the particle velocities as

$$\begin{aligned} \begin{pmatrix} \tilde{\mathbf{F}}^{H,ff} \\ \\ \mathbf{S}^{H,ff} \end{pmatrix} = & \left[\mathcal{M}^{\infty} + \begin{pmatrix} (\tilde{\mathbf{R}}_{FU}^{nf})^{-1} & 0 \\ \\ 0 & 0 \end{pmatrix} - \lambda \mathcal{M}^{\infty} \cdot \begin{pmatrix} (\tilde{\mathbf{R}}_{FU}^{nf})^{-1} & 0 \\ \\ 0 & 0 \end{pmatrix} \right]^{-1} \\ & \cdot \left[\lambda \mathcal{M}^{\infty} \cdot \begin{pmatrix} (\tilde{\mathbf{R}}_{FU}^{nf})^{-1} \cdot \mathbf{F}^{P} \\ \\ 0 \end{pmatrix} - \begin{pmatrix} (\tilde{\mathbf{R}}_{FU}^{nf})^{-1} \cdot \mathbf{F}^{P} \\ \\ -\mathbf{E}^{\infty} \end{pmatrix} \right], \end{aligned} \tag{2.33}$$

and

$$\mathbf{U} - \mathbf{u}^{\infty} = (\tilde{\mathbf{R}}_{FU}^{nf})^{-1} \cdot \left(\tilde{\mathbf{F}}^{H,ff} + \mathbf{F}^{P} \right), \tag{2.34}$$

where λ is an arbitrary coefficient, $\tilde{\mathbf{R}}_{FU}^{nf} = \mathbf{R}_{FU}^{nf} + \lambda \mathbf{I}$, $\mathbf{I}$ is the idem tensor and $\tilde{\mathbf{F}}^{H,ff} = \mathbf{F}^{H,ff} + \lambda(\mathbf{U} - \mathbf{u}^{\infty})$. Since $\mathbf{R}_{FU}^{nf}$ by itself is not always invertible, an additional diagonal tensor is added to make it positive definite. A value of unity for λ will always suffice to make $\tilde{\mathbf{R}}_{FU}^{nf}$ invertible; however, larger values of λ will yield a better conditioned tensor at volume fractions approaching maximum packing. When a shear flow is included, one must be sure to include the near-field component of the shearing force in the particle force $\mathbf{F}^{P}$ such that

$$\mathbf{F}^{P} = \tilde{\mathbf{F}}^{P} + \mathbf{R}_{FE}^{nf} \cdot \mathbf{E}^{\infty}. \tag{2.35}$$

One can include this at the outset, but the notation is less compact.

2.4 Model systems

Throughout this thesis, several model systems with certain commonalities are employed. In all cases, the colloids are modeled by rigid, no-slip spherical particles with zero poly-dispersity. Aside from the hard sphere potential preventing the particles from overlapping, there are no interparticle interactions considered. This last condition is easily modified by changing $\mathbf{F}^P$ to include pair or higher order interactions. With regard to the size and shape of the particles, however, it is known that highly eccentric particles behave differently in suspension than spheres. Similarly, poly-disperse suspensions are dynamically different than mono-disperse suspension. For small degrees of eccentricity and poly-dispersity; however, the results herein are certainly applicable. All the particulate systems discussed are constrained by macroscopic boundaries. In all cases these are infinite no-slip plane walls: either a single wall or two parallel walls. The interactions between the particles and a wall are characterized solely by the hard sphere potential as well. Particles cannot overlap with the walls. Other bounding geometries such as fluid-fluid interfaces or roughened walls require separate consideration; although, the methods and algorithms presented may be applied with some modification to these more exotic situations.

Chapter 3

A single particle near a single plane wall

3.1 Introduction

The solution of two body problems in Stokes flow originates with Jeffrey's (1915) analysis of solids of revolution rotating about their symmetry axis. Bi-spherical coordinates and separation of variables were used to compute the additional resistance to the rotation of a spherical particle about the axis normal to a plane and due to the no-slip condition on the plane wall. This particular resistance couple is finite at contact. Brenner (1961) tackled the axisymmetric problem of a sphere approaching a plane wall in much the same way, while O'Neill (1964) and Dean and O'Neill (1963), determined respectively, the resistance to the transverse translation and rotation of a sphere near a plane wall. Subsequently, Goldman, Cox and Brenner (1967) computed the force and torque required to hold a spherical particle fixed in a shear flow near a plane wall. While other investigations of these quantities both using alternative methods and superior numerical techniques have found the results sound [Cichocki and Jones (1998) and Chaoui and Feuillebois (2002)], there remains a hole in the literature regarding the complete set of force moment to velocity moment couples. This is the stresslet induced by the deformation of a sphere near a plane wall – one of the key quantities for determining the stress in a suspension of spheres. Similarly, past studies of shear flow have published values for two quantities of particular interest related to a fixed sphere and a force- and torque-free sphere above a plane wall. The components of the grand resistance tensor coupling the lateral force and torque to deformation or equivalently the stresslet to transverse translation and rotation remain virtually undiscussed.

This chapter separates the analysis of single particle motion near a single wall into two parts. The first is concerned with axisymmetric motions (those normal to the wall) of the particle and fluid while the second concerns transverse motions. The method of separation of variables in bi-spherical coordinates is used to compute these quantities as a function of the distance between the particle and the plane wall. Additionally, the asymptotic limits of these expressions are derived to log-linear order through application of the well known asymptotic expressions for nearly touching spheres in Stokes flow [see *e.g.* Corless and Jeffrey (1988)]. It is shown that the exact resistance couples match the asymptotic expressions and that the appropriate combination of these quantities reproduces known results for a particle near a plane in a shear flow.

3.2 Analysis

For a single spherical particle of radius b, a distance h from a no-slip plane wall and with normal $\mathbf{e}_3$, symmetry can be used to show that the resistance tensor can be broken down geometrically into components relating perpendicular and parallel motions to the corresponding force component of each moment. The component corresponding to tensor $\mathbf{R}$ is denoted $R/6\pi\eta b^n$ where n is chosen for dimensional consistency. For example,

$$F_3^H = 6\pi\eta b R_{FU,33} U_3, \tag{3.1}$$

$$L_3^H = 6\pi\eta b^3 R_{L\Omega,33} \Omega_3, \tag{3.2}$$

$$\tag{3.3}$$

and

$$F_i^H = -6\pi\eta b\left(R_{FU,ii}U_i + (-1)^i bR_{F\Omega}\Omega_{3-i} + bR_{FE}E_{i3}\right) \tag{3.4}$$

$$L_i^H = -6\pi\eta b^2\left((-1)^i R_{LU}U_{3-i} + bR_{L\Omega,ii}\Omega_i + (-1)^i bR_{LE}E_{(3-i)3}\right) \tag{3.5}$$

$$S_{i3}^H = -6\pi\eta b^2\left(R_{SU}U_i + (-1)^i bR_{S\Omega}\Omega_{3-i} + bR_{SE}E_{i3}\right), \tag{3.6}$$

$$\tag{3.7}$$

where $i = 1, 2$ corresponds to the parallel components of the force moment or motion, correspond to the axisymmetric and transverse motions respectively. The symmetry ascribed to Stokes flow forces the following equivalencies: $R_{F\Omega} = R_{LU}$, $R_{FE} = R_{SU}$, $R_{LE} = R_{S\Omega}$. While in general one need only compute one of the quantities in each symmetric pair by solving the appropriate Stokes flow problem, both are computed here to gauge numerical precision.

3.2.1 Axisymmetric motion

For the rotation of a spherical particle about the axis normal to a nearby wall, the resistance couple to the torque on the particle is

$$R_{L\Omega,33} = \frac{4}{3}\sum_{n=0}^{\infty} \operatorname{csch}^3(n+1)\alpha, \tag{3.8}$$

where $\alpha = \cosh^{-1}(h/b)$ [Jeffrey (1915)]. Similarly, for a spherical particle translating towards a nearby wall, the resistance couple to the force on the particle is

$$R_{FU,33} = \frac{4}{3}\sinh\alpha\sum_{n=1}^{\infty}\frac{n(n+1)}{(2n-1)(2n+3)}\left[\frac{2\sinh(2n+1)\alpha + (2n+1)\sinh 2\alpha}{4\sinh^2(n+1/2)\alpha - (2n+1)^2\sinh^2\alpha} - 1\right], \tag{3.9}$$

as discussed by Brenner (1961). These relatively simple couples were computed via separation of variables in bi-spherical coordinates. Further discussion here is unnecessary, but the same method is expanded upon in the next section where the radial symmetry present in these two problems breaks down. A detailed explanation is laborious but not especially illustrative as by symmetry there is no stresslet (S_{i3}) arising from these motions.

3.2.2 Transverse motion

Consider a particle moving near and rolling across a stationary plane wall in the midst of a shear flow. The no-slip boundary condition on the fluid velocity field at the particle's surface is

$$u_\rho = [U + \Omega(z-h)]\cos(\phi), \tag{3.10}$$

$$u_\phi = -\,[U - \Omega(z-h)]\sin(\phi), \tag{3.11}$$

$$u_z = -\Omega\rho\cos(\phi), \tag{3.12}$$

where (ρ, ϕ, z) comprise a cylindrical coordinate system with axis of rotation coincident with the plane wall normal. At the wall, the fluid is stationary such that $\mathbf{u} = 0$, while far from the particle, a shear flow dominates:

$$u_\rho = \dot{\gamma} z\cos(\phi), \tag{3.13}$$

$$u_\phi = -\dot{\gamma} z\sin(\phi), \tag{3.14}$$

$$u_z = 0, \tag{3.15}$$

where $\dot{\gamma}$ is the shear rate. As the Stokes equations are linear, we will solve for the force, torque and stresslet corresponding to each of these motions separately, though, there are common features among them which will compress the analysis. If one subtracts the shear flow from the total flow, the boundary condition at the wall remains the same, while the boundary condition far away becomes $\mathbf{u} = 0$. The condition on the particle's surface becomes

$$u_\rho = \left[(U - \dot{\gamma}h) + \left(\Omega - \frac{1}{2}\dot{\gamma}\right)(z-h)\right]\cos(\phi) - \frac{1}{2}\dot{\gamma}(z-h)\cos(\phi), \tag{3.16}$$

$$u_\phi = -\left[(U - \dot{\gamma}h) - \left(\Omega - \frac{1}{2}\dot{\gamma}\right)(z-h)\right]\sin(\phi) + \frac{1}{2}\dot{\gamma}(z-h)\sin(\phi), \tag{3.17}$$

$$u_z = -\left(\Omega - \frac{1}{2}\dot{\gamma}\right)\rho\cos(\phi) - \frac{1}{2}\dot{\gamma}\rho\cos(\phi), \tag{3.18}$$

where through careful rearrangement, we have separated out the translational, rotational and deformational components of the shear flow (*i.e.* $U - \dot{\gamma}h$, $\Omega - \dot{\gamma}/2$, $\dot{\gamma}/2$ represent the net translation, net rotation and deformation, respectively). Remember it is the coupling between the deformational contribution to the shear flow and the force moments which comprises R_{FE}, R_{LE} and R_{SE}. Now the three independent motions: translation, rotation and deformation are clear, and one can show with little difficulty that the general solution to these equations is simply

$$u_\rho = \frac{1}{2c}\left[\rho W(\rho,z) + c(X(\rho,z) + Y(\rho,z)\right]\cos\phi, \tag{3.19}$$

$$u_\phi = \frac{1}{2}\left[X(\rho,z) - Y(\rho,z)\right]\sin\phi, \tag{3.20}$$

$$u_z = \frac{1}{2c}\left[zW(\rho,z) + 2cZ(\rho,z)\right]\cos\phi, \tag{3.21}$$

$$p = \frac{\eta}{c}W(\rho,z)\cos\phi, \tag{3.22}$$

where the unknown functions of ρ and z are determined by solution of the equations:

$$\frac{\partial^2 W}{\partial\rho^2} + \frac{1}{\rho}\frac{\partial W}{\partial\rho} - \frac{W}{\rho^2} + \frac{\partial^2 W}{\partial z^2} = 0, \tag{3.23}$$

$$\frac{\partial^2 X}{\partial\rho^2} + \frac{1}{\rho}\frac{\partial X}{\partial\rho} - \frac{4X}{\rho^2} + \frac{\partial^2 X}{\partial z^2} = 0, \tag{3.24}$$

$$\frac{\partial^2 Y}{\partial\rho^2} + \frac{1}{\rho}\frac{\partial Y}{\partial\rho} + \frac{\partial^2 Y}{\partial z^2} = 0, \tag{3.25}$$

$$\frac{\partial^2 Z}{\partial\rho^2} + \frac{1}{\rho}\frac{\partial Z}{\partial\rho} - \frac{Z}{\rho^2} + \frac{\partial^2 Z}{\partial z^2} = 0. \tag{3.26}$$

Again, it is convenient to define a set of bispherical coordinates (ξ, ϕ, μ) defined by the surfaces $\xi = 0$ and $\xi = \alpha$ which correspond to the wall and the particle respectively such that

$$\rho = \frac{c\sqrt{1-\mu^2}}{\cosh\xi - \mu}, \tag{3.27}$$

$$z = \frac{c\sinh\xi}{\cosh\xi - \mu}. \tag{3.28}$$

The scale parameter c is equivalent to $b\sinh\alpha$ and the center of the sphere is located by the formula $h = b\cosh\alpha$. This defines the parameter α. In these coordinates, the unknown functions are separable and may be represented as:

$$X(\xi,\mu) = (\cosh\xi-\mu)^{\frac{1}{2}}\sqrt{1-\mu^2}\sum_{n=1}^{\infty}\left[A_n\cosh\left(n+\frac{1}{2}\right)\xi\right]P_n'(\mu), \tag{3.29}$$

$$W(\xi,\mu) = (\cosh\xi-\mu)^{\frac{1}{2}}\sqrt{1-\mu^2}\sum_{n=1}^{\infty}\left[B_n\cosh\left(n+\frac{1}{2}\right)\xi + C_n\sinh\left(n+\frac{1}{2}\right)\xi\right]P_n'(\mu), \tag{3.30}$$

$$Y(\xi,\mu) = (\cosh\xi-\mu)^{\frac{1}{2}}\sum_{n=1}^{\infty}\left[D_n\cosh\left(n+\frac{1}{2}\right)\xi + E_n\sinh\left(n+\frac{1}{2}\right)\xi\right]P_n(\mu), \tag{3.31}$$

$$X(\xi,\mu) = (\cosh\xi-\mu)^{\frac{1}{2}}\left(1-\mu^2\right)\sum_{n=1}^{\infty}\left[F_n\cosh\left(n+\frac{1}{2}\right)\xi + G_n\sinh\left(n+\frac{1}{2}\right)\xi\right]P_n''(\mu), \tag{3.32}$$

where $P_n(\mu)$ is the Legendre polynomial of degree n. In terms of these functions, the force moments are:

$$F_i = \pi\eta c\int_{-1}^{1}\left(\frac{W}{2c}\frac{\partial\rho}{\partial\xi} - \frac{\rho}{2c}\frac{\partial W}{\partial\xi} - \frac{\partial Y}{\partial\xi}\right)\bigg|_{\xi=\alpha} d\mu, \tag{3.33}$$

$$L_i = \pi\eta\,\mathrm{csch}\alpha\int_{-1}^{1}\left[\frac{\partial}{\partial\xi}\left(\frac{1}{2}zW + cZ\right)\frac{\partial\rho}{\partial\xi} - \frac{\partial}{\partial\xi}\left(\frac{1}{2}\rho W + cY\right)\frac{\partial z}{\partial\xi}\right]\bigg|_{\xi=\alpha} d\mu, \tag{3.34}$$

$$\begin{aligned} S_{i3} = \frac{\pi\eta}{48}\int_{-1}^{1}(\cosh\xi-\mu)^{-4}\bigg\{&\frac{\partial W}{\partial\xi}\sqrt{1-\mu^2}\left[(1+2\mu^2)\cosh 3\xi - 4\mu(\cosh 2\xi - 3) - (5+6\mu^2)\cosh\xi\right] \\ &-8\frac{\partial X}{\partial\xi}(1-\mu^2)\sinh\xi(1-\mu\cosh\xi) + 2\frac{\partial Y}{\partial\xi}\left[5\mu(2+\mu^2)\cosh\xi - 2(2+\mu^2)\cosh 2\xi - \mu\left(10\mu - (2-\mu^2)\cosh 3\xi\right)\right] \\ &+4\frac{\partial Z}{\partial\xi}\sqrt{1-\mu^2}\sinh\xi\left[5+4\mu^2-12\mu\cosh\xi + (1+2\mu^2)\cosh\xi\right]\bigg\}\bigg|_{\xi=\alpha} d\mu. \end{aligned} \tag{3.35}$$

In general, by applying the boundary condition at the wall, one can show that:

$$B_n = (n-1)A_{n-1} - (2n+1)A_n + (n+2)A_{n+1}, \tag{3.36}$$

$$D_n = -\frac{1}{2}\left[n(n-1)A_{n-1} + (n+1)(n+2)A_{n+1}\right], \tag{3.37}$$

$$F_n = \frac{1}{2}\left(A_{n-1} - A_{n+1}\right), \tag{3.38}$$

while more complicated and specialized expressions for C_n, E_n, G_n arise from the boundary conditions on the particle itself. These are

$$C_n = c_n - 2k_n\left[\left(\frac{n-1}{2n-1}\right)A_{n-1} - A_n + \left(\frac{n+2}{2n+3}\right)A_{n+1}\right], \tag{3.39}$$

$$E_n = e_n + k_n\left[\left(\frac{n(n-1)}{2n-1}\right)A_{n-1} - \left(\frac{(n+1)(n+2)}{2n+3}\right)A_{n+1}\right], \tag{3.40}$$

$$G_n = g_n - k_n\left[\left(\frac{1}{2n-1}\right)A_{n-1} - \left(\frac{1}{2n+3}\right)A_{n+1}\right], \tag{3.41}$$

where $k_n = (n+1)\coth(n+1/2)\alpha - \coth\alpha$ and c_n, e_n, g_n correspond to the specific inhomogeneities set by the type of flow (*i.e.* translation, rotation or shear). The values of these inhomogeneities are specified for three linearly independent cases corresponding to these respective motions –

- $U - \dot{\gamma}h = 1$, $\Omega - \dot{\gamma}/2 = 0$, $\dot{\gamma}/2 = 0$:

$$c_n = 0, \tag{3.42}$$

$$e_n = \frac{2\sqrt{2}e^{-\left(n+\frac{1}{2}\right)\alpha}}{\sinh\left(n+\frac{1}{2}\right)\alpha}, \tag{3.43}$$

$$g_n = 0. \tag{3.44}$$

- $U - \dot{\gamma}h = 0$, $\Omega - \dot{\gamma}/2 = 1$, $\dot{\gamma}/2 = 0$:

$$c_n = \frac{4c\tau_n}{\sinh\alpha \sinh\left(n+\frac{1}{2}\right)\alpha}, \tag{3.45}$$

$$e_n = \frac{\sqrt{2}c(2n+1)e^{-\left(n+\frac{1}{2}\right)\alpha} - c\tau_n \mathrm{csch}\alpha}{\sinh\left(n+\frac{1}{2}\right)\alpha}, \tag{3.46}$$

$$g_n = -\frac{4c\tau_n}{\sinh\alpha \sinh\left(n+\frac{1}{2}\right)\alpha}, \tag{3.47}$$

where

$$\tau_n = -\frac{1}{\sqrt{2}}\left[\frac{e^{-\left(n-\frac{1}{2}\right)\alpha}}{2n-1} - \frac{e^{-\left(n+\frac{3}{2}\right)\alpha}}{2n+3}\right]. \tag{3.48}$$

- $U - \dot{\gamma}h = 0$, $\Omega - \dot{\gamma}/2 = 0$, $\dot{\gamma}/2 = 1$:

$$c_n = -\frac{4c\tau_n}{\sinh\alpha \sinh\left(n+\frac{1}{2}\right)\alpha}, \tag{3.49}$$

$$e_n = -\frac{\sqrt{2}c(2n+1)e^{-\left(n+\frac{1}{2}\right)\alpha} - c\tau_n \mathrm{csch}\alpha}{\sinh\left(n+\frac{1}{2}\right)\alpha} + \frac{2\sqrt{2}ce^{-\left(n+\frac{1}{2}\right)\alpha}}{\sinh\left(n+\frac{1}{2}\right)\alpha}\left(2n+1-\coth\alpha\right), \tag{3.50}$$

$$g_n = \frac{4c\tau_n}{\sinh\alpha \sinh\left(n+\frac{1}{2}\right)\alpha}. \tag{3.51}$$

Notice that these conditions corresponding to the deformation can actually be written in terms of a rotation (the first term) and a second inhomogeneity. As the problem for translation and rotation are solved independently, the conditions used in the numerical calculation are:

$$c_n = 0, \tag{3.52}$$

$$e_n = \frac{2\sqrt{2}e^{-\left(n+\frac{1}{2}\right)\alpha}}{\sinh\left(n+\frac{1}{2}\right)\alpha}\left(2n+1-\coth\alpha\right), \tag{3.53}$$

$$g_n = 0, \tag{3.54}$$

where the force moments for the deformation problem are a linear superposition of those due to a rotation with magnitude $\dot{\gamma}/2$ and those resulting from the Stokes flow subject to these refined conditions.

From continuity one may deduce a final condition which determines the values of A_n-G_n:

$$\begin{aligned}
&[(2n-1)k_{n-1}-(2n-3)k_n]\left[\frac{(n-1)A_{n-1}}{2n-1}-\frac{nA_n}{2n+1}\right] \\
&-[(2n+5)k_n-(2n+3)k_{n+1}]\left[\frac{(n+1)A_n}{2n+1}-\frac{(n+2)A_{n+1}}{2n+3}\right] \\
&=-\frac{1}{2}(n-1)c_{n-1}+\frac{5}{2}c_n+\frac{1}{2}(n+2)c_{n+1}-\frac{1}{2}e_{n-1}+e_n-\frac{1}{2}e_{n+1} \\
&+\frac{1}{2}(n-2)(n-1)g_{n-1}-(n-1)(n+2)g_n+\frac{1}{2}(n+2)(n+3)g_{n+1}.
\end{aligned} \tag{3.55}$$

This recurrence relation for A_n was solved via truncation and iteration with a tolerance of 10^{-13}, and the series solutions for the the velocity fields were generated by summing over 300 terms.

3.2.3 Lubrication expansions

The lubrication form of these constants (R^{lub}) is easily computed by considering the well studied problem of two spheres of unequal sizes (radii a and b) moving relative to one another at low-Reynolds-number. Corless and Jeffrey (1988) have computed these in the limit that χ, the dimensionless distance between the particles' surfaces, approaches zero, where χ may be re-expressed in terms of that same distance normalized by b alone and the ratio of the particle radii ($\beta = b/a$) as

$$\chi = 2\left(\frac{\epsilon-\beta}{1+\beta}\right). \tag{3.56}$$

In the limit that β approaches zero (*i.e.* radius a becomes large), while the dimensionless distance $\epsilon = h/b-1$ remains finite, the expressions for the coupling coefficients for unequal particles become those for a particle and a wall. These are indicated below, where the order unity constant is computed in the typical fashion by fitting the lubrication expression (in this case at $\epsilon = 10^{-3}$) to the exact solution computed via separation of variables.

$$R^{lub}_{FU,ii} = \frac{8}{15}\log\epsilon^{-1} - 0.9547 + \frac{64}{375}\epsilon\log\epsilon^{-1}, \tag{3.57}$$

$$R^{lub}_{FU,33} = \epsilon^{-1} + \frac{1}{5}\log\epsilon^{-1} + 0.9714 + \frac{1}{21}\epsilon\log\epsilon, \tag{3.58}$$

$$R^{lub}_{F\Omega} = R^{lub}_{LU} = \frac{2}{15}\log\epsilon^{-1} - 0.2540 - \frac{86}{375}\epsilon\log\epsilon^{-1}, \tag{3.59}$$

$$R^{lub}_{L\Omega,ii} = \frac{8}{15}\log\epsilon^{-1} + 0.4950 + \frac{88}{125}\epsilon\log\epsilon^{-1}, \tag{3.60}$$

$$R^{lub}_{L\Omega,33} = 1.5941 + \frac{2}{3}\epsilon\log\epsilon^{-1}, \tag{3.61}$$

$$R^{\mathrm{lub}}_{FE} = R^{\mathrm{lub}}_{SU} = \frac{7}{15}\log\epsilon^{-1} - 0.6173 + \frac{221}{375}\epsilon\log\epsilon^{-1}, \tag{3.62}$$

$$R^{\mathrm{lub}}_{LE} = R^{\mathrm{lub}}_{S\Omega} = \frac{2}{15}\log\epsilon^{-1} - 0.1245 - \frac{4}{375}\epsilon\log\epsilon^{-1}, \tag{3.63}$$

$$R^{\mathrm{lub}}_{SE} = \frac{16}{15}\log\epsilon^{-1} - 1.241 + \frac{788}{375}\epsilon\log\epsilon^{-1}. \tag{3.64}$$

3.3 Results

Table 3.1 depicts the exact and lubrication approximations for the six coupling constants relating the force and torque to translation and rotation of a particle near a wall. For posterity, the symmetric quantities $R_{F\Omega}$ and R_{LU} are both computed. They arise from independent solutions of the Stokes equations and the comparison of the two is meant to measure the accuracy of the methods entailed.

In table 3.2 the exact and lubrication approximations for the five coupling constants for the stresslet or the deformation are presented. The symmetric quantities (R_{FE}, R_{SU} and R_{LE}, $R_{S\Omega}$) which are computed exactly are equivalent to one another to within six digits accuracy. Similarly, the lubrication approximations for these expressions match the exact solution to within two digits accuracy at separations between particle and surface of nearly two percent of a particle radius. Note that in the article by Bossis, Meunier and Sherwood (1991), the $O(1)$ constant stated for the lubrication expansion of R_{FE} is -0.615, and similarly, the $O(1)$ contribution for R_{LE} is -0.122. These are suggestively comparable and depend on the method used to compute the exact solution before fitting. The verification of the exact solution requires comparison to still other studies.

$\epsilon \times 10^3$	$R^{\text{exact}}_{FU,ii}$	$R^{\text{lub}}_{FU,ii}$	$R^{\text{exact}}_{FU,33}$	$R^{\text{lub}}_{FU,33}$	$R^{\text{exact}}_{L\Omega,ii}$	$R^{\text{lub}}_{L\Omega,ii}$	$R^{\text{exact}}_{L\Omega,33}$	$R^{\text{lub}}_{L\Omega,33}$	$R^{\text{exact}}_{F\Omega}$	R^{exact}_{LU}	R^{lub}_{LU}
1.000	4.640	4.640	1002	1002	4.184	4.184	1.598	1.599	0.6655	0.6655	0.6655
1.492	4.427	4.427	672.5	672.5	3.973	3.973	1.597	1.601	0.6128	0.6128	0.6115
2.226	4.215	4.214	451.4	451.4	3.763	3.762	1.595	1.603	0.5605	0.5605	0.5573
3.321	4.003	4.002	303.2	303.2	3.553	3.552	1.592	1.607	0.5085	0.5085	0.5027
4.954	3.792	3.790	203.9	203.9	3.346	3.344	1.588	1.612	0.4571	0.4571	0.4477
7.391	3.581	3.578	137.3	137.2	3.141	3.138	1.583	1.618	0.4064	0.4064	0.3920
11.02	3.372	3.368	92.62	92.62	2.939	2.934	1.576	1.627	0.3567	0.3567	0.3357
16.45	3.164	3.157	62.59	62.59	2.741	2.733	1.567	1.639	0.3082	0.3082	0.2782
24.54	2.958	2.948	42.47	42.47	2.548	2.536	1.555	1.655	0.2614	0.2614	0.2195
36.61	2.755	2.739	28.96	28.95	2.362	2.344	1.541	1.675	0.2168	0.2168	0.1593
54.62	2.555	2.532	19.88	19.87	2.185	2.157	1.523	1.700	0.1749	0.1749	0.0973
81.49	2.361	2.327	13.77	13.75	2.019	1.976	1.502	1.730	0.1365	0.1365	0.0335
121.6	2.174	2.122	9.648	9.629	1.868	1.799	1.477	1.765	0.1021	0.1021	−0.0318
181.4	1.995	1.918	6.870	6.840	1.732	1.623	1.451	1.801	0.0726	0.0726	−0.0974
270.6	1.827	1.712	4.989	4.945	1.617	1.441	1.424	1.830	0.0484	0.0484	−0.1608
403.7	1.672	1.501	3.711	3.647	1.522	1.237	1.398	1.838	0.0298	0.0298	−0.2170
602.3	1.533	1.277	2.842	2.748	1.450	0.980	1.376	1.798	0.0166	0.0166	−0.2564
898.6	1.412	1.028	2.249	2.110	1.399	0.6195	1.358	1.658	0.0083	0.0083	−0.2616
1340	1.310	0.732	1.845	1.641	1.367	0.0626	1.347	1.333	0.0036	0.0036	−0.2029
2000	1.227	0.349	1.569	1.267	1.349	−0.8508	1.340	0.6699	0.0014	0.0014	−0.0283

Table 3.1: The coupling coefficients comprising components of the grand resistance tensor for a particle in translating and rotating near a plane wall.

$\epsilon \times 10^3$	R^{exact}_{FE}	R^{exact}_{SU}	R^{lub}_{FE}	R^{exact}_{LE}	$R^{\text{exact}}_{S\Omega}$	R^{lub}_{LE}	R^{exact}_{SE}	R^{lub}_{SE}
1.000	2.610	2.610	2.610	0.7965	0.7965	0.7965	6.142	6.142
1.492	2.426	2.426	2.425	0.7432	0.7432	0.7431	5.721	5.721
2.226	2.241	2.241	2.241	0.6901	0.6901	0.6897	5.303	5.303
3.321	2.058	2.058	2.057	0.6370	0.6370	0.6363	4.887	4.887
4.954	1.877	1.877	1.875	0.5840	0.5840	0.5829	4.476	4.476
7.391	1.697	1.697	1.694	0.5313	0.5313	0.5294	4.070	4.070
11.02	1.519	1.519	1.516	0.4788	0.4788	0.4760	3.672	3.672
16.45	1.345	1.345	1.339	0.4268	0.4268	0.4224	3.284	3.282
24.54	1.176	1.176	1.166	0.3754	0.3754	0.3688	2.908	2.905
36.61	1.012	1.012	0.9975	0.3249	0.3249	0.3152	2.548	2.541
54.62	0.8549	0.8549	0.8330	0.2758	0.2758	0.2614	2.208	2.194
81.49	0.7072	0.7072	0.6732	0.2285	0.2285	0.2076	1.892	1.863
121.6	0.5705	0.5705	0.5170	0.1837	0.1837	0.1537	1.604	1.545
181.4	0.4469	0.4469	0.3619	0.1422	0.1422	0.0998	1.349	1.231
270.6	0.3381	0.3381	0.2011	0.1051	0.1051	0.0460	1.130	0.8966
403.7	0.2457	0.2457	0.0218	0.0733	0.0733	−0.0075	0.9495	0.4961
602.3	0.1704	0.1704	−0.2007	0.0475	0.0475	−0.0602	0.8079	−0.0584
898.6	0.1120	0.1120	−0.5108	0.0282	0.0282	−0.1113	0.7044	−0.9248
1340	0.0693	0.0693	−0.9856	0.0152	0.0152	−0.1594	0.6351	−2.379
2000	0.0403	0.0403	−1.758	0.0073	0.0073	−0.2021	0.5937	−4.893

Table 3.2: The coupling coefficients comprising components of the grand resistance tensor for a particle in shear flow near a plane wall.

$\epsilon \times 10^3$	$\hat{F}^{\text{exact}}$	$\hat{L}^{\text{exact}}$	$\hat{F}^{\text{G-C-B}}$	$\hat{L}^{\text{G-C-B}}$	$\hat{F}^{\text{C-J}}$	$\hat{L}^{\text{C-J}}$	$\hat{F}^{\text{C-F}}$	$\hat{L}^{\text{C-F}}$
3.202	1.69822	0.944257	1.6982	0.94427	1.6989	0.94410	1.69822	0.944257
40.53	1.66813	0.947685	1.6682	0.94769	1.6684	0.94768	1.66810	0.947688
112.8	1.61592	0.953724	1.6160	0.95374	1.6160	0.95374	1.61591	0.953725
543.1	1.43914	0.974227	1.4391	0.97419	1.4391	0.97423	1.43915	0.974226
1352	1.27796	0.990123	1.2780	0.99010	1.2780	0.99012	1.27796	0.990123

Table 3.3: A comparison of the force and torque on a sphere held fixed in a shear flow.

Consider the force and torque on a spherical particle held fixed above a plane wall in shear flow. This problem was studied by Goldman, Cox and Brenner (1967), G–C–B, using the separation of variables technique, Cichocki and Jones (1998), C–J, via Stokes eigenfunction expansion and was rigorously approached by Chaoui and Feuillebois (2002), C–F. The corresponding quantities may be computed via direct arithmetic with the transverse coupling coefficients arising from the grand resistance tensor, *viz.*

$$\hat{F} = F/(6\pi\eta b h E) = R_{FU,ii} - \frac{b}{h}\left(\frac{1}{2}R_{F\Omega} + R_{FE}\right), \tag{3.65}$$

$$\hat{L} = L/(6\pi\eta b^3 E) = R_{L\Omega} - \frac{h}{b}R_{LU,ii} - R_{LE}. \tag{3.66}$$

Note, the dependence on the distance from the wall is implicit. While there is enough information contained in $\hat{F}$ and $\hat{L}$ to compute the deformation coupling constants, the quantitative accuracy of the present results may be judged by comparison. This serves as an indirect verification of the completely novel computation of the stresslet-deformation coupling. A direct comparison to this past work is made in table 3.3.

3.4 Conclusion

The dynamic simulation of particles at low-Reynolds-number requires calculation of the grand resistance tensor. While the particle motion is governed strictly by the coupling of force and torque to relative translation, rotation and deformation, these are insufficient for determination of suspension properties (*i.e* the shear viscosity) where the relationship between stresslet and relative deformation is essential. This quantity was computed precisely for a single spherical particle above a plane wall as a function of the distance between the particle and the wall. In particular, the data within the chosen range of particle-wall separations is one of several essential components for incorporation of confinement effects into Stokesian Dynamics simulations [Swan and Brady (2007)]. There are broader applications of these results for the calculation of energy dissipation in biological systems [see *e.g.* Cisneros *et al.* (2007)] and the properties of suspensions in geometries with large radii of curvature relative to the particle radii [Liron (1984)].

Bibliography

[1] G. Bossis, A. Meunier and J.D. Sherwood. Stokesian Dynamics simulations of particle trajectoriers near a plane. *Phys. Fluids A*, 3(8):1853–1858, 1991.

[2] H. Brenner. The slow motion of a sphere through a viscous fluid towards a plane surface. *Chem. Eng. Sci.*, 16:242–251, 1961.

[3] M. Chaoui and F. Feuillebois. Creeping flow around a sphere in a shear flow close to a wall. *Q. J. Mech. Appl. Math.*, 56(3):381–410, 2002.

[4] B. Cichocki and R.B. Jones. Image representation of a spherical particle near a hard wall. *Physica A*, 258:273–302, 1998.

[5] L.H. Cisneros *et al.* Fluid dynamics of self-propelled microorganisms, from individuals to concentrated populations. *Exp. Fluids*, 43:737–753, 2007.

[6] R.M. Corless and D.J. Jeffrey. Stress moments of nearly touching spheres in low Reynolds number flow. *J. Appl. Math. and Phys.*, 39:874–884, 1988.

[7] W.R. Dean and M.E. O'Neill. A slow motion of viscous liquid caused by the rotation of a solid sphere. *Mathematika*, 10:13–24, 1963.

[8] A.J. Goldman, R.G. Cox and H. Brenner. Slow viscous motion of a sphere parallel to a plane wall. II. Couette flow. *Chem. Eng. Sci.*, 22:653–660, 1967.

[9] G.B. Jeffery. On the steady rotation of a solid of revolution in a viscous fluid. *Proc. of London Math. Soc.*, 2:1414 327–338, 1915.

[10] N. Liron. Stokeslet arrays in a pipe and their application to ciliary trasport. *J. Fluid Mech.*, 143:173–195, 1984.

[11] M.E. O'Neill. A slow motion of viscous liquid caused by a slowly moving solid sphere. *Mathematika*, 11:67–74, 1964.

[12] J.W. Swan and J.F. Brady. Simulation of hydrodynamically interacting particles near a no-slip boundary. *Phys. Fluids*, 19(11):113306, 2007.

Chapter 4

Many particles near a single plane wall

4.1 Introduction

There is a twofold motivation for developing a new approach to modeling the dynamics of many colloidal particles suspended above a plane wall. First, in order to study the Brownian motion of colloidal particles near a wall, it is essential that the mobility tensor be symmetric [Kubo (1966)]. Second, the relatively simple and physically intuitive strategy first used in unbounded Stokesian Dynamics simulations [Durlofsky, Brady and Bossis (1987)] in which the mobility tensor is constructed directly from Faxén formulas, is easy to leverage and extend to study a number interesting problems. Although others have developed simulations of colloidal particles near a single wall, these studies lack either the crucial symmetry of the method herein [Bossis, Meunier and Sherwood (1991), Jendrejack, *et al.* (2004)] or the physical and mathematical straightforwardness of the original Stokesian Dynamics technique [Cichocki *et al.* (2000)]. In section 5.2 we discuss our approach to computing the mobility tensor from multipole expansions and Faxén formulas. Included is a discussion of why two previous approaches failed to compute symmetric mobility tensors and cannot be used for Brownian dynamics simulations. Examples are given illustrating the importance of the symmetry of the resistance and mobility tensors.

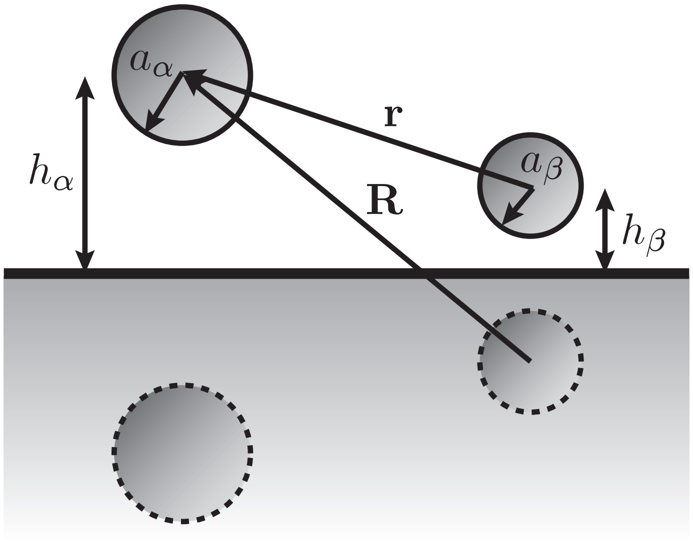

Figure 4.1: The interactions between a pair of spheres (α and β) near a plane wall where $h_\alpha = x_3^{(\alpha)} - H$ and $h_\beta = x_3^{(\beta)} - H$.

4.2 Analysis

The structure of (2.16) and its symmetries applies equally well to particles in an unbounded fluid as to particles adjacent to a wall or walls. Shown in figure 4.1 is a sample configuration of a pair of spheres (α, β) above a plane wall. The hydrodynamic flows generated by motion of these particles near the wall must produce symmetric interactions between the pair as well as between each particle and the wall. Two natural although not necessarily intuitive consequences are that for a single particle near a wall, there exists couplings between torque and translation and between force and rotation, and that these couplings are symmetric ($\mathbf{M}_{UL} = \mathbf{M}_{\Omega F}^T$). Some bacteria actually put these properties to work when swimming near a plane wall, smoothing out their almost chaotic run and tumble paths through the fluid [Lauga *et al.* (2006)]. Any model of the motion of particles in the low-Reynolds-number limit, no matter how approximate, should at a minimum preserve these traits as they are fundamental to the physics of Stokes flow. For instance, one of the reasons why the full Rotne-Prager approximation for $\mathbf{M}_{UF}$ in unbounded flows has proven so useful is that, even though it admits unphysical situations where particles may overlap, it is always symmetric, positive and definite [Rotne and Prager (1969)]. We proceed to demonstrate how to incorporate a plane wall into the hydrodynamic interactions between colloidal particles so that these tensors are symmetric, positive and definite.

Following the approach taken in the original Stokesian Dynamics method, we consider the disturbance velocity, $\mathbf{u}'(\mathbf{x})$, generated by a solid sphere of radius a_β with center at $\mathbf{x}_\beta$ a height h_β above a plane wall with force density on its surface denoted $\mathbf{f}$. This disturbance field can be separated into two parts:

$$\mathbf{u}'(\mathbf{x}) = \mathbf{u}^i(\mathbf{x}) + \mathbf{u}^w(\mathbf{x}), \tag{4.1}$$

where $\mathbf{u}^i(\mathbf{x})$ is the velocity field generated by an unbounded particle and $\mathbf{u}^w(\mathbf{x})$ is the reflection of the unbounded field off the plane wall such that the no-slip condition is satisfied:

$$\mathbf{u}^i(\mathbf{x}) + \mathbf{u}^w(\mathbf{x}) = 0, \tag{4.2}$$

when $\mathbf{x}$ is a point on the wall. We will need the Stokes flow Green's function, or Stokeslet, for the velocity field at $\mathbf{x}$ due to an isolated point force at $\mathbf{y}$:

$$\mathbf{J}(\mathbf{x}, \mathbf{y}) = \frac{1}{8\pi\eta}\left(\frac{\mathbf{I}}{r} + \frac{\mathbf{rr}}{r^3}\right), \tag{4.3}$$

where $\mathbf{I}$ is the identity tensor, $\mathbf{r} = \mathbf{x} - \mathbf{y}$, $r^2 = \mathbf{r}\cdot\mathbf{r}$ and η is the viscosity of the surrounding fluid. In addition, we need Blake's solution [Blake (1971)] for the image of a Stokeslet above a wall located at H in the fluid with normal $\boldsymbol{\delta}_3$:

$$\begin{aligned} \mathbf{J}^w(\mathbf{x}, \mathbf{y}; H) = {} & -\mathbf{J}(\mathbf{x}, \mathbf{y}') + (y_3 - H)^2 \nabla^2_{y'} \mathbf{J}(\mathbf{x}, \mathbf{y}') \cdot \mathbf{P} \\ & + 2(y_3 - H)\left(\mathbf{P} \cdot \nabla_{y'} \mathbf{J}(\mathbf{x}, \mathbf{y}') \cdot \boldsymbol{\delta}_3\right)^T, \end{aligned} \tag{4.4}$$

where $\mathbf{y}' = \mathbf{y} - 2(y_3 - H)\boldsymbol{\delta}_3$, $\mathbf{P} = \mathbf{I} - 2\boldsymbol{\delta}_3\boldsymbol{\delta}_3$ and the superscript T indicates transposition. With these we can write the exact solution for the disturbance velocity caused by particle β as:

$$\mathbf{u}'(\mathbf{x}) = \int_{S_\beta} \mathbf{G}(\mathbf{x}, \mathbf{y}; H) \cdot \mathbf{f}(\mathbf{y}) dS_y, \tag{4.5}$$

where the total Green's function is

$$\mathbf{G}(\mathbf{x}, \mathbf{y}; H) = \mathbf{J}(\mathbf{x}, \mathbf{y}) + \mathbf{J}^w(\mathbf{x}, \mathbf{y}; H). \tag{4.6}$$

From this exact expression we expand in surface moments the force density on particle β following the Stokesian Dynamics procedure to obtain

$$\begin{aligned} \mathbf{u}'(\mathbf{x}) = & \left(1 + \frac{a_\beta^2}{6}\nabla_y^2\right) \mathbf{G}(\mathbf{x}, \mathbf{y}; H)\bigg|_{\mathbf{y}=\mathbf{x}_\beta} \cdot \mathbf{F}_\beta + \frac{1}{2}\nabla_y \times \mathbf{G}(\mathbf{x}, \mathbf{y}; H)\bigg|_{\mathbf{y}=\mathbf{x}_\beta} \cdot \mathbf{L}_\beta \\ & + \left(1 + \frac{a_\beta^2}{10}\nabla_y^2\right) \mathbf{K}(\mathbf{x}, \mathbf{y}; H)\bigg|_{\mathbf{y}=\mathbf{x}_\beta} : \mathbf{S}_\beta + \ldots, \end{aligned} \tag{4.7}$$

where

$$\mathbf{K}(\mathbf{x}, \mathbf{y}; H) = \frac{1}{2}\left[\nabla_y \mathbf{G}(\mathbf{x}, \mathbf{y}; H) + (\nabla_y \mathbf{G}(\mathbf{x}, \mathbf{y}; H))^T\right]. \tag{4.8}$$

We choose to truncate these expressions at the stresslet level, though there is no reason that they cannot be expanded further to include higher order and faster decaying moments of the Green's function. The key step to obtaining the correct hydrodynamic interactions is to note that care must be used when taking the derivatives with respect to $\mathbf{y}$ of Blake's solution for the reflected velocity field: $\mathbf{J}^w(\mathbf{x}, \mathbf{y}; H)$ depends explicitly on both $\mathbf{y}$ and $\mathbf{x} - \mathbf{y}'$, reflecting the fact that the point force density $\mathbf{f}$ is distributed on the surface of the particle and not simply located at the particle's center. The correct derivatives are complex, but the following chain rules:

$$\begin{aligned}
\nabla_y \left(f(y_3)g(\mathbf{R})\right) &= \boldsymbol{\delta}_3 f'(y_3)g(\mathbf{R}) - f(y_3)\mathbf{P}\cdot\nabla_R g(\mathbf{R}),\\
\nabla_y^2 \left(f(y_3)g(\mathbf{R})\right) &= f''(y_3)g(\mathbf{R})\\
&\quad + 2f'(y_3)\boldsymbol{\delta}_3\cdot\nabla_R g(\mathbf{R}) + f(y_3)\nabla_R^2 g(\mathbf{R}),
\end{aligned} \tag{4.9}$$

where $\mathbf{R} = \mathbf{x} - \mathbf{y}'$, allow for considerable simplification of this process.

We can also use these expressions to say something about the reflections of higher order Stokes flow singularities from a plane wall. From equation 4.7, we see that a spherical particle with a constant force density on its surface denoted, $\mathbf{F}_\beta/4\pi a_\beta^2$, behaves as though it generates two singularities in the surrounding fluid at the particle's center. These singularities are the familiar Stokeslet and the source doublet ($\nabla_y^2\mathbf{J}(\mathbf{x},\mathbf{y})$). The same Fourier transform approach used to compute Blake's expression for the reflection of the Stokeslet ($\mathbf{J}^w(\mathbf{x},\mathbf{y};H)$) can be used to compute the reflection of the source doublet [Blake and Chwang (1974)]. While this procedure is arduous, the resulting reflection of the source doublet could have been used to generate the reflected field $\mathbf{u}^w(\mathbf{x})$ directly. Knowing that the Stokes equations are unique, we can see from equation 4.7 that the reflected field has only two contributions: Blake's reflection of the Stokeslet and one other which must be the reflection of the source doublet. This suggests a direct and facile way to compute reflections of higher order Stokes flow singularities, something which is quite subtle and has recently been a source of confusion [Lauga and Squires (2005)]. This approach has been used in similar circumstances [Higdon (1979)], but we state it here explicitly since it applies to any reflection of a Stokes flow singularity. Namely, no complicated Fourier transform or limiting process is needed to compute these reflections. One simply writes the higher order singularity as a derivative of the Stokeslet or other fundamental singularity with a given condition on the wall, and the reflection of that singularity is simply the same derivative (with respect to the source point, $\mathbf{y}$) of Blake's reflection or fundamental singularity. That is, we can simply write the no slip condition on the wall as:

$$\nabla_y^n\mathbf{J}(\mathbf{x},\mathbf{y}) + \nabla_y^n\mathbf{J}^w(\mathbf{x},\mathbf{y};H) = 0, \tag{4.10}$$

when $\mathbf{x}$ is a point on the plane wall ($x_3 = H$). This also suggests one way to simulate the hydrodynamics of particles constrained by more than one wall or some curvilinear geometry. If we know the reflection of the Stokeslet satisfying the boundary conditions on the wall, then we can compute the disturbance velocity generated by a particle with an arbitrary force density using the procedure just described.

The mobility tensor is constructed from the disturbance velocity field $\mathbf{u}'(\mathbf{x})$ and Faxén formulas for a particle near a wall, which, unfortunately are not known. However, we can by-pass the need to know the exact Faxén formulas with a wall by noting that the flow caused by the reflection from the wall $\mathbf{u}^w(\mathbf{x})$ is just another disturbance flow and has no singularities within the fluid region above the wall. Therefore, the usual, well-known [Kim and Karrila (2005)] Faxén formulas can be applied. That is, the Faxén formulas coupling a disturbance field in the fluid to the translational and rotational velocities of a spherical particle (α) of radius a_α centered at $\mathbf{x}_\alpha$ relative to the fluid ($\mathbf{U}_\alpha - \mathbf{U}_\alpha^\infty$, $\mathbf{\Omega}_\alpha - \mathbf{\Omega}_\alpha^\infty$) and the rate of strain of the fluid ($\mathbf{E}_\alpha^\infty$) are:

$$\mathbf{U}_\alpha - \mathbf{U}_\alpha^\infty = \frac{\mathbf{F}_\alpha}{6\pi\eta a_\alpha} + \left(1 + \frac{a_\alpha^2}{6}\nabla_x^2\right)\mathbf{u}'(\mathbf{x})\bigg|_{\mathbf{x}_\alpha}, \tag{4.11}$$

$$\mathbf{\Omega}_\alpha - \mathbf{\Omega}_\alpha^\infty = \frac{\mathbf{L}_\alpha}{8\pi\eta a_\alpha^3} + \frac{1}{2}\nabla_x \times \mathbf{u}'(\mathbf{x})\bigg|_{\mathbf{x}_\alpha}, \tag{4.12}$$

$$-\mathbf{E}_\alpha^\infty = \frac{\mathbf{S}_\alpha}{\frac{20}{3}\pi\eta a_\alpha^3} + \left(1 + \frac{a_\alpha^2}{10}\nabla_x^2\right)\mathbf{e}'(\mathbf{x})\bigg|_{\mathbf{x}_\alpha}, \tag{4.13}$$

where the disturbance rate of strain is

$$\mathbf{e}'(\mathbf{x}) = \frac{1}{2}\left(\nabla_x \mathbf{u}'(\mathbf{x}) + (\nabla_x \mathbf{u}'(\mathbf{x}))^T\right). \tag{4.14}$$

In principle, since we have a detailed knowledge of the disturbance field caused by particle β, we can compute how it interacts hydrodynamically with particle α. For that matter, if α and β are the same particle, we can compute the hydrodynamic interaction between just a single particle and a wall by only considering the reflected part of the disturbance field, $\mathbf{u}^w(\mathbf{x})$.

In order to complete our description of the hydrodynamic interactions, we need to compute the mobility and resistance tensors. Each term in the grand mobility tensor is constructed from the combination of a

Faxén formula with the singularities from a force multipole in the disturbance velocity field. As an example, we construct the term $\mathbf{M}_{UF}$ explicitly using equations 4.7 and 4.11 to characterize the coupling of a force on particle β to the relative velocity of particle α:

$$\mathbf{M}_{UF}^{\alpha\beta} = \left(1 + \frac{a_\alpha^2}{6}\nabla_x^2\right)\left(1 + \frac{a_\beta^2}{6}\nabla_y^2\right)\mathbf{G}(\mathbf{x},\mathbf{y};H)\Bigg|_{\mathbf{x}=\mathbf{x}_\alpha}^{\mathbf{y}=\mathbf{x}_\beta}. \tag{4.15}$$

The other grand mobility tensor terms are constructed analogously. One additional note is necessary, however. For the coupling between particle α and itself, we discard the disturbance velocities generated by the Stokeslet and use the reflected field alone in the Faxén formulas. This is illustrated for the term $\mathbf{M}_{UF}^{\alpha\alpha}$:

$$\mathbf{M}_{UF}^{\alpha\alpha} = \frac{\mathbf{I}}{6\pi\eta a_\alpha} + \left(1 + \frac{a_\alpha^2}{6}\nabla_x^2\right)\left(1 + \frac{a_\alpha^2}{6}\nabla_y^2\right)\mathbf{J}^w(\mathbf{x},\mathbf{y};H)\Bigg|_{\mathbf{x}=\mathbf{x}_\alpha}^{\mathbf{y}=\mathbf{x}_\alpha}. \tag{4.16}$$

All terms in the mobility tensor are given explicitly in appendix A.

The grand resistance tensor is simply the inverse of the grand mobility tensor. However, since we truncate the expansion generating the grand mobility tensor after a finite number of multipoles, this tensor is only a far-field approximation. We wish to include lubrication interactions which are only properly expressed after including a large (infinite) number of force multipoles. After inverting the fully truncated grand mobility tensor, we add in the exact lubrication forms for the resistance tensor for both the interactions between near pairs of particles [Kim and Karrila (2005)] ($\mathcal{R}^P$) and a particle near the wall [Bossis, Meunier and Sherwood (1991)] ($\mathcal{R}^W$). In addition to this, we subtract out the far-field contributions arising from the inversion of the grand mobility tensor ($\mathcal{R}^{P,\infty} + \mathcal{R}^{W,\infty}$) to avoid over counting the hydrodynamic interactions. The grand resistance tensor, $\mathcal{R}$, including these lubrication contributions is

$$\mathcal{R} = \mathcal{M}^{-1} + \mathcal{R}^P + \mathcal{R}^W - \left(\mathcal{R}^{P,\infty} + \mathcal{R}^{W,\infty}\right), \tag{4.17}$$

Elements of this resistance tensor can now be used in the Langevin equation for particle dynamics, correctly including the far-field, many-body hydrodynamic interactions and the singular, pairwise lubrication forces, and is symmetric positive-definite by construction. The details of how this is done can be found in the thorough discussion by Phung, Brady and Bossis (1996).

4.3 Results

4.3.1 Symmetric mobility and resistance tensors

The above approach follows the well-established Stokesian Dynamics procedure for constructing a symmetric, positive-definite mobility tensor, and so it is somewhat surprising that two prior studies of the problem of spherical particles moving in Stokes flow near a plane wall failed to compute symmetric mobility and resistance tensors. The first approach by Bossis, Meunier and Sherwood (1991) used a technique similar to the one discussed above in which they expand the reflection of the Stokeslet in force multipoles to derive the wall contribution to the mobility tensor. However, they did not appreciate that the reflection of the Stokeslet is a function of how far the point force is from the wall as well as the separation vector $\mathbf{x} - \mathbf{y}'$. We take care to write the reflection as $\mathbf{J}^w(\mathbf{x}, \mathbf{y}; H)$ which is an explicit function of a destination, a source and the location of the wall. Their multipole expansion presumes a dependence on $\mathbf{x} - \mathbf{y}'$ only and as a result, the mobility tensors stemming from this approach are not symmetric. In a quantitative sense, this error may not be large; however, their approach is unusable in the context of Brownian motion which requires a symmetric mobility tensor. Similarly, in their study of confined chains of Brownian particles, Jendrejack *et al.* (2004) compute numerically the reflection off a wall of the Rotne-Prager tensor. Recall that the R-P tensor is simply $\mathbf{J}^R(\mathbf{r}) = \left(1 + \frac{a^2}{3}\nabla_r^2\right)\mathbf{J}(\mathbf{r})$. They call this reflection the contribution to the mobility tensor due to the wall, but do not recognize that the Rotne-Prager tensor lacks a direct connection with the fluid velocity field surrounding the particle. It cannot be used to generate the reflection off the wall since it depends on a linear combination of the disturbance velocity generated by an isolated particle and its source doublet and not just the disturbance velocity itself. As shown earlier, the reflected velocity field is still subject to the Faxén formulas which produces extra quadrupolar and octupolar contributions to the mobility that are essential to maintaining symmetry. Again this method is unsuitable for simulating Brownian particles. Jendrejack *et.*

al. (2004) recognized that their mobility tensor was not symmetric and simply symmeterized it by adding the transpose and divding by two to conduct Brownian simulations. There is, unfortunately, no way to assess to accuracy of this manipulation.

4.3.2 Co-rotation of a doublet of particles

Illustrated in figure 4.2 is a pair of spherical particles of the same radius with equal and opposite torques applied along their line of centers. One can imagine accomplishing this by connecting a pair of spherical particles with a slender torsion wire and twisting those particles to load a torque into the wire. For a pair of particles in an unbounded fluid, the torque along the line of centers causes the particles to rotate about their line of centers in opposite directions while remaining otherwise still. However, when the doublet is brought near a wall, the particles both rotate and translate because the wall induces an additional coupling between torque and translation. Since these particles might be connected by a wire, the separation between the particles remains the same and the doublet spins about its center of mass. We can measure the tensile force on the wire as the doublet rotates, but one can show that because the grand mobility tensor is symmetric, this tensile force is exactly zero regardless of separation and height above the wall. In a model lacking symmetry, some non-zero force along the line of centers is necessary to maintain the separation between the particles. Interestingly, as indicated in figure 4.3, the rate of rotation of the doublet about its center of mass, Ω, normalized by the torque on the particles, $T/8\pi\eta a^3$, is a non-monotonic function of both the separation between the particles, r, and the height of the doublet above the wall, h. When the particles are far apart, the rate of rotation of the doublet is decreasing as r increases because the translational speed of a particle in the doublet ($\Omega r/2$) is set only by the coupling of a single particle to the wall. When the particles are far from the wall, the rate of rotation of the doublet is also decreasing as h increases. However this is caused by weakening interactions with the wall. Conversely, when the separation between the particles becomes quite small or the doublet is close to the wall, the rotation rate of the doublet also decreases because in this limit the resistance to motion of the particles becomes singular. Since the normalized rotation rate is decreasing in the limits that the particles are both near and far apart and the doublet is both near and far from the

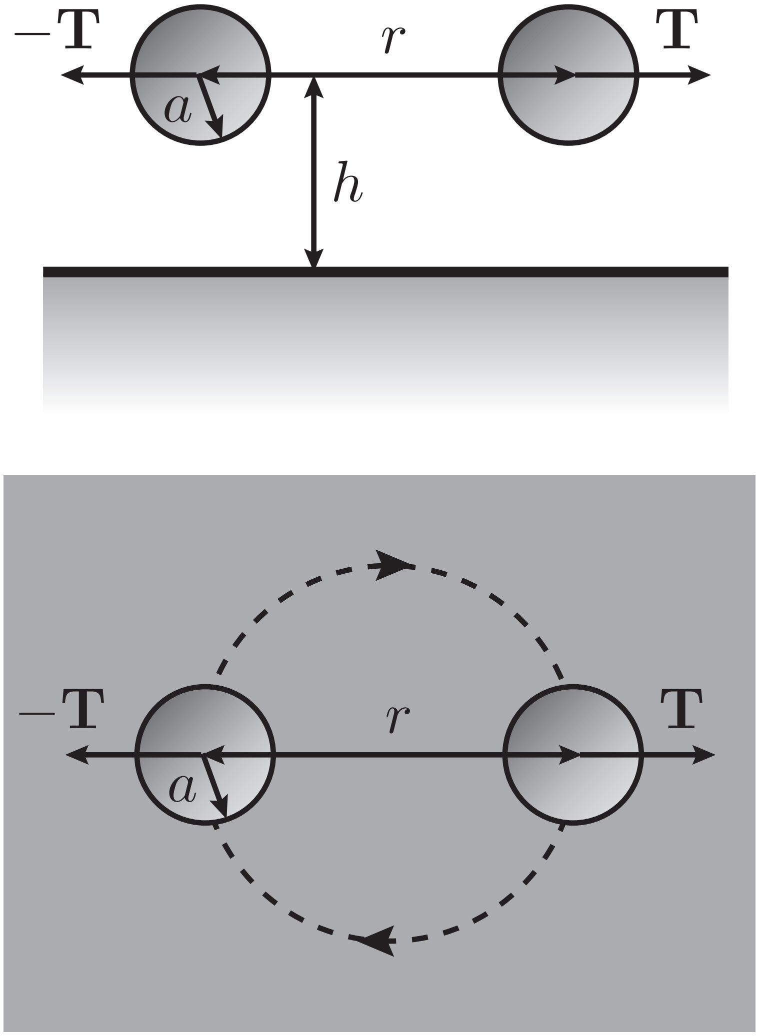

Figure 4.2: A side-on and top-down view of a pair of particles above a plane wall with equal and opposite torques T applied along their line of centers. The particles have the same radius a, are separated by a distance r and are a height h above the wall.

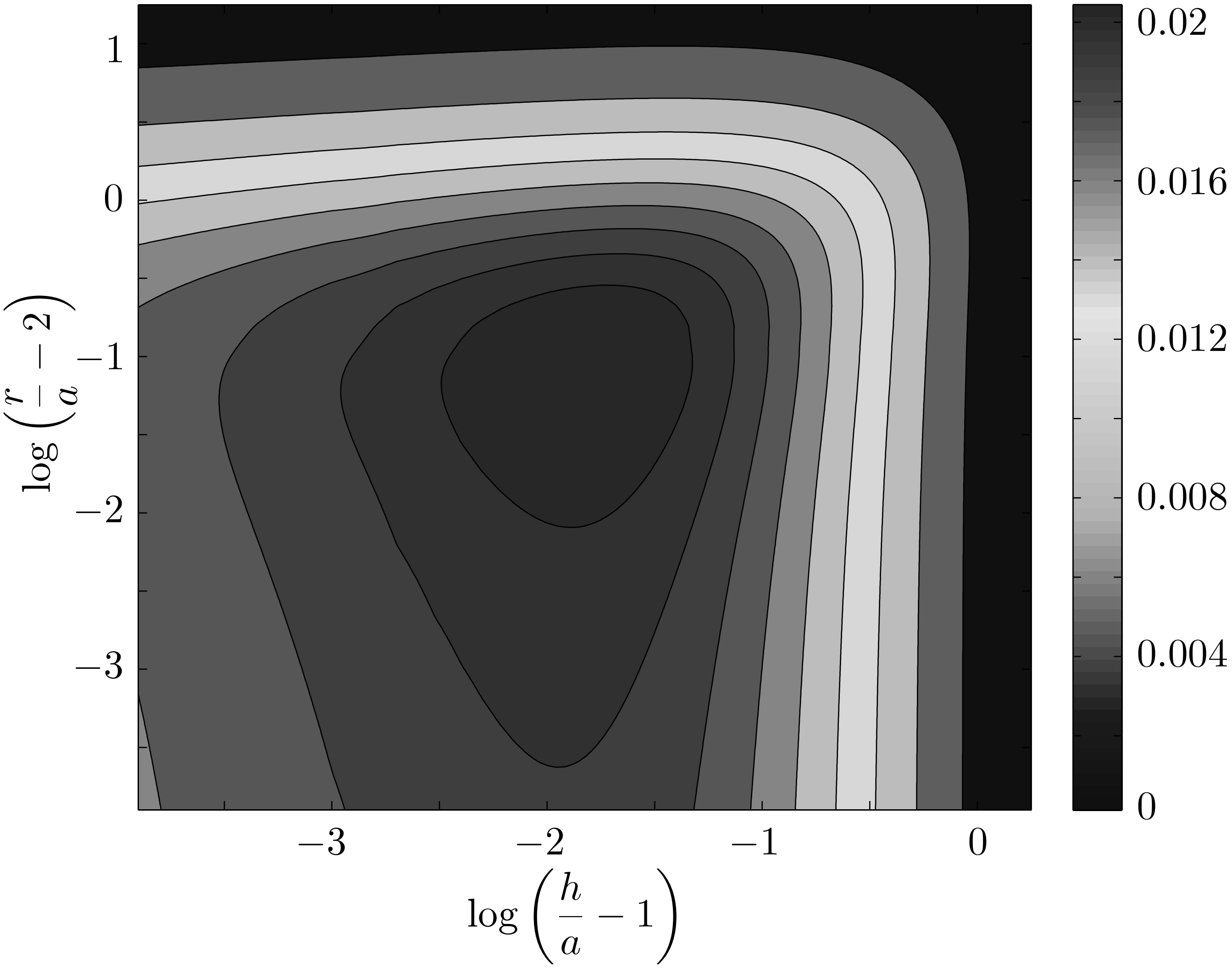

Figure 4.3: The rotation rate of the doublet about its center of mass normalized by the torque on the particles about their line of centers ($8\pi\eta a^3\Omega/T$). The normalized rate of rotation is maximum near $r = 2.1a$, $h = 1.01a$.

wall, it must reach a global maximum where the doublet rotates most quickly.

Since the torques on the particles are equal and opposite, the doublet is a force and torque free object. It can be thought of as a model for a number of different interesting systems. A recent study of bacteria swimming near a wall found that the head and flagellum of the organism co-rotate just like this doublet and for the exact same reason [Lauga *et al.* (2006)]. A swimming bacterium is a force and torque free object and in order to propel itself by torquing its flagellum it must also have an equal and opposite torque on its head. The study found that the same coupling to the wall that cause the doublet to co-rotate also cause a bacterium to sweep out arcs as it swims near a wall rather than swim straight. The only difference between the doublet and the bacterium is that the bacterium is also propelled along its line of centers.

4.3.3 Grand mobility tensors for any confining boundaries

The procedure described in section 5.2 is hardly limited to the single plane wall geometry. For any confining geometry, we can write the disturbance velocity field at $\mathbf{x}$ generated by a point force at $\mathbf{y}$ as

$$\mathbf{u}(\mathbf{x}) = \mathbf{G}(\mathbf{x}, \mathbf{y}; H_1, H_2, \ldots) \cdot \mathbf{f}(\mathbf{y}) = \mathbf{J}(\mathbf{x}, \mathbf{y}) \cdot \mathbf{f}(\mathbf{y}) + \mathbf{J}^w(\mathbf{x}, \mathbf{y}; H_1, H_2, \ldots) \cdot \mathbf{f}(\mathbf{y}), \tag{4.18}$$

where $\mathbf{J}^w(\mathbf{x}, \mathbf{y}; H_1, H_2, \ldots)$ is the reflection of the Stokeslet off the confining surfaces and $H_1, H_2, \ldots$ are just geometrical parameters. It is clear that the terms of the mobility tensor are constructed in exactly the same way as for a single plane wall. No changes in procedure are necessary since the process only relies on properties of the Stokes equations and not on the geometrical constraints.

As a specific example, consider particles in a fluid bounded by a flat and nondeformable free surface; the fluid is constrained only by a no-penetration condition at the surface. The Green's function in this case is similar to the plane wall Green's function. It is the sum of a Stokeslet above the interface and a Stokeslet with a reflected force density below the interface, *viz.*:

$$\mathbf{G}(\mathbf{x}, \mathbf{y}; H) = \mathbf{J}(\mathbf{x}, \mathbf{y}) + \mathbf{J}(\mathbf{x}, \mathbf{y}') \cdot \mathbf{P}. \tag{4.19}$$

Nothing about this Green's function precludes using equations 4.15 and 4.16 and their analogues to build up the grand mobility tensor. In fact, the same caveats for taking the derivatives with respect to the source, $\mathbf{y}$, apply to this Green's function too. A clever implementation of a traditional Stokesian Dynamics simulation can model this interface as well: by recognizing that a particle near a free surface acts as though there were an image particle with a reflected force density on its surface below the interface, one can simulate N particles near a free surface using those N particles and N image particles. The extra particles increase the computational time for conventional Stokesian Dynamics by a factor of eight over that for N unbounded particles. Using the method described herein with the Green's function in equation 4.19, that multiplicative factor is near unity.

It is worth noting further that the grand mobility tensor for particles near interfaces with even more complicated boundary conditions may be constructed by using this method directly or by using the linear combination of mobility tensors with simpler confinements. Consider particles moving near a flat and nondeformable liquid-liquid interface where the ratio of the viscosity of the confining liquid to the viscosity of the embedding liquid is λ. Constructing a simulation using image particles as in the free surface problem is now quite difficult. However, the Green's function in this case is a linear combination of the Green's functions for a free surface ($\mathbf{G}^F(\mathbf{x}, \mathbf{y}; H)$, eqn. 4.19) and a solid plane wall ($\mathbf{G}^W(\mathbf{x}, \mathbf{y}; H)$, eqn. 4.6):

$$\mathbf{G}(\mathbf{x},\mathbf{y}; H) = \left(\frac{1}{1+\lambda}\right) \mathbf{G}^F(\mathbf{x}, \mathbf{y}; H) + \left(\frac{\lambda}{1+\lambda}\right) \mathbf{G}^W(\mathbf{x}, \mathbf{y}; H), \tag{4.20}$$

so that changing λ from zero to infinity transitions from the free surface boundary to the plane wall boundary [Lee, Chadwick and Leal (1979)]. Taking this same linear combination of the grand mobility tensors for particles near a free surface and particles near a plane wall generates the grand mobility tensor for particles near a liquid-liquid interface. As before, a resistance tensor may be constructed from the mobility tensor, where now one needs the resistance interactions for a single particle adjacent to a free surface or a liquid-liquid interface.

4.4 Conclusions

We have constructed a symmetric, positive-definite mobility tensor for particles near a plane wall. Additionally, we have shown how to compute a symmetric, positive-definite mobility tensor for particles in any confining geometry given the reflection of the Stokeslet off the confining walls. Interestingly, the scaling of the Stokesian Dynamics algorithm with respect to the number of particles is independent of any confining geometry and only a few more computations per particle pair are necessary to build up the resistance and mobility tensors. While the expressions for the elements of the grand mobility terms in the appendices are algebraically complicated, they may be tabulated and used with efficient table lookup procedures for dynamic simulation. Following this approach, one can now use Stokesian Dynamics to study the behavior of suspensions of spherical particles in arbitrary confining geometries. In an even simpler approach, one may approximate certain confinements such as the parallel plate geometry by superimposing the mobility tensors due to a pair of plane walls with opposing normals. There are some indications that this approximation can be quite accurate [Dufresne, Altman and Grier (2001)], though it does trade the convenience of superposition for the fidelity of the exact two wall reflection. In the next chapter, the accuracy of this approximation is examined.

Symmetry and positive-definiteness of the mobility tensor are fundamental to the hydrodynamic interactions between particles in Stokes flow and are essential to simulating Brownian motion. We have chosen to study the static properties of particle pairs here, illustrating the importance of symmetry in the physically interesting problem of a force and torque free doublet rotating above a plane wall. The Brownian motion of particles may be generated directly from the tensors derived herein, and can be used to study various dynamic processes of Brownian particles near a plane wall including self-assembly and colloidal crystallization using these tensors in Stokesian Dynamics simulations.

Bibliography

[1] J.R. Blake. A note on the image system for a Stokeslet in a no-slip boundary. *Proc. Cam. Phil. Soc.*, 70:303–310, 1971.

[2] J.R. Blake and A.T. Chwang. Fundamental singularities of viscous flow. *J. Eng. Math.*, 8(1):23–29, January 1974.

[3] G. Bossis, A. Meunier, and J. D. Sherwood. Stokesian Dynamics simulations of particle trajectories near a plane. *Phys. Fluids*, 3(8):1853–1858, August 1991.

[4] B. Cichocki, R. B. Jones, R. Kutteh, and E. Wajnryb. Friction and mobility for colloidal spheres in stokes flow near a boundary. *J. Chem. Phys.*, 112(5):2548–2561, February 2000.

[5] E.R. Dufrense, D. Altman, and D.G. Grier. Brownian dynamics of a sphere between parallel walls. *Europhysics Letters*, 53(2):264–270, January 2001.

[6] L.J. Durlofsky, J. F. Brady, and G. Bossis. Dynamic simulation of hydrodynamically interacting particles. *J. Fluid Mech.*, 180:21–49, June 1987.

[7] L.J. Durlofsky and J.F. Brady. Dynamic simulation of bounded suspensions of hydrodynamically interaction particles. *J. Fluid Mech.*, 200:39–67, January 1989.

[8] J.J.L. Higdon. The generation of feeding currents by flagellar motions. *J. Fluid Mech.*, 94(2):305–330, 1979.

[9] R.M. Jendrejack, D.C. Schwartz, J.J. de Pablo, and M.D. Graham. Shear-induced migration in flowing polymer solutions. *J. Chem. Phys.*, 120(5):2513–25–29, February 2004.

[10] S. Kim and S.J. Karrila. *Microhydrodynamics.* Dover Publications Inc., 2 edition, 1991, 2005.

[11] R. Kubo. The fluctuation-dissipation theorem. *Reports on Progress in Physics*, 29(1):255–284, 1966.

[12] E. Lauga and T.M. Squires. Brownian motion near a partial-slip boundary. *Phys. Fluids*, 17:103102, October 2005.

[13] E. Lauga, W.R. DiLuzio, G.M. Whitesides, and H.A. Stone. Swimming in circles: motion of bacteria near solid boundaries. *Biophysical Journal*, 90:400–412, January 2006.

[14] S.H. Lee, R.S. Chadwick, and L.G. Leal. Motion of a sphere in the presence of a plane interface. part 1. an approximate solution by generalization of the method of Lorentz. *J. Fluid Mech.*, 93(4):705–726, 1979.

[15] T.N. Phung, J.F. Brady, and G. Bossis. Stokesian Dynamics simulations of brownian suspensions. *J. Fluid Mech.*, 313:181–207, December 1996.

[16] J. Rotne and S. Prager. Variational treatment of hydrodynamic interaction in polymers. *J. Chem. Phys.*, 50(11):4831–4837, June 1969.

Chapter 5

A single particle between parallel plane walls

5.1 Introduction

Some time ago, Faxén (1923) approached the problem of particle motion between parallel walls by noting the similarities between Laplace's equation and the Stokes equations. Expressing the fundamental solution to Laplace's equation in three dimensions ($1/r$) as an integral, he wrote down the general solution to the Stokes equations between a set of parallel walls in integral form. Here, we produce an equivalent result using the direct process of transforming the Stokes equations from real-space to Fourier space; after all, Faxén's procedure yields a general solution to the Stokes equations in Fourier space. Inverting this solution is rather difficult for all but a few specific geometric configurations that Faxén, to his credit, was able to interrogate. The details of this calculation are available in the text by Happel and Brenner (1986). Before solving the parallel wall problem, Faxén computed the resistance to the motion of a spherical particle in the half space above a single plane wall. In order to forego the difficulties associated with satisfying the boundary conditions on the two walls lining a channel, Oseen (1928) suggested that a linear superposition of the resistance due each plane wall separately would make for a suitable estimate. This approach has seen some empirical success, but the approximation made can be quite substantial. It poses a severe computational challenge as it fails to yield a positive-definite grand mobility tensor – something that is essential to the physics of Stokes flow and critical for the rapid computation of hydrodynamic interactions among many particles.

Blake (1974) brought an electrostatic perspective and solved the problem of a point force in the half space above a single plane wall in Stokes flow. He introduced the notion of an image flow below the plane wall that satisfies the Stokes equations and cancels the flow due to the point force exactly where the plane wall bounds the half space. The proper manipulation of this expression has proven quite useful recently in the simulation of many particles near a plane wall boundary (Swan and Brady, 2007). Following on Blake's approach, Liron and Mochon (1976) found that an infinite but convergent series of hydrodynamic images was necessary to satisfy the boundary conditions on two plane walls with a point force between them. Summation of this series is possible but ineffective for rapid simulation of particle dynamics. However, this result helps us understand why inversion of Faxén's Fourier space results into an analytical, real-space result like Blake's proves so difficult: since the Stokes equations are unique, the result must be the same as Liron and Mochon's infinite sums, which themselves are quite complicated.

There have been a number of attempts to simulate suspensions of spherical particles between parallel walls. Durlofsky and Brady (1989) discretized the force density on the walls and used this to calculate the effects of the walls on a finite set of particles embedded in the fluid. Following Nott and Brady (1994), Singh and Nott (2000) used spherical particles fixed in space as a model of channel walls in plane Couette flow. Both of these methods model the channel walls as plane surfaces which are, for lack of better terms, "leaky" and "slippery." Cichocki *et al.* (2000), Bhattacharya and Blawzdziewicz (2002) and Jones (2004) have had much success using Fourier transform techniques in addition to an eigenfunction expansion of the solution to Stokes flow in the parallel wall geometry to calculate the image flows due to two walls. While this result must be the same as Liron and Mochon's, it satisfies the boundary conditions on the walls at each level of the eigenfunction expansion, which is a clear advantage. Their expansion, however, does not make a direct physical connection to the moments of the force density on the particle's surface, and also has an implicit dependence of the solution on the channel width. Other approaches to the computation of the channel mobility have similar features (Ganatos *et al.*, 1980: boundary collocation method; Staben *et al.*, 2003: boundary integral method). Our approach utilizes a physical connection to the force moments of a particle between parallel walls, which affords, in our opinion, novel, more intuitive and applicable results.

A number of researchers have made experimental measurements of the in-plane diffusivity of a particle between parallel walls. Dufresne *et al.* (2001) did a thorough job of comparing many of the analytical approaches to the diffusivity of a single particle in a channel measured via optical tweezer microscopy. They find that all of the approaches, while giving different results, fall equally near the experimental data and well within the margins of error. Unfortunately like previous studies, these disappoint when it comes to decoupling the three separate length scales in the problem: the characteristic size of the particle, a; the separation between the channel walls, H; and the height of the particle above one of the channel walls, h. Distinguishing clearly among these is essential to understanding how *many* particles behave in a bounded geometry. As Stokes flows tend to decay slowly, the effects of interactions with the walls are often just as important as those between particles themselves. We attempt to remedy this shortcoming here.

The chapter is organized as follows. In section 5.2 we detail the development of the grand mobility tensor from Faxén formulas and multipole expansions and briefly discuss the relevant velocity fields for flow between parallel walls. We introduce the Fourier transform solution to the Stokes equations between parallel walls and demonstrate that this can be used to develop an integral expression for components of the grand mobility tensor for a single particle in a channel. In particular, we show that each element of the grand mobility tensor can be written in terms of inverse powers of the channel width. In section 5.3 we plot the elements of the grand mobility tensor for coupling between translation, rotation and rate of strain with force, torque and stresslet. We also show how these collapse down to the single wall results in the limit that the channel is infinitely wide. We use a Stokesian Dynamics simulation to calculate the fall speed and rate of rotation of a particle as it sediments down a channel. We use this same simulation to calculate the Brownian drift of a particle between parallel walls. Finally, we calculate an extension of the Einstein correction for the shear viscosity of a dilute colloidal suspension which accounts for the effects of the channel walls on the distribution of stresses in the channel. In section 5.4, we discuss the extension of these results to the study of many particles between parallel walls. In particular, we discuss how a similar approach may be fruitful in constructing Stokesian Dynamics and Accelerated Stokesian Dynamics simulations of infinite suspensions bound between parallel walls.

5.2 Analysis

5.2.1 The grand mobility tensor revisited

For Stokes flow surrounding rigid particles and contained by rigid boundaries, the governing equations and boundary conditions are linear in the velocity field and boundary data. Taking a higher level perspective on the problem, we recognize that the Faxén formulas can be used to assemble the mobility tensors. The relative velocity of a spherical particle in an unbounded fluid with center at $\mathbf{x}_0$ is related to the force on that particle and the effects of a disturbance flow denoted $\mathbf{u}'(\mathbf{x})$, by

$$\mathbf{U} - \mathbf{U}^\infty = -\frac{\mathbf{F}^H}{6\pi\eta a} + \left(1 + \frac{a^2}{6}\nabla_x^2\right)\mathbf{u}'(\mathbf{x})\bigg|_{\mathbf{x}=\mathbf{x}_0}. \tag{5.1}$$

If we knew the exact Green's function for a particle between two walls, then we could derive an equivalent Faxén formula for a particle in a channel. All that would change in the above formula would be the first term on the right hand side as seen in equation 2.18. As we shall see however, this is unnecessary since the velocity disturbance caused by a single particle in a channel can be divided into two pieces: the flow due to the particle were it in an unbounded fluid, and the correction to that flow, which cancels on the boundaries and satisfies the relevant boundary conditions. This second velocity field, termed the reflection, is nothing more than a disturbance flow which contributes to $\mathbf{u}'(\mathbf{x})$. Equivalent formulas exist for an unbounded fluid that couple the relative rotation and rate of strain to the torque and stresslet, respectively, as well as to a disturbance flow, *viz.*

$$\mathbf{\Omega} - \mathbf{\Omega}^\infty = -\frac{\mathbf{L}^H}{8\pi\eta a^3} + \frac{1}{2}\nabla_x \times \mathbf{u}'(\mathbf{x})\bigg|_{\mathbf{x}=\mathbf{x}_0}, \tag{5.2}$$

$$-\mathbf{E}^\infty = -\frac{\mathbf{S}^H}{\frac{20}{3}\pi\eta a^3} + \frac{1}{2}\left(1 + \frac{a^2}{10}\nabla_x^2\right)\left(\nabla_x\mathbf{u}'(\mathbf{x}) +^T \nabla_x\mathbf{u}'(\mathbf{x})\right)\bigg|_{\mathbf{x}=\mathbf{x}_0}, \tag{5.3}$$

where ${}^T\nabla_x$ is the front-gradient-transpose operator that takes the dyadic gradient and transposes it with the first index of the operand. Higher order Faxén formulas can be derived using procedures like those described in Happel and Brenner (1986) and Kim and Karrila (1991). The three we have presented here are adequate for illustrating our methods and results.

Since we are seeking to build the mobility tensors for a particle in a channel, we need to determine the reflected flow mentioned above. To do this, we first establish the velocity field generated by a spherical particle in an unbounded flow with one of the given force multipoles on its surface. This is most easily done with a multipole expansion. Given the fundamental point force solution to Stokes flow in an unbounded domain, called the Stokeslet,

$$\mathbf{J}(\mathbf{r}) = \frac{1}{8\pi\eta}\left(\frac{\mathbf{I}}{r} + \frac{\mathbf{rr}}{r^3}\right), \tag{5.4}$$

the velocity field surrounding a rigid, no-slip particle is written as

$$\mathbf{u}(\mathbf{x}) = \int_S \mathbf{J}(\mathbf{x}-\mathbf{y}) \cdot \mathbf{f}(\mathbf{y}) dS_y, \tag{5.5}$$

where S designates the surface of the particle and $\mathbf{f}(\mathbf{y})$ is the force density on the particle's surface. If we perform a Taylor expansion of the Stokeslet about the particle's center, we can write the velocity field generated by the particle as

$$\begin{aligned}\mathbf{u}(\mathbf{x}) = &\left(1 + \frac{a^2}{6}\nabla_y^2\right)\mathbf{J}(\mathbf{x}-\mathbf{y})\Big|_{\mathbf{y}=\mathbf{x}_0} \cdot \mathbf{F} + \frac{1}{2}\nabla_y \times \mathbf{J}(\mathbf{x}-\mathbf{y})\Big|_{\mathbf{y}=\mathbf{x}_0} \cdot \mathbf{L} \\ &+ \frac{1}{2}\left(1 + \frac{a^2}{10}\nabla_y^2\right)\left(\nabla_y + \nabla_y^T\right)\mathbf{J}(\mathbf{x}-\mathbf{y})\Big|_{\mathbf{y}=\mathbf{x}_0} : \mathbf{S} + \ldots,\end{aligned} \tag{5.6}$$

where ∇_x^T is the back-gradient transpose operator which takes the dyadic gradient and transposes it with the last index of the operand. Here, we have switched from referring to the force, torque and stresslet on the fluid to the force moments on the particle which may be represented as $\mathbf{F} = -\mathbf{F}^H$, $\mathbf{L} = -\mathbf{L}^H$ and $\mathbf{S} = -\mathbf{S}^H$. This series continues with terms that are represented as higher order derivatives of the Stokeslet and higher order force moments. These higher order terms all decay faster than the ones retained since the Stokeslet itself decays as $1/r$. This means that for relatively large separations, only a few force multipoles are necessary to accurately represent the flow. We are free to specify any force density on the particle's surface, and therefore the velocity field generated by a spherical particle with a constant force density on it's surface in an unbounded fluid is simply

$$\mathbf{u}(\mathbf{x}) = \left(1 + \frac{a^2}{6}\nabla_y^2\right)\mathbf{J}(\mathbf{x}-\mathbf{y})\bigg|_{\mathbf{y}=\mathbf{x}_0} \cdot \mathbf{F}. \tag{5.7}$$

Knowing this is crucial to deriving the reflection of the unbounded flow off all channel walls and subsequently applying the appropriate Faxén formula.

It will prove convenient to define the flow due just to a Stokeslet of magnitude $\mathbf{F}$ originating at a point $\mathbf{y}$ in an otherwise unbounded fluid as

$$\mathbf{u}^S(\mathbf{x};\mathbf{y}) = \mathbf{J}(\mathbf{x}-\mathbf{y}) \cdot \mathbf{F}. \tag{5.8}$$

The reflection of this Stokeslet off the channel walls must satisfy the Stokes equations between the walls as well as cancel the Stokeslet flow on the channel walls themselves. We denote the reflection flow as $\mathbf{u}^{S'}(\mathbf{x};\mathbf{y})$ and write the boundary condition on the channel walls in the most primitive form:

$$\mathbf{u}^{S'}(\mathbf{x};\mathbf{y}) + \mathbf{u}^S(\mathbf{x};\mathbf{y}) = 0, \quad \text{for } \mathbf{x} \in \text{ walls.} \tag{5.9}$$

We will establish a defined geometry in the next section; however, here we aim to lay out clearly the construction of the mobility tensor using reflected flows. Referring back to the flow generated by a particle with a constant force density on its surface (eq. 5.7), we see that the reflected flow, designated $\mathbf{u}'(\mathbf{x})$, must satisfy the boundary conditions

$$\mathbf{u}'(\mathbf{x}) + \left(1 + \frac{a^2}{6}\nabla_y^2\right)\mathbf{J}(\mathbf{x}-\mathbf{y})\bigg|_{\mathbf{y}=\mathbf{x}_0} \cdot \mathbf{F} = 0, \quad \text{for } \mathbf{x} \in \text{ walls.} \tag{5.10}$$

We use equation (5.9) and the Laplacian with respect to $\mathbf{y}$ of that same equation, to argue that the constant-force-particle reflection flow can be written in terms of the Stokeslet reflection flow

$$\mathbf{u}'(\mathbf{x}) = \left(1 + \frac{a^2}{6}\nabla_y^2\right) \mathbf{u}^{S'}(\mathbf{x};\mathbf{y})\Big|_{\mathbf{y}=\mathbf{x}_0}. \tag{5.11}$$

This satisfies the wall boundary condition in equation (5.10) exactly. Similar expressions hold for other multipole generated velocity fields, and we find fortuitously that we only need to work out the reflection of the Stokeslet off the channel walls to determine all the other flows which the particle might generate. Additionally, we recognize from the boundary condition that the flow $\mathbf{u}^{S'}(\mathbf{x};\mathbf{y})$ must be linear in the forcing $\mathbf{F}$. Treating $\mathbf{u}'(\mathbf{x})$ as a disturbance velocity and referring back to the Faxén formulas, the relative translational velocity of a particle in a channel can be written as

$$\mathbf{U} - \mathbf{U}^{\infty} = \frac{\mathbf{F}}{6\pi\eta a} + \left(1 + \frac{a^2}{6}\nabla_x^2\right)\left(1 + \frac{a^2}{6}\nabla_y^2\right) \mathbf{u}^{S'}(\mathbf{x};\mathbf{y})\Big|_{\mathbf{x}=\mathbf{x}_0}^{\mathbf{y}=\mathbf{x}_0}. \tag{5.12}$$

This is the mobility tensor $\mathbf{M}_{UF}$ for a particle in a channel, and similar expressions can be developed for the other pieces of the grand mobility tensor (see Swan and Brady, 2007). In the next section, we complete the development of these tensors by determining a general equation for the Stokes flow in a channel with arbitrary boundary conditions on the walls.

5.2.2 General solution to the Stokes equations between parallel walls

Given the Stokes equations (eq. 2.8) and a pair of boundary conditions on the lower and upper walls of the channel represented as

$$\mathbf{u}(\mathbf{x}) = \mathbf{u}^{L}(\mathbf{x}), \quad \text{for } \mathbf{x} \in \text{ lower wall}, \tag{5.13}$$

$$\mathbf{u}(\mathbf{x}) = \mathbf{u}^{U}(\mathbf{x}), \quad \text{for } \mathbf{x} \in \text{ upper wall}, \tag{5.14}$$

we seek a general solution for $\mathbf{u}(\mathbf{x})$. Taking cues from Faxén and Blake, we first find a solution in Fourier space by transforming the coordinates parallel to the wall; henceforth designated r_1 and r_2 with unit vectors

$\mathbf{e}_1$ and $\mathbf{e}_2$. We use the following Fourier transform and inverse in this process:

$$\hat{\zeta} = \mathcal{F}(\zeta) = \iint_{-\infty}^{\infty} e^{i(k_1 r_1 + k_2 r_2)} \zeta \, dr_1 dr_2, \tag{5.15}$$

$$\zeta = \mathcal{F}^{-1}(\hat{\zeta}) = \frac{1}{(2\pi)^2} \iint_{-\infty}^{\infty} e^{-i(k_1 r_1 + k_2 r_2)} \hat{\zeta} \, dk_1 dk_2. \tag{5.16}$$

This transform leaves unchanged the coordinate perpendicular to the walls which we designate as r_3 with unit vector $\mathbf{e}_3$. Therefore, transforming the Stokes equations and noting that in Stokes flow the pressure is also harmonic, the governing equations are reduced to a set of ordinary differential equations which depend only on the reciprocal coordinates k_1 and k_2 and the real-space coordinate r_3:

$$-k^2 \hat{p} + \frac{\partial^2 \hat{p}}{\partial r_3^2} = 0, \tag{5.17}$$

$$-k^2 \hat{u}_i + \frac{\partial^2 \hat{u}_i}{\partial r_3^2} = \frac{1}{\eta} \left(-ik_\alpha \delta_{i\alpha} \hat{p} + \frac{\partial \hat{p}}{\partial r_3} \delta_{i3} \right), \tag{5.18}$$

$$-ik_\alpha \hat{u}_\alpha + \frac{\partial \hat{u}_3}{\partial r_3} = 0, \tag{5.19}$$

where $k^2 = k_1^2 + k_2^2$. Blake (1974) first derived these expressions in his study of the Stokeslet above a single wall in an otherwise unbounded half-space. Here, we use two different summation notations where Greek indices (*e.g.* α, β) can assume the values $(1, 2)$ while Roman indices (*e.g.* i, j) can assume the values $(1, 2, 3)$. Additionally, repeated indices signal the usual summation over all attainable index values. The general solutions for the pressure and the velocity field can be written as

$$\hat{p} = A e^{-r_3 k} + B e^{r_3 k}, \tag{5.20}$$

$$\hat{\mathbf{u}} = \mathbf{A} e^{-r_3 k} + \mathbf{B} e^{r_3 k} + \frac{1}{4\eta k^2} \left[A \mathbf{d} (2 r_3 k + 1) e^{-r_3 k} + B \bar{\mathbf{d}} (2 r_3 k - 1) e^{r_3 k} \right], \tag{5.21}$$

where $d_i = ik_\alpha \delta_{i\alpha} + k\delta_{i3}$ and $\bar{d}_i = -ik_\alpha \delta_{i\alpha} + k\delta_{i3}$ are related by conjugation. The unknown coefficients A, B, $\mathbf{A}$ and $\mathbf{B}$ are related through the equation of continuity (eq. 5.19) by

$$A = 2\eta \mathbf{d} \cdot \mathbf{A}, \tag{5.22}$$

$$B = -2\eta \bar{\mathbf{d}} \cdot \mathbf{B}. \tag{5.23}$$

The remaining vectors $\mathbf{A}$ and $\mathbf{B}$ are determined directly from applying the boundary conditions on the lower and upper walls and depend only on the geometry and the reciprocal coordinates. This process is complicated mathematically and involves solving a coupled set of equations for A and B, but the result is an equation for the Fourier transform of the Stokes velocity field in a channel given arbitrary boundary conditions on the walls. We work this out explicitly in the appendix for posterity. Of course, what is really needed for determining the mobility tensors for a spherical particle between a pair of walls is the real-space solution to these equations. In the next section, we address this issue.

5.2.3 Single particle mobility in a channel

Up to this point, we have avoided writing down any specific geometry associated with the system in order to keep the analysis as general as possible. From here on, where the particle is located in the channel as well as the channel width will need to be specified. This will provide a proper origin to the coordinates in the previous section. Figure 5.1 details the geometry of the problem. The spherical particle of radius a lies a distance ΞH above the lower wall which itself is a distance H away from the upper wall. The coordinates (r_1, r_2, r_3) now have a natural origin cooresponding to the center of the particle. This means that the lower wall corresponds to $r_3 = -\Xi H$ and the upper wall corresponds to $r_3 = (1 - \Xi)H$.

As a first step, the reflection of the Stokeslet field originating from the center of the particle, $\mathbf{u}^{S'}(\mathbf{r})$, is

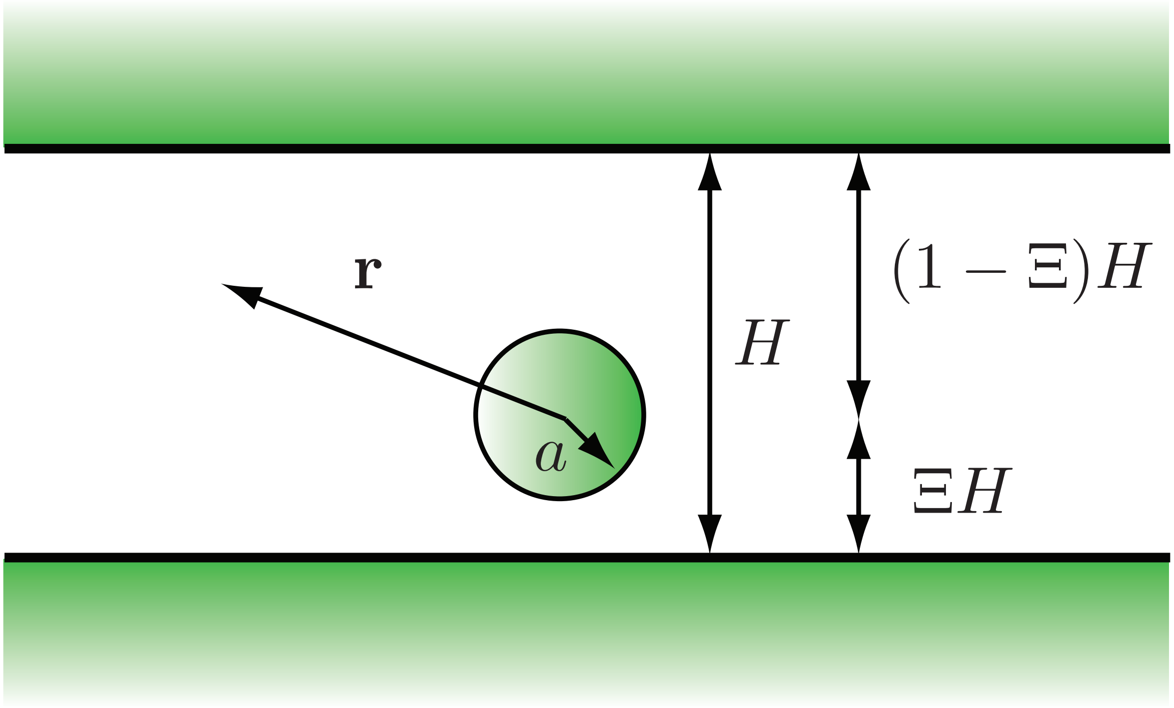

Figure 5.1: A single spherical particle of radius a in a channel of width H. The vector $\mathbf{r}$ is centered on the particle which lies a fractional distance Ξ across the channel.

found. In reciprocal space, the boundary conditions on the Stokeslet reflection are given by

$$\hat{\mathbf{u}}^{S'}(k_1, k_2, -\Xi H) = -\hat{\mathbf{u}}^{S}(k_1, k_2, -\Xi H), \tag{5.24}$$

$$\hat{\mathbf{u}}^{S'}(k_1, k_2, (1-\Xi)H) = -\hat{\mathbf{u}}^{S}(k_1, k_2, (1-\Xi)H), \tag{5.25}$$

where the Fourier transform of the Stokeslet is

$$\begin{aligned}\hat{\mathbf{u}}^{S}(k_1, k_2, r_3) = -\frac{1}{4\eta k^3}&\left[\mathbf{I}\left(\frac{\partial^2}{\partial r_3^2} - k^2\right) + \frac{1}{(2k)^2}\mathbf{d}\mathbf{d}\left(2k\frac{\partial}{\partial r_3} - \frac{\partial^2}{\partial r_3^2} - k^2\right)\right.\\ &+\frac{1}{(2k)^2}\bar{\mathbf{d}}\mathbf{d}\left(-\frac{\partial^2}{\partial r_3^2} + k^2\right) + \frac{1}{(2k)^2}\mathbf{d}\bar{\mathbf{d}}\left(-\frac{\partial^2}{\partial r_3^2} + k^2\right)\\ &\left.+\frac{1}{(2k)^2}\bar{\mathbf{d}}\bar{\mathbf{d}}\left(-2k\frac{\partial}{\partial r_3} - \frac{\partial^2}{\partial r_3^2} - k^2\right)\right]\cdot\mathbf{F}\left(1 + k\left|r_3\right|\right)e^{-|r_3|k}.\end{aligned} \tag{5.26}$$

We write this in a form suitable for our particular method, but again this result was first realized by Blake

(1974) in his previously mentioned study. We proceed by applying the boundary conditions and finding the unknown coefficients $\mathbf{A}$ and $\mathbf{B}$ associated with the Stokes flow reflection problem. These are now complicated functions of the reciprocal coordinates $(k_1,\ k_2)$, the separation between the plates (H) and the fractional distance across the channel (Ξ). They are also linear functions of the force or Stokeslet magnitude $\mathbf{F}$.

Computing the inverse transform of $\hat{\mathbf{u}}^{S'}$ is quite difficult. However, to compute the mobility of a particle in the channel, we really only need to find the the value of the reflected field at the particle's center which may be written as

$$\mathbf{u}^{S'}(\mathbf{x}_0;\mathbf{x}_0) = \frac{1}{(2\pi)^2}\iint_{-\infty}^{\infty} \hat{\mathbf{u}}^{S'}(k_1,k_2,0)\,dk_1 dk_2. \tag{5.27}$$

This integral is orders of magnitude easier to compute than the full inverse Fourier transform since the integrand depends only on a few parameters $(k_1,\ k_2,\ \Xi,\ H$ and $\mathbf{F})$. In fact, we also need to know $\nabla_x^2\mathbf{u}^{S'}(\mathbf{x};\mathbf{y})$, $\nabla_y^2\mathbf{u}^{S'}(\mathbf{x};\mathbf{y})$ and $\nabla_x^2\nabla_y^2\mathbf{u}^{S'}(\mathbf{x};\mathbf{y})$ with $\mathbf{x}$ and $\mathbf{y}$ at the center of the particle in order to apply the Faxén formula and to compute $\mathbf{M}_{UF}$. Other higher order derivatives are also necessary to compute higher order mobility tensors. Computing these derivatives is quite easy however. First, we write down the gradients with respect to the coordinates $\mathbf{x}$ and $\mathbf{y}$ in terms of the coordinate system we have established in the channel $(\mathbf{r} = \mathbf{x} - \mathbf{y})$. In this case, $\mathbf{x}$ refers to some point in the fluid while $\mathbf{y}$ refers to the origin of the coordinate system. These gradients can be written as

$$\nabla_x = \nabla_r, \tag{5.28}$$

$$\nabla_y = -\nabla_r + \frac{1}{H}\frac{\partial}{\partial\Xi}\mathbf{e}_3, \tag{5.29}$$

and higher order derivatives can be computed by successive application of these formulas. The correct transformation of the gradients with respect to $\mathbf{y}$ are important because these derivatives reflect the key point: that the force density is distributed over the particle's surface rather than originating at its center. Failing to note this will result in a grand mobility tensor which is an approximation to the correct result, but fails to be symmetric and positive-definite. Now, we can compute, for instance, $\nabla_x^2\mathbf{u}^{S'}(\mathbf{x};\mathbf{y})$ with $\mathbf{x}$ and

y pointing at the particle's center as

$$\nabla_x^2 \mathbf{u}^{S'}(\mathbf{x};\mathbf{y})\Big|_{\mathbf{x}=\mathbf{x}_0}^{\mathbf{y}=\mathbf{x}_0} = \frac{1}{(2\pi)^2}\iint_{-\infty}^{\infty}\left(-k^2+\frac{\partial^2}{\partial r_3^2}\right)\hat{\mathbf{u}}^{S'}(k_1,k_2,r_3)\Big|_{r_3=0} dk_1 dk_2, \tag{5.30}$$

where we have carefully applied the usual Fourier transform identities to move the derivatives inside the integral. The other terms are computed similarly, and although the formulas are tedious, they yield similar results. The total inverse Fourier transform needed to compute $\mathbf{M}_{UF}$ is given by

$$\begin{aligned}&\frac{1}{(2\pi)^2}\iint_{-\infty}^{\infty}\left[1+\frac{a^2}{6}\left(-k^2+\frac{\partial^2}{\partial r_3^2}\right)\right] \qquad (5.31)\\ &\left[1+\frac{a^2}{6}\left(-k^2+\frac{\partial^2}{\partial r_3^2}-\frac{2}{H}\frac{\partial^2}{\partial\Xi\partial r_3}+\frac{1}{H^2}\frac{\partial^2}{\partial\Xi^2}\right)\right]\hat{\mathbf{M}}(k_1,k_2,r_3;\Xi,H)\Big|_{r_3=0} dk_1 dk_2,\end{aligned}$$

where

$$\hat{\mathbf{u}}^{S'}(k_1,k_2,r_3) = \hat{\mathbf{M}}(k_1,k_2,r_3;\Xi,H)\cdot\mathbf{F}, \tag{5.32}$$

takes advantage of the linear dependence of the velocity on the forcing. As it happens, the reciprocal length scale k and the channel width H always appear together in the formula for $\hat{\mathbf{M}}$. By redefining the variables of integration in equation (5.31) so that $\xi_1 = k_1 H$, $\xi_2 = k_2 H$ and $\xi^2 = (kH)^2$, we integrate over ξ_1 and ξ_2 in cylindrical polar coordinates; performing the angular integration analytically and the radial integration numerically. This is quite simple as the integrand decays exponentially as ξ gets large. This yields an expression for $\mathbf{M}_{UF}$ which is an ordered sum of inverse powers of the channel width. The mobility tensor can also be separated into two pieces reflecting motions parallel and perpendicular to the walls, *viz.*

$$\begin{aligned}\mathbf{M}_{UF} = \frac{1}{6\pi\eta a}&\left[(\mathbf{I}-\mathbf{e}_3\mathbf{e}_3)\left(1-f_1^{(UF)}(\Xi)\left(\frac{a}{H}\right)+f_3^{(UF)}(\Xi)\left(\frac{a}{H}\right)^3-f_5^{(UF)}(\Xi)\left(\frac{a}{H}\right)^5\right)\right.\\ &\left.+\mathbf{e}_3\mathbf{e}_3\left(1-g_1^{(UF)}(\Xi)\left(\frac{a}{H}\right)+g_3^{(UF)}(\Xi)\left(\frac{a}{H}\right)^3-g_5^{(UF)}(\Xi)\left(\frac{a}{H}\right)^5\right)\right],\end{aligned} \tag{5.33}$$

where $\mathbf{I}$ is the idem tensor and $f_i^{(UF)}(\Xi)$ and $g_i^{(UF)}(\Xi)$ are functions of the fractional distance across the channel only. From a far-field perspective, the channel width can be decoupled from the fractional distance across the channel. This means that the functions $f_i^{(UF)}(\Xi)$ and $g_i^{(UF)}(\Xi)$ need only be computed once for all $\Xi \in (0,1)$ and the hydrodynamic interactions between the particle and the wall are determined completely for all channel widths. This is especially useful in simulations because these functions can be tabulated and referenced quickly.

Similar expressions exist for the other mobility tensors. The Faxén formulas and multipolar flows needed to compute these terms are given explicitly in the paper by Swan and Brady (2007). We show the result of taking these derivatives and then integrating the result here. Since the grand mobility tensor is symmetric, we only provide six of the nine tensors in equation 2.16. The other three can be computed directly by accounting for this symmetry. For the translation-torque and translation-stresslet couplings, we find the following expressions

$$\mathbf{M}_{UL} = \frac{1}{6\pi\eta a^2}\mathbf{e}_3 \cdot \boldsymbol{\epsilon}\left[f_2^{(UL)}(\Xi)\left(\frac{a}{H}\right)^2 + f_4^{(UL)}(\Xi)\left(\frac{a}{H}\right)^4\right], \tag{5.34}$$

$$\begin{aligned}\mathbf{M}_{US} = \frac{1}{6\pi\eta a^2}\Bigg\{&\left[(\mathbf{I}-\mathbf{e}_3\mathbf{e}_3)\,\mathbf{e}_3 + (\mathbf{I}-\mathbf{e}_3\mathbf{e}_3)\,\mathbf{e}_3^T\right]\left[-f_2^{(US)}(\Xi)\left(\frac{a}{H}\right)^2 + f_4^{(US)}(\Xi)\left(\frac{a}{H}\right)^4 - f_6^{(US)}(\Xi)\left(\frac{a}{H}\right)^6\right]\\ &+ \left[\mathbf{e}_3\,(\mathbf{I}-\mathbf{e}_3\mathbf{e}_3) + 2\mathbf{e}_3\mathbf{e}_3\mathbf{e}_3\right]\left[g_2^{(US)}(\Xi)\left(\frac{a}{H}\right)^2 - g_4^{(US)}(\Xi)\left(\frac{a}{H}\right)^4 + g_6^{(US)}(\Xi)\left(\frac{a}{H}\right)^6\right]\Bigg\}\end{aligned} \tag{5.35}$$

where $\boldsymbol{\epsilon}$ is the Levi-Civita tensor. Similarly, for the rotation-torque and rotation-stresslet couplings, the elements of the grand mobility tensor are

$$\mathbf{M}_{\Omega L} = \frac{1}{6\pi\eta a^3}\left[(\mathbf{I}-\mathbf{e}_3\mathbf{e}_3)\left(\frac{3}{4} - f_3^{(\Omega L)}(\Xi)\left(\frac{a}{H}\right)^3\right) + \mathbf{e}_3\mathbf{e}_3\left(\frac{3}{4} - g_3^{(\Omega L)}(\Xi)\left(\frac{a}{H}\right)^3\right)\right], \tag{5.36}$$

$$\mathbf{M}_{\Omega S} = \frac{1}{6\pi\eta a^3}\left(\mathbf{e}_3\cdot\boldsymbol{\epsilon}\mathbf{e}_3 + \mathbf{e}_3\cdot\boldsymbol{\epsilon}\mathbf{e}_3^T\right)\left(f_3^{(\Omega S)}\left(\frac{a}{H}\right)^3 + f_5^{(\Omega S)}\left(\frac{a}{H}\right)^5\right). \tag{5.37}$$

Finally, for the coupling between rate of strain and stresslet, the mobility tensor is

$$\begin{aligned}
\mathbf{M}_{ES} = \frac{1}{6\pi\eta a^3} \Bigg\{ & \left[-\frac{9}{30} - f_3^{(ES)}(\Xi)\left(\frac{a}{H}\right)^3 + f_5^{(ES)}(\Xi)\left(\frac{a}{H}\right)^5 - f_7^{(ES)}(\Xi)\left(\frac{a}{H}\right)^7 \right] \left[\left(\delta_{ij} - \delta_{i3}\delta_{j3}\right)\left(\delta_{kl} - \delta_{k3}\delta_{l3}\right) \right. \\
& \left. -2\left(\delta_{ij} - \delta_{i3}\delta_{j3}\right)\delta_{k3}\delta_{l3} - 2\delta_{i3}\delta_{j3}\left(\delta_{kl} - \delta_{k3}\delta_{l3}\right) + 4\delta_{i3}\delta_{j3}\delta_{k3}\delta_{l3} \right] \\
& + \left[\frac{9}{20} - g_3^{(ES)}(\Xi)\left(\frac{a}{H}\right)^3 + g_5^{(ES)}(\Xi)\left(\frac{a}{H}\right)^5 - g_7^{(ES)}(\Xi)\left(\frac{a}{H}\right)^7 \right] \\
& \times \left[\left(\delta_{ik} - \delta_{i3}\delta_{k3}\right)\left(\delta_{jl} - \delta_{j3}\delta_{l3}\right) + \left(\delta_{il} - \delta_{i3}\delta_{l3}\right)\left(\delta_{jk} - \delta_{j3}\delta_{k3}\right) \right. \\
& \left. -2\left(\delta_{ij} - \delta_{i3}\delta_{j3}\right)\delta_{k3}\delta_{l3} - 2\delta_{i3}\delta_{j3}\left(\delta_{kl} - \delta_{k3}\delta_{l3}\right) + 4\delta_{i3}\delta_{j3}\delta_{k3}\delta_{l3} \right] \\
& + \left[\frac{9}{20} - h_3^{(ES)}(\Xi)\left(\frac{a}{H}\right)^3 + h_5^{(ES)}(\Xi)\left(\frac{a}{H}\right)^5 - h_7^{(ES)}(\Xi)\left(\frac{a}{H}\right)^7 \right] \\
& \times \left[\left(\delta_{ik} - \delta_{i3}\delta_{k3}\right)\delta_{j3}\delta_{l3} + \left(\delta_{il} - \delta_{i3}\delta_{l3}\right)\delta_{j3}\delta_{k3} + \left(\delta_{jk} - \delta_{j3}\delta_{k3}\right)\delta_{i3}\delta_{l3} + \left(\delta_{jl} - \delta_{j3}\delta_{l3}\right)\delta_{i3}\delta_{k3} \right] \Bigg\} \mathbf{e}_i\mathbf{e}_j\mathbf{e}_k\mathbf{e}_l
\end{aligned} \tag{5.38}$$

Other higher order mobility tensors can be calculated in a similar fashion, but for the purposes of dynamic simulation it has proven convenient to truncate the force multipoles at the stresslet level. Therefore, we omit the calculation of any higher order terms. It is true that just as in calculations involving many particles, when the particle is close to one of the channel walls, all the force multipoles are important since this constitutes the lubrication limit. We use the Stokesian Dynamics method of constructing the grand mobility tensor and its inverse, the grand resistance tensor, to resolve this difficulty.

5.2.4 Stokesian Dynamics revisited

The Stokesian Dynamics method simplifies the calculation of hydrodynamic interactions among many bodies in Stokes flow by first computing the correct pair-wise, long-range behavior of the particles in the form of the grand mobility tensor. This is analogous to what we have done in the previous sections. Durlofsky and Brady (1987) showed that inverting the grand mobility tensor is equivalent to a method of reflections type procedure that yields the many-body long-range interactions among the particles. Since the grand mobility tensor must in every practical sense be truncated at some force multipole level, this invert alone fails to account for any pair-wise lubrication interactions which may occur when surfaces are nearly touching. The truncated invert is typically designated as $\mathcal{R}^{\infty}$ and is a far-field contribution to the grand resistance tensor which is denoted more generally as

$$\mathcal{R} = \begin{pmatrix} \mathbf{R}_{FU} & \mathbf{R}_{F\Omega} & \mathbf{R}_{FE} & \cdots \\ \mathbf{R}_{LU} & \mathbf{R}_{L\Omega} & \mathbf{R}_{LE} & \cdots \\ \mathbf{R}_{SU} & \mathbf{R}_{S\Omega} & \mathbf{R}_{SE} & \cdots \\ \vdots & \vdots & \vdots & \ddots \end{pmatrix}, \tag{5.39}$$

where the $\mathbf{R}$'s are the individual resistance tensors. The shortcomings of the far-field resistance tensor are overcome by writing the grand resistance tensor as

$$\mathcal{R} = \mathcal{R}^{\infty} + \mathcal{R}^{2B} - \mathcal{R}^{2B,\infty}, \tag{5.40}$$

where $\mathcal{R}^{2B}$ is the exact pair-wise lubrication form of the grand resistance tensor and $\mathcal{R}^{2B,\infty}$ is the two body far-field form of the grand resistance tensor. In this way, our approximation for the grand resistance tensor accounts for the correct many bodied far-field interactions and the correct pair-wise lubrication interactions. We can include the walls in these calculations by simply adding in the correct lubrication interactions of each particle with each wall individually and subtracting out the far-field interactions with that same wall as though it were in an otherwise unbounded domain. This is represented schematically as

$$\mathcal{R} = \mathcal{R}^{\infty} + \mathcal{R}^{2B} - \mathcal{R}^{2B,\infty} + \mathcal{R}^{W} - \mathcal{R}^{W,\infty}, \tag{5.41}$$

where $\mathcal{R}^{W}$ and $\mathcal{R}^{W,\infty}$ are the exact lubrication and far-field resistance tensors for interactions with each wall individually. Bossis, Meunier and Sherwood (1991) have tabulated the lubrication expressions to the stresslet level of truncation, and Swan and Brady (2007) have computed the far-field, single wall interactions to that same level.

5.3 Results

5.3.1 Components of the single particle mobility in a channel

In this section we plot and discuss the functions of the fractional channel distance, Ξ, which in essence define the different elements of the grand mobility tensor. The functions we plot here are perhaps most useful in a tabulated form for many values of Ξ distributed within $(0, 1)$ – though such tables are difficult to represent in print. A partial representation is provided in appendix C. To begin, consider the plots of $f_1^{(UF)}(\Xi)$, $f_3^{(UF)}(\Xi)$ and $f_5^{(UF)}(\Xi)$ shown in figure 5.2. Faxén computed the force F on a particle translating parallel to the walls with a velocity U, halfway and a quarter of the way across a channel. His results were presented as a ratio of the velocity to the force, *viz.*

$$\frac{6\pi\eta a U}{F} = \begin{cases} 1 - 0.6526\left(\frac{a}{h}\right) + 0.1475\left(\frac{a}{h}\right)^3 - 0.131\left(\frac{a}{h}\right)^4 - 0.0644\left(\frac{a}{h}\right)^5 + \ldots, & h = \frac{H}{4}, \\ 1 - 1.004\left(\frac{a}{h}\right) + 0.418\left(\frac{a}{h}\right)^3 + 0.21\left(\frac{a}{h}\right)^4 - 0.169\left(\frac{a}{h}\right)^5 + \ldots, & h = \frac{H}{2}, \end{cases} \tag{5.42}$$

First, notice that his expression is equivalent to the inverse of the resistance tensor $\mathbf{R}_{FU}$ and is closely related to $\mathbf{M}_{UF}$. Where $\mathbf{R}_{FU}^{-1}$ is an infinite series in powers of a/h, it is equivalent to leading order to $\mathbf{M}_{UF}$, which can be represented with a finite number of terms. The additional $(a/h)^4$ term as well as the rest of the series represented by the ellipses in Faxén's expressions are due to higher order force moments. In fact, we find that the coefficients Faxén computed are identical to our results when rescaled so that his expressions are written in terms of inverse powers of H instead of inverse powers of h. One result Faxén opted not to generate was the mobility for a particle sedimenting perpendicular to the channel walls. However, we have computed these mobility terms and find a behavior similar to the sedimentation parallel to the wall. Interesting, though perhaps not surprising, is the fact that sedimentation towards the wall is always slower than sedimentation along the wall. This must be because it is always harder to squeeze fluid out of a gap than to just push it aside at low Reynolds number.

It might be disconcerting to see the mobility coefficients diverge as Ξ approaches zero and unity. However, this behavior is correct as it leads to the conclusion that the parallel wall problem collapses to the single

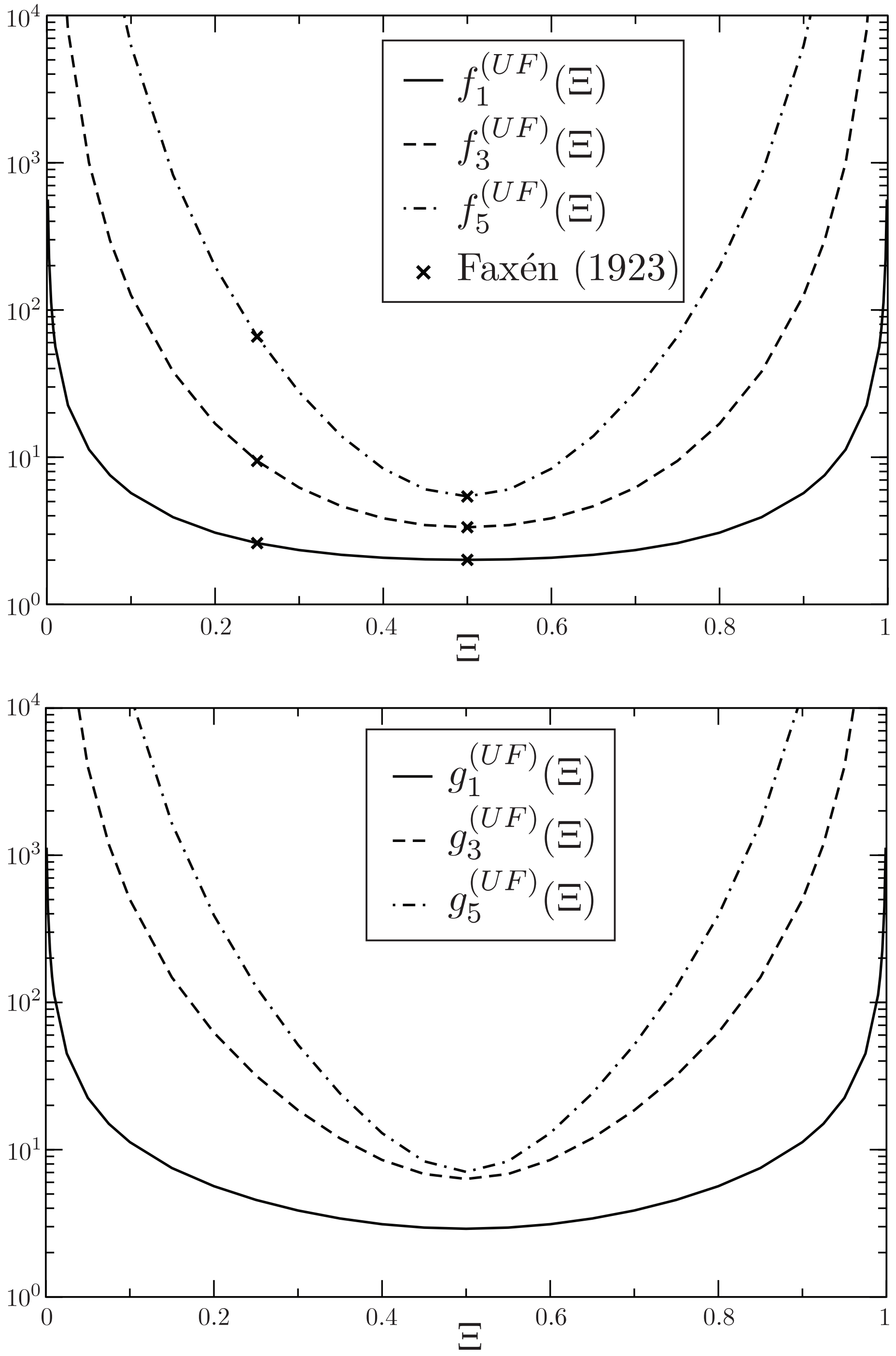

Figure 5.2: The components of the translation-force coupling in the directions parallel and perpendicular to the walls respectively.

wall problem in the limit that the channel spacing is infinitely wide. Suppose the particle is fixed against the wall such that $\Xi = a/H$. This is the closest the particle will ever get to wall regardless of the value of H and therefore, this is the smallest value of Ξ possible. We take the limit of the mobility tensor as a/H goes to zero and discover a satisfying, finite result. To simplify things, we examine the limits of each contribution to the mobility tensor individually,

$$\lim_{a/H\to 0} f_1^{(UF)}(a/H)\left(\frac{a}{H}\right) = \frac{9}{16}, \quad \lim_{a/H\to 0} g_1^{(UF)}(a/H)\left(\frac{a}{H}\right) = \frac{9}{8}, \tag{5.43}$$

$$\lim_{a/H\to 0} f_3^{(UF)}(a/H)\left(\frac{a}{H}\right)^3 = \frac{1}{8}, \quad \lim_{a/H\to 0} g_3^{(UF)}(a/H)\left(\frac{a}{H}\right)^3 = \frac{1}{2}, \tag{5.44}$$

$$\lim_{a/H\to 0} f_5^{(UF)}(a/H)\left(\frac{a}{H}\right)^5 = \frac{1}{16}, \quad \lim_{a/H\to 0} f_5^{(UF)}(a/H)\left(\frac{a}{H}\right)^5 = \frac{1}{8}. \tag{5.45}$$

These results are easily recognized as the coefficients of the single wall mobility tensor (Swan and Brady, 2007), which is sometimes written as

$$\begin{aligned} \mathbf{M}_{UF} = \frac{1}{6\pi\eta a}\Bigg[&(\mathbf{I}-\mathbf{e}_3\mathbf{e}_3)\left(1-\frac{9}{16}\left(\frac{a}{h}\right)+\frac{1}{8}\left(\frac{a}{h}\right)^3-\frac{1}{16}\left(\frac{a}{h}\right)^5\right) \\ &+\mathbf{e}_3\mathbf{e}_3\left(1-\frac{9}{8}\left(\frac{a}{h}\right)+\frac{1}{2}\left(\frac{a}{h}\right)^3-\frac{1}{8}\left(\frac{a}{h}\right)^5\right)\Bigg], \end{aligned} \tag{5.46}$$

where h is the height of the particle above that single wall. In the above limit, a/h is clearly unity. and we recognize that, indeed, the two wall problem collapses into the single wall problem when the channel width tends to infinity. This also makes it clear that the asymptotic behavior as $\Xi \to 0$ of the mobility coefficients must be

$$f_i^{(UF)}(\Xi), g_i^{(UF)}(\Xi) \sim \frac{1}{\Xi^i}, \tag{5.47}$$

where $i = 1, 3, 5$ and the coefficient of proportionality is given by the single wall value. This result is particularly useful in the computational domain since tabulation cannot be performed for all values of Ξ, and in the quickly varying regions near the walls the asymptotic result can be used as a substitute for the tabulated one.

For the coupling between translation and torque, we find a similar set of expressions. These are more challenging to visualize since they switch sign as the particle moves across the channel. This is easy to understand by considering the walls individually. For a particle above a single wall, the torque also couples to the translation of the particle. Flipping the coordinate system over so that the wall is now above the particle while keeping the torque the same results in translation in the opposite direction; hence the change in sign. The components of $\mathbf{M}_{UL}$ are plotted in figure 5.3. One interesting feature of this particular coupling is the $O(a/H)^2$ contribution. There is no analogous contribution in the single wall problem. Near the middle of a relatively large channel, this contribution dominates both the translation-torque and the rotation-force couplings. Although unexpected, this result is consistent with the single wall results as $f_2^{(UL)}(\Xi)$ is non-singular near the walls and therefore makes no contribution when only one wall is present. This term represents a lower order interaction generated by reflecting a rotlet between a pair of walls. In the single wall case where the domain is unbounded, there is only one no-slip condition to enforce and the parts of the disturbance velocity leading to this contribution are identically zero in order for the magnitude of the reflected velocity to remain finite in the far-field. An analogous set of plots shown in figure 5.4 have been generated for the translation-stresslet coupling. These show the same sign change as the particle moves from one wall to the other. This is most easily understood by recognizing that while $\mathbf{U}$ and $\mathbf{S}$ are preserved under the coordinate transformation that swaps the lower and upper walls, the tensor coupling these two is third order and depends on an odd number of tensor products of the unit vector $\mathbf{e}_3$. When the coordinate system flips, so does the sign of the unit vector and the coupling functions react accordingly to preserve the sign of the expression. Because of the symmetry between the walls, the coupling between translation and stresslet, as well as translation and torque, must go to zero when the particle is halfway across the channel. Additionally, the singular limits of each coefficient approach the corresponding single wall values.

We plot the coefficients associated with the rotation-torque coupling in figure 5.5. As with the mobility of a particle above a single wall, the no-slip condition on the boundaries retards rotation about the axes parallel to the walls more than rotation about the axis perpendicular to the walls. These coefficients are symmetric

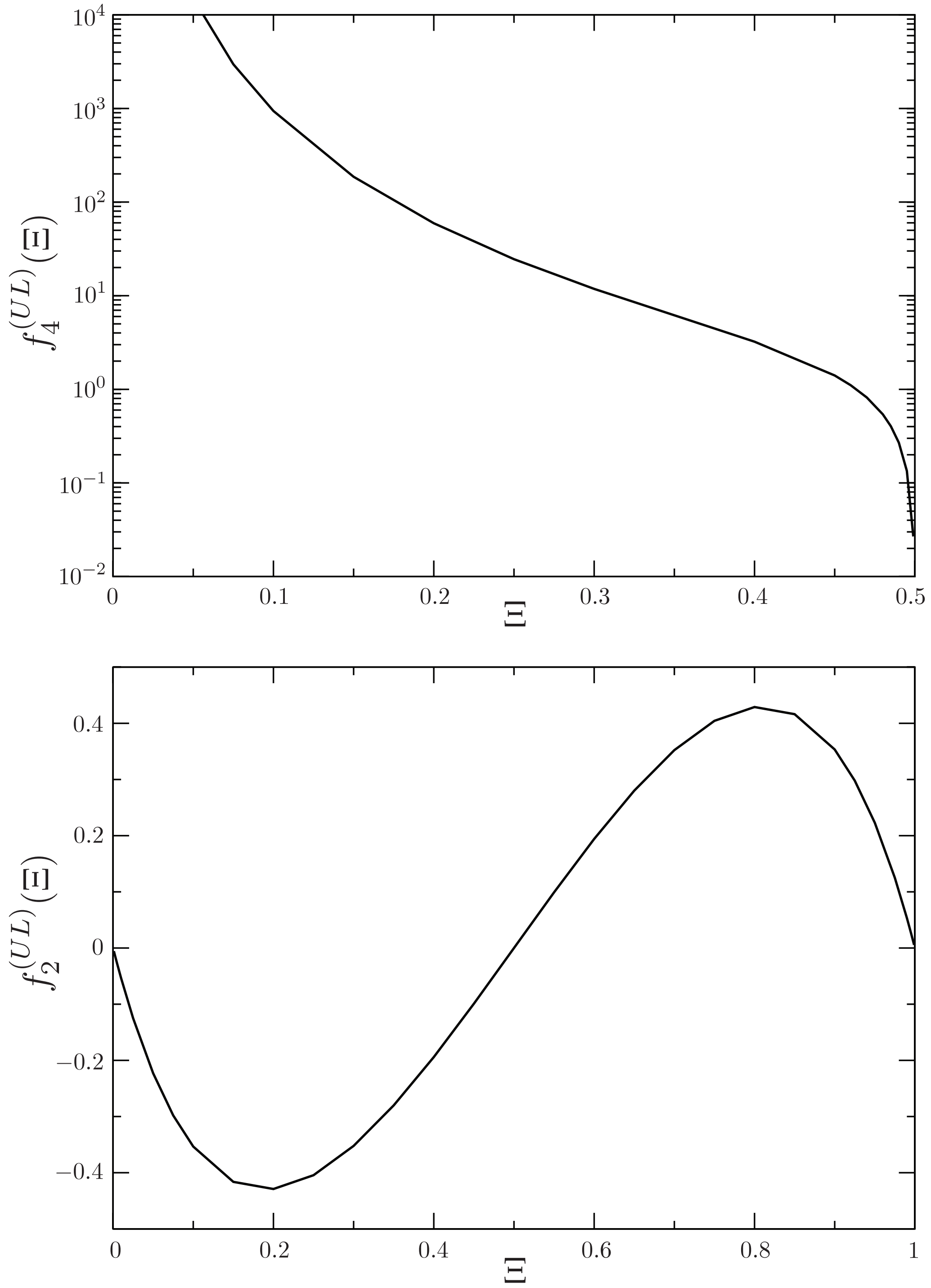

Figure 5.3: The components of the translation-torque coupling. The $O(a/H)^2$ contribution is not singular and therefore makes no contribution to the single wall problem.

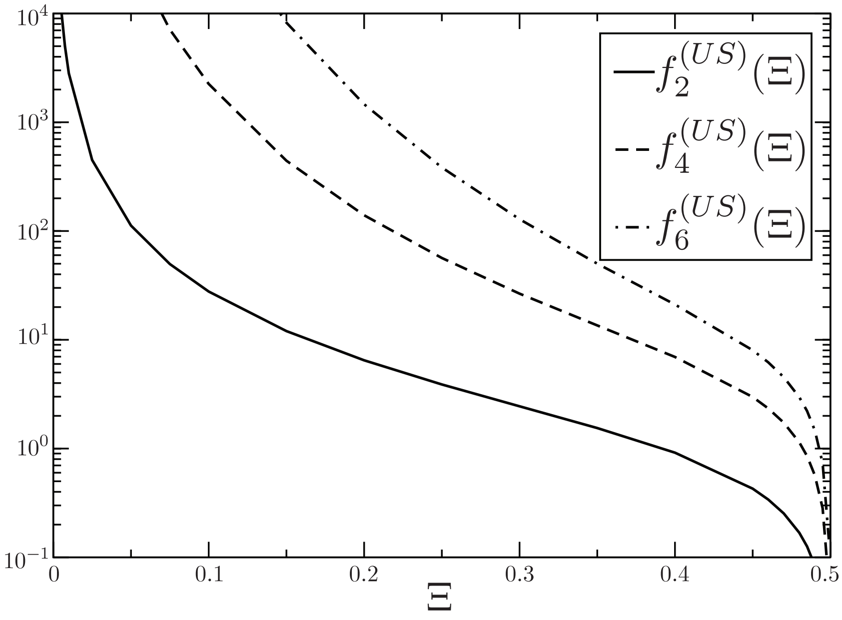

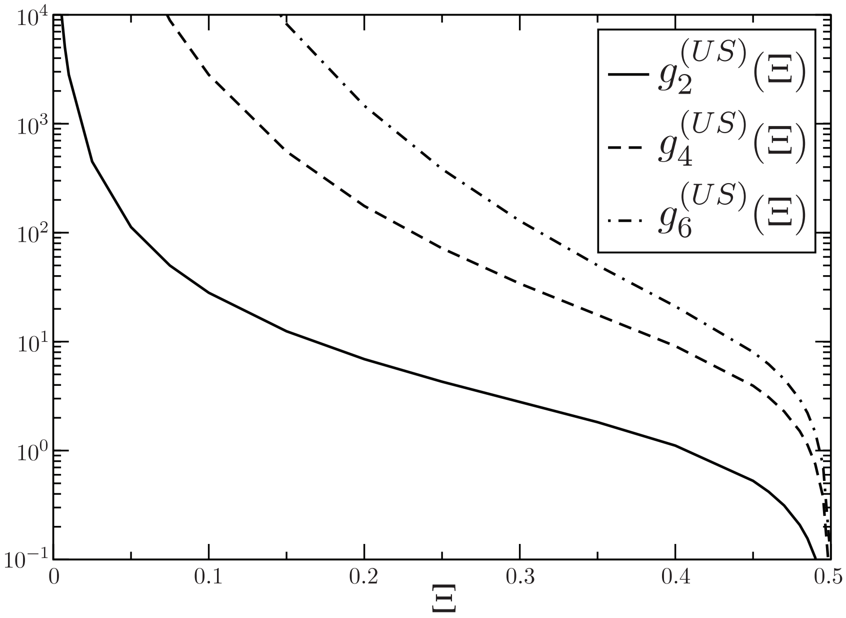

Figure 5.4: The components of the translation-stresslet coupling corresponding to couples between translation parallel to the walls and the stresslet $S_{33}$and translation perpendicular to the walls and stresslets with components parallel to the walls as well as translation perpendicular to the wall and the stresslet S_{33} via superposition.

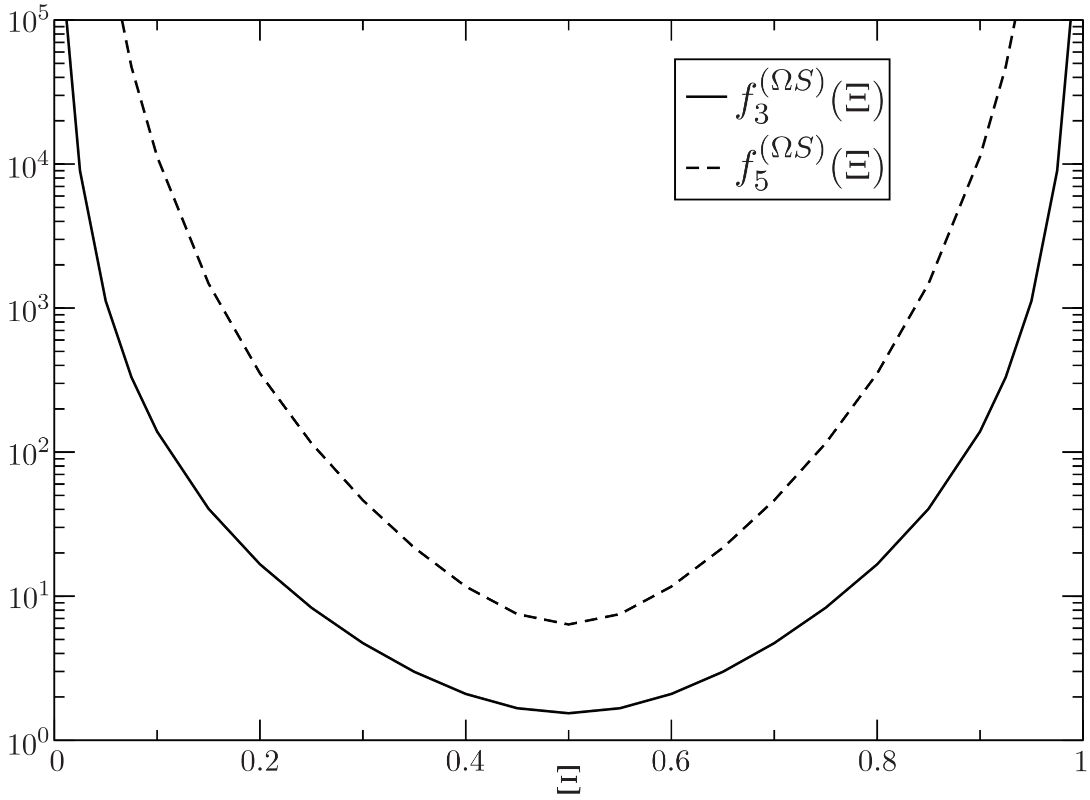

Figure 5.5: The components of the rotation-torque coupling about the axes parallel and perpendicular to the walls respectively.

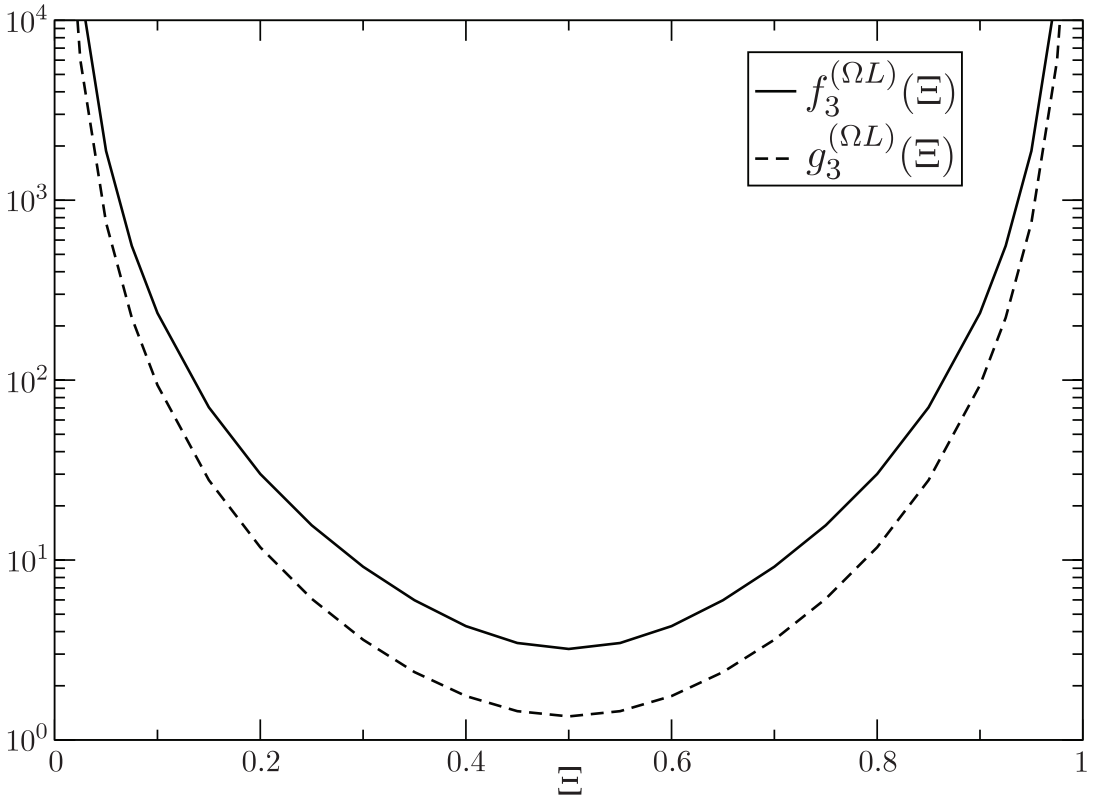

Figure 5.6: The components of the rotation-stresslet coupling which relates rotation of a particle about the axes parallel to the walls to the stresslet.

across the channel because under the coordinate inversion which switches the walls, the rotation and torque, which are handed quantities, both change sign. Similarly, the coupling between rotation and stresslet is also symmetric across the channel. These coefficients are plotted in figure 5.6. These also approach the single wall values in the limit that Ξ approaches zero and unity.

The coupling between rate of strain and stresslet is key for computing the shear stress in a force and torque free suspension. For a dilute suspension, the average of this coupling across the channel is precisely the particle contribution to the shear stress. Each of the coefficients of this coupling are plotted in figure 5.7. The single wall results are recovered as the particle approaches each wall. Interestingly, the magnitude of these coefficients is approximately a factor of ten larger than all the others presented. Relative to the scale factors $(a/H)^n$, the coupling between rate of strain and stresslet is quite strong when compared to the other equivalently scaled coefficients (*i.e.* $\mathbf{M}_{\Omega L}$, $\mathbf{M}_{\Omega S}$). Therefore, the walls should have a significant impact on

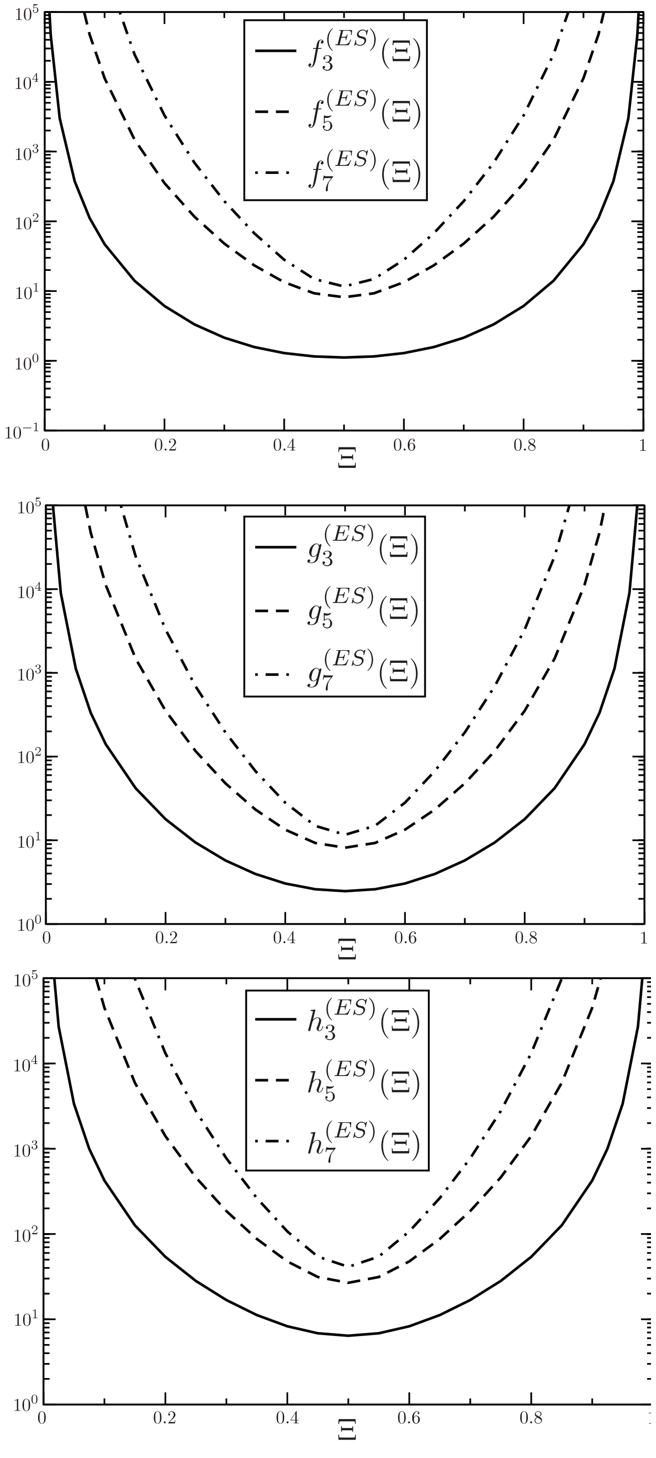

Figure 5.7: The components of the rate of strain-stresslet coupling. Between two walls, there are only three independent components of the tensor $\mathbf{M}_{ES}$ corresponding to the necessary Stokes flow symmetries and the anisotropy caused by the wall.

the measurement of the shear viscosity of a dilute suspension in a channel.

We conclude this section by examining Oseen's superposition approximation for the contribution to the mobility between a pair of walls. For the translation-force coupling terms $f_1^{(UF)}(\Xi)$ and $g_1^{(UF)}(\Xi)$, Oseen's superposition approximation would generate the approximate coefficients,

$$\bar{f}_1^{(UF)}(\Xi) = \frac{9}{16}\left(\frac{1}{\Xi} + \frac{1}{1-\Xi}\right) \tag{5.48}$$

$$\bar{g}_1^{(UF)}(\Xi) = \frac{9}{8}\left(\frac{1}{\Xi} + \frac{1}{1-\Xi}\right). \tag{5.49}$$

We plot these in figure 5.8 along with $f_1^{(UF)}(\Xi)$ and $g_1^{(UF)}(\Xi)$. The curves are qualitatively similar. Of course, since data on logarithmic axes can often appear quite close, we also compute the relative error between the exact two wall results and the superposition approximation. Near each of the walls, the superposition approximation performs quite well with less than five percent error when the particle is less than five percent of the way across the channel. However, in the middle of the channel, the error balloons quickly. In the case of translation perpendicular to the walls, the error is nearly 60 percent in the middle of the channel. This is likely because the walls leak a considerable amount of fluid in the superposition approximation as they do not satisfy the no-slip condition. However, because the error is so small near the wall, we can confidently employ the Stokesian dynamics method of adding in the lubrication forces while subtracting the single wall forces from the problem in all but the most narrow channels. Even in narrow channels, the effective superposition of resistance tensors may still be quite good, as inverting the grand mobility tensor accounts for all the reflections between the particle and the walls. The biggest contribution to this is simply the single wall portion when Ξ is near zero or unity, so removing this portion directly should be quite effective. Determining the exact error associated with this approximation is difficult in general, but a similar approximation is used to add in the pair-wise lubrication interactions among many particles and has proven very effective for determining accurate and consistent rheological data [see *e.g.* Phung, Brady and Bossis (1996)].

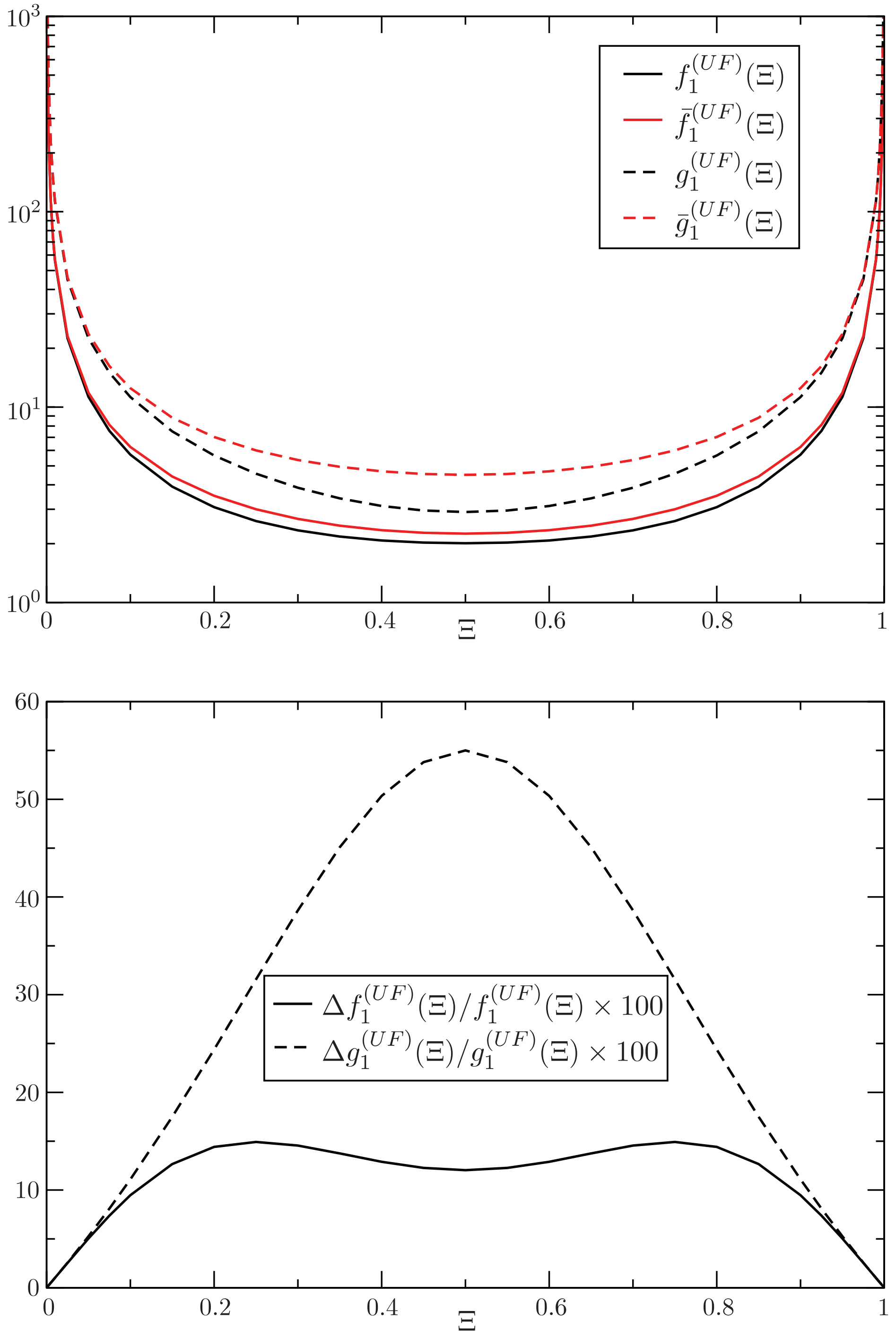

Figure 5.8: The components of the exact translation-force coupling and the translation-force coupling determined using Oseen's superposition approximation as well as the relative error between this and the Stokesian dynamics results.

5.3.2 Sedimentation of a particle between parallel walls

We use a Stokesian Dynamics simulation to compute the velocity of a particle falling due to gravity between parallel walls. In figure 5.9, we plot the parallel fall speed and rotation rate of a single particle in channels of various widths. In order to compare the results for different channel widths on the same basis, we plot them as a function of the height of the particle above the lower wall in the channel divided by the channel width (*i.e.* $\Xi - a/H$). Because of the symmetry of the channel, we only consider particles which sit less than half way across the channel. In this way, we capture both the lubrication and mid-channel behavior of the fall speed and the rotation rate graphically. Notice, that because of the interactions between the walls, the mid-channel velocity is a function of the channel width. For sufficiently wide channels ($H/a \gg 1$), the fall speed in the middle of the channel approaches unbounded value ($6\pi\eta a F_{\|}$) as a/H. This result arises directly from the expression for $\mathbf{M}_{UF}$ constructed in the previous section. Similarly, for wide channels, the $O(a/H)^2$ contribution to the rotation-force coupling is explicitly observable. In the near wall region, the lubrication forces cause the particle to rotate one direction, like a wheel rolling over the ground. However, near the middle of the channel, this rotation reverses briefly because the $O(a/H)^2$ term dominates the interaction. Remember, this term only arises because of the presence of both walls. It has no analogue in single wall problem. While this reversal may seem anomalous, we can refer back to Faxén's result for the force on a particle falling in a channel to confirm that this contribution makes a substantial contribution to the dynamics of the particle. In Faxén's solution, there was an $O(a/H)^4$ contribution to the fall speed of a particle in a channel. Of course, that problem studied a particle which did not rotate as it fell, so the effective mobility must be written as

$$\mathbf{M}_{UF} - \mathbf{M}_{UL} \cdot \mathbf{M}_{\Omega L}^{-1} \cdot \mathbf{M}_{\Omega F}. \tag{5.50}$$

We have shown that we recover Faxén's $O(a/H)$, $O(a/H)^3$ and $O(a/H)^5$ terms in $\mathbf{M}_{UF}$. Recall now that to leading order, $\mathbf{M}_{UL}$ and $\mathbf{M}_{\Omega F}$ scale like $O(a/H)^2$ and $\mathbf{M}_{\Omega L}$ is simply $O(1)$. From this, it is clear that the additional $O(a/H)^4$ piece of Faxén's result is due in part to the two wall reflection of the rotlet – the

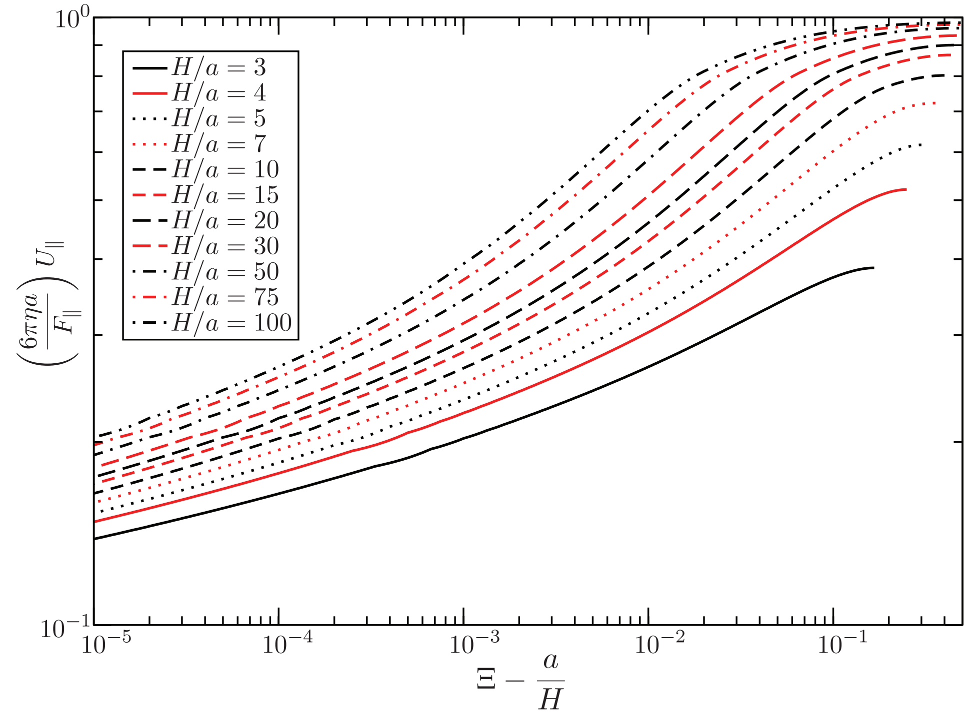

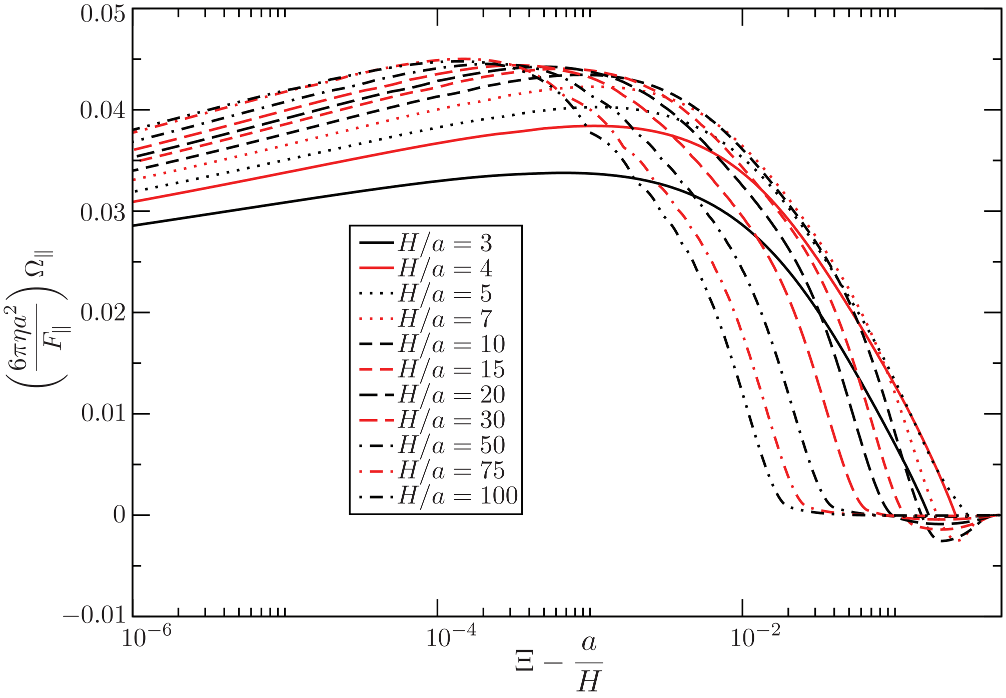

Figure 5.9: The fall speed, $U_\parallel$, and rotation rate, $\Omega_\parallel$, of a particle sedimenting along a channel. The fall speed and rotation rate are normalized by the Stokes velocity of the same particle subject to the same force in an otherwise unbounded fluid (*i.e.* $F_\parallel/6\pi\eta a$ and $F_\parallel/6\pi\eta a^2$).

rest is due to the induced stresslet. This rotational reversal may be difficult to observe experimentally as it happens only over a narrow band near the center of the channel where the rotation rate of the particle is already quite small. However, given the precise control possible with laser tweezer techniques, it seems likely that this could be measured in a particle tracking experiment.

One must be careful when making such a comparison however as we have neglected one formality in our analysis. In addition to the boundary conditions specified at the channel walls, a condition on the mean flow through or the pressure drop down the channel is necessary. These represent closed and open channel ends. Implicit in what we have calculated is the restriction that the pressure drop down the channel is zero. Since the space between the channel walls is infinite, there are no backflow effects hindering the motion of the particle. The same may not be true in the finite volume of an experimental apparatus.

We also plot the fall speed of a particle sedimenting perpendicular to the channel walls as a function of position in the channel in figure 5.10. By symmetry, there can be no rotational coupling in this case. Qualitatively, this figure is quite similar to that for sedimentation along the channel. However, one distinct difference is the decay rate of the fall speed in the near wall regime. Motion towards the wall is much more resistive in this regime since the lubrication forces scale like $(\Xi - a/H)^{-1}$. For motion along the wall, the lubrication forces are more weakly singular and scale logarithmically. Of particular interest is the fraction of the channel over which the sedimentation velocity is near the mid-channel velocity. In other words, we would like to know which region of the channel is least sensitive to the presence of the walls. To measure this, we choose an arbitrary threshold of five percent of the mid-channel velocity and measure the fractional distance across the channel where a particle first obtains this fall speed. We use this to calculate the fraction of the channel over which the mean fall speed of the particle is greater than 95% of the mid-channel fall speed. This fraction is plotted against the channel width in figure 5.11. While the particles in these channels have been seemingly well behaved, these particular results for the mid-channel speed are slightly anomalous in the narrow regime. We expect that as the channel becomes wider, the fraction of the channel where sedimentation is near the mid-channel speed will grow monotonically. However, the Stokesian Dynamics model of the near wall interactions “over counts” the resistivity of each of the walls when the separation

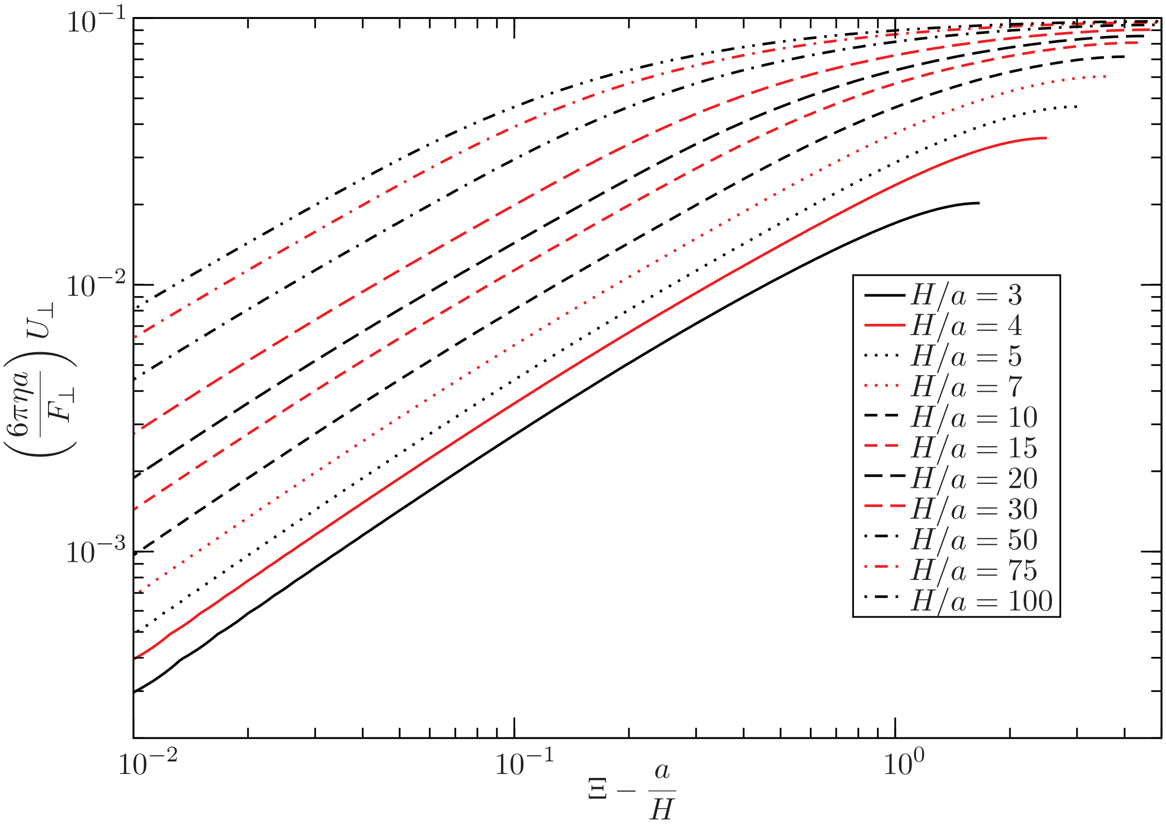

Figure 5.10: The fall speed, $U_\perp$, of a particle sedimenting along a channel normalized by the Stokes velocity of the same particle subject to the same force in an otherwise unbounded fluid (*i.e.* $F_\perp/6\pi\eta a$).

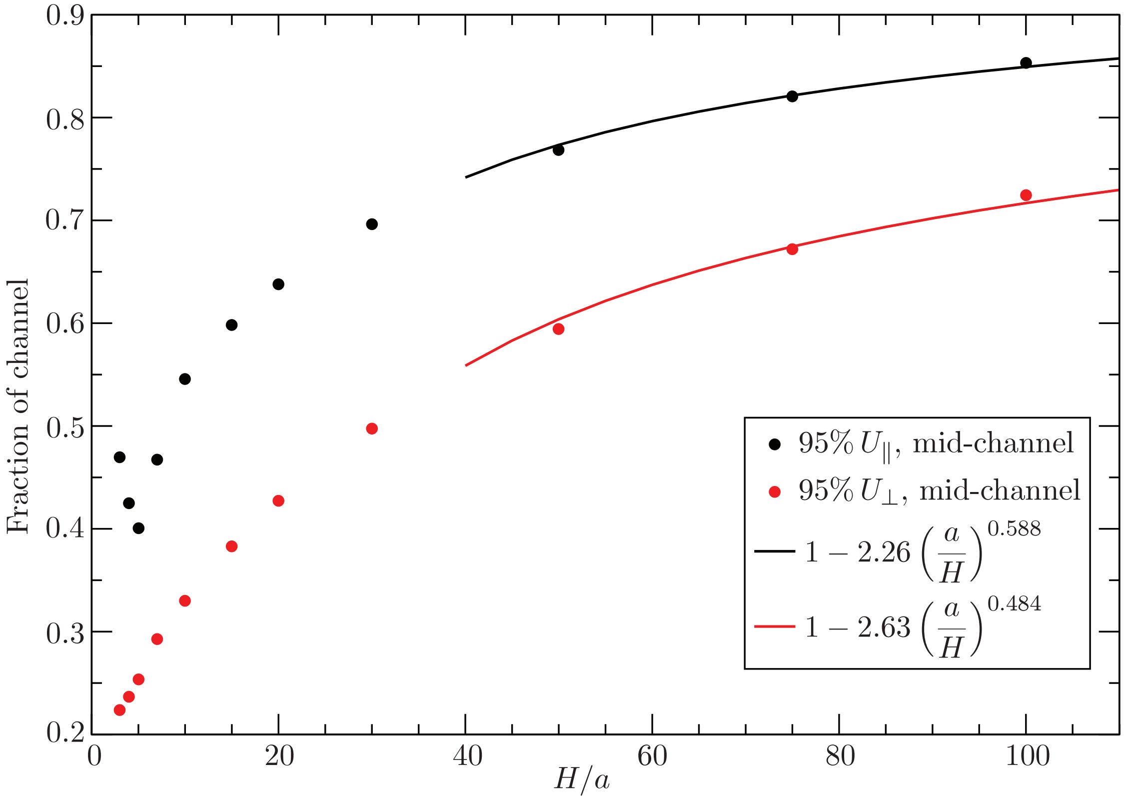

Figure 5.11: The fraction of the channel over which a particle sediments at 95% of its mid-channel fall speed.

is so small. This breaks the anticipated monotonic growth. Essentially, while the lubrication interactions each scale singularly with respect to the gap width between the particle and the wall, the presence of a nearby second wall affects the $O(1)$ contribution to the resistance in a significant way. Still, the lubrication interactions with each of the walls are in a sense independent of one another for very narrow channels, so our approach recovers the dominant hydrodynamic effect. For channels outside the narrow regime, we find that the fraction of the channel where the particle falls faster than 95% of the mid-channel speed scales roughly as the inverse square root of the channel width. Qualitatively, the fast-fall-speed fraction of channel grows in a way which is independent of the fall direction. While the absolute channel fraction for perpendicular sedimentation is always less than parallel sedimentation, the growth rate is comparable. As the channel gets very large ($H/a \gg 1$), the difference between parallel and perpendicular sedimentation becomes negligible everywhere but near the walls. We expect that these two curves coincide in the limit that the gap between the walls is infinitely wide.

5.3.3 Brownian drift of a particle in a channel

The stochastic thermal forces on a particle in a channel lead to a deterministic contribution to the particle's velocity arising from the dependence of the Brownian forces on the hydrodynamic interactions of the particle with the channel walls. Given a particle near a wall at a particular instant in time, thermal forces will drive it either toward or away from the wall with equal probability. If the particle moves toward the wall, its mobility decreases and the thermal impulse propels the particle more slowly. Conversely, if the particle moves away from the wall, the impulse propels the particle more quickly. Of course the strength of the thermal forcing varies with distance from the wall as well since it is proportional to the square root of the hydrodynamic resistance. Substituting an instantaneously correlated thermal impulse denoted $\mathbf{F}^B(t)$ of r.m.s. strength $\sqrt{2kT\mathbf{R}_{FU}(\mathbf{X}(t))}$ into equation 2.29, integrating over an interval in time (Δt) that is short with respect to the particle bare diffusion time and taking care to account for changes in the resistance as the particle diffuses yields an evolution equation for the position of the particle,

$$\mathbf{X}(t+\Delta t) = \mathbf{X}(t) + \mathbf{R}_{FU}^{-1}(\mathbf{X}(t)) \cdot \mathbf{F}^B(t)\Delta t + kT\nabla \cdot \mathbf{R}_{FU}^{-1}(\mathbf{X}(t))\Delta t + O(\Delta t^2). \tag{5.51}$$

The mean effect of the change in the hydrodynamic resistance and in the magnitude of the thermal forcing as a particle diffuses in space results in a deterministic drift away from the wall. The drift velocity is given quite simply by $kT\nabla \cdot \mathbf{R}_{FU}^{-1}$, where kT is the thermal energy [see *e.g* Batchelor (1976) and Ermak and McCammon (1978)]. There is no drift parallel to the wall because the resistance is independent of the position along the wall. In figure 5.12 we plot the Brownian drift velocity of a particle sitting above the lower wall for channels of various widths. As the walls are further separated, the particle's sense of the second wall becomes minimal and the drift velocity decays at the single wall rate as h^{-2}. However, the drift velocity decays to zero quickly as the particle approaches the midline of the channel where there is no variation in mobility. On the other side of the midline, the drift reverses sign as the particle is impelled away from the upper wall instead.

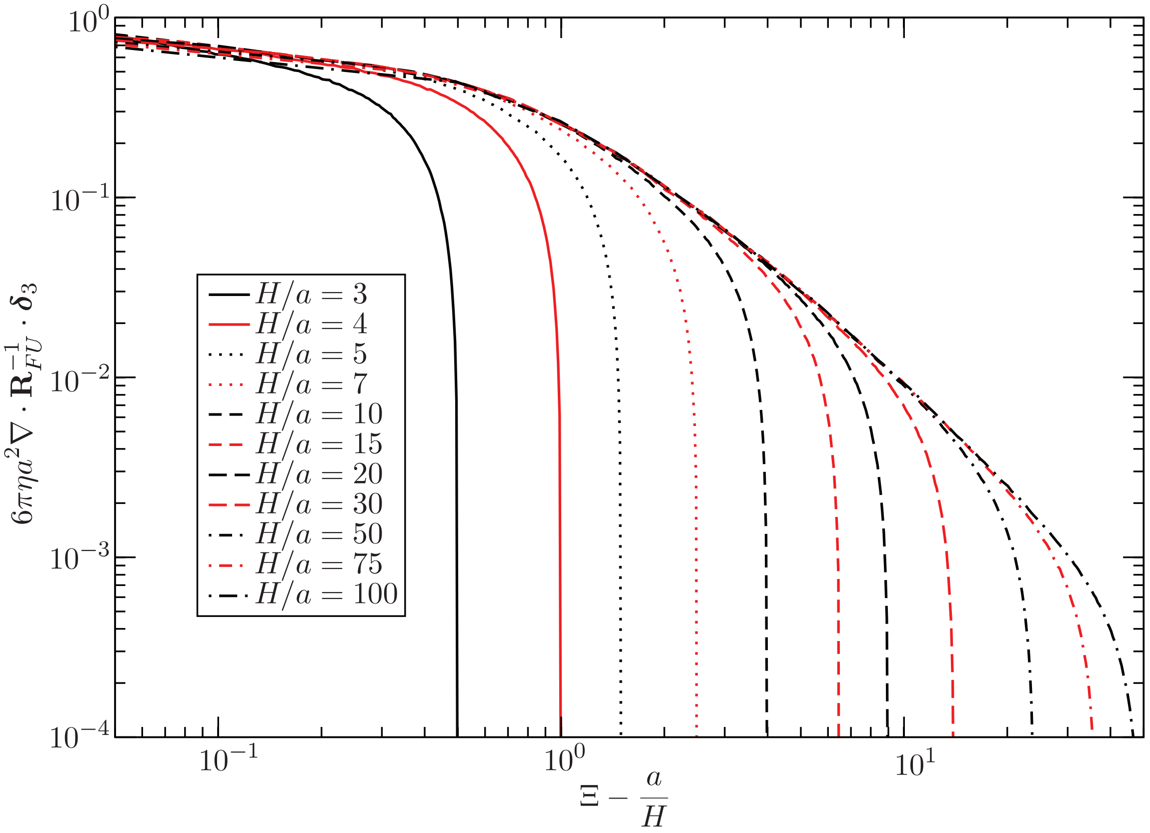

Figure 5.12: The drift velocity of a single Brownian particle in channel of width H/a plotted as a function of height above the lower channel wall.

5.3.4 Einstein viscosity for a dilute suspension between parallel walls

We begin this calculation with Brenner's definition of the viscosity as the coefficient of proportionality relating energy dissipation in two similarly strained flows, *viz.*

$$\frac{E^{(0)}}{\eta} = \frac{E^{(0)} + E^*}{\eta^*}, \tag{5.52}$$

where $E^{(0)}$ is the rate of energy dissipation in a particle free flow, E^* is the additional rate of energy dissipation in a particle laden flow with the same rate of strain and solvent viscosity and η^* is the viscosity of that suspension [see Happel and Brenner (1986)]. With some relatively simple manipulation, one can show that

$$\frac{\eta^*}{\eta} = 1 - \varphi \frac{\langle \mathbf{S} \rangle : \mathbf{E}^\infty}{\frac{8}{3}\pi\eta a^3 \mathbf{E}^\infty : \mathbf{E}^\infty}, \tag{5.53}$$

where $\langle \mathbf{S} \rangle$ is the average particle stresslet and φ is the particle volume fraction. For a force and torque free suspension, we conclude that the particle stresslet is simply

$$\mathbf{S} = -\left(\mathbf{R}_{SE} - \mathbf{R}_{SU} \cdot \mathbf{R}_{FU}^{-1} \cdot \mathbf{R}_{FE} - \mathbf{R}_{S\Omega} \cdot \mathbf{R}_{L\Omega}^{-1} \cdot \mathbf{R}_{LE}\right) : \mathbf{E}^\infty \approx -\mathbf{M}_{ES}^{-1} : \mathbf{E}^\infty, \tag{5.54}$$

where the approximation is valid when the particles are far from the walls such that lubrication forces are unimportant. We will use this approximation through the rest of this section as we are interested in the viscosity of dilute suspensions in channels which are wide. In this case, a small fraction of the particles are found near the walls and therefore, any lubrication effects make a minimal contribution to the rate of energy dissipation. With this simplification, our expression for the viscosity of the suspension becomes

$$\frac{\eta^*}{\eta} = 1 + \varphi \frac{\mathbf{E}^\infty : \left\langle \mathbf{M}_{ES}^{-1} \right\rangle : \mathbf{E}^\infty}{\frac{8}{3}\pi\eta a^3 \mathbf{E}^\infty : \mathbf{E}^\infty}. \tag{5.55}$$

This expression is general, but since we have restricted ourselves to the study of dilute suspensions ($\varphi \ll 1$), $\mathbf{M}_{ES}$ corresponds only to the "self" parts of the grand mobility tensor. In the limit that the gap between the walls becomes infinite in extent, then the inverse mobility coupling between rate of strain and stresslet becomes an isotropic tensor proportional to $\frac{20}{3}\pi\eta a^3$ and we recover the Einstein viscosity, $\frac{\eta^*}{\eta} = 1 + \frac{5}{2}\varphi$. Following this, we write the viscosity as

$$\frac{\eta^*}{\eta} = 1 + \frac{5}{2}\varphi\left(1 + z\left(\frac{H}{a}\right)\right), \tag{5.56}$$

where

$$z\left(\frac{H}{a}\right) = \frac{\mathbf{E}^\infty : \langle \mathbf{M}_{ES}^{-1} \rangle : \mathbf{E}^\infty}{\frac{20}{3}\pi\eta a^3 \mathbf{E}^\infty : \mathbf{E}^\infty} - 1. \tag{5.57}$$

Shortly after Einstein made his calculation of the viscosity of a dilute suspension, Guth and Simha (1936) attempted to include the effects of channel walls on the suspension viscosity. In their approach, the effects of each wall were superimposed *á la* Oseen, and the resulting particle stresslet was calculated while assuming the particles were evenly distributed in the channel. With this approximation, they found that

$$z\left(\frac{H}{a}\right) = \frac{5}{16}\left(\frac{H}{a}\right)\left[\left(\frac{H}{a}\right)^2 - 1\right]^{-1}. \tag{5.58}$$

Like Guth and Simha, we assume that the dilute suspension is uniformly distributed between the walls and calculate the average of $\mathbf{M}_{ES}^{-1}$ as

$$\langle \mathbf{M}_{ES}^{-1} \rangle = \frac{1}{1 - 2(a/H)} \int_{a/H}^{1-a/H} \mathbf{M}_{ES}^{-1}\left(\Xi; \frac{H}{a}\right) d\Xi. \tag{5.59}$$

To a first approximation for widely separated channel walls, and parallel plate rheometry (*i.e.* $\mathbf{E}_{ij}^\infty = \delta_{i1}\delta_{j2} + \delta_{i2}\delta_{j1}$), the contribution to the viscosity can be written quite simply, *viz.*

$$z\left(\frac{H}{a}\right) = \frac{20}{9}\left(\frac{a}{H}\right)^3 \frac{1}{1 - 2(a/H)} \int_{a/H}^{1-a/H} g_3(\Xi)\, d\Xi. \tag{5.60}$$

For wide channels ($H/a \gg 1$), the dominant contributions to the above integral are near $\Xi = 0$ and $\Xi = 1$ where $g_3(\Xi)$ scales like the single wall values, Ξ^{-3} and $(1 - \Xi)^{-3}$, respectively. Therefore, in this regime we

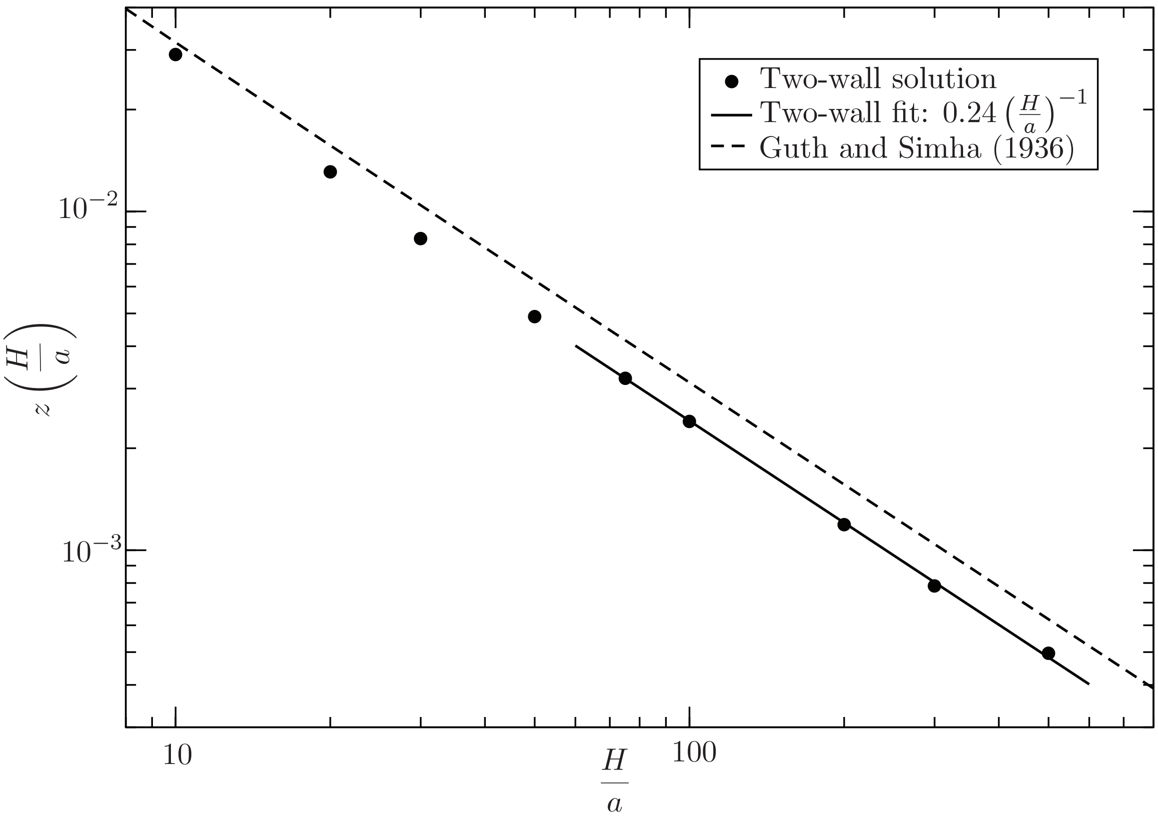

Figure 5.13: The additional contribution to the viscosity of a dilute suspension, $\frac{\eta^*}{\eta} = 1 + \frac{5}{2}\varphi\left(1 + z\left(\frac{H}{a}\right)\right)$ is plotted against the separation between the channel walls. The superposition approximation due to Guth and Simha (1936) is also plotted.

predict that $z(H/a)$, scales like a/H which is the same scaling predicted by Guth and Simha. In figure 5.13 we plot the additional contribution to the viscosity of a dilute suspension as well as the result due to Guth and Simha. We find that this additional contribution is always smaller than that predicted by superposition. Note that another measure of this same quantity was made recently by Zurita-Gotor *et. al.* (2007). They compute the viscosity over a narrower range of channel widths which do not overlap with those presented here. Similarly, our analysis is not applicable to the narrow channels they considered. Comparison of the two results is therefore difficult. Our aim in this section was to compare superposition with the Fourier transform solution in a regime where the particles spend little time in the lubrication regime near the wall. Our result is quite different from this other calculation. That the viscosity computed via superposition is larger than that due to the exact, two wall solution to the Stokes equations, is perhaps most easily understood via analogy to electrostatics. Consider a pair of potential free walls with a dielectric material in the interstice. Taken as a whole, the walls and the dielectric must be charge free. A superposition of the single wall, electrostatic Green's function given one positive charge in the channel would yield a virtual negative charge in each of the walls. In this case, the net charge on the dielectric and the walls is negative. Whereas the exact two-wall Green's function is the summation of a hierarchy of positive and negative virtual charges in both walls which must yield a charge neutral whole. Similarly, the superposition of single wall Green's functions in Stokes flow yields a net force imbalance on the system comprising both the fluid and the walls. This necessarily leads to a higher rate of energy dissipation in the fluid, hence the lower viscosity when the exact solution for the channel flow is used. A rigorous though brief proof is developed in appendix D.

5.4 Conclusions

In this chapter we computed the exact reflection of various multipolar velocity fields off of the parallel walls of a channel. These were combined with different Faxén formulas to generate the far-field mobility tensor for a single spherical particle in a channel. We found that the mobility could be written in terms of inverse powers of the channel width multiplied by functions of the fractional distance of the particle across the channel. These functions matched predictions for a particle in the middle of the channel and a quarter of the way across the channel made by Faxén in his dissertation nearly a century ago. The form we have used to represent these mobility functions is especially useful for computational studies since the functions of the fractional distance across the channel can be tabulated and used for channels of arbitrary width. The tables for the six mobility tensors discussed within are given in the appendices. Using these functions we made additional predictions of the single particle fall speed both along and perpendicular to the channel walls. We also calculated the rotation rate of a particle sedimenting along the channel and found that the direction of rotation reverses near the midline of sufficiently wide channels. We also calculated the Brownian drift velocity for a single particle and the correction to the Einstein viscosity for a dilute suspension in a wide channel.

While the method described deals only with computations for single particles, the same approach may be extended to the study of large suspensions with inter-particle hydrodynamic interactions. This could take the form of either a traditional Stokesian Dynamics simulation or an Accelerated Stokesian Dynamics simulation. The key point is that the reciprocal space representation of the hydrodynamic interactions is the most natural way to represent computationally the far-field many-bodied interactions amidst a suspension. The inverse transformation may not even be necessary if a simulation is properly constructed to represent the suspension in a set of periodic cells. Using the Poisson summation formula, one can show that adding all the interactions to a single particle and its periodic images is the same as summing over the reciprocal space representation of the interactions with a Fourier exponential weighting [see *e.g.* Beenakker (1986)]. One important piece to consider here, however, is that this summation is slowly converging in general. To make things computationally efficient, we must split the domain of interactions into two regions: one over which short-range, real-space interactions dominate and another over which long-range, reciprocal space interactions are most important. This is precisely the Ewald summation technique which turns one slowly converging summation into two rapidly converging ones. In the case of the short-range interactions, in all likelihood it will be sufficient to represent the channel walls as a superposition of two single walls only. We have already computed these contributions (see Swan and Brady, 2007). While for the long-range interactions, the full reciprocal space two wall solution will be needed. This approach will avoid the costly inversion of the solutions to the Stokes flow equations from the reciprocal space back to the real-space while still accurately reflecting the condition of no-slip on each of the walls. An approach like this one could overcome some of the difficulties which make simulations of particles in a channel difficult.

It is also possible to extend the techniques described here to the study of other particle and boundary geometries. In our approach, we only worked out the reflection of the Stokeslet off two walls explicitly. All the higher order reflections came from a multipole expansion of the boundary integral solution to the Stokes equations. A similar expansion may be performed for particles of any geometry; though, it will not truncate as succinctly as when the force density is expanded about a spherical surface. Nevertheless, this result combined with an appropriate Faxén type formula for that particular particle geometry will generate the grand mobility tensor. Similarly, if the reflection of the Stokeslet is found or is known in some other boundary geometry [see *e.g.* Liron and Shahar (1978) (cylindrical channel) or Maul and Kim (1995) (spherical container)], then calculation of the grand mobility tensor is as simple as choosing the proper multipole expansion and applying the Faxén formula. No doubt the results will be similar for particles that are roughly spherical in shape as Stokes flow is rather insensitive to geometric details. However, for extreme shapes like slender bodies, this approach offers an interesting possibility for studying their dynamics under confinement.

In closing, we want to emphasize the simplicity of this approach for treating the hydrodynamics of a particle in a confining geometry. The higher level perspective brought by the grand mobility tensor takes the complicated problem of determining the resistance on a particle and turns it into a hierarchical, method of reflections type procedure, which has a direct physical connection to the different force moments on the particle. In this chapter, we have computed once and for all the first nine components of the grand mobility tensor for a spherical particle in a parallel wall channel. While there are infinitely many higher order contributions to that tensor, those first nine have proven quite effective in other simulations for characterizing the dynamics of particles in suspensions. Similarly, these tensors provide a simple and therefore rather useful way to estimate the motion of a small particle in a channel. By tabulating these functions and separating out the length scale set by the channel width, we have enabled the rapid computation of single particle and dilute suspension dynamics in a channel.

Bibliography

[1] G.K. Batchelor. Brownian diffusion of particles with hydrodynamic interaction. *J. Fluid Mech.*, 74(1):1–29, May 1976.

[2] C.W.J. Beenakker. Ewald sum of the Rotne–Prager tensor. *J. Chem. Phys.*, 85(3):1581–1582, August 1986.

[3] S. Bhattacharya and J. Blawzdziewicz. Image system for Stokes-flow singularity between two parallel planar walls. *J. Math. Phys.*, 43(11):5720–5731, November 2002.

[4] J.R. Blake and A.T. Chwang. Fundamental singularities of viscous flow. *J. Eng. Math.*, 8(1):23–29, January 1974.

[5] G. Bossis, A. Meunier and J.D. Sherwood. Stokesian dynamics simulations of particle trajectories near a plane. *Phys. Fluids A*, 3:1853, August 1991.

[6] Cichocki B. *et al.* Friction and mobility for colloidal spheres in Stokes flow near a boundary: the multipole method and applications. *J. Chem. Phys.*, 112(5), 2548–2561, February 2000.

[7] E.R. Dufresne, D. Altman, and D.G. Grier. Brownian dynamics of a sphere between parallel walls. *Europhysics Lett,*, 53(2):264–270, January 2001.

[8] L.J. Durlofsky, J.F. Brady, and G. Bossis. Dynamic simulation of hydrodynamically interacting particles. *J. Fluid Mech.*, 180:21–49, June 1987.

[9] L.J. Durlofsky and J.F. Brady. Dynamic simulation of bounded suspensions of hydrodynamically interacting particles. *J. Fluid Mech.*, 200:39–67, January 1989.

[10] D.L. Ermak and J.D. McCammon. Brownian dynamics with hydrodynamic interactions. *J. Chem. Phys.*, 69:1352–1360, 1978.

[11] H. Faxen. *Arkiv. Mat. Astron. Fys.*, 17(27), 1923. dissertation, Uppsala University, 1921.

[12] P. Ganatos, S. Weinbaum and R. Pfeffer. A strong interaction theory for the creeping motion of a sphere between plane parallel boundaries. Part 1. Perpendicular motion. *J. Fluid Mech.*, 99(4):739-753, February 1980.

[13] E. Guth and R. Simha. Untersuchungen über die viskosität von suspensionen und lösungen. 3. Über die viskosität von kugelsuspensionen. *Colloid and Polymer Sci.*, 74(3):266, 1936.

[14] J. Happel and H. Brenner. *Low Reynolds Number Hydrodynamics*. Prentice Hall, Englewood Cliffs, 2nd edition, 1986.

[15] R.B. Jones. Spherical particle in Poiseuille flow between planar walls. *J. Chem. Phys.*, 121:483–500, March 2004.

[16] S. Kim and S.J. Karrila. *Microhydrodynamics*. Dover Publications Inc., Mineola, 2nd edition, 1991, 2005.

[17] D. Leighton and A. Acrivos. Measurement of shear-induced self-diffusion in concentrated suspensions of spheres. *J. Fluid Mech.*, 177:109–131, May 1987.

[18] N. Liron and S. Mochon. Stokes flow for a Stokeslet between two parallel flat plates. *J. Eng. Math.*, 10:287–303, 1976.

[19] N. Liron and R. Shahr. Stokes flow due to a Stokeslet in a pipe. *J. Fluid Mech.*, 86(4):727–744, 1978.

[20] C. Maul and S. Kim. Image of a point force in a spherical container and its connection to the Lorentz reflection formula. *J. Eng. Math.*, 30(1-2):119-130, March 1996.

[21] P.R. Nott and J.F. Brady. Pressure-driven flow of suspensions: simulation and theory. *J. Fluid Mech.*, 275:157-199, 1994.

[22] C.W. Oseen. *Neuere Methoden und Ergebnisse in der Hydrodynamik.* dissertation, Akademische Verlagsgesellschaft, Leipzig, 1928.

[23] T.N. Phung, J.F. Brady and G. Bossis. Stokesian dynamics simulations of Brownian suspensions. *J. Fluid Mech.*, 313:181-207, December 1996.

[24] A. Singh and P.R. Nott Normal stresses and microstructure in bounded sheared suspensions via Stokesian Dynamics simulations. *J. Fluid. Mech.*, 412:279–301, January 2000.

[25] M.E. Staben, A.Z. Zinchenko and R.H. Davis. Motion of a particle between two parallel plane walls in low-Reynolds-number Poiseuille flow. *Phys. Fluids*, 15:1711–1734, May 2003.

[26] J.W. Swan and J.F. Brady. Simulation of hydrodynamically interacting particles near a no-slip boundary. *Phys. Fluids*, 19(11), November 2007.

[27] M. Zurita-Gotor, J. Blawzdziewicz and E. Wajnryb. Motion of a rod-like particle between parallel walls with application to suspension rheology. *J. of Rheology*, 51(1): 71–97, January 2007.

Chapter 6

Many particles between parallel plane walls

6.1 Introduction

The study of colloidal particles in a bounded geometry, in particular the channel geometry, has a long history. A brief survey of prior approaches and the current state-of-the-art analytically, computationally and experimentally is offered with the intention of providing some scope to the approach advanced in this manuscript.

The calculation of the hydrodynamic resistance to the motion of a single spherical particle between parallel walls by Faxén (1921) used a method of reflections approach to generate a series solution in inverse powers of the channel width for particles located one-half and one-quarter of the way across the channel. His approach can certainly be applied to particles located elsewhere in the channel, but the fortuitous symmetry that Faxén used breaks down and makes the calculation much more difficult [see Swan and Brady (2010)]. In search of a more general expression, Oseen (1928) proposed considering the channel walls independently and superimposing the resistance due to each. While not correct, this can often be a suitable approximation. For instance, Guth and Simha (1936) repeated Einstein's calculation of the viscosity of a dilute suspension while bounding the suspension by two super-imposable no-slip walls. They recover the correct scaling for the viscosity increment with respect to the channel width. Blake (1971) brought an analogous electrostatic approach to the problem by determining the Green's function for Stokes flow above a single no-slip wall.

This same technique was employed by Liron and Mochon (1976) for computing the Green's function for Stokes flow in the parallel wall geometry. Key to this work was the conclusion that while the Green's function with a single wall requires a finite number of "reflections," the parallel wall Green's function must be represented as an infinitude of reflections. This of course poses serious challenges to modeling suspensions in channels accurately. Since Stokes flows are unique, any solution to this problem will in some sense require the computation of this infinite sum.

It appears this difficulty can only be overcome with some form of computational approximation. After all, for a single particle in even the simplest channel geometry, the hydrodynamic interactions are among three bodies – never an easy computation. A number of different models for the dynamics of a dispersion in a channel have arisen. Durlofsky and Brady (1989) combined their Stokesian Dynamics algorithm with a discretized model of the channel walls which accounts for the additional energy dissipation due to the no-slip condition on the walls. Similarly, Nott and Brady (1994) modeled the walls as an array of particles fixed in space. While qualitatively correct, this approach poses a number of physical and computational challenges such as the "leakiness" of the walls and possible errors arising from the pairwise superposition of lubrication interactions with the wall particles. An approach using Stokes flow eigenfunctions was introduced by Bhattacharya and Blawzdziewicz (2002) and has had some success in modeling suspensions in channels. However, there is a high degree of complexity associated with the implementation of this technique. Nonetheless, Jones (2004) used this technique to model the motion of a single particle due to a Poiseuille flow. Similarly, Zurita-Gotor *et al.* (2007) extended this model to study the rheology of rod-like particles in suspension. One other approach originated by Staben *et al.* (2003) relies on the boundary-integral formulation for Stokes flow and employs the Green's function for channel flow [Liron and Mochon (1976)] in the computation of the hydrodynamic resistance to the motion of a particle in a channel. These studies represent three distinct classes of technique: wall discretization, eigenfunction expansion and boundary-integral solution. A survey of the literature will show that virtually all computational studies of dispersions between walls are rooted in one of these classes. The approach here returns to the electrostatic analogy and utilizes the Fourier transformation of the Stokes flow solution and an Ewald summation to generate a log-linear algorithm for the dynamics of particles in a channel. Another study worth mentioning is that of Hernández-Ortiz *et al.* (2007) which proposes a novel method for dividing the force density in the fluid into so-called "local" and "global" contributions. In the development of the present model, a similar splitting arises and is justified analytically as a corollary to the Ewald summation technique [see *e.g.* Beenakker (1986)].

Experimental studies of colloidal particles near plane walls span the gamut. There have been many investigations of the macroscopic properties of channel confined suspensions [Goldsmith and Mason (1962), Karnis, Goldsmith and Mason (1966), Seshadri and Sutera (1970), Cox and Mason (1971), Cox and Hsu (1976), de Gennes (1979) and Gregory (1981)] perhaps culminating in Leighton and Acrivos (1987) where a direct connection to the particle micromechanics explained the observation of a time-dependent viscosity in a Couette flow device. This showed that detailed hydrodynamic and particle-particle interactions cannot be marginalized in models of confined viscoelastic materials. The experiments of Koh, Hookham and Leal (1994) for suspensions in rectangular channels were the first to measure detailed distributions of the spatial variation in particle concentration and velocity for pressure driven flows. While Lyon and Leal (1998) tested the diffusive flux [Leighton and Acrivos (1987)] and suspension balance [Nott and Brady (1994)] continuum models which incorporate this principle. Still, such models require knowledge of physical parameters based on the local suspension dynamics and rheology which have been pursued extensively [see *e.g.* Butler and Bonnecaze (1999), Dufresne, Altman and Grier (2001), Zarraga and Leighton (2002), Frank *et al.* (2003), Norman, Nayak and Bonnecaze (2005) and Ramachandran and Leighton (2007)]. While parameters for continuum models have been refined, these experiments largely represent measurements of long-time suspension properties.

The chapter is structured as follows. In section 6.2.1 a method is developed for rapidly computing the far-field hydrodyanmic interactions among the particles comprising a periodic suspension bound by two parallel channel walls. Section 6.2.5 describes the Stokesian Dynamics method [Brady *et al.* (1988)] for computing both the far-field and the near-field hydrodynamic forces and the velocities of particles in a suspension. Also discussed is the implementation of an Accelerated Stokesian Dynamics simulation [Seirou and Brady (2001)] based on the far-field interactions among particles in a channel. A detailed study of several canonical rheological measurements as a function of channel width and suspension concentration is made in section 6.3.

6.2 Analysis

This section details the solution of the Stokes equations subject to an arbitrary, periodic body force in a no-slip channel. Drawing from the Ewald summation technique yields a means to ensure rapid summation of this solution. As part of this rapid summation, a "local" velocity field is resolved separately by considering the two walls as independent and assessing the decay rate of the resulting reflection flow. The body force is redefined as that due to a set of particles in the fluid, and it is shown how one may use these velocity fields to construct the grand mobility tensor which is the essential linear coupling between velocity and force. The Faxén formulas for motion of a colloidal particle n amidst a sea of other particles are

$$\mathbf{U}_n = -\left(\mathbf{M}^{(S)}_{UF}\cdot\mathbf{F}^H_n + \mathbf{M}^{(S)}_{UL}\cdot\mathbf{L}^H_n + \mathbf{M}^{(S)}_{US}:\mathbf{S}^H_n + \cdots\right) + \left(1 + \frac{a_n^2}{6}\nabla_x^2\right)\left[\mathbf{u}^\infty(\mathbf{x}) + \mathbf{u}'_n(\mathbf{x})\right]\Big|_{\mathbf{x}_n}, \tag{6.1}$$

$$\mathbf{\Omega}_n = -\left(\mathbf{M}^{(S)}_{\Omega F}\cdot\mathbf{F}^H_n + \mathbf{M}^{(S)}_{\Omega L}\cdot\mathbf{L}^H_n + \mathbf{M}^{(S)}_{\Omega S}:\mathbf{S}^H_n + \cdots\right) + \frac{1}{2}\nabla\times\left[\mathbf{u}^\infty(\mathbf{x}) + \mathbf{u}'_n(\mathbf{x})\right]\Big|_{\mathbf{x}_n}, \tag{6.2}$$

$$0 = -\left(\mathbf{M}^{(S)}_{EF}\cdot\mathbf{F}^H_n + \mathbf{M}^{(S)}_{EL}\cdot\mathbf{L}^H_n + \mathbf{M}^{(S)}_{ES}:\mathbf{S}^H_n + \cdots\right) + \left(1 + \frac{a_\alpha^2}{10}\nabla^2\right)\left[\mathbf{e}^\infty(\mathbf{x}) + \mathbf{e}'_n(\mathbf{x})\right]\Big|_{\mathbf{x}_n}, \tag{6.3}$$

where $\mathbf{U}_n$ and $\mathbf{\Omega}_n$ are the rate of translation and rotation of particle n, $\mathbf{M}^{(S)}_{AB}$ are the self contributions to the mobility for a particle in a channel, $u^\infty(\mathbf{x})$ is an ambient flow field in the absence of the particles and $\mathbf{u}'_n(\mathbf{x})$ is the flow due to all the particles other than n.

The rest of this manuscript is focused primarily on the computation of $\mathbf{u}'_n(\mathbf{x})$, which is often referred to as the "disturbance" velocity field. Any model substituted for this quantity must yield a convergent sum of the integrals over the surfaces of the particles and the integral over the surface at infinity. Glendinning and Russel (1982) introduced the mean stress of the suspension into this formulation and found that, indeed the divergent hydrodynamic disturbances due to the particles and the integral over the surface at infinity together yield a convergent sum for an unbounded suspension. The more straightforward route inspired by

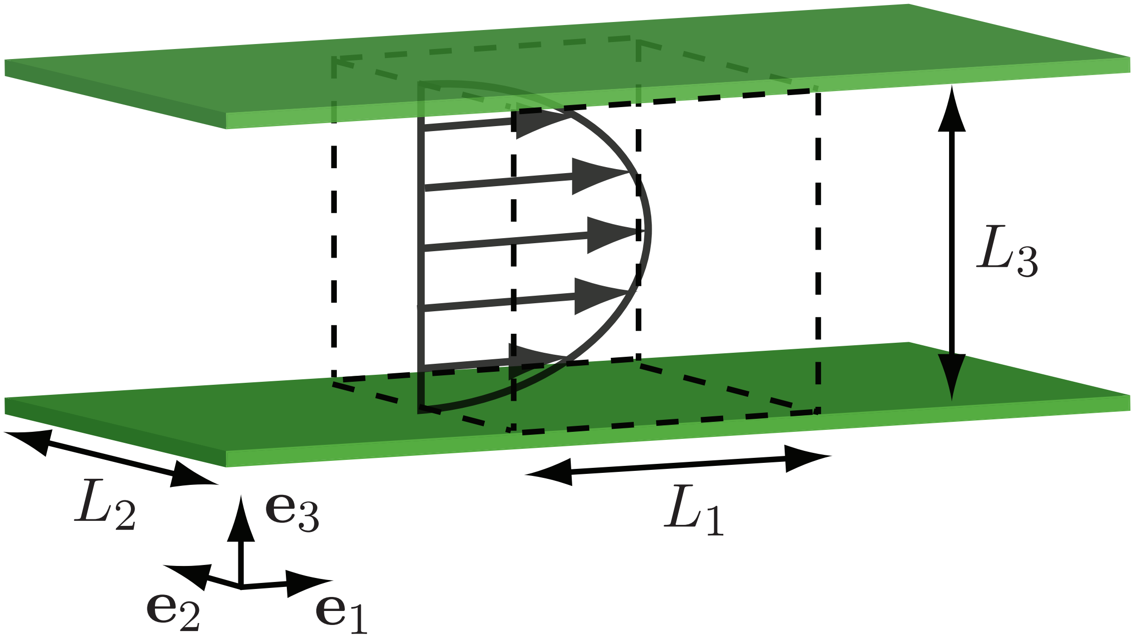

Figure 6.1: The channel geometry with periodic, fictitious streamlines is shown along with the characteristic channel and periodic cell dimensions.

Hasimoto (1959) is taken and this disturbance velocity field is computed directly in the next section.

6.2.1 Stokes flow in a channel subject to an arbitrary, periodic body force

A periodic body force, $\mathbf{f}(\mathbf{x})$, sets a viscous, incompressible fluid in motion. As the body force has periods L_1 and L_2 in the $\mathbf{e}_1$ and $\mathbf{e}_2$ directions, the fluid velocity and pressure fields, denoted by $\mathbf{u}(\mathbf{x})$ and $p(\mathbf{x})$, are similarly periodic (see figure 6.1). Two additional constraints are imposed such that the velocity field is zero at the channel boundaries ($x_3 = 0$ and $x_3 = L_3$). The Stokes equations govern the values of these dynamic quantities. Each of these periodic variables is written as a Fourier series and the equations dictating the coefficients of the Fourier series are written below.

$$\mathbf{f}(\mathbf{x}) = \sum_{k_1,k_2} e^{-2\pi i k_\alpha x_\alpha} \mathbf{f}^{(k)}(x_3), \tag{6.4}$$

$$\eta \mathbf{u}(\mathbf{x}) = \sum_{k_1,k_2} e^{-2\pi i k_\alpha x_\alpha} \mathbf{u}^{(k)}(x_3), \tag{6.5}$$

$$p(\mathbf{x}) = \sum_{k_1,k_2} e^{-2\pi i k_\alpha x_\alpha} p^{(k)}(x_3), \tag{6.6}$$

and

$$-(2\pi k)^2 \mathbf{u}^{(k)} + \frac{\partial^2 \mathbf{u}^{(k)}}{\partial x_3^2} = -2\pi i k_\alpha \mathbf{e}_\alpha p^{(k)} + \mathbf{e}_3 \frac{\partial p^{(k)}}{\partial x_3} - \mathbf{f}^{(k)}, \tag{6.7}$$

$$-2\pi i k_\alpha u_\alpha^{(k)} + \frac{\partial u_3^{(k)}}{\partial x_3} = 0, \tag{6.8}$$

where η is the fluid viscosity, $k^2 = k_\alpha k_\alpha$ and repeated Greek indices signify summation over the index values $(1,2)$. The $\mathbf{k}$'s are the so-called reciprocal lattice vectors defining the periodic geometry. For a rectilinear lattice, the wave vectors are simply $k_j = i/L_j$ for $i = 0, \pm 1, \pm 2$, *etc.* while for more complicated lattices, the wave vectors must satisfy the condition that $\mathbf{e}_3 \times \mathbf{y}_i / L_1 L_2 = \mathbf{k}_i$, where $\mathbf{y}_i$ is one of two lattice coordinates for which the velocity and pressure are invariant after an integer superposition (*e.g.* $\mathbf{x} + i\mathbf{y}_1 + j\mathbf{y}_2$). The no-slip condition at the channel walls implies that $\mathbf{u}^{(k)}(0) = \mathbf{u}^{(k)}(L_3) = 0$. The solution to these equations can be written as

$$\mathbf{u}^{(k)}(x_3) = (\mathbf{I} - 4\pi k x_3 \mathbf{m}\mathbf{m}) \cdot \mathbf{A}^{(k)} e^{2\pi k x_3} - (\mathbf{I} + 4\pi k x_3 \hat{\mathbf{m}}\hat{\mathbf{m}}) \cdot \mathbf{A}^{(k)} e^{-2\pi k x_3} + \mathbf{U}^{(k)}(x_3), \tag{6.9}$$

and

$$p^{(k)}(x_3) = 2\sqrt{2}\pi k \left(\mathbf{m} e^{2\pi k x_3} + \hat{\mathbf{m}} e^{-2\pi k x_3} \right) \cdot \mathbf{A}^{(k)} + P^{(k)}(x_3), \tag{6.10}$$

where $\mathbf{m} = (2\sqrt{2}\pi k)^{-1} (-2\pi i k_\alpha \mathbf{e}_\alpha + 2\pi k \mathbf{e}_3)$, $\hat{\mathbf{m}}$ is the complex conjugate of $\mathbf{m}$, $\mathbf{A}$ is a coefficient to be determined by the boundary conditions and $\mathbf{U}^{(k)}(x_3)$ and $P^{(k)}(x_3)$ are the particular solutions to the Stokes equations. These are written as convolutions of the body force with the homogenous part of the solution such that

$$\mathbf{U}^{(k)}(x_3) = \left[\mathbf{I} - \frac{1}{2}\left(\mathbf{m}\hat{\mathbf{m}} + \hat{\mathbf{m}}\mathbf{m}\right)\right] \cdot \mathbf{C}_1^{(k)}(x_3) + \mathbf{m}\mathbf{m} \cdot \mathbf{C}_2^{(k)}(x_3) + \hat{\mathbf{m}}\hat{\mathbf{m}} \cdot \mathbf{C}_3^{(k)}(x_3), \tag{6.11}$$

where

$$\mathbf{C}_1^{(k)}(x_3) = -\frac{1}{2\pi k}\int_0^{x_3} \sinh\left[2\pi k(x_3 - x_3')\right]\mathbf{f}^{(k)}(x_3')dx_3', \tag{6.12}$$

$$\mathbf{C}_2^{(k)}(x_3) = \frac{1}{2}\int_0^{x_3} (x_3 - x_3')e^{2\pi k(x_3 - x_3')}\mathbf{f}^{(k)}(x_3')dx_3', \tag{6.13}$$

$$\mathbf{C}_3^{(k)}(x_3) = \frac{1}{2}\int_0^{x_3} (x_3 - x_3')e^{-2\pi k(x_3 - x_3')}\mathbf{f}^{(k)}(x_3')dx_3', \tag{6.14}$$

and

$$P^{(k)}(x_3) = \sqrt{2}\left[\mathbf{m} \cdot \left(\mathbf{C}_2'(x_3) - 2\pi k\mathbf{C}_2(x_3)\right) + \hat{\mathbf{m}} \cdot \left(\mathbf{C}_3'(x_3) + 2\pi k\mathbf{C}_3(x_3)\right)\right]. \tag{6.15}$$

These equations satisfy the boundary condition on the lower wall by construction. The three integrals, $\mathbf{C}_i(x_3)$, represent the combined and separate effects of exponential decay from the lower and upper channel walls respectively. The vectors $\mathbf{m}$ and $\hat{\mathbf{m}}$ reflect the natural coordinate system for the flow field as each corresponds to gradients of a Fourier summation modulated by exponential growth and decay, respectively. Applying the no-slip condition on the upper wall resolves the remaining unknown coefficient, $\mathbf{A}^{(k)}$, *viz.*

$$\mathbf{m} \cdot \mathbf{A}^{(k)} = \left[1 + \frac{1}{2}(4\pi kH)^2 - \cosh(4\pi kH)\right]^{-1}\left[\sinh(2\pi kH)\mathbf{m} + 2\pi kHe^{-2\pi kH}\hat{\mathbf{m}}\right] \cdot \mathbf{U}^{(k)}(H), \tag{6.16}$$

$$\hat{\mathbf{m}} \cdot \mathbf{A}^{(k)} = \left[1 + \frac{1}{2}(4\pi kH)^2 - \cosh(4\pi kH)\right]^{-1}\left[2\pi kHe^{2\pi kH}\mathbf{m} + \sinh(2\pi kH)\hat{\mathbf{m}}\right] \cdot \mathbf{U}^{(k)}(H), \tag{6.17}$$

$$\mathbf{A}^{(k)} = -\frac{1}{2}\operatorname{csch}(2\pi kH)\left[\mathbf{U}^{(k)}(H) - 4\pi kH\left(e^{2\pi kH}\mathbf{m}\mathbf{m} \cdot \mathbf{A}^{(k)} + e^{-2\pi kH}\hat{\mathbf{m}}\hat{\mathbf{m}} \cdot \mathbf{A}^{(k)}\right)\right]. \tag{6.18}$$

However, these formulae for the velocity field and pressure Fourier coefficients only apply when the total wave-vector, k, is greater than zero. In the zero wave-vector limit the Fourier coefficients of the velocity field and pressure are

$$\mathbf{u}^{(0)}(x_3) = (\mathbf{I} - \mathbf{e}_3\mathbf{e}_3) \cdot \left[\frac{1}{2} x_3(x_3 - L_3)\mathbf{G} + \frac{x_3}{L_3} \int_0^{L_3} \int_0^{x_3'} \mathbf{f}^{(0)}(x_3'')dx_3''dx_3' - \int_0^{x_3} \int_0^{x_3'} \mathbf{f}^{(0)}(x_3'')dx_3''dx_3' \right], \tag{6.19}$$

$$p^{(0)}(x_3) = A^{(0)} + \mathbf{e}_3 \cdot \int_0^{x_3} \mathbf{f}^{(0)}(x_3')dx_3', \tag{6.20}$$

where $\mathbf{G}$ is a macroscopic and constant pressure gradient and $A^{(0)}$ sets the gauge for absolute pressure in the channel. A condition setting the value of the constant pressure gradient is required. In this case, the ends of the channel may be left open such that $\mathbf{G}$ is prescribed (*i.e.* drives a Poiseuille flow), or the ends of the channel may be closed so that there is no net flow through it, *viz.*

$$(\mathbf{I} - \mathbf{e}_3\mathbf{e}_3) \cdot \int_0^{H} \mathbf{u}^{(0)}(x_3)dx_3 = 0. \tag{6.21}$$

The former condition is somewhat different from unbounded Stokes flow, where as in the latter condition, conservation of mass manifests itself as the backflow pressure gradient. In this case, the backflow pressure is

$$\mathbf{G} = \frac{12}{L_3^2} (\mathbf{I} - \mathbf{e_3}\mathbf{e_3}) \cdot \left[\frac{1}{2} \int_0^{L_3} \int_0^{x_3'} \mathbf{f}^{(0)}(x_3'')dx_3''dx_3' - \frac{1}{L_3} \int_0^{L_3} \int_0^{x_3} \int_0^{x_3'} \mathbf{f}^{(0)}(x_3'')dx_3''dx_3'dx_3 \right]. \tag{6.22}$$

Indeed both of these conditions still conserve the momentum of the entire system (particles, fluid and walls). The stress on the upper and lower walls are periodic in the same fashion as the body force, pressure and velocity field. When the Fourier coefficients of the stress in the fluid are denoted as $\boldsymbol{\sigma}^{(k)}(x_3)$, the total force on the channel walls over one period is

$$\mathbf{F}_w = \mathbf{e}_3 \cdot \left(\boldsymbol{\sigma}^{(0)}(0) - \boldsymbol{\sigma}^{(0)}(L_3) \right) = -\int_0^{L_3} \mathbf{f}^{(0)}(x_3')dx_3' + L_3\mathbf{G}. \tag{6.23}$$

It is apparent that when the channel walls are left open, this is essentially a statement of Newtonian mechanics since the force on the walls must be equal and opposite to the total force applied to the fluid. The zero wave-vector contributions to the pressure and velocity fulfill this imperative. Even for arbitrary values of $\mathbf{G}$, one finds that the additional stress in the fluid due to the superimposed Poiseuille flow is transmitted to the walls. In the case of a closed channel, the pressure gradient $\mathbf{G}$ assumes a very particular form, however. In this case, the sealed ends of the channel bear some of the load due the particles as well. This reduces the stress on the walls by the amount given exactly by $L_3\mathbf{G}$.

With the substitution of an appropriate, periodic body force, these expressions completely define the pressure and velocity fields in a no-slip channel. For these purposes, the body force will be that due to a dispersion of colloidal particles suspended in the fluid. However, this solution could find equal applicability in studying electro-osmotic flow in the weak field limit or the flow generated in certain microfluid devices. Appendix E treats the case of rigid, impenetrable, shear stress free walls which might model a viscous fluid bound between two inviscid layers with planar interfaces maintained by a sufficiently large surface tension. While an algorithm for slipping channels is not developed any further, every step described from here on is just as suitable to that particular case.

6.2.2 The Ewald summation technique

The velocity field generated by a three dimensionally periodic body force in a viscous fluid is

$$\eta\mathbf{u}(\mathbf{x}) = \sum_{\boldsymbol{\xi}\neq 0} e^{-2\pi i\boldsymbol{\xi}\cdot\mathbf{x}} \left(2\pi\xi\right)^{-2} \left(\mathbf{I} - \hat{\boldsymbol{\xi}}\hat{\boldsymbol{\xi}}\right) \cdot \mathbf{f}^{(\xi)}, \tag{6.24}$$

where the $\boldsymbol{\xi}$'s are the three dimensional reciprocal lattice vectors and the $\mathbf{f}^{(\xi)}$ term represents the three dimensional Fourier coefficients of the body force. As Hasimoto found, for even the simplest body force (an array of point forces) this summation is slowly converging. The standard technique for accelerating the convergence of solutions subject to Poisson like equations is referred to as the Ewald summation method. Rather than detail the entire calculation in general, the result for the preceding hydrodynamic case is shown and then expanded. The Ewald summation form of equation (6.24) is

$$\begin{aligned}\eta\mathbf{u}(\mathbf{x}) = \frac{1}{4\pi}\int_V &\left[\frac{\phi_{-1/2}\left(\frac{\pi r^2}{\alpha}\right)}{\alpha^{1/2}}\mathbf{I} - \frac{\pi r^2\phi_{1/2}\left(\frac{\pi r^2}{\alpha}\right)}{\alpha^{3/2}}\left(\mathbf{I}-\hat{\mathbf{r}}\hat{\mathbf{r}}\right)\right]\cdot\mathbf{f}(\mathbf{x}')d\mathbf{x}' \\ &+\sum_{\xi\neq 0} e^{-2\pi i\boldsymbol{\xi}\cdot\mathbf{x}}\left(2\pi\xi\right)^{-2}\left(1+\pi\alpha\xi^2\right)e^{-\pi\alpha\xi^2}\left(\mathbf{I}-\hat{\boldsymbol{\xi}}\hat{\boldsymbol{\xi}}\right)\cdot\mathbf{f}^{(\xi)}.\end{aligned} \tag{6.25}$$

where $\mathbf{r} = \mathbf{x} - \mathbf{x}'$, $r^2 = \mathbf{r}\cdot\mathbf{r}$ and α is the so called splitting parameter. For a splitting parameter of appropriate magnitude, both the integral and the Fourier summation are rapidly convergent. The function ϕ_ν is the incomplete Γ-function and is represented as the integral

$$\phi_\nu(y) = \int_1^\infty \psi^\nu e^{-y\psi}d\psi. \tag{6.26}$$

While the details of this calculation are hardly trivial and difficult to apply to the two dimensional geometry, inspiration is drawn from it in order to achieve a rapidly converging solution to the problem of fluid motion in a channel. Notice that the summation in (6.25) is the exact solution for a velocity field subject to a force with Fourier coefficients $(1+\pi\alpha\xi^2)\exp(-\pi\alpha\xi^2)\mathbf{f}^{(\xi)}$. The key to ensuring rapid convergence in Stokes flow is modulating the force density by a Gaussian. This body force is denoted as $\mathbf{f}_g(\mathbf{x})$ – the "global" body force – since it contains the long-range effects on the fluid. Conversely $\mathbf{f}(\mathbf{x}) - \mathbf{f}_g(\mathbf{x})$ encompasses the body force giving rise to short range effects on the fluid. The two dimensional Fourier coefficients of $\mathbf{f}_g(\mathbf{x})$ are found directly via the convolution theorem for Fourier transformations, *viz.*

$$\mathbf{f}_g^{(k)}(x_3) = \frac{1}{2\alpha^{1/2}}\int_{-\infty}^{\infty}\left(3+2\pi\alpha k^2 - \frac{2\pi x_3'^2}{\alpha}\right)e^{-\left(\pi\alpha k^2+\frac{\pi x_3'^2}{\alpha}\right)}\mathbf{f}^{(k)}(x_3-x_3')dx_3'. \tag{6.27}$$

Similarly, the global force contribution itself is

$$\mathbf{f}_g(\mathbf{x}) = \frac{1}{\alpha^{3/2}}\int_V\left(\frac{5}{2}-\frac{\pi r^2}{\alpha}\right)e^{-\frac{\pi r^2}{\alpha}}\mathbf{f}(\mathbf{x}')d\mathbf{x}', \tag{6.28}$$

where once again $\mathbf{r} = \mathbf{x} - \mathbf{x}'$ and $r^2 = \mathbf{r} \cdot \mathbf{r}$. This is identical to the force density that Hernández-Ortiz *et al.* (2007) found "convenient" for their Ewald-like simulation method in that it produces a computationally friendly pressure and velocity field. This body force is not only convenient but is a direct consequence of the Ewald summation technique in an unbounded geometry. Substituting $\mathbf{f}_g^{(k)}(x_3)$ into equations (6.4)-(6.20) yields a rapidly converging summation describing the long-range effects of the body force and boundaries on the fluid which is denoted $\mathbf{u}_g(\mathbf{x})$ – the "global" velocity field. What remains is to solve the problem

$$\eta \nabla^2 \mathbf{u}_l = \nabla p_l - \mathbf{f}(\mathbf{x}) + \mathbf{f}_g(\mathbf{x}), \tag{6.29}$$

$$\nabla \cdot \mathbf{u}_l = 0. \tag{6.30}$$

describing the local fluid motion ($\mathbf{u}_l(\mathbf{x})$) and local pressure ($p_l(\mathbf{x})$) due to the rapidly decaying modes of the body force. In this way, the velocity field generated by a body force in a channel may be represented as a one to one superposition of $\mathbf{u}_g(\mathbf{x})$ and $\mathbf{u}_l(\mathbf{x})$.

6.2.3 Reflections in real-space

The local body force ($\mathbf{f}(\mathbf{x}) - \mathbf{f}_g(\mathbf{x})$) yields a velocity field in an unbounded fluid that decays exponentially fast with respect to both α and $\mathbf{x}$. However, since this is a confined geometry, the interplay of body force and no-slip condition must be explored further before deciding on an appropriate approximation of $\mathbf{u}_l(\mathbf{x})$. One method of representing the Stokes flow between two channel walls is through the use of the method of reflections. This method treats the material outside the channel walls as fluid subject to an appropriate "image" body force. Often, the channel walls are treated as independent and the fluid flow is represented as a superposition of the flow above and below the half space on either side of the channel such that the combined flow results in a no-slip condition at that single wall only. Take as an example a Stokeslet

$$\mathbf{J}(\mathbf{r}) = (8\pi\eta r)^{-1}(\mathbf{I} - \hat{\mathbf{r}}\hat{\mathbf{r}}) \tag{6.31}$$

located at $\mathbf{x}'$ and a distance x_3' above a no-slip wall. Blake (1971) determined the reflected flow field that preserves a no-slip condition at $x_3 = 0$, *viz.*

$$\mathbf{J}_w(\mathbf{R}, x_3') = -\mathbf{J}(\mathbf{R}) + {x_3'}^2 \nabla_x^2 \mathbf{J}(\mathbf{R}) \cdot (\mathbf{I} - 2\mathbf{e}_3\mathbf{e}_3) - 2x_3' \left[(\mathbf{I} - 2\mathbf{e}_3\mathbf{e}_3) \cdot \nabla_x \mathbf{J}(\mathbf{R}) \cdot \mathbf{e}_3\right]^T \tag{6.32}$$

where $\mathbf{R} = \mathbf{r} + 2x_3'\mathbf{e}_3$ and the superscript T indicates transposition. While the Stokeslet decays as r^{-1}, the reflected flow decays as R^{-1}. That is, the reflected flow appears as a source located a significant distance from original point force. If the second channel wall is reintroduced and the subsequent reflections to satisfy the no-slip condition at $x_3 = L_3$ calculated, one finds that they act as sources located even further away from the initial point force. Liron and Mochon (1976) showed that the decay of the subsequent reflections is at its slowest algebraic and at its fastest exponential. Since the local velocity field already decays as a Gaussian, only one reflection of the body force is considered as higher order reflections will decay at more than twice the exponential rate. To that end, the Stokeslet and its reflection are invoked as the Green's functions for Stokes flow above a no slip wall such that the locally reflected velocity field is:

$$\mathbf{u}_l(\mathbf{x}) = \int_V \left[\mathbf{J}(\mathbf{r}) + \mathbf{J}_w(\mathbf{R}, x_3')\right] \cdot \left\{ \int_V \left[\delta\left(\mathbf{r}'\right) - \frac{1}{\alpha^{3/2}} \left(\frac{5}{2} - \frac{\pi {r'}^2}{\alpha} \right) e^{-\frac{\pi {r'}^2}{\alpha}} \right] \mathbf{f}(\mathbf{x}'') d\mathbf{x}'' \right\} d\mathbf{x}', \tag{6.33}$$

where $\mathbf{r}' = \mathbf{x}' - \mathbf{x}''$ and ${r'}^2 = \mathbf{r}' \cdot \mathbf{r}'$ and the term in braces is the local force density. Because the Stokes equations are unique, switching the order of integration above demonstrates that the Stokeslet contribution to the integral in equation (6.33) corresponds directly to the real-space integrand in equation (6.25), *viz.*

$$\begin{aligned} \mathbf{G}(\mathbf{r}''; \alpha) &= \int_V \mathbf{J}(\mathbf{r}) \left[\delta(\mathbf{r}') - \frac{1}{\alpha^{3/2}} \left(\frac{5}{2} - \frac{\pi {r'}^2}{\alpha} \right) e^{-\frac{\pi {r'}^2}{\alpha}} \right] d\mathbf{x}' \qquad (6.34) \\ &= \frac{1}{4\pi\eta} \left[\frac{\phi_{-1/2}\left(\frac{\pi {r''}^2}{\alpha}\right)}{\alpha^{1/2}} \mathbf{I} - \frac{\pi {r''}^2 \phi_{1/2}\left(\frac{\pi {r''}^2}{\alpha}\right)}{\alpha^{3/2}} \left(\mathbf{I} - \hat{\mathbf{r}}''\hat{\mathbf{r}}''\right) \right], \end{aligned}$$

where $\mathbf{r}'' = \mathbf{x} - \mathbf{x}''$ and ${r''}^2 = \mathbf{r}'' \cdot \mathbf{r}''$. As the integral in equation (6.33) is rather difficult to compute since the $\mathbf{r}$ and $\mathbf{r}'$ directors are not concentric with respect to $\mathbf{x}'$, this represents a fortuitous simplification which is useful in simplifying the integrals over $\mathbf{J}_w(\mathbf{R}, x_3')$ and produces an expression for the local velocity field in terms of a single integral over the total force density. The details of this calculation are tedious but explained in appendix G. The result is quite simple however,

$$\mathbf{u}_l(\mathbf{x}) = \int_V \left[\mathbf{G}(\mathbf{r};\alpha) + \mathbf{G}_w(\mathbf{R}, x_3';\alpha)\right] \cdot \mathbf{f}(\mathbf{x}')d\mathbf{x}', \tag{6.35}$$

where the tensor, $\mathbf{G}_w(\mathbf{R}, x_3';\alpha)$, is the reflection of the local velocity field and is provided in the cited appendix. With this, the local velocity field including the reflection off the lower wall is completely defined. To find the flow due to the no-slip condition on the upper wall, Blake's reflection is applied again, albeit with a slightly different set of coordinates, *viz.*

$$\mathbf{J}_w(\tilde{\mathbf{R}}, x_3') = -\mathbf{J}(\tilde{\mathbf{R}}) + (L_3 - x_3')^2\, \nabla_x^2 \mathbf{J}(\tilde{\mathbf{R}}) \cdot (\mathbf{I} - 2\mathbf{e}_3\mathbf{e}_3) - 2\,(L_3 - x_3')\left[(\mathbf{I} - 2\mathbf{e}_3\mathbf{e}_3) \cdot \nabla_x \mathbf{J}(\tilde{\mathbf{R}}) \cdot \mathbf{e}_3\right]^T, \tag{6.36}$$

where $\tilde{\mathbf{R}} = \mathbf{r} - 2(L_3 - x_3')\mathbf{e}_3$. Precisely the same operations apply to this reflected field as well such that a one to one superposition of the reflections due to each wall independently approximates the local contribution to the velocity field in the channel.

Appendix G demonstrates that the reflected flow decays at its slowest as $\exp(-\pi R^2/\alpha)$ while the flow due to the local velocity field decays like $\exp(-\pi r^2/\alpha)$. For any source point ($\mathbf{x}'$) or field point ($\mathbf{x}$) near the wall, the connecting vector and its reflection are similar in magnitude (*i.e.* $r \approx R$), and the reflected flow is just as strong as the unreflected flow itself. This is a stark contrast to the claim of Hernández-Ortiz *et al.* (2007) that no reflection of the local force density is necessary. In fact, the flow due to local force density alone is entirely insufficient, and the reflected flow must be included to avoid errors which are on the order of one-hundred percent in the local velocity field. This fact is illustrated in figure 6.2.

This approximation is best for values of the splitting parameter such that $\sqrt{\alpha} \leq L_3$. Under those circumstances, the reflected flow decays quickly enough that it is essentially unfelt on the opposing wall. However, if the value of α is determined on this basis alone, the wave-space summation may not converge rapidly. This raises an interesting issue as one of the problems of interest in this field is the dynamics of

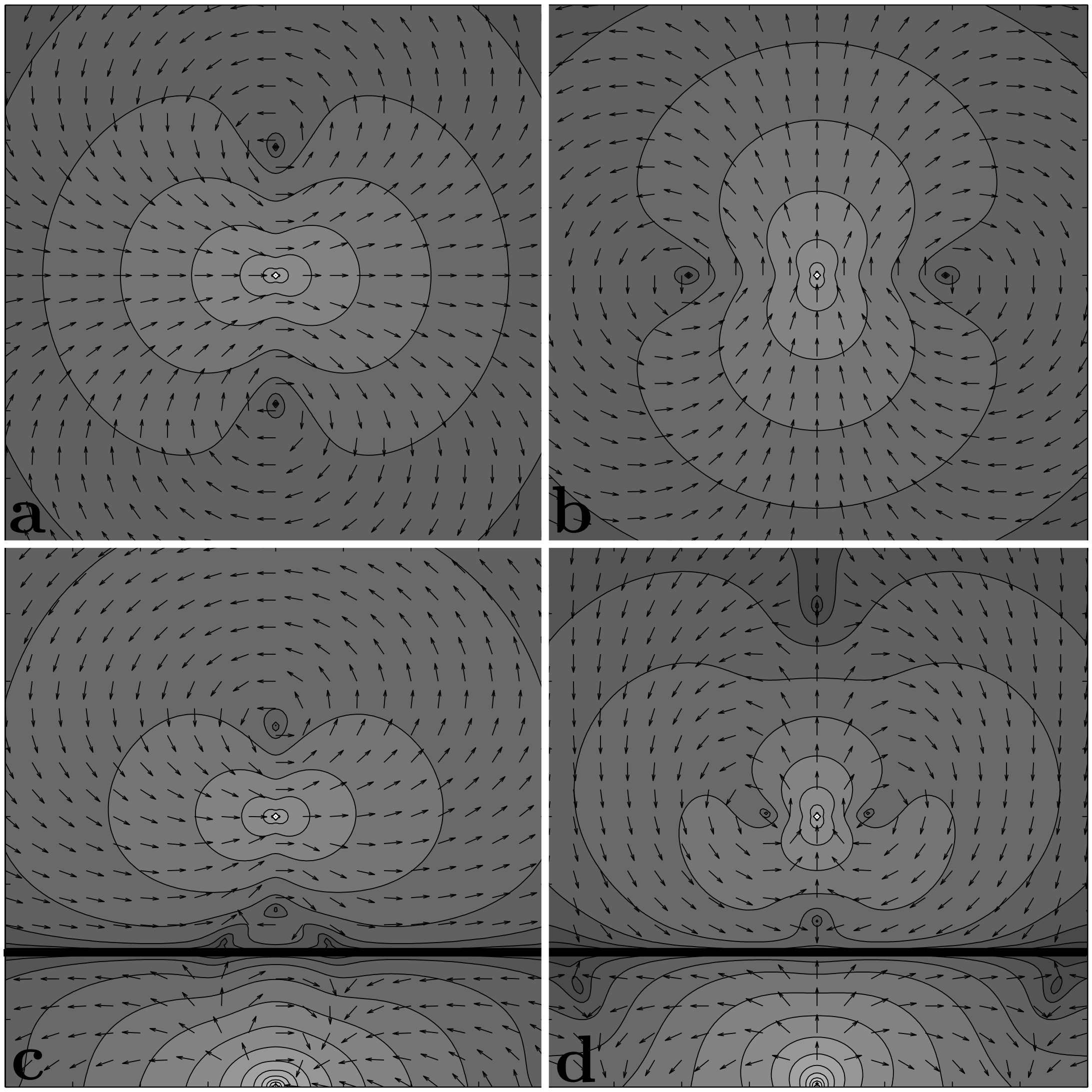

Figure 6.2: The real-space contribution to the velocity field generated by a point force differs significantly when unbounded (a,b) and when near a wall (c,d). In this case, the distance of the source from the wall (indicated by the thick line) is $\sqrt{\alpha/10}$. The figures depict the flow due to a force parallel to the wall (a,c) and perpendicular to the wall (b,d) as streamlines and contours of the flow magnitude. While the absolute magnitude is inconsequential, the contour lines are logarithmically distributed. The Gaussian decay is evident for the unbounded flows; however, a stronger decay is present for the bounded flows.

suspensions in suitably narrow channels (*i.e.* $L_3 \approx$ a few particle diameters). In this case, however, the lubrication interactions between the particles and the channel walls dominate the hydrodynamic resistance. In the rest of this section, it is shown that this solution for the velocity field due to a periodic body force constitutes a far-field approximation to the hydrodynamic resistance felt by particles in a suspension. This does not replicate the singular lubrication forces, however. Instead, the Stokesian Dynamics method is used to model those interactions explicitly.

6.2.4 Computations in wave-space

The calculation must now evolve from the abstract perspective of body forces and fluid velocities to that of force moments on and velocities of particles in suspension. To this end, the body force in the fluid is written as

$$\mathbf{f}(\mathbf{x}) = \sum_n \delta(\mathbf{x} - \mathbf{x}_n)\mathbf{F}_n, \tag{6.37}$$

which reflects a periodically replicated system of spherical particles with force $\mathbf{F}_n$ on the particle with center at $\mathbf{x}_n$. Although particles themselves are not adequately represented as point forces, a multipole expansion of the force density on the particle surfaces always yields a linear summation of the particle force moments (*e.g.* force, torque, stresslet, *etc.*). Later discussion will explain how higher order force moments are incorporated into this formulation. For now focus is restricted to the simpler case of point forces. With this, the global force density becomes

$$\mathbf{f}_g^{(k)}(x_3) = \frac{1}{2\alpha^{1/2}} \sum_n \left(3 + 2\pi\alpha k^2 - \frac{2\pi {\Delta x_3^{(n)}}^2}{\alpha} \right) e^{-\pi\alpha k^2 - \frac{\pi {\Delta x_3^{(n)}}^2}{\alpha}} \mathbf{F}_n^{(k)}, \tag{6.38}$$

where $\Delta x_3^{(n)} = x_3 - x_3^{(n)}$ and $\mathbf{F}_n^{(k)} = \exp\left(2\pi i k_\alpha x_\alpha^{(n)}\right)\mathbf{F}_n$. Applying this to the solution developed earlier in the section completely defines a rapidly converging Ewald summation for the global contribution to the fluid velocity. Equations (6.12-6.14) are calculated in appendix F using this force density. The key here is the recovery of the essential linearity associated with Stokes flow. The local and global velocity fields, while comprising two different levels of computation are in the end just linear transformations of the forces on the particles.

The multipole expansion allows the incorporation of higher order force moments into this formulation. Returning to equations (6.4) and (6.9), recognize that the global contribution to the disturbance velocity due to a suspension of particles can be written as:

$$\mathbf{u}_g(\mathbf{x}) = \sum_n^N \int_{S_n} \sum_{k_1,k_2} e^{2\pi i k_\alpha x_\alpha} \mathbf{G}^{(k)}(x_3, x_3') \cdot \sum_{k_1',k_2'} e^{2\pi k_\alpha' x_\alpha'} \mathbf{f}_g^{(k')}(x_3') d\mathbf{x}', \tag{6.39}$$

where $\mathbf{G}^{(k)}(\mathbf{x}, \mathbf{x}')$ is simply the Fourier coefficient of the Green's function for Stokes flow in a channel. This is computed using the solution developed in subsection 6.2.1 with the substitution of a delta-function for the force density. Because the velocity field is still a solution to the Stokes equations, it is bi-harmonic. Therefore, the typical Taylor expansion of the Green's function about the center of each particle is used to eliminate the integral, *viz.*

$$\begin{aligned}\mathbf{u}_g(\mathbf{x}) = \sum_n^N &\left[\left(1 + \frac{a_n^2}{6}\nabla_{\mathbf{x}'}\right)\mathbf{F}_n \cdot -\frac{1}{2}\mathbf{L}_n \cdot \nabla_{\mathbf{x}'} \times + \frac{1}{2}\left(\nabla_{\mathbf{x}'} + \frac{1}{2}\nabla_{\mathbf{x}'}^T\right)\left(1 + \frac{a_n^2}{10}\nabla_{\mathbf{x}'}^2\right) \cdot \mathbf{S}_n \cdot + \dots\right] \\ &\sum_{k_1,k_2} e^{2\pi i k_\alpha x_\alpha'} \mathbf{G}^{(k)^T}(x_3, x_3') \left[\frac{1}{2\alpha^{1/2}} \sum_n \left(3 + 2\pi\alpha k^2 - \frac{2\pi \Delta x_3'^{(n)^2}}{\alpha}\right) e^{-\pi\alpha k^2 - \frac{\pi \Delta x_3'^{(n)^2}}{\alpha}}\right]\Bigg|_{\mathbf{x}'=\mathbf{x}_n} .\end{aligned} \tag{6.40}$$

In this way, the disturbance flow generated by particle n can be represented as contributions due to each of the moments of the force density on its surface. Note that the force moments each propagate via an effective Green's function and much care must be taken in evaluating the derivatives with respect to the source point of the flow. This has a far-reaching influence on the implementation of a rapid summation algorithm.

6.2.5 Simulation methods

In this section, the Stokesian Dynamics method for computing hydrodynamic interactions among many particles is illustrated. Since the mobility and resistance tensors are purely a function of the system geometry, the formal construction of a Stokesian Dynamics simulation does not depend on any sort of boundary geometry [Brady and Bossis (1988)]. The same is true of Accelerated Stokesian Dynamics. Therefore, the

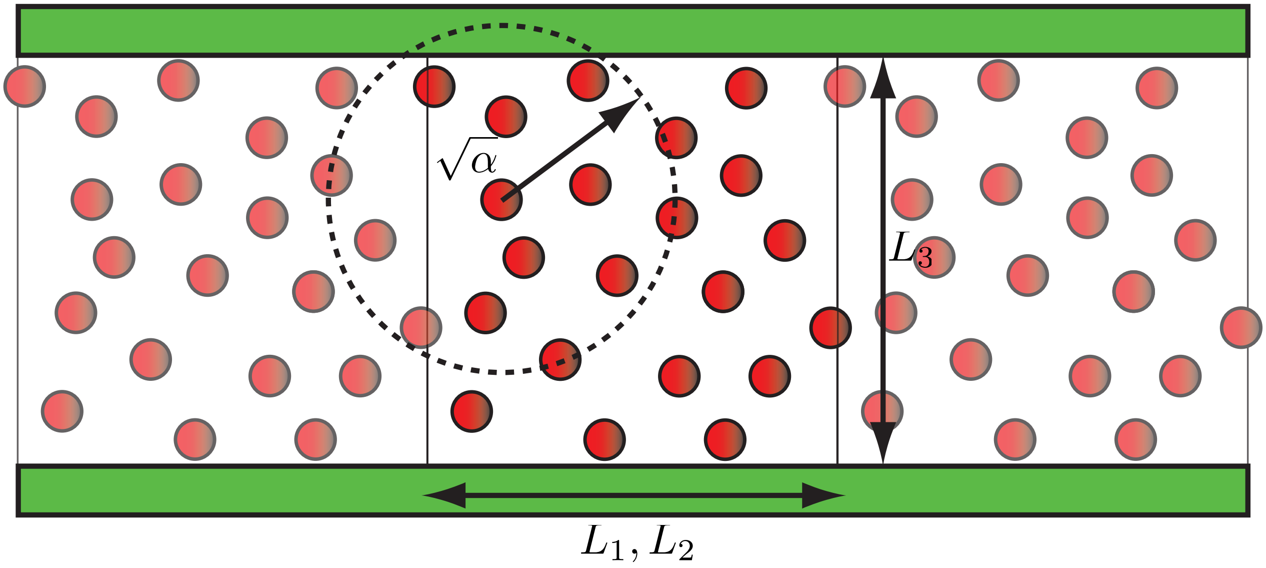

Figure 6.3: The periodic simulation cell has walls that are infinite in extent bounding the top and bottom of the channel. The interaction regime dominated by the local velocity field is indicated for one particle and characterized by the distance $\sqrt{\alpha}$.

solution for the velocity field in a channel can be used to generate a rapid simulation of many colloidal particles as in the Accelerated Stokesian Dynamics simulations of Seirou and Brady (2001).

The Accelerated Stokesian Dynamics technique is an application of the so-called particle-mesh Ewald algorithm used regularly in computational physics to accelerate lattice sums [see *e.g.* Darden, York and Pedersen (1993)]. Previous subsections have developed a solution for Stokes flow in a channel subject to a periodic though otherwise arbitrary body force, split that solution into wave-space and real-space contributions which are both rapidly converging and then attributed the body force to the force on the fluid due to colloidal particles in suspension. The aim in this subsection is to discuss one method of building a particle-mesh Ewald algorithm and emulating the Accelerated Stokesian Dynamics technique. This requires the calculation of three quantities: the real-space and the wave-space contributions to the disturbance velocity felt by particle n, which are characterized by equation (6.9) with substitution of the global force density and equation (6.35), respectively and the lubrication contributions to the resistance tensors denoted R^{nf}_{FU}, R^{nf}_{FE} and R^{nf}_{SE}, which reflect the near-field coupling of force and velocity, force and strain and stresslet and strain respectively. The first two quantities allow for the calculation of $\mathcal{M}^{\infty}$ via the Faxén formulas in equations

(4.11), (2.22) and (2.23) while the remaining lubrication pieces complete the prerequisites for the Stokesian Dynamics algorithm described in the preliminary chapter of this thesis.

Consider first, the real-space contribution to the grand mobility tensor. Particle n feels a disturbance flow from other particles in the fluid that decays exponentially fast with respect to $|\mathbf{x} - \mathbf{x}^{(n)}|$. Remember that this arises from the local force density and the reflection of that flow off of the lower and upper walls of the channel, independently [see appendix G]. The rate of decay is of course modulated by the splitting parameter. However, for a sufficiently small value of α this rapid decay suggests that the real-space part of the flow affecting particle n originates only from disturbances that are roughly $\sqrt{\alpha}$ away. Any further away, and the flows due to those disturbances have decayed to miniscule magnitudes and have no practical effect on the motion of particle n. This means that the computation of the real-space contribution to the flow felt by particle n depends on disturbances generated by particles within a nearby neighborhood roughly $\sqrt{\alpha}$ in extent. This lends itself quite nicely to the so-called linked cell method (a.k.a. the chaining mesh method) which allows for exactly that sort of procedure [see *e.g.* Allen and Tildesley (1989)]. Rather than checking the distances between all pairs of particles and computing the disturbance flows (something which requires $O(N^2)$ computations), the linked cell technique allows for computation of the flow due only to particles close enough to particle n subject to some explicit cutoff distance (*i.e.* $\sqrt{\alpha}$). This is accomplished by dividing the periodic cell into sub-cells which are approximately $\sqrt{\alpha} \times \sqrt{\alpha} \times \sqrt{\alpha}$ in dimension and then binning the particles in their corresponding sub-cells. Only particles residing in the same sub-cell, or in a neighboring sub-cell generate flows strong enough to affect one another. Therefore, the computation of the real-space contributions to the disturbance flow around each and every particle can be completed in $O(N)$ computations.

Recall that a multipole expansion of the disturbance velocity generated by the particle produces a series of terms linear in the particle force moments and proportional to derivatives of the channel Green's function [see (6.40)]. Rather than take these derivatives explicitly, one can follow the usual scheme of distributing the force moments as a series of point forces of an appropriate magnitude located on a self similar grid [Hockney and Eastwood (1989)]. This step is essential as the efficiency of the algorithm is derived from the application of fast Fourier transformation methods on a regular grid. Consider the velocity field generated by a point force of magnitude $\mathbf{F}$ located at point $\mathbf{y}$,

$$\sum_k e^{-2\pi i k_\alpha (x_\alpha - y_\alpha)} \mathbf{G}^{(k)}(x_3, y_3) \cdot \mathbf{F}, \tag{6.41}$$

which can be approximated as a set of forces pointing in the same direction as $\mathbf{F}$ but located on the grid points denoted $\mathbf{y}^{(\gamma)}$ and of magnitude $A^{(\gamma)}$,

$$\sum_\gamma A^{(\gamma)} \sum_k e^{-2\pi i k_\alpha (x_\alpha - y_\alpha^{(\gamma)})} \mathbf{G}^{(k)}(x_3, y_3^{(\gamma)}) \cdot \frac{\mathbf{F}}{|\mathbf{F}|}. \tag{6.42}$$

A Taylor expansion of the grid approximate in terms of $\mathbf{y}^{(\gamma)}$ and about $\mathbf{y}$ results in a hierarchy of equations governing the grid coefficients such that in one dimension

$$\sum_\gamma^n A^{(\gamma)} (y^{(\gamma)} - y)^m = \delta_{m0}, \tag{6.43}$$

for $m = 0, 1, 2, \ldots n-1$ and where the δ_{m0} is the Kronecker delta. One might recognize the algebraic structure here – this is the transpose Vandermonde matrix operating on a vector of all the $A^{(\gamma)}$'s. The apparent algebraic analogy to least squares polynomial approximation is striking. The number of grid nodes n defines the coarseness of the approximation such that the error is on the order of the nth power of the grid spacing. As it happens, the solution to these equations can be written as the superposition of unity and $n-1$ finite difference stencils. For instance, the values of $A^{(\gamma)}$ in a one dimensional approximation satisfying the grid hierarchy for $n = 3$ are simply

$$\left(-\frac{\Delta'}{2\Delta} + \frac{\Delta'^2}{2\Delta^2}, 1 - \frac{\Delta'^2}{\Delta^2}, \frac{\Delta'}{2\Delta} + \frac{\Delta'^2}{2\Delta^2} \right) \tag{6.44}$$

where Δ is the spacing between nodes and Δ' is the distance between the actual point source and the nearest grid node. This same procedure can be extended to any value of n and without loss of generality, the grid coefficients will be a superposition of weighted difference stencils of ever increasing order. Since all but the zeroth order grid equation sum exactly to zero, one physical interpretation is that the grid approximate is generated in such a way that the structure of force moments up to order $n - 1$ is preserved. As the algorithm in this chapter contains force moments up to the octuple, coefficients satisfying the grid equations to degree $n = 4$ are necessary to maintain consistency. Incorporating higher order force moments into this formulation is straightforward as well. The grid force density is written as being linearly proportional to the force multipole, and the same hierarchy of equations is constructed. Though, the single, non-zero summation corresponds to the force moment in question. An extension to three dimensions is not trivial since any symmetric stencil will introduce a rank deficient problem. This, however, may be solved in the least squares sense such that a similar and unique set of finite difference-like weightings emerge. This approach is generalizable to any Green's function and allows for arbitrary control of the accuracy of the mesh distribution.

Given a set of point forces on a grid, the calculation of the global contribution to the resulting disturbance velocity is uncomplicated. The process is begun by the fast Fourier transformation of each discretized plane of the force mesh parallel to the channel walls. For each transformed plane, the Fourier components of the disturbance velocity at that level due to all the point forces on the grid is calculated. Then the global disturbance velocity at each plane level is computed via an inverse fast Fourier transformation. Finally, the disturbance velocity located at any point in the simulation cell is approximated by a set of local Lagrange polynomials. Similarly, the derivatives of the disturbance velocity can be computed directly from the Fourier transformation of the gridded force or from derivatives of the interpolating polynomials. Note that the "fineness" of the discretization in the $\mathbf{e}_3$ direction (perpendicular to the channel walls) is independent of the number of particles in the simulation cell for a fixed channel width and volume fraction. Therefore, the computation of the disturbance velocity and its derivatives is dominated by the fast Fourier transformations which require roughly $O(N \log N)$ computations. Throughout the entire algorithm, this step alone has super-linear computational scaling and dominates the computation for simulations of a large number of particles.

It is undesirable to repeat the calculation of the wave-space contribution to the flow felt by every particle in the simulation cell due to the disturbance from every *other* particle individually. This would require solving the problem for the disturbance velocity N times and is computationally prohibitive. Instead one computes the wave-space contribution to the flow generated by *all* the particles and then removes individually the "self" contribution due to the particle that "feels" the flow. This quantity may by computed in advance as

$$\mathbf{u}_S(\mathbf{x}_n) = \int_V e^{-2\pi i k_\alpha x_\alpha^{(n)}} \mathbf{u}^{(k)}(x_3^{(n)}) d\mathbf{k}, \tag{6.45}$$

where the Fourier coefficients of the force density are simply $\exp(2\pi i k_\alpha x^{(n)})\mathbf{F}_n$. This quantity depends on one length scale, namely the channel width (L_3), and two dimensionless parameters $\Xi = x_3^{(n)}/L_3$ and $\beta = \alpha/L_3^2$. While Ξ will always reside within the range of zero to unity, the rescaled splitting parameter is potentially boundless. However, in practice $\sqrt{\alpha}$ of about three particle radii generates a sufficiently accurate approximation of the disturbance flows [see Seirou and Brady (2001)]. The wave-space part of the disturbance flow generated and felt by a single particle denoted again as n is computed for values of β ranging from 0.01 to 5 which is a diverse enough spread to study the motion of particles in rather wide channels and rather narrow channels, respectively. One simply applies the appropriate Faxén formulas to this particular disturbance velocity.

The channel geometry introduces an inherent anisotropy in the structure of the mobility tensors, and symmetry arguments suggest that the so-called "self" mobility tensors (denoted $\mathbf{M}_{UF}^S$, $\mathbf{M}_{UD}^S$, $\mathbf{M}_{\nabla F}^S$ and $\mathbf{M}_{\nabla D}^S$ for the coupling of velocity and force, velocity and doublet, gradient velocity and force and gradient velocity and doublet) have a well defined structure. For instance:

$$\begin{aligned}\mathbf{M}_{UF}^S = -\frac{1}{6\pi\eta a_n}\Bigg\{&\left[f_1^{(UF)}(\Xi,\beta)\left(\frac{a_n}{L_3}\right) - f_3^{(UF)}(\Xi,\beta)\left(\frac{a_n}{L_3}\right)^3 + f_5^{(UF)}(\Xi,\beta)\left(\frac{a_n}{L_3}\right)^5\right](\mathbf{I}-\mathbf{e}_3\mathbf{e}_3)\\ &+\left[g_1^{(UF)}(\Xi,\beta)\left(\frac{a_n}{L_3}\right) - g_3^{(UF)}(\Xi,\beta)\left(\frac{a_n}{L_3}\right)^3 + g_5^{(UF)}(\Xi,\beta)\left(\frac{a_n}{L_3}\right)^5\right]\mathbf{e}_3\mathbf{e}_3\Bigg\},\end{aligned} \tag{6.46}$$

while the structure of the others are described in appendix H. For simplicity the doublet to which the torque and the stresslet are the antisymmetric and symmetric contributions is introduced. The gradient velocity to which the rate of rotation and rate of strain are similarly related is used as well. This, of course, is the same structure that was discussed in the reflection of the flow generated by a single particle in the parallel wall geometry [see Swan and Brady (2010)]. In fact, in the limit that β approaches zero, those results are recovered. However, since the simulation of suspensions has required a more sophisticated analysis, the disturbance flow is modulated by the splitting parameter. The velocity-force couple is plotted in figure 6.4 as a function of Ξ for various values of β in the range described. In practice, however, the difference between the actual mobility for a single particle in the parallel wall geometry ($\beta \rightarrow 0$) and the wave-space contribution to that mobility for the specified value of the splitting parameter is all that is required. Perhaps the most efficient computational implementation of this is via tabulation of the quantities: $\mathbf{M}^S(\beta \rightarrow 0) - \mathbf{M}^S(\beta)$. Note that any explicit dependence on the channel width has been removed from the calculation and reduced the dimensionality of the tabulation. Additionally the table is bounded by fixed limits for the values of Ξ and by practical but flexible limits on the values of β.

The lubrication contributions to the resistance tensors play a critical role in the dynamics and rheology of colloidal dispersions. As a pair of particles nearly touches or a single particle passes near a wall, the resistance to relative motion of that pair or motion of that particle is singular. This arises from large pressure gradients required to squeeze fluid out of the narrow gap separating the two surfaces. For many particles near one another, these singularities are effectively pairwise additive since the fluid in a gap between two nearly touching surfaces is to a first approximation independent of the fluid in the other gaps. While the same does not hold for the regular contributions to the resistance, numerous studies have found that treating the lubrication contributions to the resistance as pairwise additive regardless produces quantitatively accurate results [see *e.g.* Brady *et al.* (1990), Bossis, Meunier and Sherwood (1991) and Phung, Brady and Bossis (1996)]. In fact, this approach is the touchstone in the field. To that end, one may use the pairwise (*i.e.* particle-particle and particle-wall) resistance tensors to generate $\mathbf{R}_{FU}^{lub}$, $\mathbf{R}_{FE}^{lub}$ and $\mathbf{R}_{SE}^{lub}$ [see Kim and Karrila (2005), Happel and Brenner (1986) and O'neill and Stewartson (1967), *etc.*]. These are well known quantities that are readily available in the cited literature.

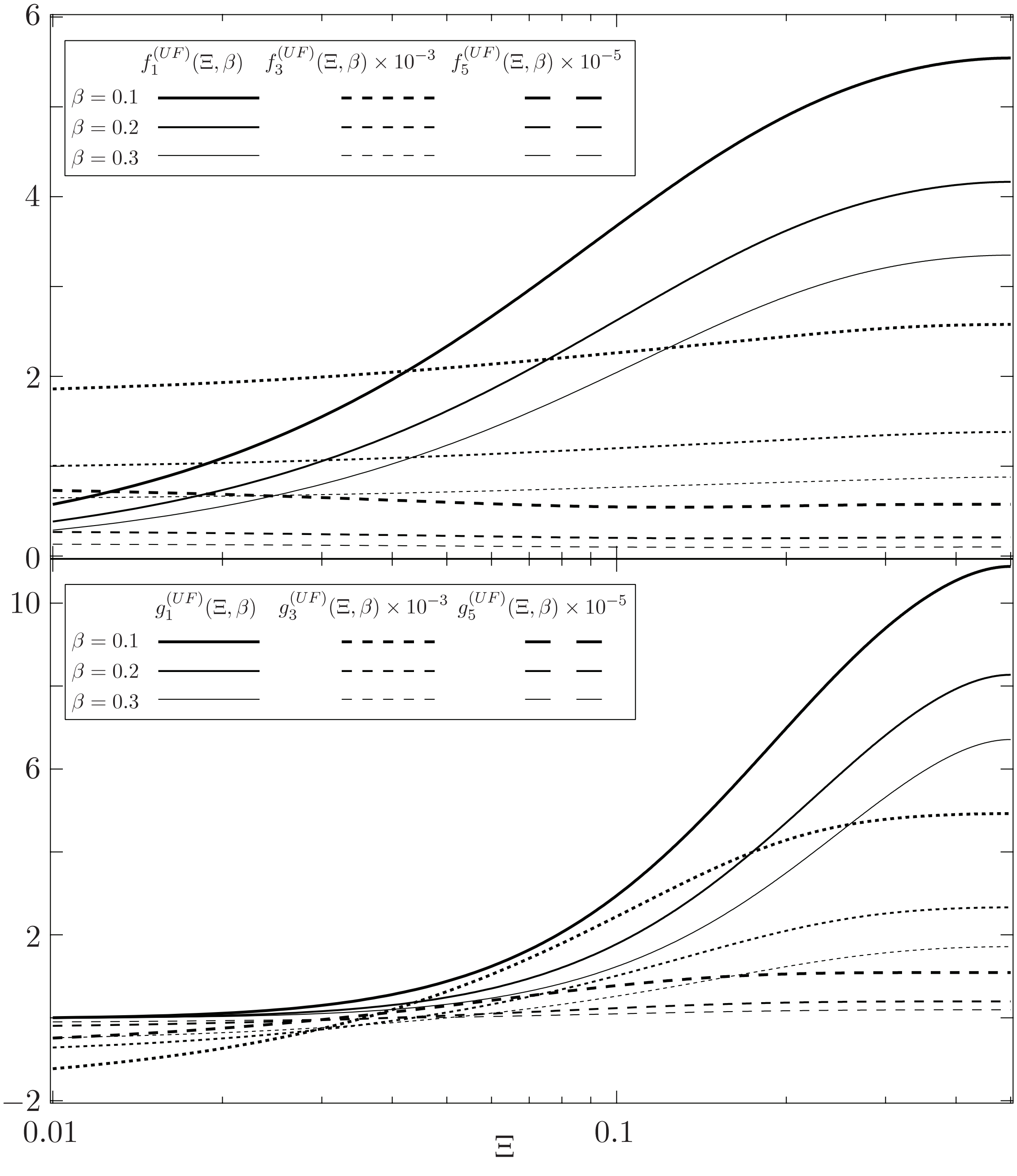

Figure 6.4: The so-called "self" contribution to the mobility due to the wave-space disturbance flow depends both the dimensionless splitting parameter and the fractional distance across the wall. This can be computed and tabulated easily for all values of these two parameters which are effectively independent of the the channel width in much the same manner as Swan and Brady (2010).

6.3 Results

There are relatively few measurements of the short-time properties of confined suspensions (either analytical, computational or experimental) beyond the dilute regime. However, knowing that as the channel widens, the viscoelastic properties of a suspension cannot deviate from their equivalent in the well studied, unbounded limit serves as a useful guide. Still, a direct comparison between this simulation method and one other concerning the cooperative motion of particles in a channel is possible. Save that, predictions are made of the high-frequency viscosity, short-time self diffusivity and sedimentation rate which must be compared with and analyzed in the context of those for unbounded suspensions. For these suspension properties, equilibrium configurations of particles between the channel walls were generated using the Monte Carlo method for volume fractions less than thirty percent [Frenkel and Smit (2001)] and via molecular dynamics simulation for volume fractions greater than thirty percent [Donev, Stillinger and Torquato (2005)]. Figure 6.5 depicts the distribution of number density, $n(x_3)$, at equilibrium across channels with a variety of widths for many "bulk" or averaged volume fractions, $\phi = 4\pi a^3/3(\int_0^{L_3} n(x_3)dx_3)/L_3$. These static properties depend intimately on the structure of the suspension between the channel walls. However, the effects of packing and confinement on the equilibrium structure of the suspension are beyond the purview of this thesis. The presented results are limited to volume fractions less than forty percent in part because the walls induce ordering in the suspension which may trigger crystallization. One can understand this by considering that while the number density of particles in the channel is $3\phi/(4\pi a^3)$, the centers of the particles cannot access areas nearer the wall than one particle radius. This would lead to overlap with the hard walls. As such, the center accessible number density is $3\phi/(4\pi a^3)L_3/(L_3 - 2a)$ which for values of L_3 not too much bigger than a can be significantly larger, hence, the induction of crystallization at lower bulk volume fraction.

6.3.1 Cooperative motion of regular lattices

Bhattacharya (2008) used the method of moments approach originating with Cichocki *et al.* (2000) and Bhattacharya and Blawzdziewicz (2002) to study the cooperative motion of particles arranged in an infinite square or rectangular lattice residing on the center plane of a parallel wall channel. There, only the motion

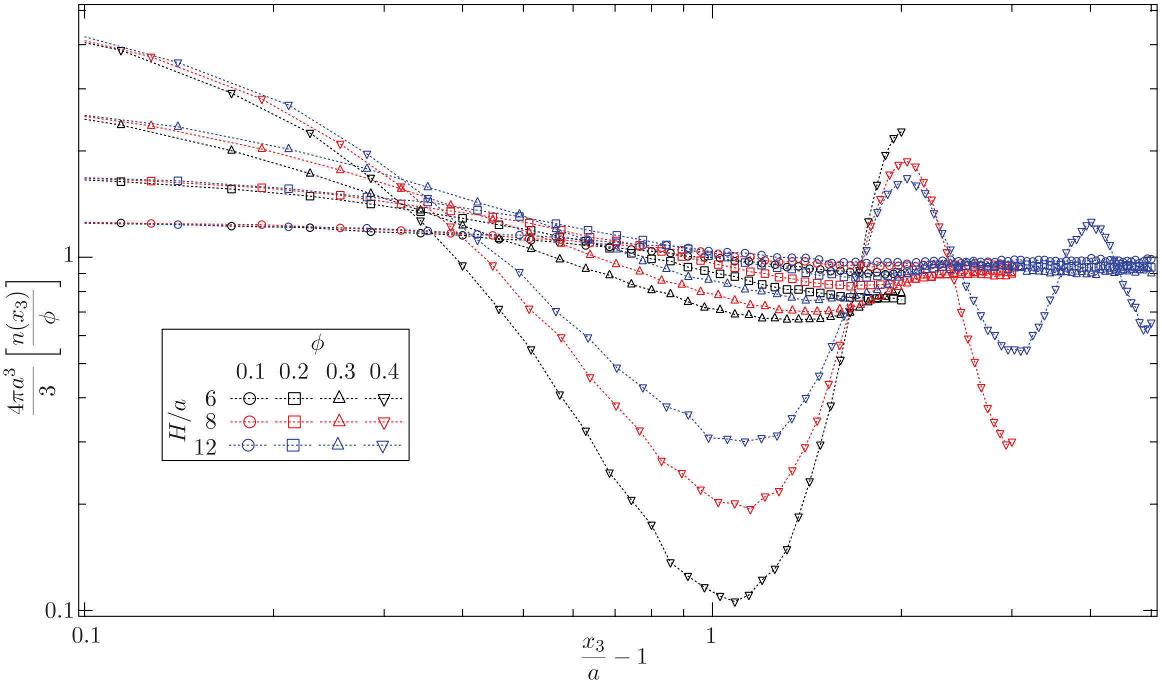

Figure 6.5: The equilibrium density profile across the channel $n(x_3)$ for several bulk channel volume fractions and channel widths. Notice the systematic deviations in the density profiles at high volume fractions. These structural variations can have a strong influence on the short-time rheology of concentrated suspensions.

parallel to the channel walls was studied for channels with a width of twelve particle radii ($L_3 = 12a$). Here, both the cooperative motion parallel and perpendicular to the channel walls (*i.e.* the sedimentation rate of the lattice) is measured as a function of the channel width and the spacing between individual particles in a square lattice solely.

In figure 6.6, the parallel sedimentation rate relative to the particle weight ($6\pi\eta aU/F$) is plotted for two cases: one where the applied pressure difference (ΔP) down the channel is zero and one where the mean flow of material down the channel (Q) is zero. With no applied pressure gradient, the present method reproduces the predictions of Bhattacharya (2008) exactly. The same cannot be said of the predictions of collective motion in the “no-flow” limit. While the present prediction reflects the behavior typical of sedimentation of fully three dimensional lattices (for which the condition $Q = 0$ is implicit), those of Bhattacharya (2008) trend in the opposite direction. They find that as the lattice becomes more concentrated it falls faster. It should be the case that the backflow hinders concentrated suspensions more than dilute ones as the pressure gradient generating that parabolic flow balances the weight of the particles exactly (*i.e.* the sum of the forces causing

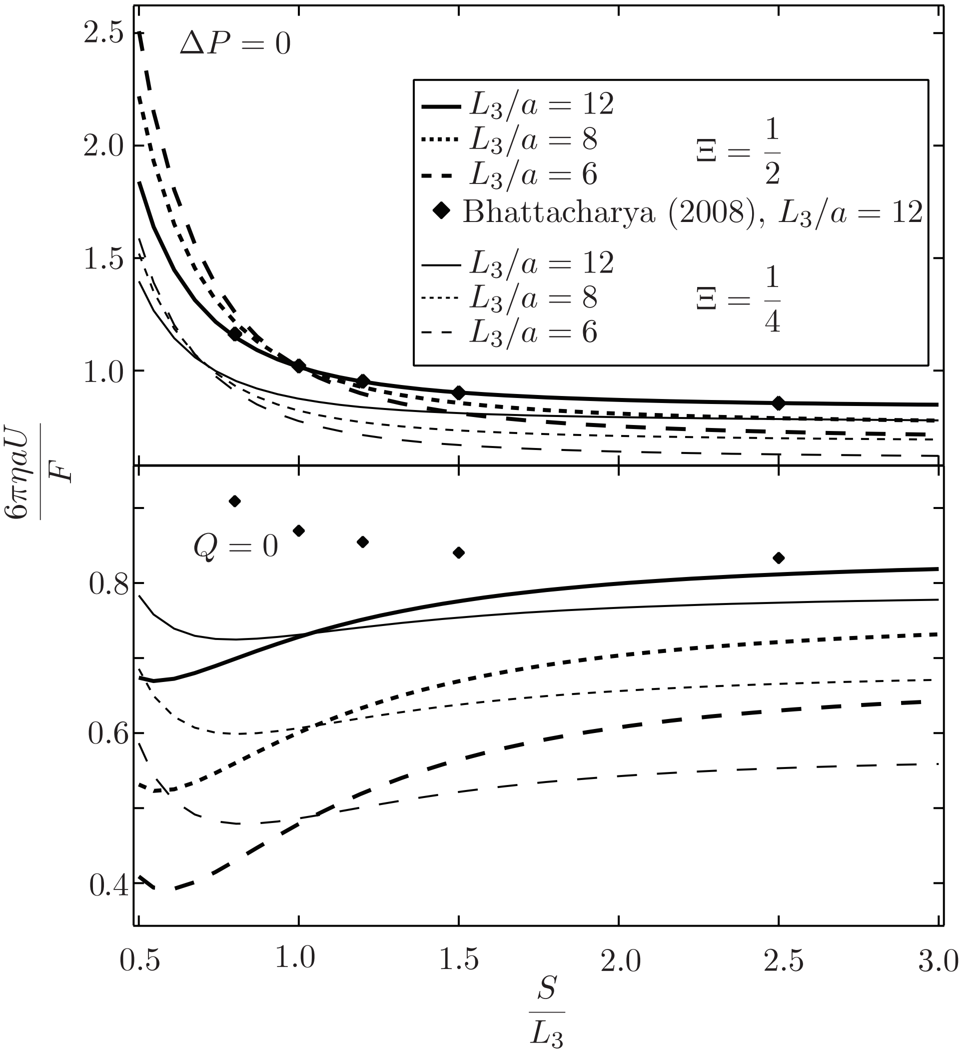

Figure 6.6: The sedimentation rate of spherical particles residing on a square lattice falling parallel to the channel walls. The rates for lattices residing in the middle of the channel, $\Xi = 1/2$, and a quarter of the way across the channel, $\Xi = 1/4$, are qualitatively the same, though lattices nearer to the wall fall slower due to the increased drag.

the particles to move collectively). While the exact expression for the backflow pressure in the channel is given by equation 6.22, in the dilute limit, it can be approximated by substituting the total force on the particles (with opposite sign) for **G** which subtracts resulting Poiseuille flow from the sedimentation velocity in an open channel ($\Delta P = 0$). This reproduces the trend of decreasing sedimentation rate with increasing density as conventionally expected. As there is neither art nor artifice in the present implementation of the closed channel condition, the discrepancy with Bhattacharya (2008) must be explained by the particular approximation they employed.

Nearer the wall and for no mean flow ($Q = 0$), an interesting trend emerges. While the sedimentation rate drops as the number density increases, there is a point beyond which the bare fall speed of the particles supersedes the backflow which falls off quadratically from the channel center. As a result, a lattice near the wall can fall faster than the same lattice mid-channel. A milder version of the same trend is observable under the same circumstances and mid-channel. It is easier for a dense lattice to slip through the fluid as the streamlines curve less around the lattice particles. As a result, the backflow hinders the particles less efficiently.

The collective motion of a square lattice perpendicular to the channel walls is an entirely different matter and is plotted in figure 6.7. There is always the condition of "no flow" in the direction normal to the channel walls, and there is always a pressure gradient implicitly exerted to balance the weight of the sedimenting particles. However, and unlike unbounded sedimentation, the lattice moves relative to the nearby channel walls so that fluid is always forced to pass between the particles. In consequence, the denser lattices sediment at a significantly slower rate than an isolated particle. Again, this is in accord with what is anticipated in situations where a zero mean flux constraint is imposed.

For either motion parallel or perpendicular to the channel walls and regardless of restrictions on the flow, the enhancement of or hindrance to sedimentation decays rapidly with respect to the ratio of lattice spacing to channel width (S/L_3). In fact, above a ratio of approximately two, the lattice sedimentation rate is within just a few percent of the single particle sedimentation rate in all the cases simulated. This is an important observation as it is well known that the measurement of suspension diffusivity is skewed in periodic systems

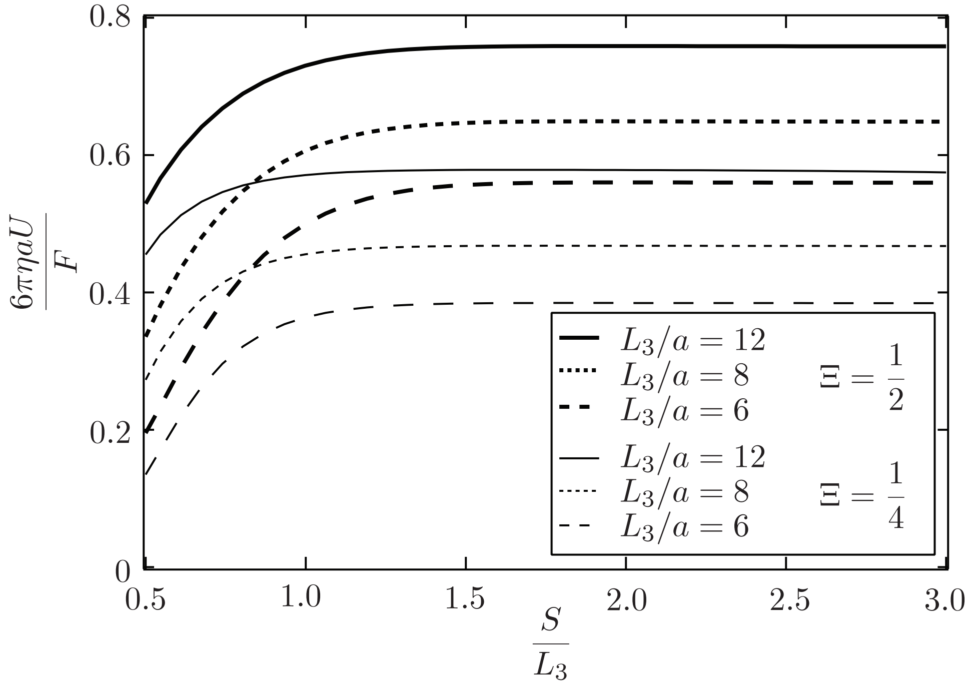

Figure 6.7: The sedimentation rate of spherical particles residing on a square lattice falling perpendicular to the channel walls at positions one-half and one-quarter ($\Xi = 1/2$, and $\Xi = 1/4$ respectively) across the channel. Fluid must squeeze through the lattice gaps for particles to come nearer the walls in order to satisfy continuity throughout the domain; therefore, denser lattices fall more slowly.

by precisely these cooperative effects. Given the more rapid decay of the disturbance generated by a point force in a channel and these observations, one can conclude that measurements of diffusivity in periodic channels with an aspect ratio larger than two are within only a few percent of what could be expected in the limit that the aspect ratio approaches infinity. This belies the strong (S^{-1}) dependence of the sedimentation rate for a three dimensional cubic lattice and is a consequence of the hydrodynamic screening induced by the channel walls. In the limit that the $S/a \to \infty$, the result for a single particle is recovered exactly regardless of the condition at the channel ends.

In figure 6.8, the convergence of the algorithm towards the known result due to Bhattacharya (2008) is demonstrated by varying the both the splitting parameter and the number of nodes used to discretize the wave-space solution. In particular, for a channel twelve particle radii across, thirty-two nodes are used in the direction normal to the wall while the number of nodes parallel to the wall is varied from $2^4 - 2^7$. As the lattice dimension varies, the density of nodes parallel to the wall, denoted M/a, changes as well. Similarly, four distinct values of the splitting parameter are employed. The value chosen for all the results discussed in this section is $\alpha = L_3^2/8$ which in this particular case is eighteen. In particular, when the density of wave-space nodes is greater than one per particle radius, the predicted sedimentation rate is virtually identical for all discretization choices and splitting parameters. For less dense discretizations, the predicted sedimentation rate is smaller than the converged values and smaller values of the splitting parameter yield less accurate results. This is to be expected as a smaller splitting parameter necessitates finer discretization in wave-space. Additionally, because the real-space interactions are calculated only for particle pairs within some cutoff distance larger than $\sqrt{\alpha}$, there is an insufficient number of terms in the real-space summation for larger values of α. Throughout these results, an empirical standard for the wave-space discretization in which a minimum of two nodes per particle radius is practiced. This same standard was employed with success in the calculations of Seirou and Brady (2001) for systems of unbounded colloids.

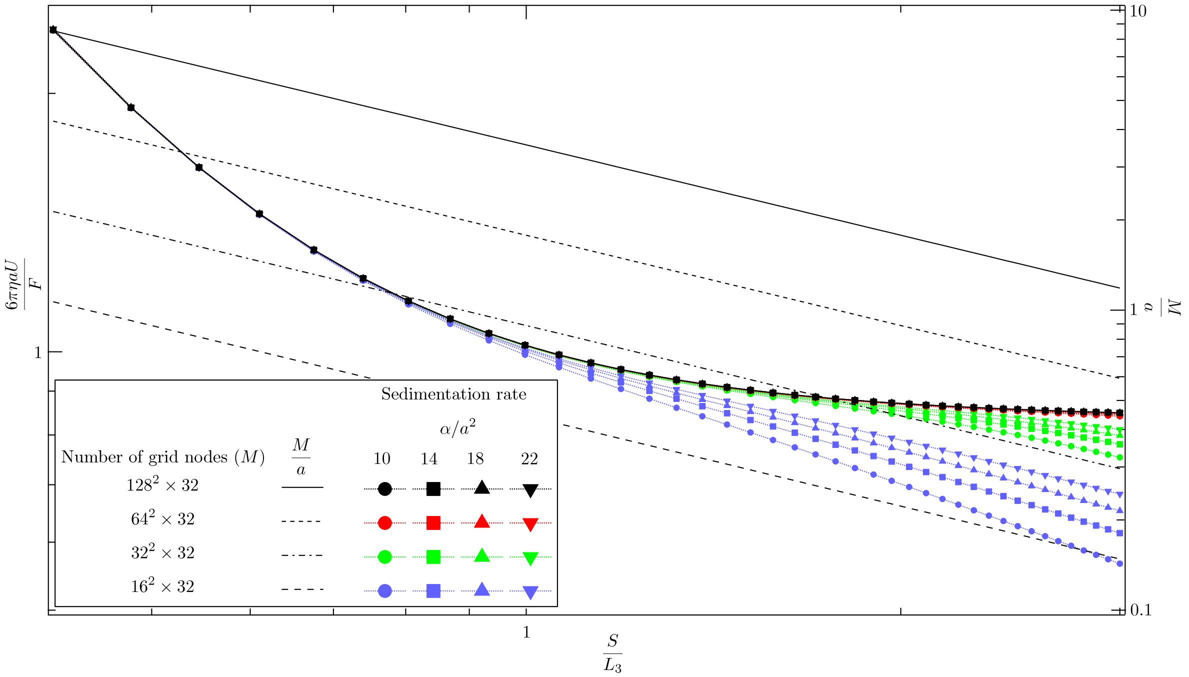

Figure 6.8: As in figure 6.6, the sedimentation rate along the channel with no applied pressure gradient is plotted. It was previously demonstrated that this calculation reproduces the known result due to Bhattacharya (2008). In this case, however, the empiricism employed throughout the simulations in this section (*i.e.* $\alpha = L_3^2/8$ and a minimum of wave-space discretization density of two nodes per particle radii) is justified by demonstrating the algorithm's stability and convergence as the splitting parameter and wave-space discretization are varied. Note that there is virtually no difference in the sedimentation rate for discretizations of $64^2 \times 32$ and $128^2 \times 32$ (red and black respectively). Hence they may be difficult to distinguish on the plot.

6.3.2 High-frequency dynamic viscosity

The high-frequency dynamic viscosity is the result of an experiment where one of the channel walls is oscillated rapidly and with small amplitude. The time averaged ratio of the speed of the wall to the force required to push it is the high-frequency dynamic viscosity, denoted η'_∞. Since this is done in the limit that the oscillatory time scale is shorter than all other time scales, the motion of the particles is inconsequential and what is actually probed is simply the mean particle stresslet for an equilibrium configuration of particles, *viz.*

$$\frac{\eta'_\infty}{\eta_0} = 1 - \frac{1}{2\eta \mathbf{E}^\infty : \mathbf{E}^\infty} \int_0^{L_3} n(x_3) < \mathbf{S} >_{x_3} : \mathbf{E}^\infty dx_3, \tag{6.47}$$

where the average $< \mathbf{S} >_{x_3}$ is the mean particle stresslet conditioned over a particular position (x_3) in the suspension at equilibrium. In particular, one is interested in the response to a shear flow generated by differential translation of the channel walls. In that case, the only non-zero components of $\mathbf{E}^\infty$ are the $\mathbf{e}_1\mathbf{e}3$ and the $\mathbf{e}_3\mathbf{e}_1$ dyads. While one can certainly measure the conditioned average itself, this is not a particularly germane quantity. Instead, the high-frequency viscosity is plotted as a function of suspension volume fraction and channel width in figure 6.9. Additionally, the increment to the Einstein viscosity $[\eta(1+5/2\phi)]$ is measured and plotted. This is an $O(\phi)$ quantity since there is additional dissipation associated with the motion of a single particle in the channel which is not present in an unbounded, dilute suspension.

Notice that at low and high particle concentrations and regardless of channel width, the high-frequency viscosity is near that of an unbounded suspension. At moderate volume fractions, there is a systematic deviation which grows as the channel width decreases. While at high volume fractions it is the particle-particle lubrication which dominates the dissipation, at low and moderate volume fractions, the lubrication interactions with the walls substantially increment the suspension viscosity. This is borne out by the trend in the viscosity with respect to channel width: the narrower the channel, the larger fraction of particles near the wall and therefore the larger the viscosity increment. Interestingly, however, the measured deviation from the bulk viscosity is not more than fifteen percent at low volume fractions and decreases to only a few percent at higher volume fractions. These trends are directly observable in a plot of the mean stresslet distribution as

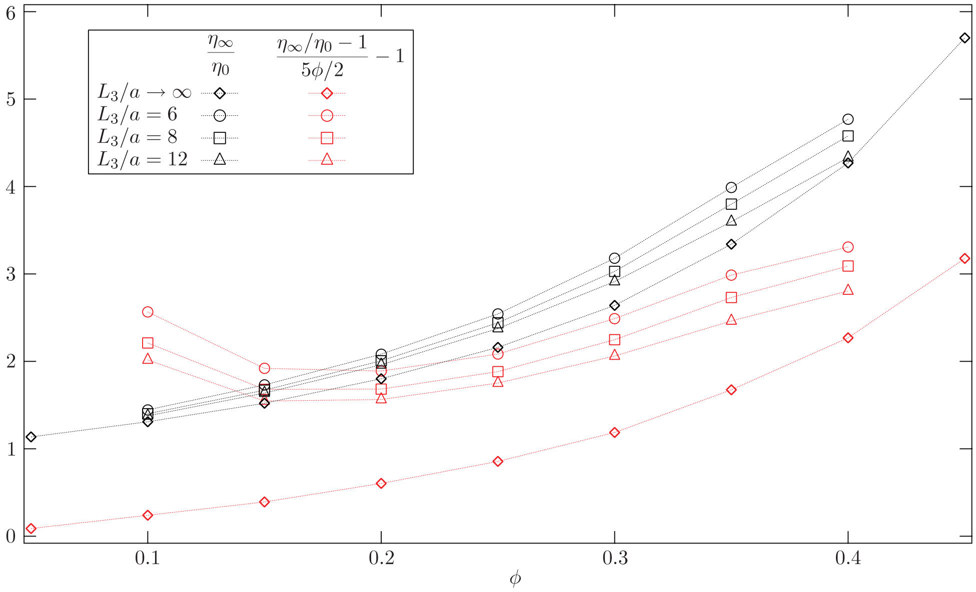

Figure 6.9: The high-frequency dynamic viscosity and viscosity increment less the Einstein contribution ($5\phi/2$) plotted as a function of volume fraction and channel width. Note the non-monotonic trend in the viscosity increment. This is due to a combination of hydrodynamic screening and the additional resistance due to the channel walls.

a function of position across the channel (see figure 6.10). While near the wall, the mean particle stresslet is effectively invariant with respect to both channel width and volume fraction – a consequence of lubrication – in the mid-channel region, the mean stresslet grows with volume fraction. This is because as the suspension becomes more dense, the inter-particle spacing decreases and lubrication interactions between the particles contribute significantly to mean stresslet. It is important to recognize that the particle contribution to the suspension stress is the integral of the product of this stress distribution and the number density distribution. Therefore, even though the near wall stresslet is invariant, it is more heavily weighted in denser suspensions since there are more particles near the wall. So unlike in unbounded suspensions, the single particle structure plays an important role in determining the suspension stress. Notice too that for denser systems, the suspension stress begins to approach a nearly constant value as the lubrication interactions among particle pairs and between particles and the walls are indistinguishable from on another. As such, in channels larger than a dozen particle radii, deviations from the bulk rheology are likely inscrutable experimentally. The same, however, is not true of the particle dynamics.

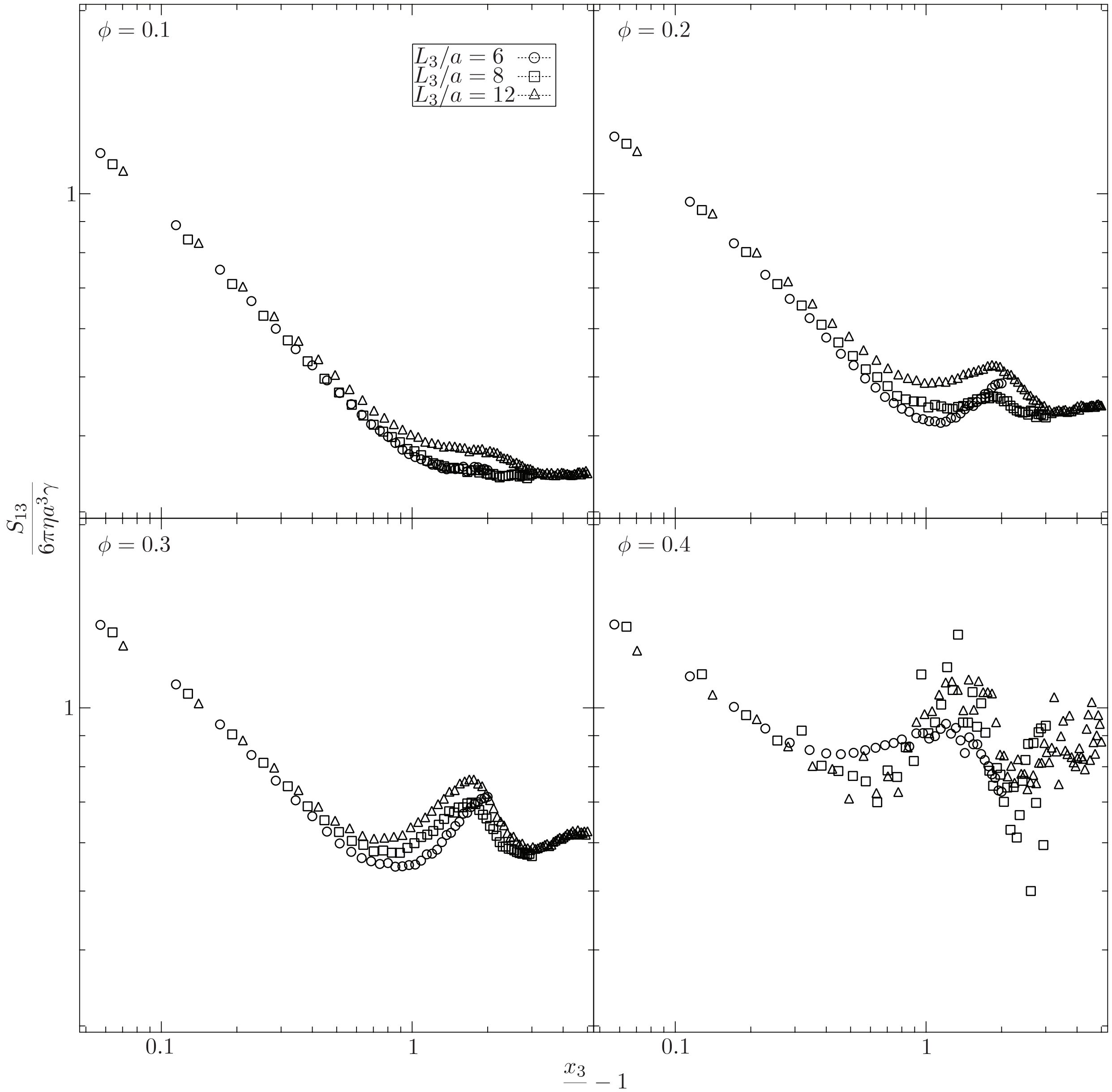

Figure 6.10: The distribution of particle stresslet across channels of varying width for different volume fractions. Notice that the near wall contribution is effectively invariant while the mid-channel contribution grows with increasing volume fraction.

6.3.3 Short-time self-diffusivity

The short-time self-diffusivity is measured using the stochastic process first introduced by Seirou and Brady (2001). Each particle is propelled by an independent and identically distributed random force such that there is no correlation of the forces among different particles and the covariance matrix for each force is diagonal. An ensemble average of the product of the resulting particle velocities and their forces can be shown to measure the diagonal components of $\mathbf{R}_{FU}^{-1}$. Averaged over many equilibrium particle configurations, this is simply the short-time self-diffusivity. As the distance of each particle from the wall is known explicitly, the dependence of the short-time self-diffusivity on position in the channel is accessible. Similarly, since the components of the individual random forces are uncorrelated, the diffusion parallel and perpendicular to the walls is also apparent. In fact, it is the *inhomogenous* and *anisotropic* short-time self-diffusivity, denoted $\mathbf{D}_0^S(\phi, x_3/a; L_3/a)$ that distinguishes the dynamics of a confined system from that of a bulk material. This quantity is plotted for several bulk volume fractions in figure 6.11.

One might anticipate that for concentrated systems, the influence of the walls is minimal. As such, over much of the channel the short-time self-diffusivity should deviate little from its bulk value, denoted $D_0^S(\phi)$. Similarly, for dilute systems, the channel screens the long-range hydrodynamic interactions, so the hindrance to the particle dynamics is due primarily to the channel walls themselves as well as lubrication interactions with a few nearby particles. In this case, the short-time self-diffusivity should be a product of its bulk value and the mobility of a single particle in the channel, *viz.*

$$\mathbf{D}_0^S\left(\phi, \frac{x_3}{a}; \frac{L_3}{a}\right) \approx 6\pi\eta a \mathbf{M}_{UF}^S\left(\frac{x_3}{a}; \frac{L_3}{a}\right) D_0^S(\phi). \tag{6.48}$$

In essence, the dynamics would be those of a single particle in a channel with the same width but in a solvent of effective viscosity $kT/6\pi a D_0^S(\phi)$. While these two models for the self-diffusivity apply at high and low volume fraction [$D_0^S(\phi)$ and 6.48 respectively], the range of applicability with respect to the width of the channel is not obvious. For instance, in the widest channels, the short-time self-diffusivity should converge on the bulk value and the two models become equivalent. However, when the channel becomes more narrow,

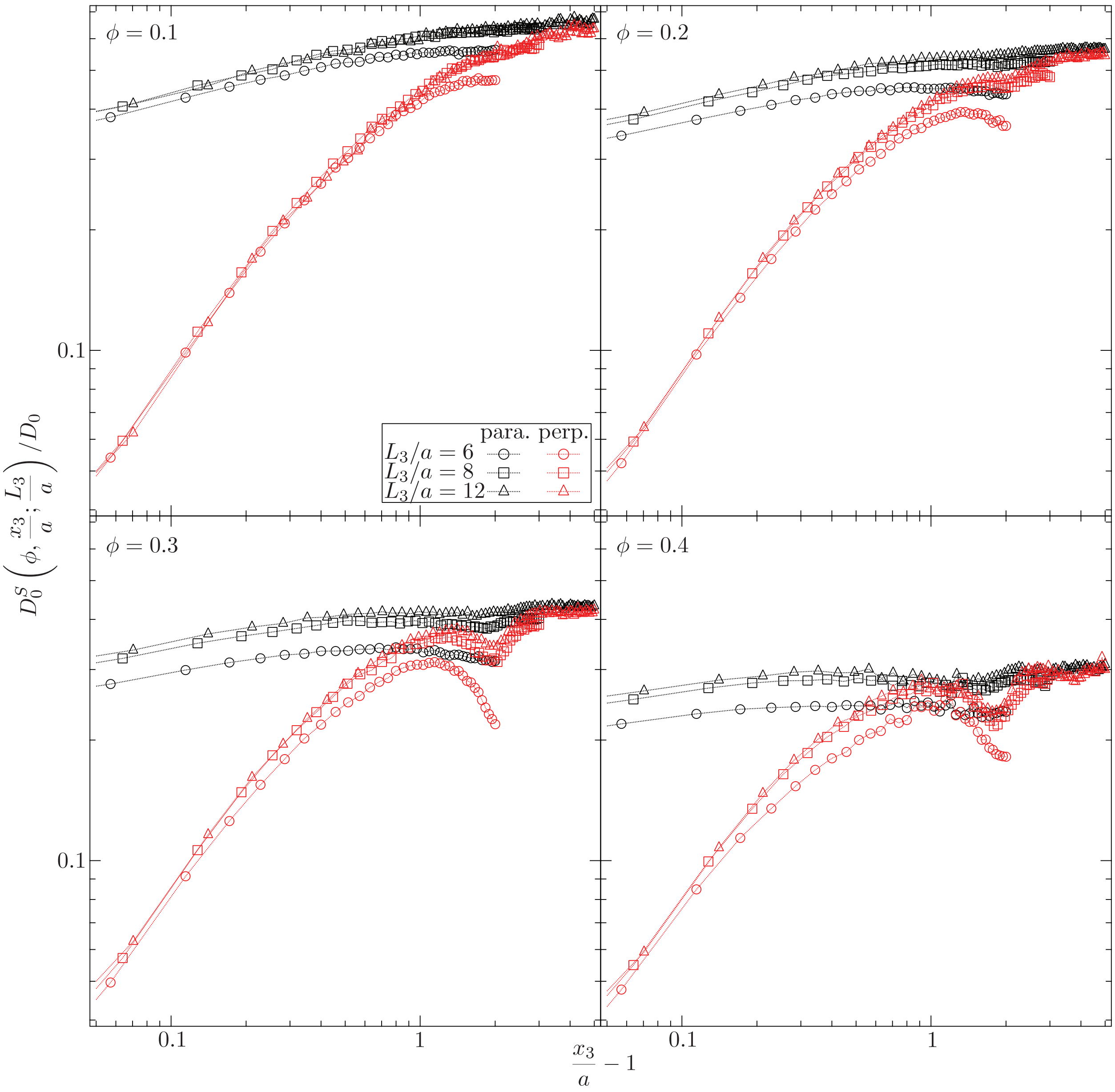

Figure 6.11: The short-time self-diffusivity of particles in suspensions of volume fraction $\phi = 0.1$, 0.2, 0.3 and 0.4 as a function of the distance across the channel and channel width. Note that near the wall, the channel width is a relatively unimportant factor in setting the scale of the self-diffusivity for all volume fractions while far from the channel walls, there is an intimate relationship between the suspension structure and the hydrodynamic interactions among the particles and with the channel walls.

not only does the structure of the dispersion change dramatically, but the influence of wall and inter-particle hydrodynamic interactions become indistinguishable. The consequence being that neither model can predict suitably the dynamics of the suspension. The effectiveness and breakdown of these models is illustrated by figures 6.12-6.14.

Three channel widths ($L_3/a = 6, 8, 12$) and three volume fractions ($\phi = 0.1, 0.25, 0.4$) are considered. For the widest channel and the lowest volume fraction, the single particle approximation is virtually an exact match for the simulation data. Similarly, for the widest channel and the highest volume fraction, the bulk approximation for the self-diffusivity is an excellent prediction as the diffusivity is isotropic over much of the channel. For the moderately concentrated suspension in the widest channel, however, the self-diffusivity is nearly isotropic, but far smaller than the bulk prediction. Similarly, it is larger than either the parallel or perpendicular single particle approximations. As the channel shrinks, these same trends persist, though it appears that the bulk prediction for the highest volume fraction remains a better model. For the smallest channel studied, neither approximation is suitable for the most and least dense suspensions, and throughout, the dynamics of moderately dense suspension are not well approximated.

There is more to be drawn from this figure however. Notice that the bulk diffusivity is *always* an overestimate of the diffusivity mid-channel. This is because the bulk limit does not account for the energy dissipated due to the no-slip condition on the channel walls. This additional hinderance is always present and always larger than what one would get by replacing the solid wall with a porous structure such as a collection of other colloidal particles. Similarly, rescaling the solvent viscosity on the bulk diffusivity and measuring the diffusivity of a single particle in the equivalent channel filled with the fictitious fluid *always* underestimates the self-diffusivity. This is because the inter-particle hydrodynamic interactions are actually weaker than the bulk limit predicts as they are screened by the walls. In the high density regime, the bulk limit is approached from below, while as the walls become further apart, the single particle rescaling is approached from above. Presumably, for wide enough channels, these two limits become indistinguishable.

This line of analysis is suggestive of a "phase" diagram describing the particle dynamics in terms of either the wall dominated or bulk dominated regimes. Of particular interest to researchers, theoreticians and

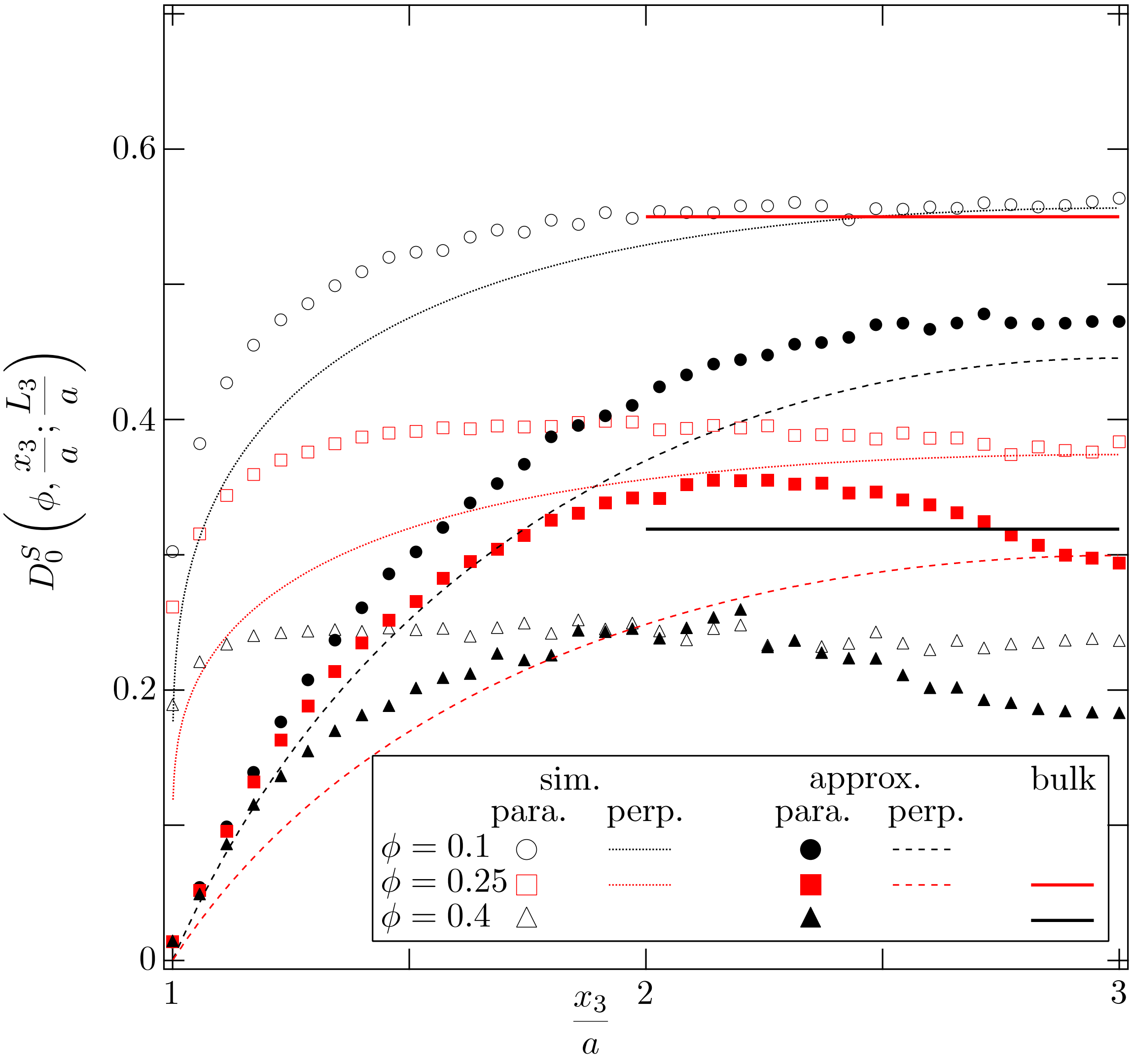

Figure 6.12: The short-time self-diffusivity is measured via simulation and compared to an approximation for the diffusivity of a single particle in the channel for an effective viscosity $kT/6\pi a D_0^S(\phi)$ as well as the bulk short-time self-diffusivity. This is a computation for $L_3 = 6a$.

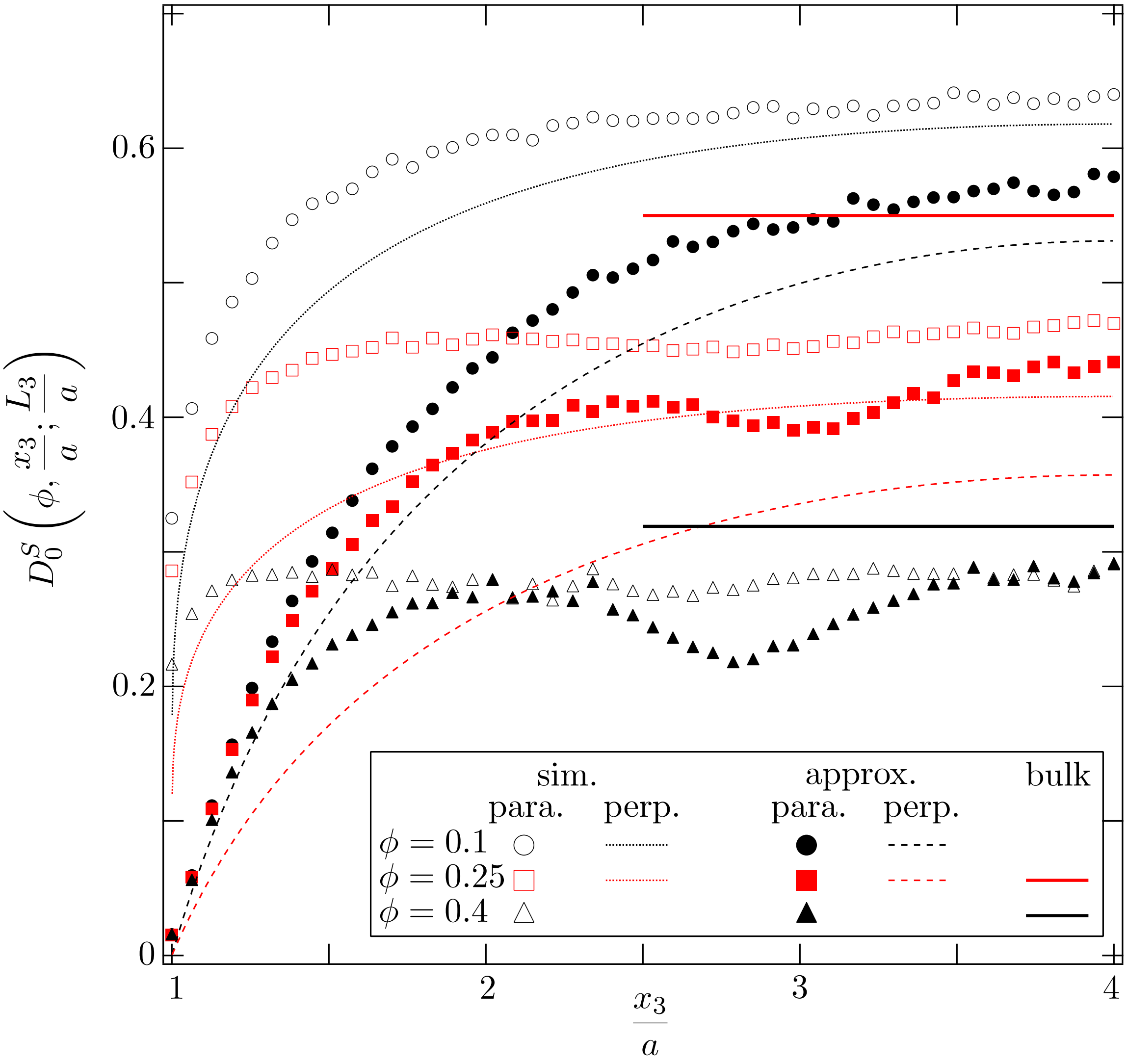

Figure 6.13: The short-time self-diffusivity is measured via simulation and compared to an approximation for the diffusivity of a single particle in the channel for an effective viscosity $kT/6\pi a D_0^S(\phi)$ as well as the bulk short-time self-diffusivity. This is a computation for $L_3 = 8a$.

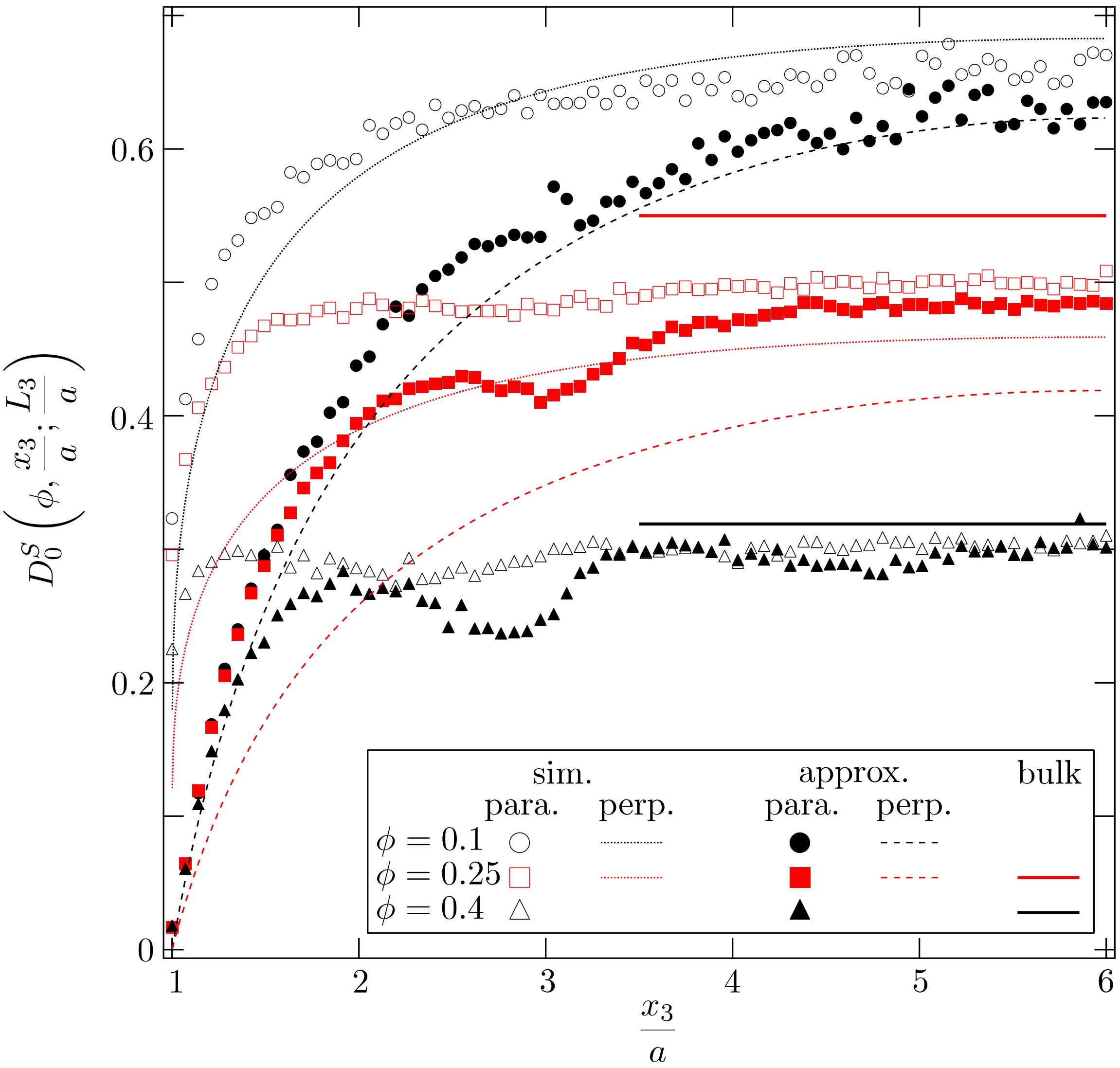

Figure 6.14: The short-time self-diffusivity is measured via simulation and compared to an approximation for the diffusivity of a single particle in the channel for an effective viscosity $kT/6\pi a D_0^S(\phi)$ as well as the bulk short-time self-diffusivity. This is a computation for $L_3 = 12a$.

experimentalists alike, should be the breakdown region where the suspension dynamics cannot be described by any simple combination of "local" properties. Such a diagram is sketched in figure 6.15, though the details remain to be firmly worked through. Indeed, the boundaries of such a diagram are fuzzy and to some degree subjective, though as a qualitative tool it may suggest a "sweet-spot" for future studies of confined soft-matter. Here, the dynamics are complicated by an intricate combination of suspension structure and particle-particle and particle-wall hydrodynamic interactions which remain largely unstudied. Additionally, there is a region of high confinement which has been widely studied and in which a pseudo-two-dimensional dynamic behavior is observed [see *e.g.* Marcus, Lin and Rice (1996)]. This is not pursued here, though the hydrodynamic method presented does not preclude such measurements.

6.3.4 Sedimentation rate

The mean fall speed of particles within a suspension bound in a channel as a function of volume fraction, channel width and position across the channel is determined. In this case, not only is the sedimentation rate anisotropic and inhomogenous, it also depends on whether the channel is left open such that there is no backflow pressure gradient or closed such that there is no mean flux of material (particles and fluid) down the channel. The former only occurs for sedimentation parallel to the channel walls. At lower volume fractions, it is the hydrodynamic interactions which dominate the behavior of the suspension as the number density of particles across the channel is relatively constant. At higher volume fractions, however, the number density of particles varies significantly and therefore so does the local particle flux. This gives rise to different behaviors for different end conditions in the channel.

The sedimentation rate U for particles falling down the channel with no net flux and those falling normal to the channel walls with force F are plotted in figure 6.16 as a function of channel width, volume fraction and position across the channel. At low volume fractions the particle flux down the channel is effectively parabolic as anticipated. One can recognize this as parabolic because of the monotonic increase followed by a characteristic uptick in the sedimentation rate near the center of the channel. At higher volume fractions the sedimentation rate fluctuates significantly about a plug flow profile as the mean gravitational body force

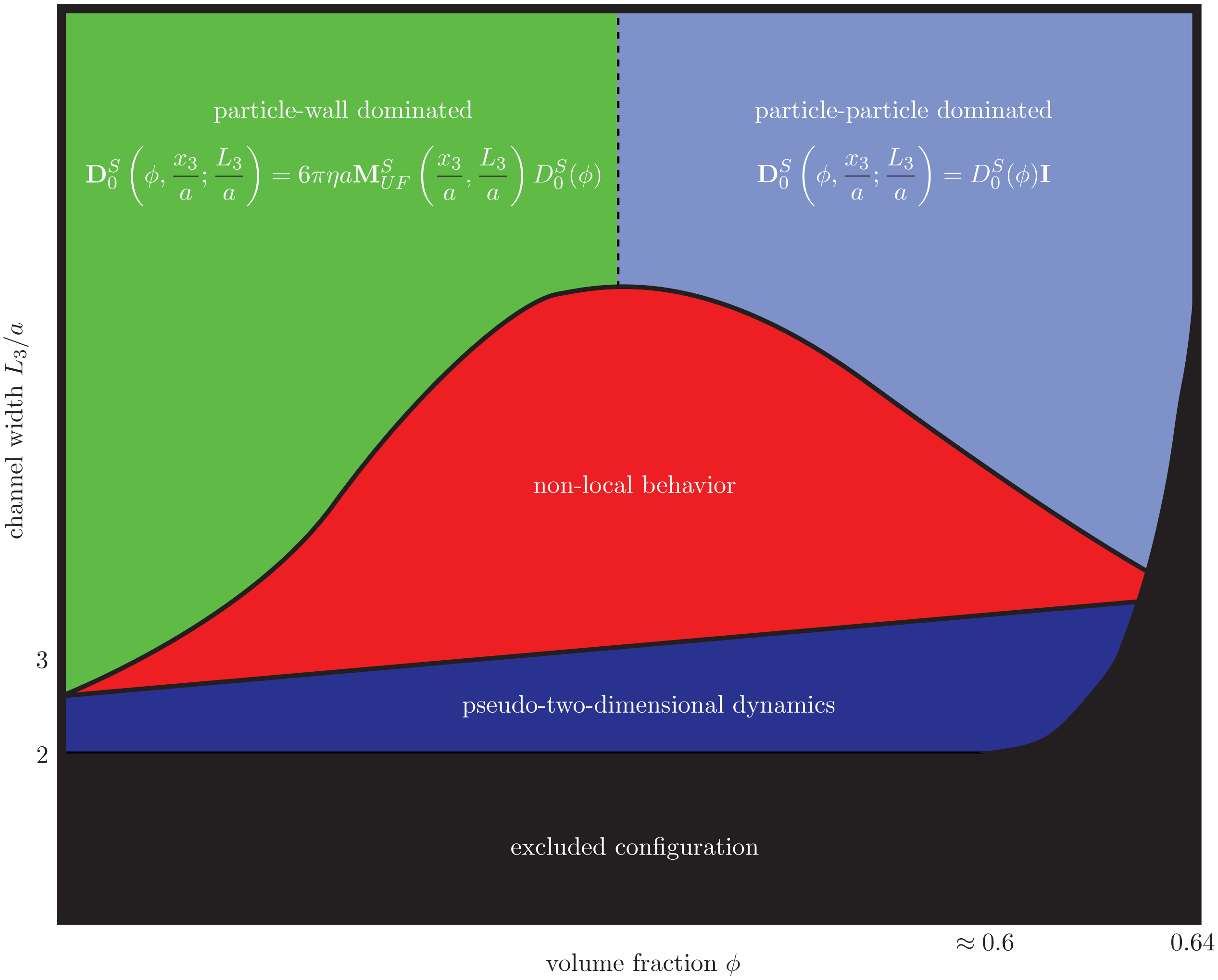

Figure 6.15: A "phase" diagram suggesting the dynamical behavior observed by particles bound by channels of varying widths at varying volume fractions. The key regions are: the particle-wall dominated regime at low density and moderate to large channel widths for which the dynamics are essentially those of a single particle immersed in a fluid of effective viscosity $kT/6\pi a D_0^S(\phi)$; the particle-particle dominated regime at high concentrations and moderate channel widths where the dynamics are indistinguishable from the bulk material; and the non-local regime in which the interplay of particle-particle and particle-wall hydrodynamics are inseparable and the details of suspension structure and hydrodynamics are necessary for accurate prediction of the particle dynamics.

on the suspension varies directly with the local number density. It is the interplay of this local number density variation and the backflow that gives rise to the fluctuations. Notice though that at no point is the sedimentation rate negative. The backflow can never be strong enough to cause particles to levitate rather than fall. Additionally, there is a weak dependence of the sedimentation rate on channel width at low volume fractions. That is, as a function of position across the channel, the sedimentation rate channels of different widths is nearly indistinguishable at both ten and twenty percent volume fraction. This is what one would expect of Poiseuille flow where the pressure gradient is independent of the channel width (*i.e.* it depends only on the mean density of the suspension). In the normal direction, however, there is a much stronger dependence on the channel width at all volume fractions. This is largely due to the comparatively stronger hinderance to motion of even a single particle in the normal direction. While one might expect that the particle-particle hydrodynamic interactions are insignificant because of the exponential rate hydrodynamic screening for motion in the normal direction, the strong variations in the number density and consequently the sedimentation rate at higher volume fractions demonstrate that local, collective motion whose rate is set precisely by those hydrodynamic interactions is not only perceptible but significant. As expected, with increasing particle volume fraction, the sedimentation rate decreases in situations where the mean flux of material is zero.

In figure 6.17, the sedimentation rate of a suspension along a channel with no restriction on the flux is presented. As would be expected, with no pressure gradient applied down the channel, heavier suspensions fall faster. This statement must be taken in a particular context though. The mean flux of the heavier suspension is always larger. Additionally, the profile of the sedimentation rate across the channel shows an interesting dependence on the volume fraction. For less dense suspensions, the typical parabolic flow profile emerges, while for denser suspensions plug flow prevails. This is intriguing as observations of this behavior have been made [see *e.g.* Nott and Brady (1994) and Lyon and Leal (1998)] for suspensions driven by a pressure gradient down a channel and near steady-state with markedly different number density distributions. It appears that regardless of the distribution, at higher volume fractions, the hydrodynamic screening nullifies the effect of the walls and produces a nearly uniform velocity profile. The uniform velocity profile appears

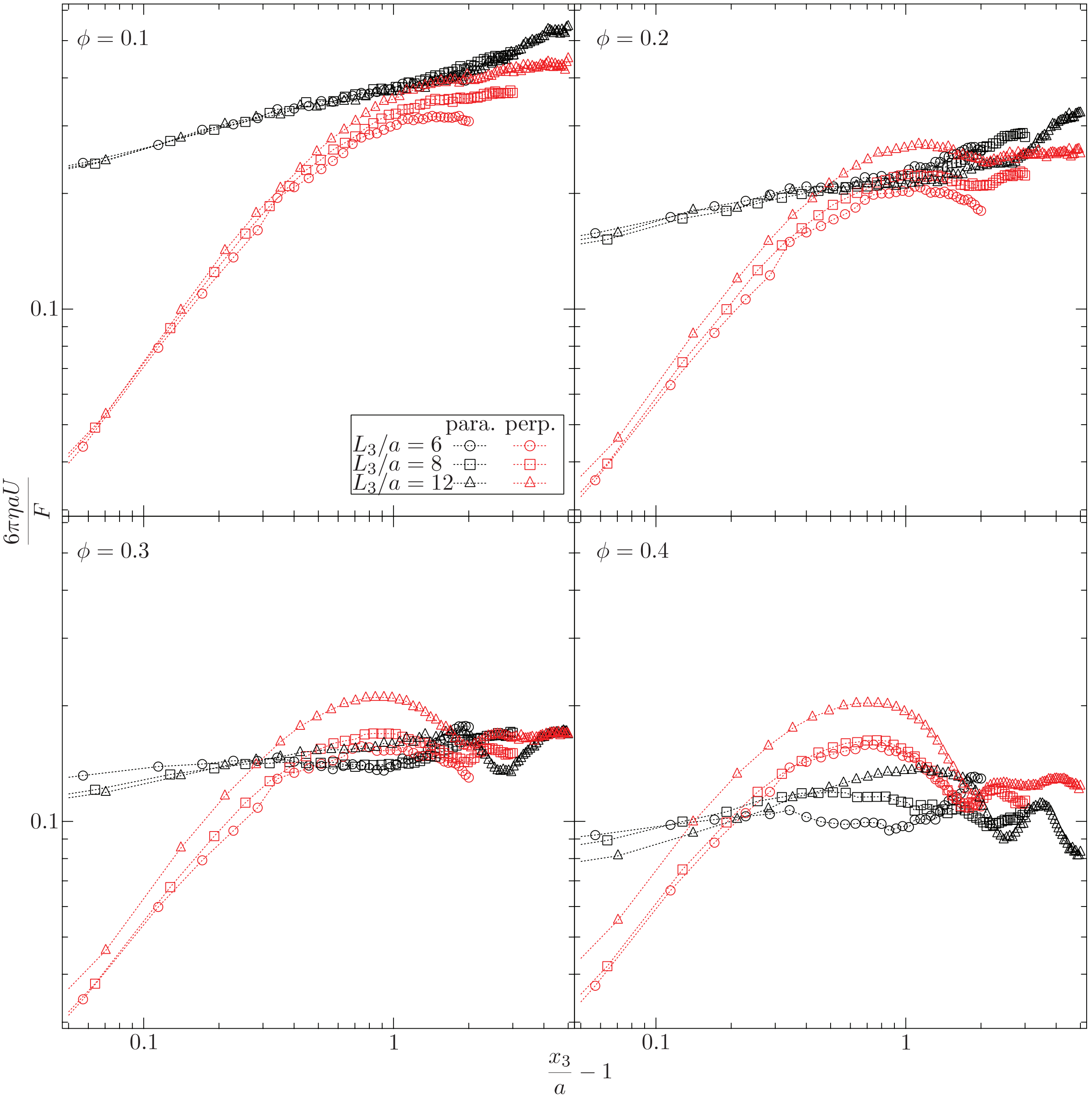

Figure 6.16: Plotted here is the sedimentation rate of a suspension of particles in a sealed channel (*i.e.* no mean flow) in the directions along and normal to the channel walls.

to set in at lower volume fractions for more narrow channels as well. This is likely due to the fact that for narrower channels, it is the lubrication interactions with the walls that dominate. These are more or less indistinguishable from particle-particle lubrication interactions.

6.4 Conclusions

It is no simple task accurately accounting for the low-Reynolds-number hydrodynamic interactions among many colloidal particles in a confined geometry. Not only are there the intrinsic length scales set by the bounding geometry, but the many-bodied interactions are important over different scales as well. Identifying these length scales, minimizing their interdependence and then approximating them with both speed and fidelity is the key to not only reproducing known computations and experiments but predicting novel behavior. In this chapter, the hydrodynamic interactions among a suspension of particles bound between parallel walls were separated into near-field and far-field components following the typical Stokesian Dynamics methodology. Then, the far-field interactions were further divided into those mediated by both channel walls and those mediated by a single wall. This introduces the so-called splitting parameter typical of Ewald-summation procedures. By and large, it is the channel width which sets the magnitude of this parameter when the channel is on the order of a few to tens of particle radii wide. The reason for this scaling is simply to optimize the process of summing over interactions among particle pairs. As a consequence of this splitting, the far-field interactions mediated by both channel walls are reproduced exactly while those mediated by a single wall are a superposition approximation which introduces an error that is exponentially small. The process of summing over both sets of interactions requires only log-linear time to compute with respect to the number of particles.

The static rheology and short-time dynamics that emerge from the simulations conducted suggest a sophisticated interplay of particle-particle and particle-wall hydrodynamic interactions. For the volume fractions and channel widths considered, the density striations throughout the channel play a secondary role. The high-frequency dynamic viscosity deviates little from the value expected for an unbounded suspension.

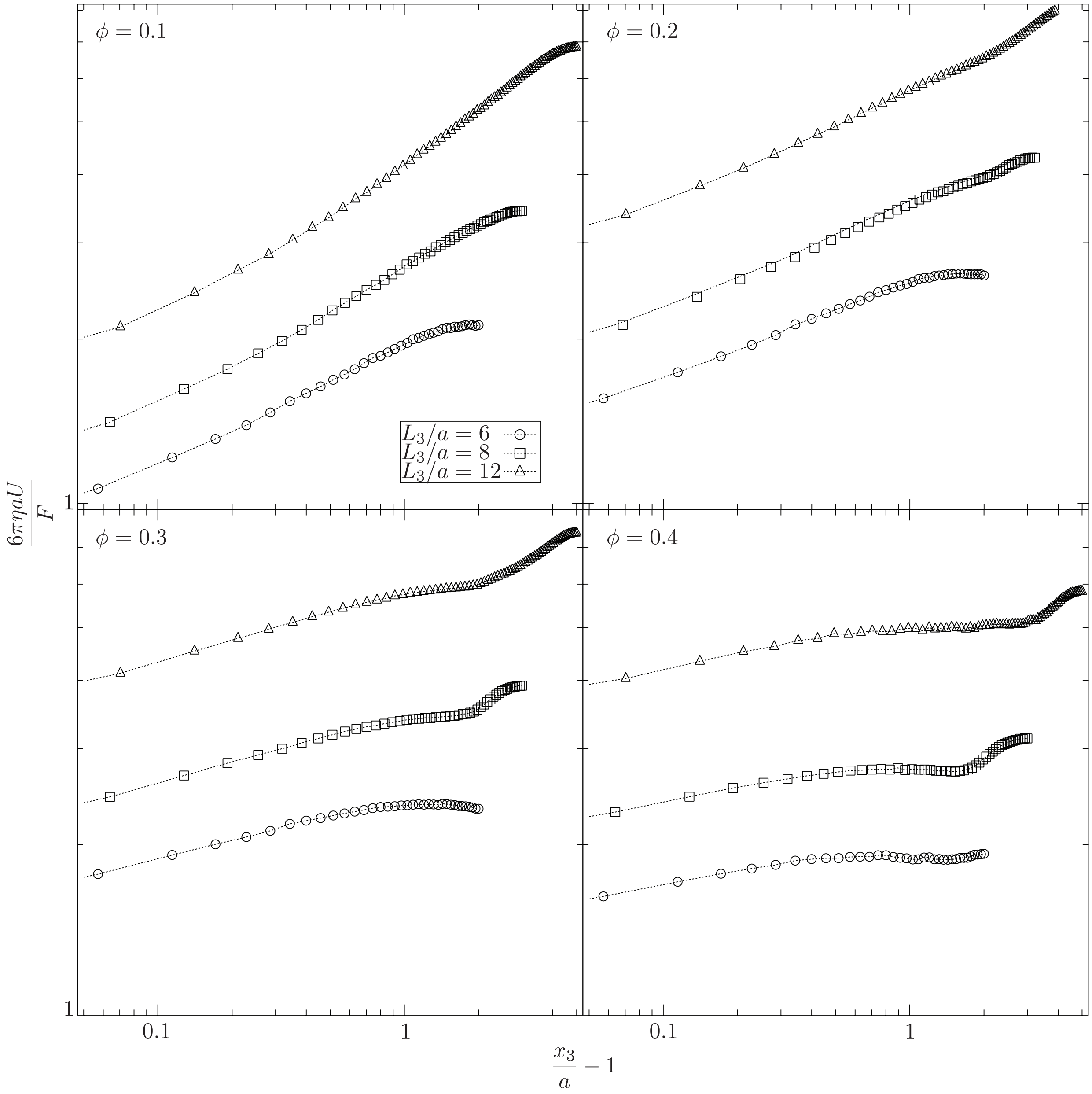

Figure 6.17: The sedimentation rate down a channel with no applied pressure gradient changes from parabolic to uniform profiles with increasing volume fraction while the mass flow rate similarly increases.

While there is the anticipated dependence on the channel width (the viscosity grows as the channel narrows), the difference between that increment and the bulk value was less than fifteen percent for all volume fractions and channel widths considered. However, the increment beyond the Einstein contribution to the viscosity ($5\phi/2$) reveals that at low volume fractions the particle-wall interactions make the predominant contribution to the viscous dissipation. At high volume fractions, the particle-particle hydrodynamic interactions dominate instead, and the bulk rheology is nearly recovered. This same trend is observed for the short-time self-diffusivity as well. One finds that there is a range of moderate suspension density and channel width for which there is an intimate and inseparable connection between hydrodynamic interactions among the particles and the walls.

Returning to the questions with which this thesis opened, while it may be the case that a continuum approach is often suitable for modeling suspensions, there is in effect a Knudsen number which can be of order one and limits the effectiveness of such an approach. Namely, when the length scale of interest is on the order of the particle size, the detailed micromechanics become a necessary part of the model formulation. Similarly though, there are approximations to be made within this regime that can avoid such complexities. When the average distance between the particles, $n(x_3)^{-1/3}$, is small relative to a macroscopic length scale, L_3 for instance, then even though a/L_3 is order one, the bulk properties dominate. When the opposite is true such that a/L_3 is order one while $n(x_3)^{-1/3}/L_3$ is large, the short-time particle dynamics are the same as those of a single particle in a fluid with effective viscosity $kT/6\pi a D_0^S(\phi)$. It is seen thus that the local approximation can, in case of an order unity Knudsen number be extended with little effort. This of course requires further analysis to determine the particular ranges of applicability.

Future studies will focus on the non-equilibrium rheology and dynamics of confined suspensions. The rule-of-thumb for short-time dynamics laid out in figure 6.15 will certainly change with the introduction of a dynamic variable such as the shear-rate, sedimentation rate or applied pressure gradient. As the suspension structure was of varied importance to the rheology, dynamics and sedimentation rate, and this is what will change in a dynamic experiment, it is difficult to predict this change *a priori* or in general. Regardless, the method proposed is suitable for such studies and the results are forthcoming. There is fruitful ground here for looking beyond the suspension's particle-pair structure to larger scale morphologies, how those change in confinement and how this affects viscoelastic properties such as shear thickening and jamming.

Bibliography

[1] M.P. Allen and D.J. Tildesley. *Computer Simulation of Liquids*. Oxford University Press, 1989.

[2] C.W.J. Beenakker. Ewald sum of the Rotne–Prager tensor. *J. Chem. Phys.*, 85(3):1581–1582, 1986.

[3] S. Bhattacharya and J. Blawzdziewicz. Image system for Stokes-flow singularity between two parallel planar walls. *J. Math. Phys.*, 43(11):5720–5731, 2002.

[4] S. Bhattacharya. Cooperative motion of spheres arranged in periodic grids between two walls. *J. Chem. Phys.*, 128:074709, 2008.

[5] J.R. Blake. A note on the image system for a stokeslet in a no-slip boundary. *Proc. Camb. Phil. Soc.*, 70:303–310, 1971.

[6] G. Bossis, A. Meunier and J.D. Sherwood. Stokesian Dynamics simulations of particle trajectoriers near a plane. *Phys. Fluids A*, 3(8):1853–1858, 1991.

[7] J.F. Brady, R.J. Phillips, J.C. Lester and G. Bossis. Dynamic simulation of hydrodynamically interacting suspensions. *J. Fluid Mech.*, 195:257–280, 1988.

[8] J.F. Brady and G. Bossis. Stokesian Dynamics. *Ann. Rev. Fluid Mech.*, 20:111–157, 1988.

[9] J.E. Butler and R.T. Bonnecaze. Imaging of particle shear migration with electrical impedance tomography. *Phys. Fluids*, 11(8):1982–, 1999.

[10] B. Cichocki *et al.* Friction and mobility for colloidal spheres in Stokes flow near a boundary: the multipole method and applications. *J. Chem. Phys.*, 112(5):2548–2561, 2000.

[11] R.G. Cox and S.K. Hsu. The lateral migration of solid particles in a laminar flow near a plane. *Int. J. Multiphase Flow*, 3(3):201–222, 1977.

[12] R.G. Cox and S.G. Mason. Suspended particles in fluid flow through tubes. *Ann. Rev. Fluid Mech.*, 3:291-316, 1971.

[13] T. Darden, D. York and L. Pedersen. Particle mesh Ewald: An $N \cdot \log(N)$ method for Ewald sums in large systems. *J. Chem. Phys.*, 98(12):10089–10093, 1993.

[14] A. Donev, F.H. Stillinger and S. Torquato. Neighbor List Collision-Driven Molecular Dynamics Simulation for Nonspherical Particles. I. Algorithmic Details II. Applications to Ellipses and Ellipsoids. *J. Comp. Phys.*, 202(2):737–793, 2005.

[15] E.R. Dufresne, D. Altman and D.G. Grier. Brownian dynamics of a sphere between parallel walls. *Europhysics Lett.*, 53(2):264–270, 2001.

[16] L.J. Durlofsky and J.F. Brady. Dynamic simulation of bounded suspensions of hydrodynamically interacting particles. *J. Fluid Mech.*, 200:39–67, 1989.

[17] A.B. Glendinning and W.B. Russel. A pairwise additive description of sedimentation and diffusion in concentrated suspensions of hard spheres. *J. Colloid and Interface Sci.*, 89(1):123–143, 1982.

[18] J. Gregory. Flocculation in laminar tube flow. *Chem. Eng. Sci.*, 36(11):1789–1794, 1981.

[19] E. Guth and R. Simha. Untersuchungen über die viskosität von suspensionen und lösungen. 3. Über die viskosität von kugelsuspensionen. *Colloild and Polymer Sci.*, 74(3):266–, 1936.

[20] H. Faxén. Disserations, Uppsala University. *Arkiv. Mat. Astron. Fys.*, 17:27–, 1921.

[21] M. Frank *et al.* Particle migration in pressure-driven flow of a Brownian suspension. *J. Fluid Mech.*, 493:363–378, 2003.

[22] D. Frenkel and B. Smit. *Understanding Molecular Simulations*, 2nd edn. Academic Press, 2001.

[23] P.G. de Gennes. Conjectures on the transition from Poiseuille to plug flow in suspensions. *J. de Physique*, 40(8):783–787, 1979.

[24] H.L. Goldsmith and S.G. Mason. The of suspensions through tubes. I. Single spheres, rods and discs. *J. Colloid Sci.*, 17(5):448–476, 1962.

[25] J. Happel and H. Brenner. *Low Reynolds Number Hydrodynamics*, 2nd edn. Prentice Hall, 1986.

[26] H. Hasimoto. On the periodic fundamental solutions of the Stokes equations and their application to viscous flow past a cubic array of spheres. *J. Fluid Mech.*, 5(2):317–328, 1959.

[27] J.P. Hernández-Orthiz, J.J. de Pablo and M.D. Graham. Fast computation of many-particle hydrodynamic and electrostatic interactions in a confined geometry. *Phys. Rev. Lett.*, 98(14):140602–140606, 2007.

[28] R.W. Hockney and J.W. Eastwood. Computer simulation using particles. Taylor and Francis, 1989.

[29] R.B. Jones. Spherical particle in Poiseuille flow between planar walls. *J. Chem. Phys.*, 121:483–500, 2004.

[30] A. Karnis, H.L. Goldsmith and S.G. Mason. The kinetics of flowing dispersions: I. Concentrated suspensions of rigid particles. *J. Colloid and Interface Sci.*, 22(6):521–553, 1966.

[31] S. Kim and S.J. Karrila. *Microhydrodynamics*, 2nd edn. Dover Publications Inc., 2005.

[32] C.J. Koh, P. Hookham and L.G. Leal. An experimental investigation of concentrated suspension flows in a rectangular channel. *J. Fluid Mech.*, 266:1–32, 1994.

[33] O.A. Ladyzhenskaya. *The Mathematical Theory of ViscousIncompressible Flow*. Gordon and Breach, 1963.

[34] S.H. Lee, R.S. Chadwick and L.G. Leal. Motion of a sphere in the presence of a plane interface. Part 1: an approximate solution by generalization of the method of Lorentz. *J. Fluid Mech.*, 93(4):705–726, 1979.

[35] D.T. Leighton and A. Acrivos. Measurement of shear-induced self-diffusion in concentrated suspensions of spheres. *J. Fluid Mech.*, 177:109–131, 1987.

[36] N. Liron and S. Mochon. Stokes flow for a stokeslet between two parallel flat plates. *J. Eng. Math.*, 10:287–303, 1976.

[37] N. Liron. Stokeslet arrays in a pipe and their application to ciliary transport. *J. Fluid Mech.*, 143:173–195, 1984.

[38] M.K. Lyon and L.G. Leal. An experimental study of the motion of concentrated suspensions in two-dimensional channel flow. *J. Fluid Mech.*, 363:25–56, 1998.

[39] A.H. Marcus, B. Lin and S.A. Rice. Self-diffusion in quasi-two-dimension hard sphere suspensions. *Phys. Rev. E*, 53(2):1765-1776, 1996.

[40] J.T. Norman, H.V. Nayak and R.T. Bonnecaze. Migration of buoyant particles in low-Reynolds-number pressure driven flows. *J. Fluid Mech.*, 523:1–35, 2005.

[41] P.R. Nott and J.F. Brady. Pressure driven flow of suspensions: simulation and theory. *J. Fluid Mech.*, 275:157–199, 1994.

[42] M.E. O'neill and K. Stewartson. On the slow motion of a sphere parallel to a nearby plane wall. *J. Fluid Mech.*, 27(4):705–724, 1967.

[43] C.W. Oseen. Neuere Methoden und Ergebnisse in der Hydrodynamik. Dissertation, Akademische Verlagsgesellschaft, Leipzig, 1928.

[44] T.N. Phung, J.F. Brady and G. Bossis. Stokesian Dynamics simulation of Brownian suspensions. *J. Fluid Mech.*, 313:181–207, 1996.

[45] A. Ramachandran and D.T. Leighton. Viscous resuspension in a tube: the impact of secondary flows resulting from second normal stress differences. *Phys. Fluids*, 19(5):053301, 2007.

[46] A. Seirou and J.F. Brady. Accelerated Stokesian Dynamics simulations. *J. Fluid Mech.*, 448:115–146, 2001.

[47] V. Seshadri and S.P. Sutera. Apparent viscosity of coarse concentrated suspensions in tube flow. *J. Rheol.*, 14(3):351-373, 1970.

[48] M.E. Staben, A.Z. Zinchenko and R.H. Davis. Motion of a particle between two parallel plane walls in low-Reynolds-number Poiseuille flow. *Phys. Fluids*, 15:1711-1734, 2003.

[49] J.W. Swan and J.F. Brady. Particle motion between parallel walls: hydrodynamics and simulation. *Phys. Fluids*, *At press*, 2010.

[50] M. Zurita-Gotor, J. Blawzdziewicz and E. Wajnryb. Motion of a rod-like particle between parallel walls with application to suspension rheology. *J. of Rheol.*, 51(1):71-97, 2007.

[51] I.E. Zarraga and D.T. Leighton. Meausurement of an unexpectedly large shear-induced self-diffusivity in a dilute suspension of spheres. *Phys. Fluids*, 14(7):2194, 2002.

Chapter 7

Anisotropic diffusion in concentrated colloidal dispersions: the evanescent diffusivity

7.1 Introduction

Dynamic light scattering is one of the principle means of measuring the diffusivity of colloidal dispersions [see *e.g.* Berne and Pecora (2003) and Russel, Saville and Schowalter (1986)]. In cases where particles are too small to observe via optical microscopy and diffuse too quickly to track the trajectory accurately, fluctuations in the density of the dispersion provide another method of directly observing the particle dynamics. In an experiment, one measures the time auto-correlation of the intensity of laser light scattered from the suspension. This is termed the intermediate scattering function and the time rate of change of this quantity measures the diffusivity. This diffusivity is characterized by the time and length scales inherent to the scattering experiment. The scattering angle, related directly to the wavenumber of the scattered light which itself is denoted q, sets the length scale over which density fluctuations are probed. Over short times and a length scale small relative to the particle size, denoted a, (this is the limit $qa \to \infty$, $t \to 0$), the density fluctuations due to a single particle are measured and the self-diffusivity is probed. Over short-time scales and large length scales indicative of small angle scattering ($qa \to 0$, $t \to 0$), the fluctuations in density are those due to the collective motion of particles within the scattering volume. The measured dynamics are those characterized by collective or gradient diffusivity which reflect the Fickian flux due to a macroscopic gradient in the suspension density. While for long-times and large length scales, correlation among different particles vanishes though the auto-correlation of the scattering intensity among single particles persists and the long-time self-diffusivity is probed. A comprehensive study of the relationship between fluctuations in the local density of the suspension and its short-time dynamics was performed by Rallison and Hinch (1986). Similarly, Brady (1994) continued this line of investigation in pursuit of the long-time dynamics of the suspension. The key result being that while the short-time correlation of the fluctuations in suspension density measure the short-time self-diffusivity, the long-time correlation is approximately the same rescaled by a factor related to the suspension microstructure, *i.e.*

$$D_\infty^S(\phi) \approx \frac{D_0^S(\phi)}{1 + 2\phi g(2, \phi)}, \tag{7.1}$$

where $D_\infty^S(\phi)$ and $D_0^S(\phi)$ are the long- and short-time self-diffusivities, ϕ is the suspension volume fraction and $\phi g(2, \phi)$ is a measure of the mean number of neighbors contacting a particular particle. Experiments employing this type of light scattering measure the hydrodynamic and structural properties isotropically and homogenously. Within a particular scattering volume there is no mechanism to distinguish directionality or spatial variation in the hydrodynamic interactions or mean structure – two essential traits of colloidal dispersions in bounded geometries.

Light scattered by evanescent waves, in contrast, samples a scattering volume asymmetrically because the intensity of the wave (before it is scattered) decays exponentially fast with respect to distance from its origin. The decay rate is controlled by the so-called evanescent penetration depth which in essence parameterizes the measured light scattering intensity auto-correlation while distinguishing inhomogeneities in the suspension structure and hydrodynamic interactions. It was Holmqvist, Dhont and Lang (2006) who showed experimentally that for very dilute suspensions (less that one-tenth of a percent fraction by volume) the scattering due to evanescent waves also reveals the hydrodynamic anisotropy long anticipated theoretically [see Faxen (1923), Oseen (1928), Happel and Brenner (1986), Blake (1971) and Swan and Brady (2007)]. And indeed, we proposed a more general theory for the scattering of evanescent waves by Brownian particles in the short-time regime for suspensions of all volume fractions [Michailidou *et al.* (2009)] which exposes these same features. We used this theory to predict the dynamics of dilute suspensions and confirmed the predictions by independent experimentation for volume fractions up to one percent. Further comparison between Stokesian dynamics simulations and experiments has been made for volume fractions up to forty percent [Michailidou *et al.* (2010) to appear], though the complete details of the theory appear for the first time in the subsequent text. It was reserved until a comprehensive set of data for the short-time self- and collective diffusivities for a wide range of volume fractions and penetration depths was prepared.

This chapter proceeds in the following manner. In section 7.2.1 we derive expressions for the evanescent wave dynamic light scattering diffusivites using an elementary approach derived from traditional light scattering analysis. In section 7.2.2 we describe the simulation methods implemented for modeling the hydrodynamic interactions among the particles by first describing the Stokesian dynamics method briefly, then expanding on that with a description of the accelerated Stokesian dynamics method for suspensions bound within a channel. In section 7.2.3 we take care to explain how both the static and dynamic measurements of the evanescent wave diffusivities may be made, though only the static approach is employed presently. In sections 7.3 and 7.4 we present the results of our simulations (the short-time self- and collective diffusivities) as a function of volume fraction and evanescent penetration depth and offer some physical interpretations of these results while concluding with a discussion of the applications for and experimental implications of this new technique.

7.2 Analysis

7.2.1 Statistical theory

When a laser strikes the interface between a glass plane with refractive index n_1 and a solution with refractive index n_2 at a sufficiently high angle (measured with respect to the surface normal) such that it is totally reflected, an evanescent wave is formed on the solution side of the interface (see figure 7.1). This evanescent wave decays exponentially with distance from the interface and scatters off the particles in the solution. The intensity of the scattered electric field due to a particle α is:

$$E_\alpha(\mathbf{q}, t; \kappa) = I_0 e^{-\frac{\kappa}{2}\mathbf{e}_3\cdot\mathbf{x}_\alpha(t) + i\mathbf{q}\cdot\mathbf{x}_\alpha(t)}, \tag{7.2}$$

where I_0 is the intensity of the unscattered field, $\kappa/2$ is the inverse penetration depth of the evanescent wave governing the rate of exponential decay, $\mathbf{x}_\alpha(t)$ is the position of particle α relative to the wall and $\mathbf{q}$ is the difference between the incident and scattered beams. The penetration depth of the evanescent wave is a well-defined quantity that depends on the angle at which the incident beam strikes the interface θ_i, the vacuum wavelength of the laser λ_0 and the refractive indices of the materials, *viz.*

$$\frac{\kappa}{2} = \frac{2\pi}{\lambda_0}\sqrt{(n_1 \sin\theta_i)^2 - n_2^2}. \tag{7.3}$$

Again, an evanescent wave is only emitted when the angle of incidence is greater than the critical angle, denoted θ_c and given by

$$\theta_i > \theta_c = \arcsin\left(\frac{n_1}{n_2}\right). \tag{7.4}$$

One example of this process in a hemispherical experimental cell is illustrated in figure 7.1.

Because of the coherence of laser light, we can write the intensity of the beam scattered by many particles, $E(\mathbf{q}, t; \kappa)$, as a linear superposition of that scattered by a single particle:

$$E(\mathbf{q}, t; \kappa) = \sum_{\alpha=1}^{N} I_0 e^{-\frac{\kappa}{2}\mathbf{e}_3\cdot\mathbf{x}_\alpha(t) + i\mathbf{q}\cdot\mathbf{x}_\alpha(t)} = \sum_{i=1}^{N} I_0 e^{i\mathbf{k}\cdot\mathbf{x}_\alpha(t)}, \tag{7.5}$$

where we have defined an effective, complex wave vector $\mathbf{k}$ such that

$$\mathbf{k} = \mathbf{q} + i\frac{\kappa}{2}\mathbf{e}_3. \tag{7.6}$$

This effective wave vector will prove especially convenient in connecting the light scattering experiments to the dynamics of the suspension. It also corresponds to one particularly interesting interpretation of evanes-

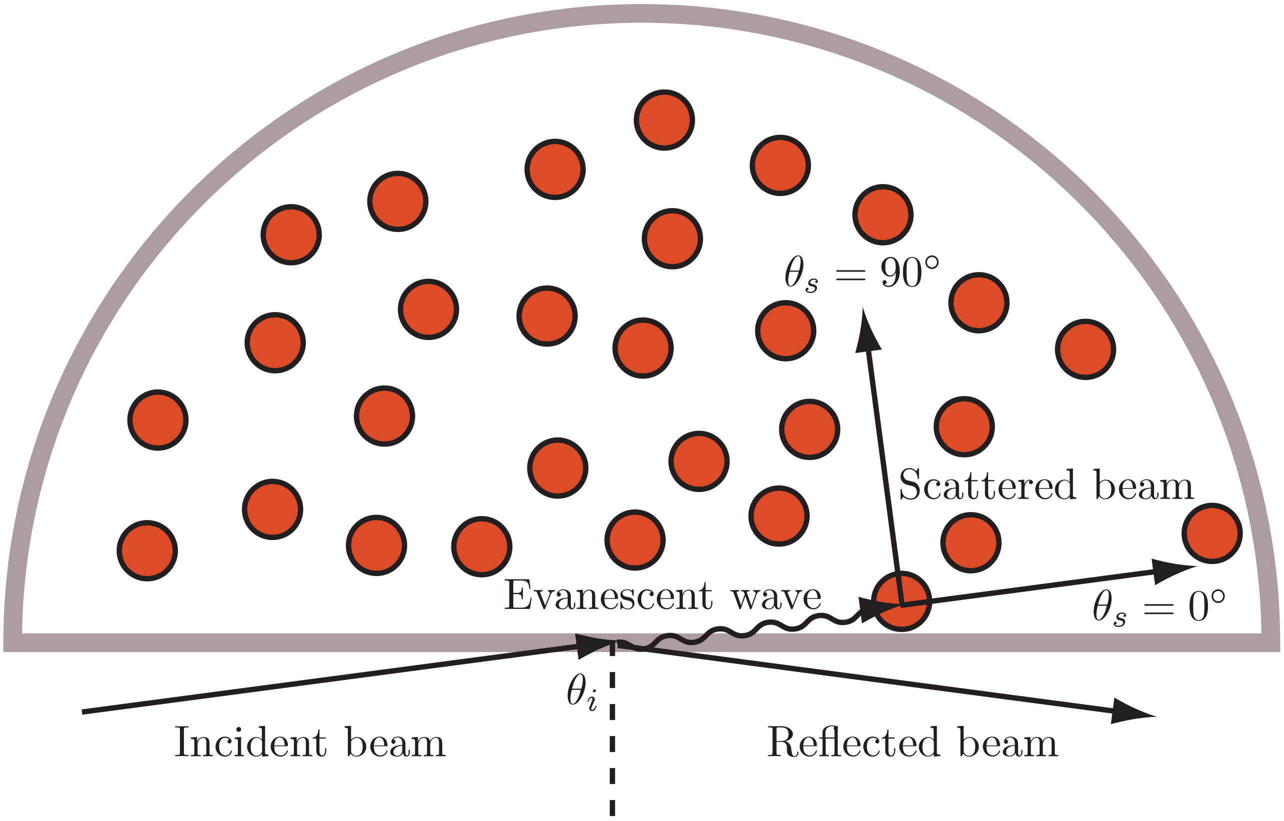

Figure 7.1: An example of an evanescent wave dynamic light scattering cell with the incident and scattering angles specifically labeled.

cent waves. Our original perspective noted that the intensity of an evanescent wave decays exponentially with distance from the interface. However, another view suggests that the wave vector associated with an evanescent wave is the same as that from directly scattered light except an evanescent wave vector has a complex component. While both of these are equivalent, the second viewpoint allows us to recast the problem of scattering from evanescent waves into the conventional light scattering construction.

As in many light scattering experiments, the connection to the dynamics of the scattering medium is made through the time autocorrelation of the intensity of the scattered beam and its complex conjugate. The conjugate of the intensity, $\bar{E}(\mathbf{q}, t; \kappa)$, is simply:

$$\bar{E}(\mathbf{q}, t; \kappa) = \sum_{i=1}^{N} I_0 e^{-\frac{\kappa}{2}\mathbf{e}_3 \cdot \mathbf{x}_\alpha(t) - i\mathbf{q}\cdot\mathbf{x}_\alpha(t)} = \sum_{\alpha=1}^{N} I_0 e^{-i\bar{\mathbf{k}}\cdot\mathbf{x}_\alpha(t)}, \tag{7.7}$$

and depends on the conjugate of the evanescent wave vector ($\bar{\mathbf{k}}$) instead of the wave vector itself as in conventional light scattering.

We now concern ourselves with the correlation of the light scattering intensity with its complex conjugate averaged over a large number of particle configurations or realizations. This is often called the intermediate scattering function and we denote it as $F(\mathbf{q}, t; \kappa)$, *viz.*

$$\begin{aligned} F(\mathbf{q}, t; \kappa) &= \left(\left\langle E(\mathbf{q}, t; \kappa)\bar{E}(\mathbf{q}, 0; \kappa)\right\rangle - \left\langle E(\mathbf{q}, t; \kappa)\right\rangle \left\langle \bar{E}(\mathbf{q}, 0; \kappa)\right\rangle\right) \Big/ I_0^2 \qquad (7.8) \\ &= \left\langle \sum_{\alpha,\beta=1}^{N} e^{i\mathbf{k}\cdot\mathbf{x}_\beta(t) - i\bar{\mathbf{k}}\cdot\mathbf{x}_\alpha(0)} \right\rangle - \left\langle \sum_{\alpha=1}^{N} e^{i\mathbf{k}\cdot\mathbf{x}_\alpha(t)} \right\rangle \left\langle \sum_{\beta=1}^{N} e^{-i\bar{\mathbf{k}}\cdot\mathbf{x}_\beta(0)} \right\rangle. \end{aligned}$$

The angular brackets denote an average over a large number of configurations of scattering particles in solution. This may be represented mathematically as an integral over the quantity in the brackets multiplied by the probability of finding the particles in that configuration. We make one additional simplification by noting that the particles in the solution are not tagged and may be thought of as identical. With this, we write intermediate scattering function as

$$F(\mathbf{q},t;\kappa)=\frac{1}{(N-1)!}\int\left[e^{i\mathbf{k}\cdot\mathbf{x}_1(t)}+(N-1)e^{i\mathbf{k}\cdot\mathbf{x}_2(t)}\right]e^{-i\bar{\mathbf{k}}\cdot\mathbf{x}_1(0)}P_N(\mathbf{x}^N(t),\mathbf{x}^N(0))\,d\mathbf{x}^N(t)\,d\mathbf{x}^N(0) \qquad (7.9)$$
$$-\,\delta\left[(\mathbf{I}-\mathbf{e}_3\mathbf{e}_3)\cdot\mathbf{k}\right]G(\mathbf{e}_3\cdot\mathbf{k})\bar{G}(\mathbf{e}_3\cdot\mathbf{k}),$$

where $P_N(\mathbf{x}^N(t),\mathbf{x}^N(0))$ is the joint probability of finding all N particles in the configuration denoted $\mathbf{x}^N(t)$ at time t and in configuration denoted $\mathbf{x}^N(0)$ initially. The factor proportional to $\delta\left[(\mathbf{I}-\mathbf{e}_3\mathbf{e}_3)\cdot\mathbf{k}\right]$, a delta function, is the square of

$$G(\mathbf{e}_3\cdot\mathbf{k})=\frac{1}{(N-1)!}\int e^{i\mathbf{k}\cdot\mathbf{e}_3\mathbf{e}_3\cdot\mathbf{x}_1(0)}P_N(\mathbf{x}^N(0))\,d\mathbf{x}^N(0)=\int e^{i\mathbf{k}\cdot\mathbf{e}_3 z}n(z)dz, \qquad (7.10)$$

where $n(z)$ is the density distribution of the suspension as a function of the coordinate normal to the wall. The same factor arises in conventional light scattering theory as $\delta(\mathbf{q})$ though we will investigate the peculiarities of its form as well as its significance after developing the full theory. For convenience, we define a new probability distribution $\hat{P}_N(\mathbf{x}^N(t))$ which contains all the dependence of $F(\mathbf{q},t;\kappa)$ on $\mathbf{x}^N(0)$ such that:

$$\hat{P}_N(\mathbf{x}^N(t))=\int P_N(\mathbf{x}^N(t)|\mathbf{x}^N(0))e^{-i\bar{\mathbf{k}}\cdot\mathbf{x}_1(0)}P_N^0(\mathbf{x}^N(0))\,d\mathbf{x}^N(0), \qquad (7.11)$$

where $P_N(\mathbf{x}^N(t)|\mathbf{x}^N(0))$ is the conditional probability of finding the particles in configuration $\mathbf{x}^N(t)$ at time t given they began in configuration $\mathbf{x}^N(0)$, and $P_N^0(\mathbf{x}^N(0))$ is the probability of finding the particles in configuration $\mathbf{x}^N(0)$ initially. Using this, we rewrite the intermediate scattering function as:

$$F(\mathbf{q},t;\kappa)=\frac{1}{(N-1)!}\int\left[e^{i\mathbf{k}\cdot\mathbf{x}_1(t)}+(N-1)e^{i\mathbf{k}\cdot\mathbf{x}_2(t)}\right]\hat{P}_N(\mathbf{x}^N(t))\,d\mathbf{x}^N(t)-\delta\left[(\mathbf{I}-\mathbf{e}_3\mathbf{e}_3)\cdot\mathbf{k}\right]G(\mathbf{e}_3\cdot\mathbf{k})\bar{G}(\mathbf{e}_3\cdot\mathbf{k}). \qquad (7.12)$$

Consider first the contribution to the intermediate scattering function due only to the correlation of scattering from the same particle, called the self-intermediate scattering function:

$$F_S(\mathbf{q},t;\kappa) = \frac{1}{(N-1)!}\int e^{i\mathbf{k}\cdot\mathbf{x}_1(t)}\hat{P}_N(\mathbf{x}^N(t))\,d\mathbf{x}^N(t) - \delta\left[(\mathbf{I}-\mathbf{e}_3\mathbf{e}_3)\cdot\mathbf{k}\right]G(\mathbf{e}_3\cdot\mathbf{k})\bar{G}(\mathbf{e}_3\cdot\mathbf{k}). \tag{7.13}$$

The intermediate scattering function then can be written as

$$F(\mathbf{q},t;\kappa) = F_S(\mathbf{q},t;\kappa) + \frac{1}{(N-2)!}\int e^{i\mathbf{k}\cdot\mathbf{x}_2(t)}\hat{P}_N(\mathbf{x}^N(t))\,d\mathbf{x}^N(t). \tag{7.14}$$

In the limit that $t \to 0$, the probability density $\hat{P}_N(\mathbf{x}^N(t))$ becomes

$$\hat{P}_N^0(\mathbf{x}^N(t)) = \int \delta(\mathbf{x}^N(t)-\mathbf{x}^N(0))e^{-i\bar{\mathbf{k}}\cdot\mathbf{x}_1(0)}P_N^0(\mathbf{x}^N(0))\,d\mathbf{x}^N(0), \tag{7.15}$$

where we have made the substitution $P_N(\mathbf{x}^N(t)|\mathbf{x}^N(0)) = \delta(\mathbf{x}^N(t)-\mathbf{x}^N(0))$ as t approaches zero. Therefore, we write the self-intermediate scattering function at $t=0$ as:

$$F_S(\mathbf{q},0;\kappa) = \frac{1}{(N-1)!}\int e^{-\kappa\mathbf{e}_3\cdot\mathbf{x}_1(0)}P_N^0(\mathbf{x}^N(0))\,d\mathbf{x}^N(0) - \delta\left[(\mathbf{I}-\mathbf{e}_3\mathbf{e}_3)\cdot\mathbf{k}\right]G(\mathbf{e}_3\cdot\mathbf{k})\bar{G}(\mathbf{e}_3\cdot\mathbf{k}), \tag{7.16}$$

and the intermediate scattering function at $t=0$ as:

$$F(\mathbf{q},0;\kappa) = F_S(\mathbf{q},0;\kappa) + \frac{1}{(N-2)!}\int e^{i\mathbf{k}\cdot(\mathbf{x}_2(0)-\mathbf{x}_1(0))-\kappa\mathbf{e}_3\cdot\mathbf{x}_1(0)}P_N^0(\mathbf{x}^N(0))\,d\mathbf{x}^N(0). \tag{7.17}$$

Recognize that the integrand of the zero-time self-intermediate scattering function is a probability density weighted by the exponential decay of the evanescent wave. We can see this more clearly be rewriting it as:

$$F_S(\mathbf{q},0;\kappa) = \int e^{-\kappa\mathbf{e}_3\cdot\mathbf{x}_1(0)}P_1^0(\mathbf{x}_1(0))d\mathbf{x}_1(0) - \delta\left[(\mathbf{I}-\mathbf{e}_3\mathbf{e}_3)\cdot\mathbf{k}\right]G(\mathbf{e}_3\cdot\mathbf{k})\bar{G}(\mathbf{e}_3\cdot\mathbf{k}), \tag{7.18}$$

where $P_1^0(\mathbf{x}_1(0))$ is the probability of finding a particle at location $\mathbf{x}_1(0)$ initially. This is calculated by averaging the initial density over the positions of the other $N-1$ particles, *viz.*

$$P_1^0(\mathbf{x}_1(0)) = \frac{1}{(N-1)!}\int P_N^0(\mathbf{x}^N(0))d\mathbf{x}^{N-1}(0). \tag{7.19}$$

Similarly, the zero-time intermediate scattering function is:

$$F(\mathbf{q},0;\kappa) = F_S(\mathbf{q},0;\kappa) + \int e^{i\mathbf{k}\cdot(\mathbf{x}_2(0)-\mathbf{x}_1(0))-\kappa\mathbf{e}_3\cdot\mathbf{x}_1(0)} P_2^0(\mathbf{x}_1(0),\mathbf{x}_2(0))\, d\mathbf{x}_1(0)\, d\mathbf{x}_2(0), \tag{7.20}$$

where $P_2^0(\mathbf{x}_1(0),\mathbf{x}_2(0))$ is the probability of finding a pair of particles at positions $\mathbf{x}_1(0)$ and $\mathbf{x}_2(0)$ initially such that:

$$P_2^0(\mathbf{x}_1(0),\mathbf{x}_2(0)) = \frac{1}{(N-2)!}\int P_N^0(\mathbf{x}^N(0))d\mathbf{x}^{N-2}(0). \tag{7.21}$$

Were this conventional light scattering ($\kappa \to 0$), we would recognize the quantity $F(\mathbf{q},0;0)$ as the static structure factor ($S(\mathbf{q})$); however, because this is the correlation of scattering by an evanescent wave, the integrand of the static structure factor is mediated by an exponential decay. These static quantities are measurements of the configuration of the scattering particles only and contain no information about their dynamic behavior. Here, we redesignate the zero-time intermediate scattering function as the evanescent static structure factor and denote it $S(\mathbf{q},\kappa)$.

Consider now, the time derivative of the self-intermediate scattering function:

$$\frac{\partial}{\partial t}F_S(\mathbf{q},t;\kappa) = \frac{1}{(N-1)!}\int e^{i\mathbf{k}\cdot\mathbf{x}_1(t)}\frac{\partial \hat{P}_N(\mathbf{x}^N(t))}{\partial t}\, d\mathbf{x}^N(t). \tag{7.22}$$

To describe this quantity further we require information about how the conditional probability density changes as a function of time. This can be obtained from the N-particle Smoluchowski equation:

$$\frac{\partial P_N(\mathbf{x}(t)|\mathbf{x}(0))}{\partial t} + \sum_{\alpha=1}^{N}\nabla_{\mathbf{x}_\alpha(t)}\cdot\mathbf{j}_\alpha = 0, \tag{7.23}$$

where $\mathbf{j}_\alpha$ is the flux of probability density associated with the inter-particle and thermal forces on particle α

given by:

$$\mathbf{j}_\alpha = \sum_{\beta=1}^{N} \mathbf{M}_{\alpha\beta} \cdot \left(\mathbf{F}_\beta^P - kT \nabla_{\mathbf{x}_\beta(t)} \log P_N(\mathbf{x}^N(t)|\mathbf{x}^N(0)) \right) P_N(\mathbf{x}^N(t)|\mathbf{x}^N(0)). \tag{7.24}$$

Here, $\mathbf{M}_{\alpha\beta}$ is the mobility tensor coupling forces on particle β to the motion of particle α in the presence of the wall, $\mathbf{F}_\beta^P$ is the inter-particle force on particle β due to non-hydrodynamic interactions with other particles and the wall and kT is the thermal energy (a shearing motion could also be added to $\mathbf{F}_\beta^P$). The mobility tensor is a purely geometric quantity that describes the motion of the particles in the fluid domain bounded by the wall. The additional resistance and hydrodynamic screening associated with particle motion in bounded geometries is included explicitly in these terms. Multiplying these expressions by $\exp(-i\bar{\mathbf{k}} \cdot \mathbf{x}_1(0)) P_N^0(\mathbf{x}^N(0))$ and integrating over the initial configuration allows us to write down a differential equation for the modified probability density:

$$\begin{aligned} \frac{\partial \hat{P}_N(\mathbf{x}^N(t))}{\partial t} &= -\sum_{\alpha=1}^{N} \nabla_{\mathbf{x}_\alpha(t)} \cdot \hat{\mathbf{j}}_\alpha \qquad (7.25) \\ &= -\sum_{\alpha,\beta=1}^{N} \nabla_{\mathbf{x}_\alpha(t)} \cdot \mathbf{M}_{\alpha\beta} \cdot \Big(\mathbf{F}_\beta^P - kT \nabla_{\mathbf{x}_\beta(t)} \log \hat{P}_N(\mathbf{x}^N(t)) \Big) \hat{P}_N(\mathbf{x}^N(t)). \end{aligned}$$

Substituting this into equation 7.22 and integrating by parts and noting that the flux of the particles decays to zero far away (and at particle-particle or particle-wall contact) yields:

$$\frac{\partial}{\partial t} F_S(\mathbf{q}, t; \kappa) = \frac{1}{(N-1)!} \int e^{i\mathbf{k} \cdot \mathbf{x}_1(t)} i\mathbf{k} \cdot \hat{\mathbf{j}}_1 \, d\mathbf{x}^N(t). \tag{7.26}$$

A similar set of manipulations allows us to write the time derivative of the intermediate scattering function as:

$$\frac{\partial}{\partial t} F(\mathbf{q}, t; \kappa) = \frac{\partial}{\partial t} F_S(\mathbf{q}, t; \kappa) + \frac{1}{(N-2)!} \int e^{i\mathbf{k} \cdot \mathbf{x}_2(t)} i\mathbf{k} \cdot \hat{\mathbf{j}}_2 \, d\mathbf{x}^N(t). \tag{7.27}$$

Consider the initial values of the fluxes $\hat{\mathbf{j}}_1$ and $\hat{\mathbf{j}}_2$. If we assert that the suspension was initially in equilibrium such that

$$P_N^0(\mathbf{x}^N(0)) \sim P_N^{eq} \sim e^{-V/kT}, \tag{7.28}$$

where P_N^{eq} is the equilibrium probability density (adjacent to the wall) and $\mathbf{F}_\beta = -\nabla_{\mathbf{x}_\beta} V$, then we can show quite naturally that the zero-time fluxes must be:

$$\hat{\mathbf{j}}_1\Big|_{t=0} = ikT\mathbf{M}_{11} \cdot \bar{\mathbf{k}}\hat{P}_N^0(\mathbf{x}^N(0)), \tag{7.29}$$

and

$$\hat{\mathbf{j}}_2\Big|_{t=0} = ikT\mathbf{M}_{21} \cdot \bar{\mathbf{k}}\hat{P}_N^0(\mathbf{x}^N(0)). \tag{7.30}$$

Therefore, by writing the usual zero-time scattering function operation – the time derivative of the logarithm of the scattering autocorrelation – we find that for the self-intermediate scattering function,

$$\frac{\partial}{\partial t}\log F_S(\mathbf{q}, 0; \kappa) = -\frac{\int \mathbf{k} \cdot \mathbf{D}_{11} \cdot \bar{\mathbf{k}} e^{-\kappa \mathbf{e}_3 \cdot \mathbf{x}_1(0)} P_N^0(\mathbf{x}^N(0))\, d\mathbf{x}^N(0)}{\int e^{-\kappa \mathbf{e}_3 \cdot \mathbf{x}_1(0)} P_N^0(\mathbf{x}^N(0))\, d\mathbf{x}^N(0)}, \tag{7.31}$$

where we have substituted the diffusivity for the mobility: $\mathbf{D} = kT\mathbf{M}$. We recognize that this is the form of the single particle diffusivity measured in the dilute limit by Holmqvist, Dhont and Lang (2006) via a cumulant expansion; however, our more general expression represents a weighted measure of the short-time self-diffusivity of particles in the vicinity of a plane wall interface. This reflects an "evanescent-mean" short-time self-diffusivity which depends on the volume fraction of the particles, the orientation of the scattering wave vector and the penetration depth.

It is more natural to express this mean diffusivity in terms of parallel and perpendicular diffusivites:

$$D_0^S(\phi, \mathbf{q}, \kappa) = -\frac{1}{\mathbf{k} \cdot \bar{\mathbf{k}}}\frac{\partial}{\partial t}\log F_S(\mathbf{q}, 0; \kappa) = \frac{q_\parallel^2 \left\langle D_\parallel^S \right\rangle + \left(q_\perp^2 + \frac{\kappa^2}{4}\right)\left\langle D_\perp^S \right\rangle}{q_\parallel^2 + q_\perp^2 + \frac{\kappa^2}{4}}, \tag{7.32}$$

where $\mathbf{q}\cdot\mathbf{q} = q_{\|}^2 + q_{\perp}^2$, $q_{\perp} = \mathbf{q}\cdot\mathbf{e_3}$,

$$D_{\|}^S(\phi,\kappa) = \frac{\int \mathbf{D}_{11} : (\mathbf{I} - \mathbf{e}_3\mathbf{e}_3) e^{-\kappa \mathbf{e}_3\cdot\mathbf{x}_1(0)} P_N^0(\mathbf{x}^N(0))\, d\mathbf{x}^N(0)}{\int e^{-\kappa \mathbf{e}_3\cdot\mathbf{x}_1(0)} P_N^0(\mathbf{x}^N(0))\, d\mathbf{x}^N(0)}, \tag{7.33}$$

and

$$D_{\perp}^S(\phi,\kappa) = \frac{\int \mathbf{D}_{11} : \mathbf{e}_3\mathbf{e}_3 e^{-\kappa \mathbf{e}_3\cdot\mathbf{x}_1(0)} P_N^0(\mathbf{x}^N(0))\, d\mathbf{x}^N(0)}{\int e^{-\kappa \mathbf{e}_3\cdot\mathbf{x}_1(0)} P_N^0(\mathbf{x}^N(0))\, d\mathbf{x}^N(0)}. \tag{7.34}$$

Note carefully that the component of the parallel diffusivity is written in terms of the parallel dyads of $\mathbf{D}_{11}$ (proportional to $\mathbf{I} - \mathbf{e}_3\mathbf{e}_3$), which assumes that the suspension structure and hydrodynamics are transversely isotropic. This result again matches with that of Holmqvist, Dhont and Lang (2006), but the diffusivities parallel and perpendicular to the wall are now averaged over the positions of all the particles and not just the scattering test particle. In the dilute limit, $\phi \to 0$, the initial probability density $P_N^0(\mathbf{x}^N(0))$ is such that the positions of all the particles are completely uncorrelated, subject to the requirement that the particles must reside above the plane wall. We are hardly restricted to this limit however, and the above expression is valid over the entire range of volume fractions. Thus, we can probe not just the single particle diffusivity, but the short-time self-diffusivity of one particle immersed in a sea of other particles at any concentration.

Similarly, the time derivative of the logarithm of the intermediate scattering function becomes:

$$\begin{aligned}\frac{\partial}{\partial t}\log F(\mathbf{q},0;\kappa) = -\frac{1}{(N-1)!F(\mathbf{q},0;\kappa)} \int \mathbf{k}\cdot\left[\mathbf{D}_{11} + (N-1)\mathbf{D}_{21} e^{i\mathbf{k}\cdot(\mathbf{x}_2(0)-\mathbf{x}_1(0))}\right]\cdot\bar{\mathbf{k}} \\ \times e^{-\kappa \mathbf{e}_3\cdot\mathbf{x}_1(0)} P_N^0(\mathbf{x}^N(0))\, d\mathbf{x}^N(0).\end{aligned} \tag{7.35}$$

This naturally leads to a description of what is termed the wave vector dependent diffusivity, D, which is a function of the wave vector, the volume fraction and the penetration length. Again, this differs from conventional light scattering in the sense that this is an “evanescent-mean” diffusivity, which is an exponentially weighted average of the self and inter-particle mobilities of particles at different distances from the interface.

We write down this diffusivity explicitly as:

$$D(\phi,\mathbf{q},\kappa) = -\frac{1}{\mathbf{k}\cdot\bar{\mathbf{k}}}\frac{\partial}{\partial t}\log F(\mathbf{q},0;\kappa) = \frac{q_\parallel^2\left\langle D_*\right\rangle + \left(q_\perp^2+\frac{\kappa^2}{4}\right)\left\langle D_\perp\right\rangle}{q_\parallel^2+q_\perp^2+\frac{\kappa^2}{4}}, \tag{7.36}$$

where

$$D_*(\phi,\mathbf{q},\kappa) = \frac{1}{(N-1)!F(\mathbf{q},0;\kappa)}\int\left[\mathbf{D}_{11}+(N-1)\mathbf{D}_{21}e^{i\mathbf{k}\cdot(\mathbf{x}_2(0)-\mathbf{x}_1(0))}\right] : \left(\mathbf{k}\bar{\mathbf{k}} - \left(q_\perp^2+\frac{\kappa^2}{4}\right)\mathbf{e}_3\mathbf{e}_3\right)\frac{1}{q_\parallel^2} \tag{7.37}$$

$$\times\, e^{-\kappa\mathbf{e}_3\cdot\mathbf{x}_1(0)}P_N^0(\mathbf{x}^N(0))\,d\mathbf{x}^N(0),$$

and

$$D_\perp(\phi,\mathbf{q},\kappa) = \frac{1}{(N-1)!F(\mathbf{q},0;\kappa)}\int\left[\mathbf{D}_{11}+(N-1)\mathbf{D}_{21}e^{i\mathbf{k}\cdot(\mathbf{x}_2(0)-\mathbf{x}_1(0))}\right] : \mathbf{e}_3\mathbf{e}_3 \tag{7.38}$$

$$\times\, e^{-\kappa\mathbf{e}_3\cdot\mathbf{x}_1(0)}P_N^0(\mathbf{x}^N(0))\,d\mathbf{x}^N(0).$$

In conventional light scattering, the collective diffusivity is recovered in the limit that $\mathbf{q}\to 0$. Applying the same limit here yields the following near-wall collective diffusivity

$$D_0^C(\phi,\kappa) = \int\left[\mathbf{D}_{11}e^{-\kappa\mathbf{e}_3\cdot\mathbf{x}_1(0)}+(N-1)\mathbf{D}_{21}e^{-\frac{\kappa}{2}\mathbf{e}_3\cdot(\mathbf{x}_2(0)+\mathbf{x}_1(0))}\right] : \mathbf{e}_3\mathbf{e}_3 P_N^0(\mathbf{x}^N(0))\,d\mathbf{x}^N(0) \tag{7.39}$$

$$\Bigg/\left\{\int\left[e^{-\kappa\mathbf{e}_3\cdot\mathbf{x}_1(0)}+(N-1)e^{-\frac{\kappa}{2}\mathbf{e}_3\cdot(\mathbf{x}_2(0)+\mathbf{x}_1(0))}\right]P_N^0(\mathbf{x}^N(0))\,d\mathbf{x}^N(0) - G\left(\frac{i\kappa}{2}\right)\bar{G}\left(\frac{i\kappa}{2}\right)\right\},$$

which measures the collective hydrodynamics of a suspension but only in the direction normal to the wall. The evanescent wave is unable to recover information about the parallel wall dynamics in the zero scattering angle limit because the decaying intensity of the scattered wave screens out the correlation of any in-plane density fluctuations. Effectively, the averaged hydrodynamics parallel to the wall are $O(\mathbf{q})$ and small, and so they make no measurable contribution as they are overwhelmed by perpendicular fluctuations. The collective diffusivity measured by evanescent wave spectroscopy is a sum of the self-diffusivity contribution ($\mathbf{D}_{11}$) weighted exponentially by the distance of a single particle from the wall and the inter-particle contribution ($\mathbf{D}_{21}$) weighted exponentially by the mean distance of any two particles from the wall. In the limit that $\kappa \to 0$ we see that indeed, the typical collective diffusivity is recovered as expected.

Equations (7.33), (7.34) and (7.39) are new statistical descriptions of what is measured in dynamic light scattering experiments utilizing evanescent waves. These expressions also have the same form as those introduced by Brady (1994) for conventional dynamic light scattering. Namely, they represent the ratio of a hydrodynamic quantity (a weighted average of $\mathbf{D}$) to a thermodynamic quantity (a structure factor). The difference here is the introduction of an exponential weighting to the averages brought on by decay of the evanescent wave. These expressions are valid over the whole range of volume fractions, and can be used to interrogate directly the results of EWDLS experiments on bounded particles for near-wall diffusivities as well as the results of computational simulations of systems with analogous particles and geometries. Of course, the ideal system for study would be an infinite suspension above a single solid wall. However, this is difficult to model as the suspension is aperiodic. Instead, we simulate particles in a parallel wall channel knowing that in the limit that the separation between the channel walls becomes large this approximates the single wall system.

7.2.2 Simulation methods

We simulate a periodic suspension of particles bounded from above and below by two impenetrable, parallel plates which are infinite in extent (see figure 7.2). In the following, we briefly describe the Stokesian dynamics method and refer the reader to more detailed articles when the computational material is beyond the current purview.

For a collection of small colloidal particles of negligible Stokes number ($St = Re\rho_p/\rho_f$), where Re is the Reynolds number, ρ_p is the density of the particles and ρ_f is the density of the fluid), the sum of the forces

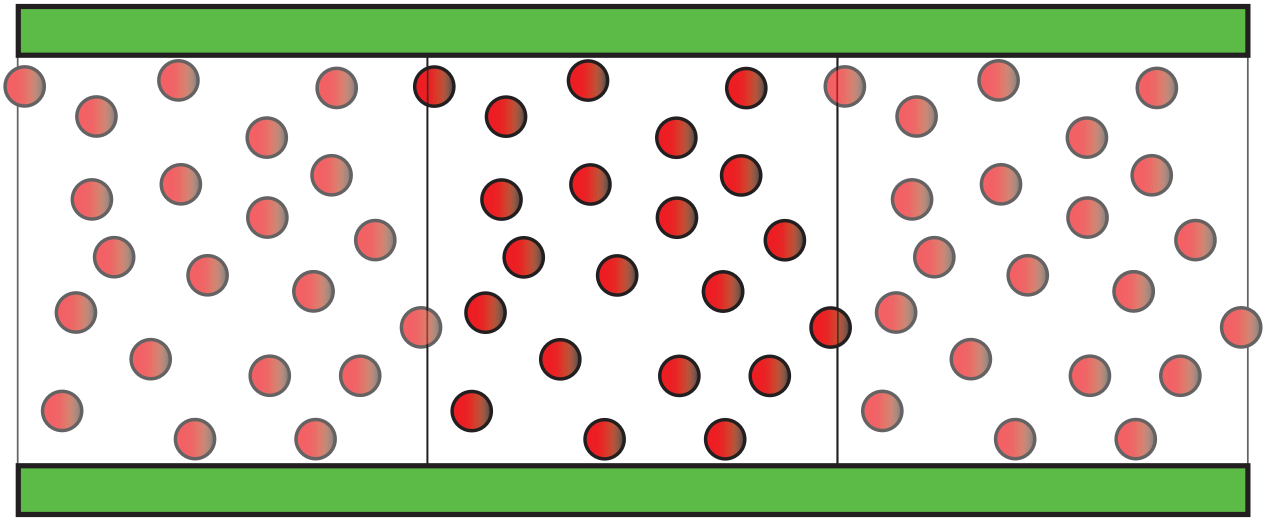

Figure 7.2: The periodic simulation cell with particles fixed along the bottom and representing both the top and bottom walls of a channel.

on the particles are approximately equal to zero, *viz.*

$$0 = \mathbf{F}_h + \mathbf{F}_p, \tag{7.40}$$

where F_h is the hydrodynamic force on the particles and F_p is any other force on the particles (*e.g.* Brownian forces and gravitation).

As the hydrodynamic force on the particles is related linearly to the particle velocities, the key element of all low-Reynolds number hydrodynamic simulations is the calculation of this linear couple, the so-called resistance tensor, $\mathbf{R}_{FU}$ or its inverse, the diffusivity: $\mathbf{D} = kT\mathbf{R}_{FU}^{-1}$. One method of computing this linear couple, the Stokesian dynamics technique [see *e.g.* Durlofsky and Brady (1987)], separates the hydrodynamic interactions into two classes: near-field and far-field. In the near-field, the hydrodynamic forces required for relative motion of particles in the fluid are asymptotically large and therefore the interactions can be treated as pair-wise. In the far-field, however, the hydrodynamic interactions are long-ranged (scaling like r^{-2} in the presence of a macroscopic boundary, where r is the distance between particles). As such, the hydrodynamic interactions are many bodied. The Stokesian dynamics technique determines two sets of forces due to the near- and far-fields, respectively, subject to the constraint that the resulting rigid body motion of the particles is consistent with both sets of forces. The details are beyond the purview of this chapter; however, the work by Seirou and Brady (2001) is comprehensive in its development of the method for unbounded systems. Similarly, we refer the reader to the companion paper by Swan and Brady (2010) which describes in detail the modeling of the hydrodynamic interactions among many particles in a suspension between macroscopic boundaries. Additionally, this chapter describes an accelerated Stokesian dynamics technique for computing these interactions with $O(N \log N)$ computations. This is quite rapid given the long-ranged nature of hydrodynamic interactions.

With this approach, we are free to explore the diffusive motion of particles confined between parallel walls in the short time limit. As we intend to use EWDLS to measure the dynamics of the suspension between the walls, a full range of penetration depths may be employed. However, for practical reasons it makes sense to only consider penetration depths smaller than $H/2$, where H is the width of the channel so that we only probe the dynamics near the walls and over only half the channel. This provides an opportunity to actually multiplex the data by considering the hypothetical situation where evanescent waves originate from both the top and bottom walls of the channel.

7.2.3 Measurement techniques

Using the simulation techniques described in the previous section, we seek to determine the evanescent short-time self- and collective diffusivities of a dispersion bound between a pair of walls. This can be accomplished using both static and dynamic measurements which we will proceed to describe. The resultant data, however, represents completely new results which quantify the anisotropic dynamics of bounded suspensions. We describe the dynamic measurement technique though we do not employ it here as it measures the same quantities but is more computationally intensive.

7.2.3.1 Static measurements

A static measurement of the evanescent short-time diffusivity is made by considering the averages in equations (7.33), (7.34) and (7.39) as ensemble averages of the particle velocities due to forces proportional to the evanescent exponential in each respective case. For instance, $D_{\|}^S(\phi,\kappa)$ is the ensemble average of the velocity of one particle parallel to the wall due to a force on that particle *only* in that same direction and of magnitude $\exp(-\kappa z)$ divided by the average of $\exp(-\kappa z)$ where z is the height of the particle above the wall, *viz.*

$$D_{\|}^S(\phi,\kappa) = kT\left\langle \mathbf{e}_1 \cdot \mathbf{M}_{11} \cdot \mathbf{e}_1 \frac{e^{-\kappa z}}{\langle e^{-\kappa z}\rangle} \right\rangle . \tag{7.41}$$

A similar physical interpretation can be developed for $D_{\perp}^S(\phi,\kappa)$ such that

$$D_{\perp}^S(\phi,\kappa) = kT\left\langle \mathbf{e}_3 \cdot \mathbf{M}_{11} \cdot \mathbf{e}_3 \frac{e^{-\kappa z}}{\langle e^{-\kappa z}\rangle} \right\rangle . \tag{7.42}$$

The products $\mathbf{M}_{11} \cdot \mathbf{e}_1 \exp(-\kappa z)/\left\langle \exp(-\kappa z)\right\rangle$ and $\mathbf{M}_{11} \cdot \mathbf{e}_3 \exp(-\kappa z)/\left\langle \exp(-\kappa z)\right\rangle$ are easy to simulate using the methods we described above. One simply proposes that a particle in a particular configuration is forced either parallel or perpendicular to the wall with the appropriate magnitude and then measures the velocity of that particle in the same direction. This calculation is repeated for all the particles in the configuration and the results are averaged. Other configurations are generated since the simulations are finite in size and the same results for all configurations are combined to form the ensemble average.

This approach requires N inversions per configuration and is quite slow. However, we can multiplex the data recovered from a single inversion by appealing to a stochastic technique similar to the one developed in Seirou and Brady (2001). Let ξ_i be a random vector such that $\langle \xi_i \xi_j \rangle = \delta_{ij}$. Then apply a force to each particle such that particle i is forced with magnitude $\xi_i \exp(-\kappa z_\alpha/2)$ in the $\mathbf{e}_3$ direction. We denote this force on the particles as $\boldsymbol{\Xi}$ and recognize that the perpendicular short time self-diffusivity is simply

$$D_{\perp}^S(\phi,\kappa) = kT\frac{\left\langle \boldsymbol{\Xi} \cdot \mathbf{R}_{FU}^{-1} \cdot \boldsymbol{\Xi} \right\rangle}{\left\langle \boldsymbol{\Xi} \cdot \boldsymbol{\Xi} \right\rangle}, \tag{7.43}$$

where the ensemble average is now over configurations and instantiations of the randomly distributed forces. A similar expression for $D_{\|}^S(\phi,\kappa)$ can be developed if all the forces are in the $\mathbf{e}_1$ direction.

By analogy with the previous expression, consider what happens when the forces on the particles have magnitude $\xi \exp(-\kappa z_i/2)$, where ξ is a randomly distributed variable with mean square of one. If the forces all point in the $\mathbf{e}_3$ direction, then the short-time collective diffusivity may be written in exactly the same manner, *viz.*

$$D_0^C(\phi, \kappa) = kT \frac{\langle \mathbf{\Xi} \cdot \mathbf{R}_{FU}^{-1} \cdot \mathbf{\Xi} \rangle}{\langle \mathbf{\Xi} \cdot \mathbf{\Xi} \rangle}, \tag{7.44}$$

where $\mathbf{\Xi}$ is the collection of the forces weighted by ξ. These are remarkable results which demonstrate how flexible the light scattering approach to colloid dynamics can be. The evanescent wave samples the suspension as though it were a series of forces $(\mathbf{\Xi}/\sqrt{\langle \mathbf{\Xi} \cdot \mathbf{\Xi} \rangle})$ of precisely the right magnitude to yield these particular self- and collective motions of particles. This physical interpretation can be applied to DLS as well, but it is surprising that it translates so directly to EWDLS. Interestingly, the radiation pressure exerted by the scattered light is proportional to $\mathbf{q} \exp(i\mathbf{k} \cdot \mathbf{x})$. Therefore, while this approach has decomposed the directionality of the scattering, it can be interpreted as measuring the response of the particle to the forcing from radiation pressure. While the scattering may be isotropic so that no net force is imposed on the particle, from a ray-optic perspective, there is indeed a force and the correlated response to that force is the diffusivity. In that way, light-scattering may be thought of as an experimental implementation of the ideas behind the fluctuation-dissipation theorem.

7.2.3.2 Dynamic measurements

Given that the Brownian trajectories of the particles are known, we seek to measure the intermediate scattering function for a given penetration depth and through that, the evanescent diffusivities. To that end, we are free to choose an evanescent wave vector that will suit our purposes, and because the intermediate scattering function at short times is a convolution of the parallel and perpendicular diffusivities, we must select two independent wave vectors. Since the collective diffusivity comes from the $\mathbf{q} \to 0$ limit of the scattering function, we choose $\mathbf{q} = 0$. This also allows for the direct computation of $D_\perp^S(\phi, \kappa)$. To measure $D_\parallel^S(\phi, \kappa)$, any other non-zero value of $q_\parallel$ will suffice. Therefore, we choose $q_\parallel = 1$ and $q_\perp = 0$. With these particular values for the wave vector, one may perform dynamic simulations or experiments and compute the following averages using the known trajectories of particles α and β, $\mathbf{x}_\alpha(t)$ and $\mathbf{x}_\beta(t)$ respectively,

$$F_S(0,t;\kappa) = \left\langle \sum_{\alpha=1}^{N} e^{-\frac{\kappa}{2}\mathbf{e}_3\cdot[\mathbf{x}_\alpha(t)+\mathbf{x}_\alpha(0)]} \right\rangle, \tag{7.45}$$

$$F_S(\mathbf{e}_1,t;\kappa) = \left\langle \sum_{\alpha=1}^{N} e^{i\mathbf{e}_1\cdot[\mathbf{x}_\alpha(t)-\mathbf{x}_\alpha(0)]-\frac{\kappa}{2}\mathbf{e}_3\cdot[\mathbf{x}_\alpha(t)+\mathbf{x}_\alpha(0)]} \right\rangle, \tag{7.46}$$

and

$$F(0,t;\kappa) = \left\langle \sum_{\alpha,\beta=1}^{N} e^{-\frac{\kappa}{2}\mathbf{e}_3\cdot[\mathbf{x}_\alpha(t)+\mathbf{x}_\beta(0)]} \right\rangle. \tag{7.47}$$

Clearly the time derivative of the logarithm of these functions at $t = 0$ are the evanescent diffusivities. For conventional light scattering, the same procedures apply, though only one scattering wave vector is needed since the hydrodynamics and structure of a bulk suspension with volume fraction less than 0.55 are isotropic. Similarly, because the pair hydrodynamic interactions are conditionally convergent, the usual process of extrapolating the initial slope of the intermediate scattering function as $\mathbf{q} \to 0$ is unnecessary [see *e.g.* Leshansky and Brady (2004)]. This quantity is directly measurable.

7.3 Results

Simulations on suspensions of volume fractions between ten and forty percent volume fraction were studied in channels of twelve particle radii in width. Equilibrium configurations of particles were generated via a Monte Carlo method for volume fractions up to thirty percent and via a molecular dynamics algorithm [see *e.g.* Donev, Stillinger and Torquato (2005)] for more dense systems. In the region near the walls, the dynamics of a suspension are largely governed by lubrication interactions corresponding to the drag induced by the wall itself. These hinder the suspension asymptotically such that the self-diffusivity of a particle near a wall scales at its slowest like $\mathbf{e}_3 \cdot \mathbf{x}_\alpha - 1$. Here, there is a weak dependence of the hydrodynamics on the channel width. In the results following, the penetration depth is such that the bulk of the suspension sampled is in this near wall region (*i.e.* $\kappa H/2 > 1$). Therefore, the effect of the channel width on the hydrodynamics is minimal (no more than ten percent as determined by comparison of results from larger channels). Similarly, the near wall structure has a weak dependence on the channel width for the volume fractions studied. We avoided volume fractions larger than forty percent because in unbounded colloidal dispersions there is a phase boundary at which the suspension would crystallize were it only ten percent more concentrated. The confinement introduces ordering which may propagate via this same mechanism throughout the channel. While the theory and simulations may be used for any channel width and volume fraction, those chosen for this study are appropriate for a model of the single wall system. The reason for this choice is two-fold: first, the diffusivity computed via simulation of periodic suspensions (bounded or unbounded) has a strong dependence on the periodic wavelength. It was observed that in channels an aspect ratio of at least two-to-one wavelength to channel width is necessary to get within five percent of the diffusivity in an aperiodic suspension. As such, the number of particles simulated (between 300 and 800) is such that the simulation cell always exceeds this aspect ratio. For reference, 200 realizations of equilibrium suspension configurations were used in computing the average diffusivities presented. The ninety-five percent confidence interval associated with these samples was always smaller than eight percent of the measured value. Error bars are omitted from the figures for clarity, though a confidence interval of eight percent defines a very narrow envelope around each data set.

In the limit of large scattering wave vector the initial slope of the intermediate scattering function is the short-time self-diffusivity. In figure 7.4, this is plotted for various values of penetration depth and volume fraction. Because of the nearby wall, the diffusivity is anisotropic, and the components parallel and perpendicular to the channel wall are distinct. In this case, and for all volume fractions, the near-wall region is dominated by the lubrication interactions between the particle and the walls. Therefore, the expectation is that the parallel short-time self diffusivity will scale as $\log(\kappa a)$ and $(\kappa a)^{-1}$ in the limit that $\kappa a \to \infty$ for the parallel and perpendicular components respectively. This expectation holds for all volume fractions studied though the coefficient of proportionality varies.

Consider that the self-diffusivity can be computed via direct simulation or observed via optical microscopy as a function of the distance from a wall by measuring the mean force required to move any particle in the

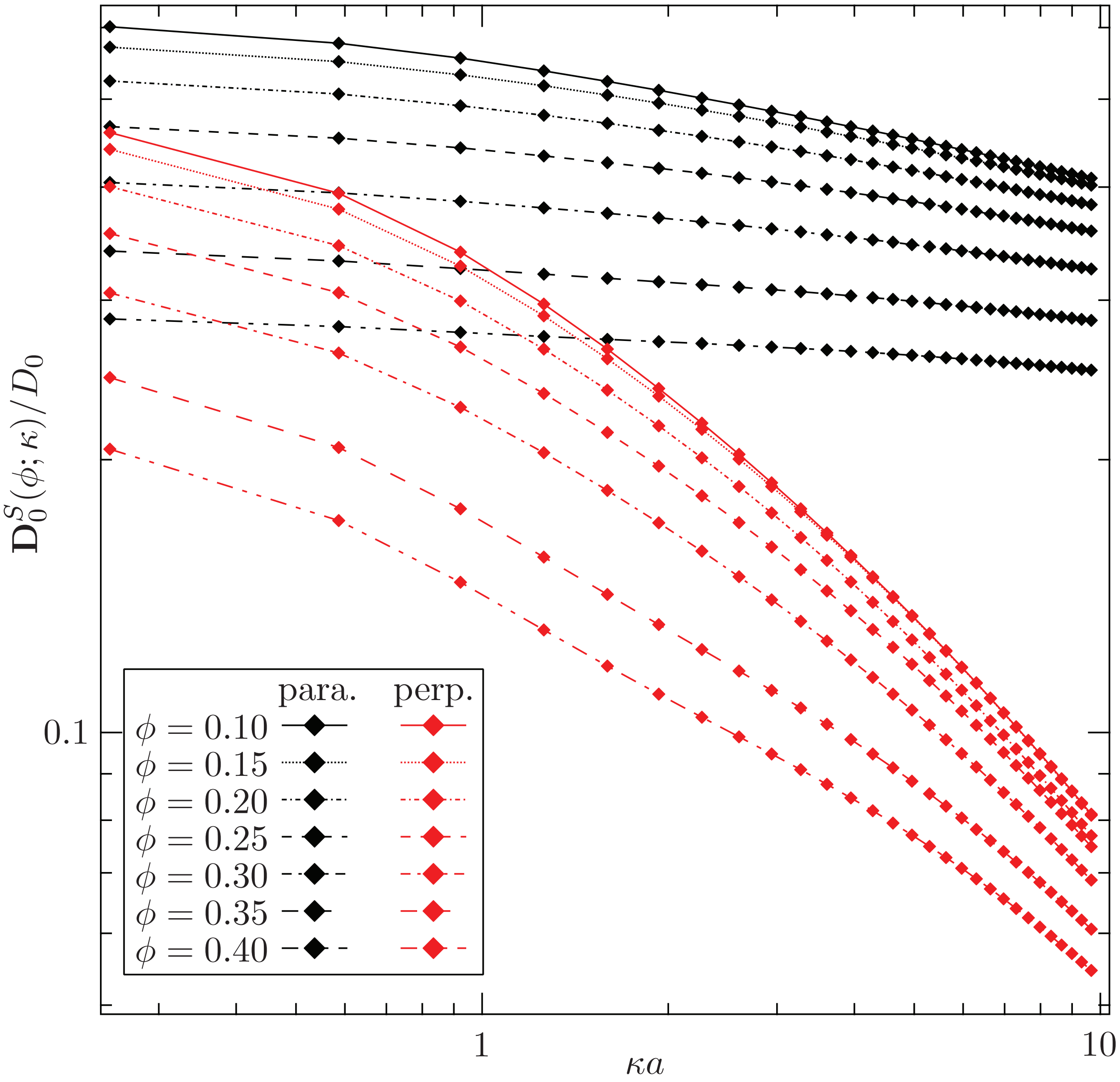

Figure 7.3: The evanescent short-time self-diffusivity parallel and normal to the bounding wall plotted as a function of the penetration depth and bulk suspension volume fraction. These are the result of simulations in a channel which is twelve radii in width. It has been shown that the effect of a finite channel width on both the structure and the self-diffusivity is minimal for this range of volume fractions [see *e.g.* Swan and Brady (2010)].

suspension a short distance. The ratio of the particle velocity to the force applied is the diffusivity which must be averaged conditionally with respect to that particle's position in the channel *i.e.*

$$\bar{\mathbf{D}}_0^S(\phi, h) = \frac{1}{(N-1)!} \int \mathbf{D}_{11} P_N^0(\mathbf{x}^N(0) | x_3^1(0) = h) \, d\mathbf{x}^{N-1}(0) \, dx_1^1(0) \, dx_2^1(0), \tag{7.48}$$

where h is the distance from the wall. The evanescent diffusivity is simply

$$\mathbf{D}_0^S(\phi, \kappa) = \int \bar{\mathbf{D}}_0^S(\phi, h) \exp(-\kappa h) n(\phi, h) \, dh \Bigg/ \int \exp(-\kappa h) n(\phi, h) \, dh, \tag{7.49}$$

where $n(\phi, h)$ is the number density distribution of the suspension near the wall. This transformation allows for the direct comparison of short-time self-diffusivities measured via evanescent wave dynamic light scattering and optical microscopy. Note that extremes in the number density have a deceiving effect on the evanescent wave short-time self-diffusivity as it is in the numerator and denominator of the above expression and would appear to irrelevant. Instead, extremum in the density (for instance at higher volume fractions) heavily weight the diffusivity with respect to the layering of particles known to occur near a wall. That is, the diffusivity is sampled preferentially at positions very near contact with the wall, in the region where the second layer of particles forms, *etc.*

As the volume fraction increases and especially for the component of the self-diffusivity parallel to the wall, notice that there is little variation in the diffusivity for large penetration depths. In fact, for more dilute systems, we expect the evanescent self-diffusivity to scale as,

$$\mathbf{D}_0^S(\phi, \kappa) \approx D_0^S(\phi) \left[\mathbf{I} + \frac{9}{16} \kappa \left(\gamma + \log(\kappa) \right) \left(\mathbf{I} + \mathbf{e}_3 \mathbf{e}_3 \right) \right] + O(\kappa^2) \tag{7.50}$$

where $\gamma \approx 0.57722$ is the Euler-Mascheroni constant. We have assumed the well known far-field form of the single particle mobility in the presence of a wall is valid ($\mathbf{M}_{11} = (6\pi\eta a)^{-1}[\mathbf{I} - 9/16 h^{-1}(\mathbf{I} + \mathbf{e}_3\mathbf{e}_3])$ and that far from the wall, the uniform, bulk microstructure persists. The additional hindrance beyond the Stokes drag in the direction parallel to the wall is half that in the normal direction. In this case, $D_0^S(\phi)$ is the short-time self-diffusivity of the bulk. Ideally, as $\kappa \rightarrow 0$, the evanescent self-diffusivity should approach this bulk value. This scaling provides an opportunity to examine the impact of a finite channel width on the measurement. Indeed, we find that equation 7.50 is an overestimate of the self-diffusivity in a channel as the presence of the second wall introduces an additional hindrance which scales like a/H. The factor $9/16$ is the culprit and should change to reflect the presence of the second wall. Similarly, the ratio of parallel to perpendicular hinderance drifts away from one-half with changes in volume fraction and as the penetration depth shrinks.

In the limit of small scattering wave-vector, one recovers the evanescent short-time collective diffusivity which is a bit peculiar when compared with that for the bulk. In this case, the collective diffusivity only has components normal to the nearby wall as the evanescent wave selectively weights the probability distribution along that dimension. Additionally, for small penetration depths, this quantity can become quite small relative to the bare diffusivity. This of course is because of the lubrication interactions with the wall which hinder the suspension strongly in the normal direction. In fact, the hinderance is so strong that for all but the most tightly packed systems, it dominates the scaling of the diffusivity. As such, it is no surprise that for $\kappa a \rightarrow \infty$, the pair component of the mobility $\mathbf{D}_{12}$ makes a negligible contribution and the collective diffusivity is proportional to the self-diffusivity. The pre-factor differs however, because the self-diffusivity is normalized by the self-intermediate scattering function $F_S(0,0;\kappa)$ while the collective diffusivity is normalized by the intermediate scattering function $F(0,0;\kappa)$ which in the limit of very small penetration depths are not necessarily the same. The evanescent collective diffusivity is plotted in figure 7.4. The evanescent wave collective diffusivity appears to diverge in the limit that $\kappa \rightarrow 0$. This arises precisely because of the terms proportional to $\mathbf{G}\bar{\mathbf{G}}$ which relate to the mean value of the scattering intensity. When $\kappa \rightarrow 0$, the mean fluctuations in the number density, as in standard dynamic light scattering, play an important role in setting the magnitude of the intermediate scattering function. From equilibrium thermodynamics one can show that the fluctuation in the number of particles within the scattering volume is proportional to the isothermal compressibility [Berne and Pecora (1982)]. Near the wall, the suspension microstructure is nearly incompressible, and therefore, the value of $F(0,0;0)$ is quite small. Though, the time rate of change of the fluctuations is not so that there is no corresponding decay in the hydrodynamic contribution to the

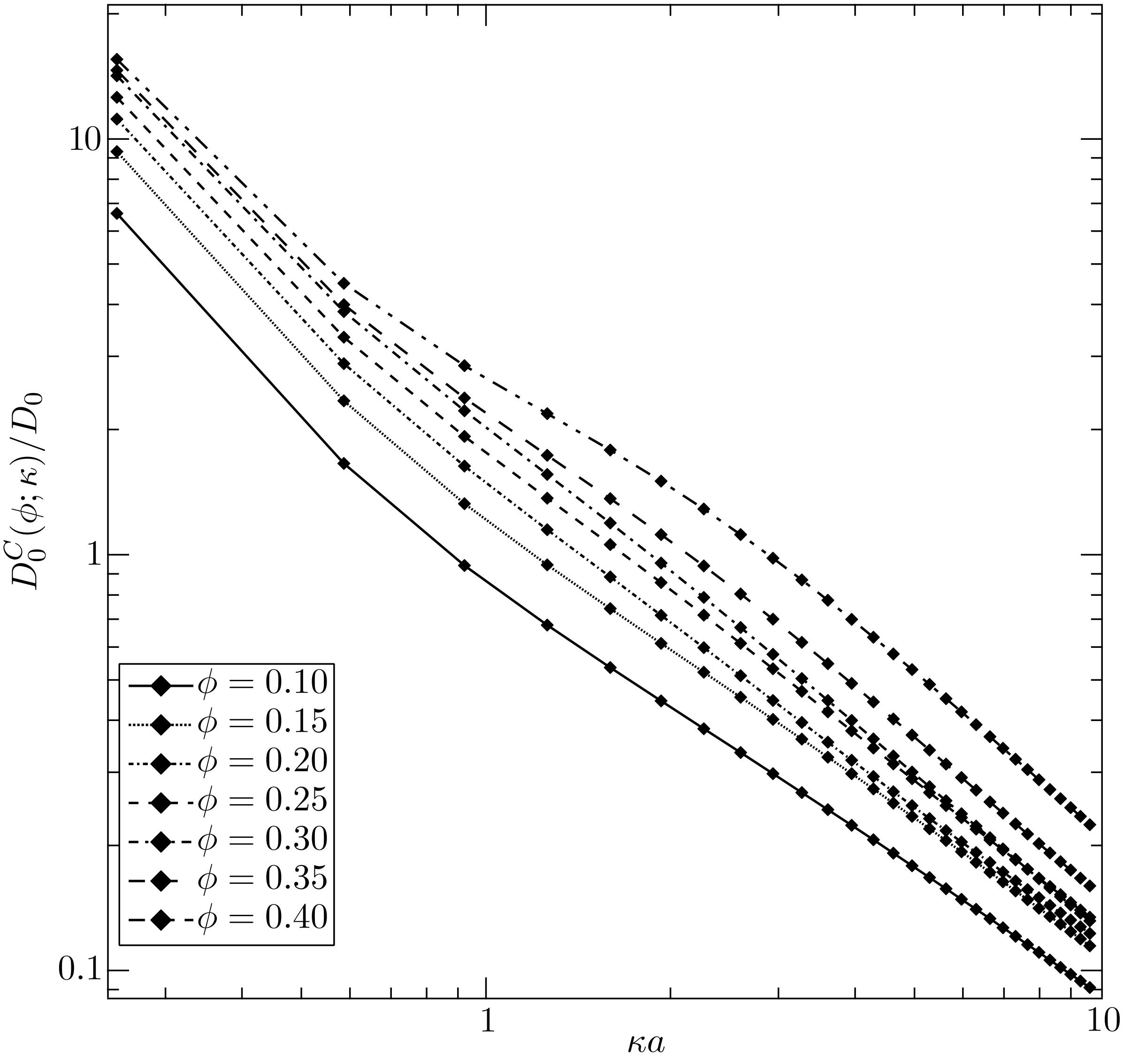

Figure 7.4: The evanescent collective self-diffusivity plotted as a function of the penetration depth and bulk suspension volume fraction. These are the result of simulations in a channel which is twelve radii in width. It has been shown that the effect of a finite channel width on both the structure and the sedimentation rate in the channel is minimal for this range of volume fractions [see *e.g.* Swan and Brady (2010)].

collective diffusivity. This component simply corresponds to the sedimentation rate of a suspension normal to the channel walls. The collective diffusivity is the ratio of these two contributions which must grow rapidly with increasing penetration depth.

Consider a suspension of neutrally buoyant index of refraction matched colloidal particles seeded dilutely with heavy and optically active particles. The distribution of particles in the suspension, denoted $\tilde{P}_N^0(\mathbf{x}_N(0))$ will be Boltzmann such that

$$\tilde{P}_N^0(\mathbf{x}_N(0)) = \exp\left[-\left(\frac{4}{3}\pi a^3\right)\left(\frac{\Delta\rho g}{kT}\right)\sum_h \mathbf{e}_3\cdot\mathbf{x}_h(0)\right] P_N^0(\mathbf{x}_N(0)), \tag{7.51}$$

where $4/3\pi a^3\Delta\rho g$ is the buoyant force on the heavy particles and the summation over h denotes the heavy particles only. Interestingly, this pre-factor weighting the equilibrium distribution for neutrally buoyant particles, $P_N^0(\mathbf{x}_N(0))$, introduces an effective penetration depth $kT/(4/3\pi a^3\Delta\rho g)$. In this way, evanescent wave light scattering type measurements can be made via a conventional light scattering apparatus. The effect of buoyancy of the dilute, heavy particles is to weight the equilibrium probability distribution with respect to the distance from the boundary where the suspension settles. A scattering volume near that boundary will probe this weighted equilibrium distribution without altering the hydrodynamics. A typical penetration depth for one micron particles with a density difference of 193 kg/m^3 (PMMA in water) at room temperature is 519 nm, which is of the same magnitude as those accessed in evanescent light scattering experiments. This value is set experimentally by the low angle of incidence of the internally reflected wave. In this case, κ scales as the cube of the particle radius, so that increasing the particle size shifts the diffusivity curves presented in this chapter (with respect to the dimensionless independent variable κa) as a^4. This is a high degree of sensitivity and can allow easy access to the entire range of penetration depth. One caveat is necessary, however. This method of modeling the evanescent wave light scattering experiment is applicable for comparison of the self-diffusivity only. The reason being that the collective diffusivity weights the self component of the mobility by an exponential decay with respect to the distance of a single particle from the wall, while the pair component is weighted by the average distance of those two particles from the wall. The buoyant distribution does not capture the appropriate weighting for the pair contribution.

The long-time diffusion measured when the limit that the scattering wave vector is small and the correlation time is long. In the limit that the penetration depth approaches infinity, this is simply the bulk diffusivity. However, for finite penetration depths, the scattering signal decorrelates rapidly as the fraction of time a particle spends within the scattering volume is exponentially small. This of course is not true for suspension bound in narrow channels, but rather for suspension bound largely in one dimension. There is no analogue of the long-time self-diffusivity above a single boundary to that in a channel as the particle in the channel will spend a finite amount of time in the scattering volume resulting in a finite and measurable correlation.

7.4 Conclusions

Propagating evanescent waves through a dispersion of optically active colloidal particles results in scattering very much like what is expected in conventional light scattering. As such, it is not so surprising that analysis of the intensity correlation in terms of the intermediate scattering function can by mapped directly on the classical interpretation [Rallison and Hinch (1986)] by recognizing that the evanescent scattering wave vector is complex (the imaginary component being linearly proportional to the penetration depth of the wave). Performing an analysis which respects algebraic characteristics of the scattering correlation produces a startlingly simple and powerful result. The time rate of change of the intermediate scattering function is a diffusivity which depends on the scattering wave vector in exactly the same way as conventional light scattering, with the caveat that transpose of the complex wave vector is needed in some places. In the limits of large and small scattering angle respectively, this diffusivity measures the average short-time self- and collective diffusivities where the average is weighted to decay exponentially with the distance of the scattering particles from the boundary emitting the evanescent wave. This explicit dependence on position is key as it allows experimentalists to measure both the inhomogenous and the anisotropic nature of the hydrodynamic interactions among particles in the presence of a macroscopic boundary. The former task is affected by the penetration depth of the evanescent wave which itself is controlled by the angle of incidence between the scattered wave and the boundary. The latter measurement is affected by the scattering angle itself and in principle the two can be controlled independently. However, this can prove difficult to accomplish with some experimental apparatuses. Fortunately, no such limitation exists computationally and in this chapter we have predicted the self- and collective diffusivities for a variety of penetration depths and volume fractions. In the limit of small penetration depths, the lubrication interactions with the wall dominate both the self- and collective diffusivities while for larger penetration depths, the bulk properties of the suspension can be recovered. The relative influence of interparticle hydrodynamic interactions, hydrodynamic interactions with the boundaries and the influence of the suspension's structure are not easily separable, however. As even the combined influence had not been predicted in any thorough fashion, these results are novel and vital.

Bibliography

[1] B.J. Berne and R. Pecora. *Dynamic Light Scattering: with applications to chemisty, biology and physics.* Dover Publications, Mineola, 2003.

[2] J.R. Blake. A note on the image system for a stokeslet in a no-slip boundary. *Proc. Cam. Phil. Soc.*, 70:303–310, 1971.

[3] J.F. Brady. The long-time self-diffusivity in concentrated colloidal dispersions. *J. Fluid Mech.*, 272:109–133, 1994.

[4] A. Donev, F.H. Stillinger and S. Torquato. Neighbor List Collision-Driven Molecular Dynamics Simulation for Nonspherical Particles. I. Algorithmic Details II. Applications to Ellipses and Ellipsoids. *J. Comp. Phys.*, **202**(2), 737–793, 2005.

[5] L.J. Durlofsky, J.F. Brady, and G. Bossis. Dynamic simulation of hydrodynamically interacting particles. *J. Fluid Mech.*, 180:21–49, 1987.

[6] H. Faxen. *Arkiv. Mat. Astron. Fys.*, 17(27), 1923. dissertation, Uppsala University, 1921.

[7] J. Happel and H. Brenner. *Low Reynolds Number Hydrodynamics.* Prentice Hall, Englewood Cliffs, 2nd edition, 1986.

[8] P. Holmqvist, J.K.G. Dhont and P.R. Lang. Anisotropy of Brownian motion caused only by hydrodynamic interaction with a wall. *Phys. Rev. E*, 74(2):021402, 2006.

[9] V.N. Michailidou, G. Petekidis, J.W. Swan and J.F. Brady. Dynamics of Concentrated Hard-Sphere Colloids Near a Wall. *Phys. Rev. Lett.*, 109:068302, 2009.

[10] V.N. Michailidou, G. Petekidis, J.W. Swan and J.F. Brady. No title. To be published, 2010.

[11] C.W. Oseen. *Neuere Methoden und Ergebnisse in der Hydrodynamik.* dissertation, Akademische Verlagsgesellschaft, Leipzig, 1928.

[12] J.M. Rallison and E.J. Hinch. The effect of particle interactions on dynamic light scattering from a dilute suspension. *J. Fluid Mech.*, 167:131–168, 1986.

[13] W.B. Russel, D.A. Saville and W.R. Schowalter. *Colloidal Dispersions.* Cambridge University Press, Cambridge, 1989.

[14] A. Seirou and J.F. Brady. Accelerated Stokesian Dynamics simulations. *J. Fluid Mech.*, 448:115–146, 2001.

[15] J.W. Swan and J.F. Brady. Simulation of hydrodynamically interacting particles near a no-slip boundary. *Phys. Fluids*, 19(11):113306, 2007.

[16] J.W. Swan and J.F. Brady. The hydrodynamics of concentrated and confined colloidal dispersions. To be published, 2010.

Chapter 8

Conclusion

In many ways, this thesis constitutes a definitive study of the hydrodynamic interactions among particles in confined geometries. While restricted to cases where particles are bound by planar no-slip surfaces, this study by and large represents the qualitative behavior of all confined colloidal systems. While a broad generalization to be sure, this claim is supported by the fact that the geometric details of Stokes flows are largely irrelevant. The addition of macroscopic boundaries introduces inherent hydrodynamic inhomogeneities and anisotropies which are not accounted for in unbounded systems. Whether bound to a rectangular channel, a tube or within a sphere, these same general features emerge. Whereas the time scale for the equilibrium dynamics of hydrodynamically active suspensions is set by the short-time self-diffusivity of the suspension, the same claim cannot be made for bound systems. For one thing, there is not just *one* relevant short-time self-diffusivity and for another, the inherent anisotropies in the system mean that the dynamics normal and along the macroscopic boundaries occur at different rates. Again, the plane wall models reflect all of these details, and this study has quantified them for various degrees of confinement (*i.e.* differing channel widths and suspension volume fractions). Studies of colloid dynamics and suspension rheology in more complicated geometries are possible, especially given the methods developed herein. These may be important in biological situations such as modeling the flow inside the body of a cell.

Care must be taken to recognize phenomena captured directly, indirectly and not at all by the model employed throughout this thesis. Firstly, the only explicit restrictions needed to reproduce the results herein are the conditions of zero Reynolds number and rigid, no-slip surfaces for both the walls and the spherical particles. Indirectly, however, any number of phenomena may be added and studied via these same methodologies. With at least three exceptions, these can be incorporated via an additional force on the particles (*e.g.* van der Waals forces, electrostatic forces, depletion forces, Brownian forces *etc.*). The inclusion of these additional driving forces is discussed implicitly in the “Preliminaries” chapter of this work. The consequences of additional forces are two-fold: they generate particle motion subject to multiplication by the inverse of the resistance tensor ($\mathbf{R}_{FU}^{-1}$), and they may alter the equilibrium microstructure of the suspension if conservative in nature. Excluded from this group are particle inertia which may be included via the Langevin equation in the limit of finite Stokes number along with a more sophisticated integration of the particle trajectories. Lastly, including fluid inertia and modeling the motion of fluid droplets are outside the scope of this work. The former introduces non-linearities in the fluid velocity fields which cannot be accounted for easily or in a general fashion. The latter requires modification of the integral representation for Stokes flow to include the double layer potential on the surfaces of droplets. Therefore, the methodology developed cannot be extended directly to account for these phenomena. Rather, the principles developed throughout may provide direction for and assistance in further research of both finite Reynolds number flows and droplets in confinement.

The present work dealt only with the short-time or equilibrium properties of confined suspensions. While these measurements are mostly novel as it is only recently that experimentalists have begun using light scattering and optical microscopy to make similar measurements, there is a large body of work on the long-time and non-equilibrium dynamics of confined colloids. In particular, researchers have spent considerable effort studying the pressure-driven flow of suspensions down channels via both experiment and simulation. It is well known that the time required for the suspension microstructure to reach steady state scales as $(H/a)^3$ when the particles undergo Brownian motion. Therefore, for even moderately wide channel (*i.e.* 6–12 particle radii as in this study), it can take quite long to reach steady-state. However, the algorithm described in Chapter 6 can be readily extended to dynamic simulation. In fact, if the algorithm is constructed carefully, then the iterative inversion of the far-field and near-field hydrodynamics can by accelerated significantly by using the solution at the previous time step as the initial guess in the next time step. Since the particles migrate little from one time step to another as the time to reach equilibrium is itself long, this proves to be an excellent guess. The number of iterations required can be reduced by as much as a factor of ten. Consequently, unlike typical Stokesian Dynamics where the inversion of the far-field mobility tensor may be needed at every time step, the iterative inversion can be calculated at each and every time step with little to no computational penalty.

The pressure-driven flow of non-colloidal particles is a two parameter system (channel width and suspension volume fraction) as the pressure gradient driving the flow simply sets the time scale in the problem. One would like to know the steady-state distribution of particle velocities and number density across the channel as these are most frequently measured by experimentalists. However, perhaps even more elucidating will be the steady-state velocity auto-correlation function which itself is anisotropic. In particular, the integral of this quantity measures the shear-induced diffusivity of the suspension. However, there is typically a long-time tail which decays with fractional power as a function of time. It is not known whether the decay rate of the velocity auto-correlations normal to and along the wall are the same. In fact, one might guess that they are not as normal to the channel walls, the hydrodynamic interactions decay exponentially, rather than algebraically fast. Similarly, near the walls, the lubrication interactions take on very different characters. This difference in the decay rate of the long-time tail presumably indicates the hydrodynamic mode which sets the time scale for the long-time dynamics of the system. It is not at all clear whether the normal or transverse hindrances (or some combination thereof) controls the long-time diffusion rate. For that matter, it is equally possible that a normal mode analysis can decouple the normal and transverse motions entirely with the corresponding hydrodynamic interactions setting the respective diffusive time scales. This is an open and important question as this is one of the key ways in which confined systems differ from unbounded ones.

The latter measurements are potentially an order of magnitude easier to carry out than a study of the long-time self-diffusivity of particles in suspensions confined between parallel walls. Again, this is a two parameter system, with the bare diffusivity setting the time scale. The difficulty arises because simulation of the Brownian motion of particles requires one to compute the square root of the resistance tensor. This weights the stochastic Brownian forces correctly. While schemes exist for performing this calculation (and some of these are quite fast). These same schemes typically require a minimum of ten-fold additional computational effort. As the particles diffuse throughout the channel, they sample the entire space and the long-time self-diffusivity represents an average of the hydrodynamic hinderance across the channel subject in part to the equilibrium number density distribution. Like the shear-induced diffusivity, this quantity will also be anisotropic; however, the source of the anisotropy arises *solely* from the bounding geometry. There is no imposed flow to bias motion in one direction over another. The same questions remain though. How are the velocity auto-correlations normal to and along the wall related? How do the dynamics of the system set the decay rate of this correlation and what are the implications for other long-time properties of confined systems? This challenge is more difficult to attack still, though the methods developed in this thesis are a first step towards the accomplishing just that.

Further on the horizon is the study of systems far from equilibrium or subject competing forces (*i.e.* a combination of shear and pressure-driven flows). There are tantalizing questions to be answered including: do predictions and deductions of the short-time dynamics carry over to long-time measurements, and how do phenomena like shear thickening and jamming change when a suspension is confined. Of course, the previous two parameter systems must be extended with another parameter representing the relative strengths of the operative forces in the system (*e.g.* the Peclet number representing the relative rate of shearing to the bare diffusive time scale). Such complications will eventually be tackled as well, though probably through a more brute force methodology such as active and thoughtful parallelization of the algorithms already mentioned.

As one final note, consider that the methods used to simplify the hydrodynamic equations in this thesis apply equally well to any system governed by harmonic equations. This includes the computation of the electrostatic potential in systems of charged or uncharged colloids confined in some manner. In fact, some work not included in this thesis computed just that quite successfully. Similarly, this same approach can be extended to computations of the displacement of elastic systems with rigid inclusions and rigid boundaries as well. Like the original Stokesian Dynamics, this methodology is general and easily extendable.

Appendix A

Simulation of hydrodynamically interacting particles near a no-slip boundary

A.1 Reflected stokeslet contributions to the grand mobility tensor

As in equation 4.15, we can write explicit expressions for all of the terms in the mobility tensor. For the purposes of this appendix we only concern ourselves with the contributions due to reflection of the stokeslet. The interactions due to the stokeslet itself yield the well-known far-field grand mobility tensor for unbounded pairs of particles and can be found in ref. 4. We write the contribution to the grand mobility matrix due to the reflected field, $\mathbf{J}^w(\mathbf{x}, \mathbf{y}; H)$, as $\hat{\mathcal{M}}$, and the contributions to the sub-tensors are denoted $\hat{\mathbf{M}}_{UF}, \hat{\mathbf{M}}_{UL}, \ldots$. When this is added to the grand mobility tensor for an unbounded set of particles, we recover the complete grand mobility tensor, $\mathcal{M}$. Without loss of generality, these expressions can be used to generate the single particle-wall and particle pair-wall interactions as described in section 5.2. Note that we define the operator ∇_x^T such that $\nabla_x^T \mathbf{u}(\mathbf{x}) = (\nabla_x \mathbf{u}(\mathbf{x}))^T$.

$$\hat{\mathbf{M}}^{\alpha\beta}_{UF,ij} = \left(1 + \frac{a_\alpha^2}{6}\nabla_x^2\right)\left(1 + \frac{a_\beta^2}{6}\nabla_y^2\right)\mathbf{J}^w\left(\mathbf{x}, \mathbf{y}; H\right)\Bigg|_{\mathbf{x}=\mathbf{x}_\alpha}^{\mathbf{y}=\mathbf{x}_\beta} \tag{A.1}$$

$$\hat{\mathbf{M}}^{\alpha\beta}_{\Omega F,ij} = \frac{1}{2}\nabla_x \times \left(1 + \frac{a_\beta^2}{6}\nabla_y^2\right) \mathbf{J}^w\left(\mathbf{x},\mathbf{y};H\right)\Bigg|_{\mathbf{x}=\mathbf{x}_\alpha}^{\mathbf{y}=\mathbf{x}_\beta} \tag{A.2}$$

$$\hat{\mathbf{M}}^{\alpha\beta}_{EF,ijk} = \frac{1}{2}\left(\nabla_x + \nabla_x^T\right)\left(1 + \frac{a_\alpha^2}{10}\nabla_x^2\right)\left(1 + \frac{a_\beta^2}{6}\nabla_y^2\right) \mathbf{J}^w\left(\mathbf{x},\mathbf{y};H\right)\Bigg|_{\mathbf{x}=\mathbf{x}_\alpha}^{\mathbf{y}=\mathbf{x}_\beta} \tag{A.3}$$

$$\hat{\mathbf{M}}^{\alpha\beta}_{UL,ij} = \left(1 + \frac{a_\alpha^2}{6}\nabla_x^2\right)\frac{1}{2}\nabla_y \times \mathbf{J}^w\left(\mathbf{x},\mathbf{y};H\right)\Bigg|_{\mathbf{x}=\mathbf{x}_\alpha}^{\mathbf{y}=\mathbf{x}_\beta} \tag{A.4}$$

$$\hat{\mathbf{M}}^{\alpha\beta}_{\Omega L,ij} = \frac{1}{2}\nabla_x \times \frac{1}{2}\nabla_y \times \mathbf{J}^w\left(\mathbf{x},\mathbf{y};H\right)\Bigg|_{\mathbf{x}=\mathbf{x}_\alpha}^{\mathbf{y}=\mathbf{x}_\beta} \tag{A.5}$$

$$\hat{\mathbf{M}}^{\alpha\beta}_{EL,ijk} = \frac{1}{2}\left(\nabla_x + \nabla_x^T\right)\left(1 + \frac{a_\alpha^2}{10}\nabla_x^2\right)\frac{1}{2}\nabla_y \times \mathbf{J}^w\left(\mathbf{x},\mathbf{y};H\right)\Bigg|_{\mathbf{x}=\mathbf{x}_\alpha}^{\mathbf{y}=\mathbf{x}_\beta} \tag{A.6}$$

$$\hat{\mathbf{M}}^{\alpha\beta}_{US,ijk} = \left(1 + \frac{a_\alpha^2}{6}\nabla_x^2\right)\left(1 + \frac{a_\beta^2}{10}\nabla_y^2\right)\mathbf{K}^w\left(\mathbf{x},\mathbf{y};H\right)\Bigg|_{\mathbf{x}=\mathbf{x}_\alpha}^{\mathbf{y}=\mathbf{x}_\beta} \tag{A.7}$$

$$\hat{\mathbf{M}}^{\alpha\beta}_{\Omega S,ijk} = \frac{1}{2}\nabla_x \times \left(1 + \frac{a_\beta^2}{10}\nabla_y^2\right)\mathbf{K}^w\left(\mathbf{x},\mathbf{y};H\right)\Bigg|_{\mathbf{x}=\mathbf{x}_\alpha}^{\mathbf{y}=\mathbf{x}_\beta} \tag{A.8}$$

$$\hat{\mathbf{M}}^{\alpha\beta}_{ES,ijkl} = \frac{1}{2}\left(\nabla_x + \nabla_x^T\right)\left(1 + \frac{a_\alpha^2}{10}\nabla_x^2\right)\left(1 + \frac{a_\beta^2}{10}\nabla_y^2\right)\mathbf{K}^w\left(\mathbf{x},\mathbf{y};H\right)\Bigg|_{\mathbf{x}=\mathbf{x}_\alpha}^{\mathbf{y}=\mathbf{x}_\beta} \tag{A.9}$$

A.2 Particle-wall "self" mobility tensor ($\alpha\alpha$)

Presented below is the contribution to the grand mobility tensor due to a single particle (α) interacting with a plane wall. All of the following terms are normalized by $6\pi\eta a_\alpha^n$, where n is chosen to keep things dimensionally consistent. Additionally, h is the normalized height of the particle above the wall such that $h = h_\alpha / a_\alpha$. Note that since the mobility tensor is symmetric by construction, we include only six of nine sub-tensors. The other three can be computed directly by taking a transposition.

$$\hat{M}^{\alpha\alpha}_{UF,ij} = -\frac{1}{16}\left(9h^{-1} - 2h^{-3} + h^{-5}\right)\left(\delta_{ij} - \delta_{i3}\delta_{j3}\right) - \frac{1}{8}\left(9h^{-1} - 4h^{-3} + h^{-5}\right)\delta_{i3}\delta_{j3} \tag{A.10}$$

$$\hat{M}^{\alpha\alpha}_{\Omega F,ij} = \frac{3}{32}h^{-4}\epsilon_{3ij} \tag{A.11}$$

$$\hat{M}^{\alpha\alpha}_{\Omega L,ij} = -\frac{15}{64}h^{-3}\left(\delta_{ij} - \delta_{i3}\delta_{j3}\right) - \frac{3}{32}h^{-3}\delta_{i3}\delta_{j3} \tag{A.12}$$

$$\begin{aligned}\hat{M}^{\alpha\alpha}_{EF,ijk} = &-\frac{3}{160}\left(15h^{-2} - 12h^{-4} + 5h^{-6}\right)\left[\left(\delta_{ik} - \delta_{i3}\delta_{k3}\right)\delta_{j3} + \left(\delta_{jk} - \delta_{j3}\delta_{k3}\right)\delta_{i3}\right] \\ &+ \frac{3}{32}\left(3h^{-2} - 3h^{-4} + h^{-6}\right)\left(\delta_{ij} - \delta_{i3}\delta_{j3}\right)\delta_{k3} - \frac{3}{16}\left(3h^{-2} - 3h^{-4} + h^{-6}\right)\delta_{i3}\delta_{j3}\delta_{k3}\end{aligned} \tag{A.13}$$

$$\hat{M}^{\alpha\alpha}_{EL,ijk} = -\frac{9}{320}\left(5h^{-3} - 4h^{-5}\right)\left(\delta_{j3}\epsilon_{3ik} + \delta_{i3}\epsilon_{3jk}\right) \tag{A.14}$$

$$\begin{aligned}\hat{M}^{\alpha\alpha}_{ES,ijkl} = &-\frac{3}{640}\left(10h^{-3} - 24h^{-5} + 9h^{-7}\right)\left(\delta_{ij} - \delta_{i3}\delta_{j3}\right)\left(\delta_{kl} - \delta_{k3}\delta_{l3}\right) \\ &- \frac{9}{640}\left(10h^{-3} - 8h^{-5} + 3h^{-7}\right)\left[\left(\delta_{ik} - \delta_{i3}\delta_{k3}\right)\left(\delta_{jl} - \delta_{j3}\delta_{l3}\right) + \left(\delta_{il} - \delta_{i3}\delta_{l3}\right)\left(\delta_{jk} - \delta_{j3}\delta_{k3}\right)\right] \\ &+ \frac{3}{160}\left(20h^{-3} - 24h^{-5} + 9h^{-7}\right)\left[\left(\delta_{ij} - \delta_{i3}\delta_{j3}\right)\delta_{k3}\delta_{l3} + \left(\delta_{kl} - \delta_{k3}\delta_{l3}\right)\delta_{i3}\delta_{j3}\right] \\ &- \frac{9}{320}\left(15h^{-3} - 16h^{-5} + 6h^{-7}\right)\left[\left(\delta_{ik} - \delta_{i3}\delta_{k3}\right)\delta_{j3}\delta_{l3} + \left(\delta_{il} - \delta_{i3}\delta_{l3}\right)\delta_{j3}\delta_{k3}\right. \\ &\left. + \left(\delta_{jk} - \delta_{j3}\delta_{k3}\right)\delta_{i3}\delta_{l3} + \left(\delta_{jl} - \delta_{j3}\delta_{l3}\right)\delta_{i3}\delta_{k3}\right] - \frac{3}{80}\left(20h^{-3} - 24h^{-5} + 9h^{-7}\right)\delta_{i3}\delta_{j3}\delta_{k3}\delta_{l3}\end{aligned} \tag{A.15}$$

A.3 Particle-wall "pair" mobility tensor ($\alpha\beta$)

Here we present the contributions to the grand mobility tensor due to interactions between an identically sized particle pair ($\alpha\beta$) and a plane wall. One can generate these tensors for particles of different sizes just as easily using the expressions in appendix A.1. However, the expressions for those tensors are significantly longer. As above, the mobility terms are normalized by $6\pi\eta a^n$, where $a = a_\alpha = a_\beta$ and n is selected to provide the correct dimensionality. We define the following as well:

$$\mathbf{R} = \frac{1}{a}\left(\mathbf{x}_\alpha - \mathbf{x}_\beta + 2h_\beta \boldsymbol{\delta}_3\right) \tag{A.16}$$

and $\mathbf{e} = \mathbf{R}/R$ where $R = \sqrt{\mathbf{R}\cdot\mathbf{R}}$. Additionally, we define a rescaled height above the wall as $\hat{h} = h_\beta/(aR_3)$. As in the previous section we include six of the nine sub-tensors. The others may be generated through transposition.

$$\begin{aligned}
\hat{M}^{\alpha\beta}_{UF,ij} &= -\frac{1}{4}\left[3\left(1+2\hat{h}\left(1-\hat{h}\right)e_3^2\right)R^{-1}+2\left(1-3e_3^2\right)R^{-3}-2\left(1-5e_3^2\right)R^{-5}\right]\delta_{ij} \\
&\quad -\frac{1}{4}\left[3\left(1-6\hat{h}\left(1-\hat{h}\right)e_3^2\right)R^{-1}-6\left(1-5e_3^2\right)R^{-3}+10\left(1-7e_3^2\right)R^{-5}\right]e_ie_j \\
&\quad +\frac{1}{2}e_3\left[3\hat{h}\left(1-6\left(1-\hat{h}\right)e_3^2\right)R^{-1}-6\left(1-5e_3^2\right)R^{-3}+10\left(2-7e_3^2\right)R^{-5}\right]e_i\delta_{j3} \\
&\quad +\frac{1}{2}e_3\left(3\hat{h}R^{-1}-10R^{-5}\right)\delta_{i3}e_j-\left[3\hat{h}^2e_3^2R^{-1}+3e_3^2R^{-3}+\left(2-15e_3^2\right)R^{-5}\right]\delta_{i3}\delta_{j3}
\end{aligned} \tag{A.17}$$

$$\begin{aligned}
\hat{M}^{\alpha\beta}_{\Omega F,ij} &= \frac{3}{4}R^{-2}\epsilon_{ijk}e_k+\frac{3}{2}\left[6\hat{h}e_3^2R^{-2}+\left(1-10e_3^2\right)R^{-4}\right]\epsilon_{3ki}e_k\delta_{j3} \\
&\quad -\frac{3}{2}e_3\left(3\hat{h}R^{-2}-5R^{-4}\right)\epsilon_{3ki}e_ke_j-\frac{3}{2}e_3\left(\hat{h}R^{-2}-R^{-4}\right)\epsilon_{3ij}
\end{aligned} \tag{A.18}$$

$$\hat{M}^{\alpha\beta}_{\Omega L,ij} = \frac{3}{8}\left(1-6e_3^2\right)R^{-3}\delta_{ij}-\frac{9}{8}R^{-3}e_ie_j+\frac{9}{4}e_3R^{-3}\delta_{i3}e_j+\frac{9}{4}R^{-3}\epsilon_{3ki}\epsilon_{3lj}e_ke_l \tag{A.19}$$

$$\begin{aligned}
\hat{M}^{\alpha\beta}_{EF,ijk} &= \frac{6}{5}e_3\left[\left(5-2\hat{h}\right)R^{-4}-15R^{-6}\right]\delta_{i3}\delta_{j3}\delta_{k3}+3R^{-6}\delta_{i3}\delta_{j3}e_k \\
&\quad -\frac{3}{10}e_3\left[5\hat{h}\left(1-6\left(1-\hat{h}\right)e_3^2\right)R^{-2}-2\left(5-\hat{h}-5\left(5-2\hat{h}\right)e_3^2\right)R^{-4}+10\left(2-7e_3^2\right)R^{-6}\right]\delta_{ij}\delta_{k3} \\
&\quad -\frac{3}{10}\left[\left(5-2\hat{h}\right)R^{-4}-10R^{-6}\right]e_3\left(\delta_{ik}\delta_{j3}+\delta_{i3}\delta_{jk}\right)+\frac{3}{2}e_3\left[\left(5-2\hat{h}\right)R^{-4}-14R^{-6}\right]\left(\delta_{j3}e_ie_k+\delta_{i3}e_je_k\right) \\
&\quad +\frac{3}{2}\left[6\hat{h}\left(1-\hat{h}\right)e_3^2R^{-2}+\left(1-4\left(5-2\hat{h}\right)e_3^2\right)R^{-4}-2\left(2-21e_3^2\right)R^{-6}\right]\left(e_i\delta_{j3}\delta_{k3}+e_j\delta_{i3}\delta_{k3}\right) \\
&\quad -\frac{3}{10}\left[15\hat{h}\left(1-\hat{h}\right)e_3^2R^{-2}+\left(4-5\left(5-2\hat{h}\right)e_3^2\right)R^{-4}-5\left(1-7e_3^2\right)R^{-6}\right]\left(e_i\delta_{jk}+e_j\delta_{ik}\right) \\
&\quad +\frac{3}{2}e_3\left[3\hat{h}\left(1-10\left(1-\hat{h}\right)e_3^2\right)R^{-2}-2\left(5-\hat{h}-7\left(5-2\hat{h}\right)e_3^2\right)R^{-4}+14\left(2-9e_3^2\right)R^{-6}\right]e_ie_j\delta_{k3} \\
&\quad +\frac{3}{20}\left[5\left(1-6\hat{h}\left(1-\hat{h}\right)e_3^2\right)R^{-2}-2\left(4-5\left(5-2\hat{h}\right)e_3^2\right)R^{-4}+10\left(1-7e_3^2\right)R^{-6}\right]\delta_{ij}e_k \\
&\quad -\frac{3}{4}\left[3\left(1-10\left(1-\hat{h}\right)e_3^2\right)R^{-2}-2\left(4-7\left(5-2\hat{h}\right)e_3^2\right)R^{-4}-14\left(1-9e_3^2\right)R^{-6}\right]e_ie_je_k
\end{aligned} \tag{A.20}$$

$$\begin{aligned}
\hat{M}^{\alpha\beta}_{EL,ijk} &= -\frac{9}{8}R^{-3}\left(e_j\epsilon_{ikl}e_l+e_i\epsilon_{jkl}e_l\right)-\frac{9}{10}R^{-5}\left(\delta_{j3}\epsilon_{3ik}+\delta_{i3}\epsilon_{3jk}\right) \\
&\quad +\frac{9}{4}\left(R^{-3}-2R^{-5}\right)\left(e_i\delta_{j3}\epsilon_{3kl}e_l+\delta_{i3}e_j\epsilon_{3kl}e_l\right)-\frac{9}{4}e_3\left[\left(1-2\hat{h}\right)R^{-3}-2R^{-5}\right]\left(e_j\epsilon_{3ik}+e_i\epsilon_{3jk}\right) \\
&\quad +\frac{9}{2}e_3\left[\left(1-\hat{h}\right)R^{-3}-R^{-5}\right]\delta_{ij}\epsilon_{3kl}e_l-\frac{9}{2}e_3\left[5\left(1-\hat{h}\right)R^{-3}-7R^{-5}\right]e_ie_j
\end{aligned} \tag{A.21}$$

$$
\begin{aligned}
\hat{M}^{\alpha\beta}_{ES,ijkl} &= \frac{9}{5}R^{-7}\delta_{i3}\delta_{j3}\delta_{kl} - \frac{18}{5}e_3\left(5R^{-5}-21R^{-7}\right)\left(\delta_{i3}\delta_{j3}e_k\delta_{l3}+\delta_{i3}\delta_{j3}\delta_{k3}e_l\right) \\
&+ \frac{9}{10}e_3\left(5R^{-5}-14R^{-7}\right)\left(e_i\delta_{j3}\delta_{kl}+\delta_{i3}e_j\delta_{kl}+\delta_{il}\delta_{j3}e_k+\delta_{i3}\delta_{jl}e_k+\delta_{i3}\delta_{jk}e_l+\delta_{ik}\delta_{j3}e_l\right) \\
&+ \frac{9}{5}\left[5\hat{h}\left(1-\hat{h}\right)e_3^2R^{-3}+\left(1-10e_3^2\right)R^{-5}-\left(2-21e_3^2\right)R^{-7}\right]\left(\delta_{ik}\delta_{j3}\delta_{l3}+\delta_{il}\delta_{j3}\delta_{k3}+\delta_{i3}\delta_{jk}\delta_{l3}+\delta_{i3}\delta_{jl}\delta_{k3}\right) \\
&- \frac{9}{10}\left[5\hat{h}\left(1-\hat{h}\right)e_3^2R^{-3}+\left(1-5e_3^2\right)R^{-5}-\left(1-7e_3^2\right)R^{-7}\right]\left(\delta_{il}\delta_{jk}+\delta_{ik}\delta_{jl}\right) \\
&+ \frac{3}{20}\left[5\left(1-6\hat{h}\left(1-\hat{h}\right)e_3^2\right)R^{-3}-6\left(1-5e_3^2\right)R^{-5}+6\left(1-7e_3^2\right)R^{-7}\right]\delta_{ij}\delta_{kl} \\
&- \frac{36}{5}\left[5\hat{h}\left(1-\hat{h}\right)e_3^2R^{-3}+\left(1-15e_3^2\right)R^{-5}-3\left(1-14e_3^2\right)R^{-7}\right]\delta_{i3}\delta_{j3}\delta_{k3}\delta_{l3} \\
&- \frac{9}{5}\left[5\left(1-10\hat{h}\left(1-\hat{h}\right)e_3^2\right)e_3^2R^{-3}-10\left(2-7e_3^2\right)R^{-5}-\left(1-42e_3^2+126e_3^4\right)R^{-7}\right]\delta_{ij}\delta_{k3}\delta_{l3} \\
&- \frac{9}{5}e_3\left[5\left(1-20\hat{h}\left(1-\hat{h}\right)e_3^2\right)R^{-3}-30\left(1-7e_3^2\right)R^{-5}+84\left(1-6e_3^2\right)R^{-7}\right]\left(e_i\delta_{j3}\delta_{k3}\delta_{l3}+\delta_{i3}e_j\delta_{k3}\delta_{l3}\right) \\
&+ \frac{9}{20}e_3\left[5\left(1-20\hat{h}\left(1-\hat{h}\right)e_3^2\right)R^{-3}-10\left(3-14e_3^2\right)R^{-5}+14\left(2-9e_3^2\right)R^{-7}\right] \\
&\quad \times\left(e_i\delta_{jk}\delta_{l3}+e_i\delta_{jl}\delta_{k3}+\delta_{ik}e_j\delta_{l3}+\delta_{il}e_j\delta_{k3}\right) \\
&- \frac{9}{20}\left[5\left(1-10\hat{h}\left(1-\hat{h}\right)e_3^2\right)R^{-3}-10\left(1-7e_3^2\right)R^{-5}+14\left(1-9e_3^2\right)R^{-7}\right]\left(e_ie_j\delta_{kl}+\delta_{ij}e_ke_l\right) \\
&+ \frac{9}{5}\left[25\left(1-14\hat{h}\left(1-\hat{h}\right)e_3^2\right)e_3^2R^{-3}-70\left(2-9e_3^2\right)R^{-5}-7\left(1-54e_3^2+198e_3^4\right)R^{-7}\right]e_ie_j\delta_{k3}\delta_{l3} \\
&+ \frac{9}{10}e_3\left[5\left(1-10\hat{h}\left(1-\hat{h}\right)e_3^2\right)R^{-3}-5\left(3-14e_3^2\right)R^{-5}+14\left(2-9e_3^2\right)R^{-7}\right]\left(\delta_{ij}e_k\delta_{l3}+\delta_{ij}\delta_{k3}e_l\right) \\
&- \frac{9}{40}\left[5\left(1-20\hat{h}\left(1-\hat{h}\right)e_3^2\right)R^{-3}-20\left(1-14e_3^2\right)R^{-5}+28\left(1-9e_3^2\right)R^{-7}\right] \\
&\quad \times\left(e_i\delta_{jl}e_k+\delta_{il}e_je_k+e_i\delta_{jk}e_l+\delta_{ik}e_je_l\right) \\
&+ \frac{9}{20}\left[5\left(1-20\hat{h}\left(1-\hat{h}\right)e_3^2\right)R^{-3}-20\left(1-14e_3^2\right)R^{-5}+28\left(2-27e_3^2\right)R^{-7}\right] \\
&\quad \times\left(e_i\delta_{j3}e_k\delta_{l3}+\delta_{i3}e_je_k\delta_{l3}+e_i\delta_{j3}\delta_{k3}e_l+\delta_{i3}e_j\delta_{k3}e_l\right) \\
&- \frac{9}{10}e_3\left[25\left(1-14\hat{h}\left(1-\hat{h}\right)e_3^2\right)R^{-3}-105\left(1-6e_3^2\right)R^{-5}+126\left(2-11e_3^3\right)R^{-7}\right]\left(e_ie_je_k\delta_{l3}+e_ie_j\delta_{k3}e_l\right) \\
&- \frac{63}{5}R^{-7}\delta_{i3}\delta_{j3}e_ke_l-\frac{63}{10}\left(5R^{-5}-9R^{-7}\right)\left(\delta_{i3}e_je_ke_l+e_i\delta_{j3}e_ke_l\right) \\
&+ \frac{9}{20}\left[25\left(1-14\hat{h}\left(1-\hat{h}\right)e_3^2\right)R^{-3}-70\left(1-9e_3^2\right)R^{-5}+126\left(1-11e_3^2\right)R^{-7}\right]e_ie_je_ke_l
\end{aligned}
\tag{A.22}
$$

Appendix B

Solution to the Stokes equations for arbitrary boundary conditions on the channel walls

In this appendix we conclude the derivation of the solution to the Stokes flow equations with arbitrary boundary conditions on a set of parallel walls. We designate the lower wall as $r_3 = r_l$ and the upper wall as $r_3 = H + r_l$ and write the boundary conditions on the flow as

$$\begin{aligned} \hat{\mathbf{u}}^L &= \mathbf{A}e^{-r_l k} + \mathbf{B}e^{r_l k} + \frac{1}{4\eta k^2}\left[A\mathbf{d}\left(2r_l k + 1\right)e^{-r_l k} + B\bar{\mathbf{d}}\left(2r_l k - 1\right)e^{r_l k}\right], \qquad \text{(B.1)} \\ \hat{\mathbf{u}}^U &= \mathbf{A}e^{-(H+r_l)k} + \mathbf{B}e^{(H+r_l)k} + \frac{1}{4\eta k^2}\left[A\mathbf{d}\left(2(H+r_l)k + 1\right)e^{-(H+r_l)k} + B\bar{\mathbf{d}}\left(2(H+r_l)k - 1\right)e^{(H+r_l)k}\right]. \end{aligned}$$

The solution to these equations is more conveniently written in the typical matrix vector form

$$\begin{aligned} \begin{pmatrix} \mathbf{A} \\ \mathbf{B} \end{pmatrix} &= \frac{1}{2}\left(\coth(Hk) - 1\right)e^{Hk} \begin{pmatrix} e^{(H+r_l)k} & -e^{r_l k} \\ -e^{-(H+r_l)k} & e^{-r_l k} \end{pmatrix} \qquad \text{(B.2)} \\ &\times \begin{pmatrix} \hat{\mathbf{u}}^L - \frac{1}{4\eta k^2}\left[A\mathbf{d}\left(2r_l k + 1\right)e^{-r_l k} + B\bar{\mathbf{d}}\left(2r_l k - 1\right)e^{r_l k}\right] \\ \hat{\mathbf{u}}^U - \frac{1}{4\eta k^2}\left[A\mathbf{d}\left(2(H+r_l)k + 1\right)e^{-(H+r_l)k} + B\bar{\mathbf{d}}\left(2(H+r_l)k - 1\right)e^{(H+r_l)k}\right] \end{pmatrix}. \end{aligned}$$

We still need to determine the coefficients A and B, but since the velocity field is divergence free, equation 5.23 sets the relationship between these coefficients and the vectors $\mathbf{A}$ and $\mathbf{B}$. Applying this relationship and solving for the unknown coefficients yields the following:

$$\begin{pmatrix} A \\ B \end{pmatrix} = -\left(\frac{2\eta}{1+2(Hk)^2-\cosh(2Hk)}\right)\begin{pmatrix} \sinh(Hk) & -Hke^{k(H+2r_l)} \\ -Hke^{-k(H+2r_l)} & \sinh(Hk) \end{pmatrix} \\ \times \begin{pmatrix} \mathbf{d}\cdot\left(\hat{\mathbf{u}}^L e^{(H+r_l)k} - \hat{\mathbf{u}}^U e^{r_l k}\right) \\ \bar{\mathbf{d}}\cdot\left(\hat{\mathbf{u}}^L e^{-(H+r_l)k} - \hat{\mathbf{u}}^U e^{-r_l k}\right) \end{pmatrix}. \tag{B.3}$$

This completes the derivation of the solution of the Stokes equations in the space bounded by parallel walls with arbitrary boundary conditions. Of course, this is only the wave space solution to the problem. The inversion of these results to find the real space solution will depend on the details of the vectors $\hat{\mathbf{u}}^L$ and $\hat{\mathbf{u}}^U$. For even simple boundary conditions, this process can be quite difficult, and it is necessary to combine a clear physical picture of the problem at hand with a detailed knowledge of integral transform techniques. In the above article, we illustrate the inversion of the reflection of a Stokeslet, but only at the place where the reflected flow field corresponds to the location of the point force. The techniques employed are useful for calculating hydrodynamic interactions among particles though perhaps less useful for imaging the flow field or making more general calculations.

Appendix C

The mobility coefficients for a single

particle in a channel

Ξ	$\log f_1^{(UF)}(\Xi)$	$\log f_3^{(UF)}(\Xi)$	$\log f_5^{(UF)}(\Xi)$	$\log g_1^{(UF)}(\Xi)$	$\log g_3^{(UF)}(\Xi)$	$\log g_5^{(UF)}(\Xi)$
0.001	6.332	18.64	31.77	7.026	20.03	32.46
0.010	4.030	11.74	20.25	4.723	13.12	20.95
0.020	3.337	9.657	16.79	4.03	11.04	17.48
0.030	2.932	8.440	14.76	3.624	9.827	15.45
0.040	2.645	7.577	13.32	3.337	8.963	14.01
0.050	2.423	6.908	12.21	3.114	8.294	12.90
0.060	2.242	6.362	11.29	2.931	7.747	11.99
0.070	2.089	5.900	10.52	2.777	7.285	11.22
0.080	1.958	5.501	9.856	2.644	6.884	10.55
0.090	1.844	5.149	9.267	2.526	6.531	9.960
0.100	1.742	4.835	8.741	2.421	6.214	9.434
0.110	1.651	4.552	8.264	2.325	5.928	8.957
0.120	1.569	4.294	7.830	2.239	5.667	8.522
0.130	1.495	4.058	7.430	2.159	5.427	8.122
0.140	1.427	3.841	7.060	2.085	5.204	7.751
0.150	1.365	3.641	6.716	2.016	4.997	7.407
0.160	1.308	3.454	6.394	1.952	4.803	7.084
0.170	1.256	3.281	6.092	1.892	4.621	6.781
0.180	1.208	3.119	5.808	1.836	4.449	6.495
0.190	1.163	2.968	5.539	1.782	4.287	6.225
0.200	1.123	2.827	5.285	1.732	4.132	5.969
0.210	1.085	2.695	5.044	1.685	3.986	5.725
0.220	1.050	2.571	4.814	1.639	3.846	5.492
0.230	1.017	2.455	4.596	1.597	3.712	5.270
0.240	0.9873	2.347	4.388	1.556	3.585	5.057
0.250	0.9595	2.245	4.189	1.517	3.462	4.853
0.260	0.9339	2.150	3.999	1.481	3.345	4.657
0.270	0.9102	2.061	3.818	1.446	3.232	4.469
0.280	0.8883	1.977	3.644	1.413	3.124	4.287
0.290	0.8681	1.900	3.479	1.382	3.020	4.112
0.300	0.8494	1.827	3.320	1.352	2.920	3.943
0.310	0.8323	1.760	3.169	1.324	2.824	3.780
0.320	0.8165	1.698	3.025	1.297	2.732	3.623
0.330	0.8019	1.640	2.888	1.272	2.644	3.471
0.340	0.7886	1.586	2.758	1.248	2.560	3.324
0.350	0.7764	1.537	2.635	1.226	2.480	3.183
0.360	0.7653	1.492	2.518	1.205	2.404	3.047
0.370	0.7553	1.450	2.409	1.186	2.332	2.917
0.380	0.7461	1.412	2.306	1.168	2.264	2.792
0.390	0.7379	1.378	2.211	1.152	2.201	2.674
0.400	0.7305	1.348	2.123	1.137	2.142	2.562
0.410	0.724	1.320	2.043	1.124	2.087	2.457
0.420	0.7182	1.296	1.970	1.111	2.038	2.359
0.430	0.7132	1.275	1.905	1.101	1.994	2.271
0.440	0.7089	1.257	1.849	1.091	1.955	2.191
0.450	0.7053	1.241	1.800	1.084	1.922	2.122
0.460	0.7024	1.229	1.760	1.077	1.894	2.063
0.470	0.7001	1.219	1.729	1.072	1.873	2.017
0.480	0.6985	1.212	1.707	1.069	1.857	1.983
0.490	0.6976	1.208	1.693	1.067	1.848	1.962
0.500	0.6973	1.207	1.689	1.066	1.845	1.956

Table C.1: The coupling coefficients comprising components of the grand resistance tensor for a particle in translating and rotating near a plane wall.

Ξ	$\log f_3^{(\Omega L)}(\Xi)$	$\log g_3^{(\Omega L)}(\Xi)$	$\log f_2^{(UL)}(\Xi)$	$\log f_4^{(UL)}(\Xi)$
0.001	19.27	18.36	−5.190	25.26
0.010	12.36	11.45	−2.928	16.05
0.020	10.29	9.369	−2.280	13.28
0.030	9.069	8.153	−1.920	11.66
0.040	8.206	7.290	−1.678	10.51
0.050	7.537	6.620	−1.501	9.616
0.060	6.991	6.073	−1.364	8.887
0.070	6.530	5.611	−1.256	8.270
0.080	6.130	5.210	−1.169	7.737
0.090	5.778	4.857	−1.098	7.266
0.100	5.463	4.541	−1.040	6.845
0.110	5.179	4.255	−0.9920	6.464
0.120	4.920	3.994	−0.9529	6.117
0.130	4.681	3.754	−0.9212	5.798
0.140	4.461	3.532	−0.8960	5.503
0.150	4.256	3.325	−0.8764	5.228
0.160	4.065	3.132	−0.8619	4.971
0.170	3.885	2.951	−0.8520	4.730
0.180	3.716	2.780	−0.8463	4.503
0.190	3.556	2.618	−0.8446	4.289
0.200	3.404	2.466	−0.8464	4.085
0.210	3.260	2.320	−0.8518	3.892
0.220	3.123	2.182	−0.8604	3.707
0.230	2.992	2.051	−0.8723	3.531
0.240	2.867	1.926	−0.8873	3.363
0.250	2.747	1.806	−0.9054	3.200
0.260	2.632	1.692	−0.9266	3.044
0.270	2.522	1.582	−0.9509	2.894
0.280	2.416	1.478	−0.9784	2.748
0.290	2.315	1.378	−1.009	2.607
0.300	2.217	1.282	−1.043	2.469
0.310	2.124	1.191	−1.081	2.335
0.320	2.034	1.104	−1.123	2.204
0.330	1.948	1.022	−1.168	2.075
0.340	1.866	0.9431	−1.218	1.947
0.350	1.787	0.8688	−1.272	1.820
0.360	1.713	0.7987	−1.332	1.694
0.370	1.643	0.7328	−1.398	1.567
0.380	1.576	0.6712	−1.470	1.439
0.390	1.514	0.6140	−1.550	1.308
0.400	1.456	0.5612	−1.640	1.173
0.410	1.403	0.5130	−1.739	1.031
0.420	1.355	0.4695	−1.852	0.882
0.430	1.311	0.4308	−1.981	0.721
0.440	1.273	0.3970	−2.132	0.542
0.450	1.241	0.3681	−2.311	0.340
0.460	1.213	0.3444	−2.531	0.100
0.470	1.192	0.3258	−2.817	−0.200
0.480	1.177	0.3125	−3.221	−0.615
0.490	1.168	0.3045	−3.914	−1.313
0.500	1.165	0.3018	− inf	− inf

Table C.2: The coupling coefficients comprising components of the grand resistance tensor for a particle in translating and rotating near a plane wall.

Ξ	$\log f_1^{(US)}(\Xi)$	$\log f_3^{(US)}(\Xi)$	$\log f_5^{(US)}(\Xi)$	$\log g_1^{(US)}(\Xi)$	$\log g_3^{(US)}(\Xi)$	$\log g_5^{(US)}(\Xi)$	$\log g_3^{(\Omega S)}(\Xi)$	$\log g_5^{(\Omega S)}(\Xi)$
0.001	12.55	26.14	39.08	13.24	27.06	39.77	18.76	32.36
0.010	7.942	16.93	25.26	8.635	17.85	25.96	11.85	20.85
0.020	6.555	14.16	21.10	7.249	15.07	21.80	9.774	17.38
0.030	5.744	12.53	18.68	6.438	13.45	19.37	8.558	15.35
0.040	5.168	11.38	16.95	5.862	12.30	17.64	7.694	13.91
0.050	4.721	10.49	15.61	5.416	11.41	16.30	7.024	12.79
0.060	4.355	9.762	14.51	5.051	10.68	15.21	6.476	11.88
0.070	4.045	9.145	13.59	4.743	10.06	14.28	6.012	11.11
0.080	3.776	8.611	12.79	4.476	9.528	13.48	5.609	10.44
0.090	3.537	8.140	12.08	4.240	9.057	12.77	5.253	9.855
0.100	3.323	7.718	11.45	4.029	8.635	12.14	4.935	9.328
0.110	3.129	7.337	10.88	3.838	8.254	11.57	4.646	8.852
0.120	2.950	6.988	10.35	3.663	7.906	11.05	4.382	8.417
0.130	2.785	6.668	9.874	3.503	7.586	10.57	4.138	8.017
0.140	2.631	6.371	9.430	3.353	7.290	10.12	3.912	7.646
0.150	2.487	6.094	9.016	3.214	7.014	9.709	3.700	7.301
0.160	2.351	5.835	8.629	3.083	6.756	9.322	3.502	6.979
0.170	2.222	5.592	8.265	2.960	6.513	8.958	3.316	6.676
0.180	2.099	5.362	7.922	2.843	6.285	8.615	3.139	6.390
0.190	1.981	5.145	7.598	2.732	6.068	8.291	2.972	6.120
0.200	1.869	4.938	7.290	2.626	5.863	7.983	2.813	5.863
0.210	1.760	4.742	6.997	2.524	5.668	7.691	2.662	5.619
0.220	1.655	4.554	6.718	2.426	5.481	7.411	2.517	5.387
0.230	1.553	4.374	6.452	2.331	5.303	7.145	2.378	5.165
0.240	1.454	4.201	6.196	2.239	5.132	6.889	2.246	4.952
0.250	1.357	4.035	5.951	2.149	4.967	6.644	2.118	4.748
0.260	1.262	3.874	5.716	2.061	4.809	6.409	1.996	4.552
0.270	1.168	3.719	5.489	1.975	4.655	6.182	1.878	4.363
0.280	1.076	3.569	5.271	1.890	4.507	5.964	1.766	4.182
0.290	0.9848	3.423	5.059	1.806	4.363	5.752	1.657	4.007
0.300	0.8940	3.280	4.855	1.722	4.223	5.548	1.553	3.838
0.310	0.8034	3.141	4.657	1.638	4.086	5.350	1.453	3.675
0.320	0.7126	3.005	4.464	1.554	3.952	5.157	1.357	3.517
0.330	0.6211	2.871	4.277	1.469	3.820	4.970	1.265	3.366
0.340	0.5285	2.739	4.094	1.382	3.690	4.787	1.177	3.219
0.350	0.4343	2.607	3.915	1.294	3.561	4.608	1.093	3.078
0.360	0.3379	2.476	3.739	1.203	3.433	4.432	1.014	2.942
0.370	0.2384	2.345	3.566	1.109	3.303	4.259	0.9384	2.812
0.380	0.1352	2.212	3.394	1.011	3.173	4.087	0.8676	2.687
0.390	0.0269	2.077	3.222	0.9078	3.040	3.915	0.8014	2.568
0.400	−0.0876	1.938	3.050	0.7977	2.903	3.743	0.740	2.456
0.410	−0.2103	1.794	2.875	0.6791	2.760	3.568	0.6835	2.351
0.420	−0.3434	1.641	2.695	0.5495	2.609	3.388	0.6322	2.254
0.430	−0.4905	1.477	2.506	0.4058	2.446	3.199	0.5863	2.165
0.440	−0.6563	1.296	2.304	0.2428	2.266	2.997	0.546	2.086
0.450	−0.8484	1.091	2.081	0.0531	2.063	2.775	0.5114	2.016
0.460	−1.080	0.8498	1.825	−0.1761	1.822	2.518	0.4829	1.958
0.470	−1.373	0.5479	1.512	−0.4684	1.521	2.205	0.4605	1.911
0.480	−1.783	0.1323	1.088	−0.877	1.106	1.781	0.4444	1.878
0.490	−2.479	−0.5669	0.3837	−1.572	0.407	1.077	0.4347	1.857
0.500	− inf	− inf	− inf	− inf	− inf	− inf	0.4315	1.850

Table C.3: The coupling coefficients comprising components of the grand resistance tensor for a particle in translating and rotating near a plane wall.

Ξ	$\log f_3^{(ES)}(\Xi)$	$\log f_5^{(ES)}(\Xi)$	$\log f_7^{(ES)}(\Xi)$	$\log g_3^{(ES)}(\Xi)$	$\log g_5^{(ES)}(\Xi)$	$\log g_7^{(ES)}(\Xi)$	$\log h_3^{(ES)}(\Xi)$	$\log h_5^{(ES)}(\Xi)$	$\log h_7^{(ES)}(\Xi)$
0.001	17.66	32.35	45.19	19.74	33.74	46.57	20.44	34.43	47.27
0.010	10.76	20.84	29.07	12.83	22.23	30.46	13.53	22.92	31.15
0.020	8.676	17.38	24.22	10.76	18.76	25.60	11.45	19.45	26.30
0.030	7.459	15.35	21.38	9.539	16.73	22.77	10.23	17.43	23.46
0.040	6.596	13.91	19.37	8.676	15.30	20.75	9.369	15.99	21.45
0.050	5.927	12.79	17.80	8.006	14.18	19.19	8.700	14.87	19.88
0.060	5.380	11.88	16.53	7.459	13.27	17.91	8.153	13.96	18.61
0.070	4.918	11.11	15.45	6.997	12.50	16.84	7.690	13.19	17.53
0.080	4.518	10.44	14.51	6.597	11.83	15.90	7.290	12.52	16.59
0.090	4.165	9.855	13.69	6.244	11.24	15.08	6.937	11.93	15.77
0.100	3.849	9.328	12.95	5.928	10.71	14.34	6.621	11.41	15.03
0.110	3.565	8.852	12.29	5.643	10.24	13.67	6.336	10.93	14.36
0.120	3.305	8.417	11.68	5.382	9.803	13.06	6.075	10.50	13.76
0.130	3.067	8.017	11.12	5.143	9.403	12.50	5.836	10.10	13.20
0.140	2.847	7.646	10.60	4.922	9.033	11.98	5.615	9.726	12.68
0.150	2.643	7.302	10.11	4.717	8.688	11.50	5.410	9.381	12.19
0.160	2.453	6.979	9.66	4.526	8.365	11.05	5.219	9.059	11.74
0.170	2.276	6.676	9.238	4.346	8.063	10.62	5.040	8.756	11.32
0.180	2.111	6.391	8.838	4.178	7.777	10.22	4.871	8.471	10.92
0.190	1.955	6.121	8.460	4.020	7.508	9.846	4.713	8.201	10.54
0.200	1.810	5.866	8.101	3.871	7.252	9.487	4.564	7.945	10.18
0.210	1.673	5.623	7.760	3.730	7.009	9.146	4.423	7.702	9.839
0.220	1.544	5.392	7.434	3.596	6.778	8.820	4.290	7.471	9.514
0.230	1.423	5.171	7.123	3.470	6.557	8.510	4.163	7.251	9.203
0.240	1.309	4.960	6.826	3.351	6.347	8.212	4.044	7.040	8.905
0.250	1.202	4.759	6.540	3.238	6.145	7.927	3.931	6.838	8.620
0.260	1.102	4.566	6.267	3.131	5.952	7.653	3.824	6.645	8.346
0.270	1.008	4.380	6.003	3.030	5.767	7.389	3.723	6.460	8.083
0.280	0.9204	4.203	5.750	2.934	5.589	7.136	3.627	6.282	7.829
0.290	0.8383	4.033	5.505	2.844	5.419	6.892	3.537	6.112	7.585
0.300	0.7616	3.869	5.270	2.759	5.255	6.656	3.452	5.949	7.349
0.310	0.6903	3.712	5.042	2.678	5.099	6.429	3.371	5.792	7.122
0.320	0.6241	3.562	4.823	2.603	4.949	6.209	3.296	5.642	6.902
0.330	0.5627	3.419	4.611	2.532	4.805	5.998	3.225	5.498	6.691
0.340	0.5061	3.281	4.407	2.466	4.667	5.793	3.159	5.361	6.486
0.350	0.4539	3.150	4.210	2.404	4.536	5.596	3.097	5.229	6.289
0.360	0.4061	3.025	4.020	2.347	4.412	5.406	3.040	5.105	6.099
0.370	0.3624	2.907	3.837	2.293	4.294	5.223	2.987	4.987	5.917
0.380	0.3227	2.796	3.662	2.245	4.182	5.048	2.938	4.875	5.742
0.390	0.2869	2.691	3.495	2.200	4.078	4.881	2.893	4.771	5.574
0.400	0.2547	2.594	3.336	2.159	3.980	4.723	2.853	4.674	5.416
0.410	0.2260	2.504	3.187	2.123	3.891	4.573	2.816	4.584	5.266
0.420	0.2007	2.423	3.047	2.090	3.809	4.434	2.783	4.502	5.127
0.430	0.1787	2.349	2.919	2.062	3.735	4.305	2.755	4.429	4.998
0.440	0.1598	2.284	2.803	2.037	3.671	4.189	2.730	4.364	4.883
0.450	0.1440	2.229	2.701	2.016	3.615	4.087	2.709	4.308	4.781
0.460	0.1312	2.182	2.615	1.999	3.569	4.001	2.692	4.262	4.694
0.470	0.1214	2.146	2.546	1.986	3.532	3.932	2.679	4.225	4.625
0.480	0.1143	2.120	2.495	1.977	3.506	3.881	2.670	4.199	4.574
0.490	0.1101	2.104	2.464	1.971	3.490	3.850	2.664	4.183	4.543
0.500	0.1088	2.099	2.453	1.969	3.485	3.840	2.662	4.178	4.533

Table C.4: The coupling coefficients comprising components of the grand resistance tensor for a particle in translating and rotating near a plane wall.

Appendix D

Relative rate of energy dissipation in slipping versus no-slip channels

Consider the bilinear functional,

$$E(\mathbf{a},\mathbf{b}) = \int_V \boldsymbol{\sigma}[\mathbf{a}] : \mathbf{e}[\mathbf{b}]\, dV, \tag{D.1}$$

which represents the rate of virtual work of flow **a** on flow **b**. Here, $\boldsymbol{\sigma}[\mathbf{a}]$ and $\mathbf{e}[\mathbf{b}]$ represent the stress in and the rate of strain of flows **a** and **b** respectively. If **a** and **b** are solenoidal and satisfy the Stokes equations for a fluid of viscosity η to within an arbitrary body force $\mathbf{f}[\mathbf{a}]$ or $\mathbf{f}[\mathbf{b}]$, then two independent expressions emerge, *viz.*

$$E(\mathbf{a},\mathbf{b}) = 2\eta \int_V \mathbf{e}[\mathbf{a}] : \mathbf{e}[\mathbf{b}]\, dV, \tag{D.2}$$

$$E(\mathbf{a},\mathbf{b}) = \int_S \mathbf{b}\cdot\boldsymbol{\sigma}[\mathbf{a}]\cdot\mathbf{n}\, dS + \int_V \mathbf{b}\cdot\mathbf{f}[\mathbf{a}]\, dV, \tag{D.3}$$

where S is the boundary defining the volume V with normal $\mathbf{n}$.

There two flows $\mathbf{u}$ and $\mathbf{u}^*$ such that $\mathbf{f}(\mathbf{u}) = \mathbf{f}(\mathbf{u}^*)$ and where $\mathbf{u}^*$ is zero on the boundary S. Then by linearity, there exists a flow $\mathbf{v} = \mathbf{u} - \mathbf{u}^*$ which satisfies the homogenous Stokes equations. The relative rate of energy dissipation of $\mathbf{u}$ to $\mathbf{u}^*$ is simply

$$\Delta E(\mathbf{u},\mathbf{u}^*) = E(\mathbf{u},\mathbf{u}) - E(\mathbf{u}^*,\mathbf{u}^*) = E(\mathbf{v},\mathbf{v}) + E(\mathbf{u}^*,\mathbf{v}), \tag{D.4}$$

via identity D.3. It can be shown that $E(\mathbf{v}, \mathbf{u}^*)$ is zero and therefore, via identity D.2, $E(\mathbf{u}^*, \mathbf{v})$ is also zero. Therefore, the relative rate of energy dissipation is

$$\Delta E(\mathbf{u}, \mathbf{u}^*) = E(\mathbf{v}, \mathbf{v}) \geq 0. \tag{D.5}$$

The conclusion to draw from this last statement is that the no-slip flow dissipates less energy than the slipping flow. As such, the superposition approximation often employed to account for the drag induced by a set of parallel wall boundaries in Stokes flow dissipates more energy than the solution exactly satisfying the no-slip boundary conditions on the channel walls.

Appendix E

Confinement by a slipping channel

The velocity field due to a periodic body force in a channel with shear stress free walls is subject to equations (6.4)-(6.8); however, the solution to the governing differential equations is slightly different, *viz.*

$$\mathbf{u}^{(k)}(x_3) = (\mathbf{I} - 2\pi k x_3 \mathbf{m}\mathbf{m}) \cdot \mathbf{A}^{(k)} e^{2\pi k x_3} + (\mathbf{I} + 2\pi k x_3 \hat{\mathbf{m}}\hat{\mathbf{m}}) \cdot \mathbf{B}^{(k)} e^{-2\pi k x_3} + \mathbf{U}^{(k)}(x_3), \tag{E.1}$$

for which $\mathbf{U}^{(k)}(x_3)$ remains unchanged. The unknown coefficients, $\mathbf{A}^{(k)}$ and $\mathbf{B}^{(k)}$, are determined by satisfying the no-penetration conditions: $u_3^{(k)}(0) = u_3^{(k)}(L_3) = 0$ and the zero shear stress conditions: $\partial_{x_3} u_\alpha^{(k)}(0) = \partial_{x_3} u_\alpha^{(k)}(L_3) = 0$, for $\alpha = (1, 2)$, at the channel walls. As a vector equation, these boundary conditions may be written as

$$2\pi k \mathbf{e}_3\mathbf{e}_3 \cdot \mathbf{u}^{(k)}(x_3) + (\mathbf{I} - \mathbf{e}_3\mathbf{e}_3) \cdot \frac{\partial \mathbf{u}^{(k)}}{\partial x_3} = 0, \tag{E.2}$$

for $x_3 = 0$ and $x_3 = L_3$. The solution of these equations is simplified by writing the vector normal to the walls in terms of $\mathbf{m}$ and $\hat{\mathbf{m}}$ (*i.e.* $(\mathbf{m} + \hat{\mathbf{m}}) \cdot \mathbf{u}^{(k)}(x_3) = 0$ and $(\mathbf{m} - \hat{\mathbf{m}}) \cdot \partial_{x_3} \mathbf{u}^{(k)}(x_3) = 0$ when $x_3 = 0, L_3$).

The resulting coefficients are

$$\begin{aligned}
\mathbf{m}\cdot\mathbf{A}^{(k)} &= -\hat{\mathbf{m}}\cdot\mathbf{B}^{(k)} = -\frac{1}{12\pi k}\operatorname{csch}(2\pi kH)\left[\mathbf{m}\cdot\left(2\pi k\mathbf{U}^{(k)}(H) + \left.\frac{\partial\mathbf{U}^{(k)}}{\partial x_3}\right|_H\right)\right. \\
&\quad \left. +\hat{\mathbf{m}}\cdot\left(2\pi k\mathbf{U}^{(k)}(H) - \left.\frac{\partial\mathbf{U}^{(k)}}{\partial x_3}\right|_H\right)\right], \qquad \text{(E.3)}\\
\hat{\mathbf{m}}\cdot\mathbf{A}^{(k)} &= -\mathbf{m}\cdot\mathbf{B}^{(k)} = -\frac{1}{3\pi k}e^{4\pi kH}\left(1-e^{4\pi kH}\right)^{-2}\left\{2\pi kH\cosh(2\pi kH)\left[\mathbf{m}\cdot\left(2\pi k\mathbf{U}^{(k)}(H) + \left.\frac{\partial\mathbf{U}^{(k)}}{\partial x_3}\right|_H\right)\right.\right. \\
&\quad \left. +\hat{\mathbf{m}}\cdot\left(2\pi k\mathbf{U}^{(k)}(H) - \left.\frac{\partial\mathbf{U}^{(k)}}{\partial x_3}\right|_H\right)\right] + \sinh(2\pi kH)\left[\mathbf{m}\cdot\left(4\pi k\mathbf{U}^{(k)}(H) - \left.\frac{\partial\mathbf{U}^{(k)}}{\partial x_3}\right|_H\right)\right. \\
&\quad \left.\left. +\hat{\mathbf{m}}\cdot\left(4\pi k\mathbf{U}^{(k)}(H) + \left.\frac{\partial\mathbf{U}^{(k)}}{\partial x_3}\right|_H\right)\right]\right\}, \qquad \text{(E.4)}
\end{aligned}$$

while

$$\tilde{\mathbf{m}}\cdot\mathbf{A}^{(k)} = \tilde{\mathbf{m}}\cdot\mathbf{B}^{(k)} = -\frac{1}{4\pi k}\operatorname{csch}(2\pi kH)\tilde{\mathbf{m}}\cdot\left.\frac{\partial\mathbf{U}^{(k)}}{\partial x_3}\right|_H, \tag{E.5}$$

where $\tilde{\mathbf{m}} = (2\pi k)^{-1}(2\pi k_2\mathbf{e}_1 - 2\pi k_1\mathbf{e}_2)$ and $\mathbf{I} = \mathbf{mm} + \hat{\mathbf{m}}\hat{\mathbf{m}} + \tilde{\mathbf{m}}\tilde{\mathbf{m}}$. Since the particular solution to the Stokes equations are independent of the boundary conditions, the procedures introduced in section 6.2.2 are equally applicable. One necessary change is in the reflection of the local contribution to the velocity field. The analogue to equation (6.35) for the velocity field generated by a Stokeslet above a zero shear stress boundary is simply

$$\mathbf{u}_l(\mathbf{x}) = \int_V \left[\mathbf{G}(\mathbf{r};\alpha) - \mathbf{G}(\mathbf{R};\alpha)\right]\cdot\mathbf{f}(\mathbf{x}')d\mathbf{x}'. \tag{E.6}$$

With this, similar computations of the motion of particles in a shear stress free channel are straightforward. Before concluding this section, consider a channel bounded above and below by another fluid with viscosity denoted η_w. The velocity field in this channel, $\mathbf{u}(\mathbf{x})$, can always be written as a linear superposition of the flow in a no-slip channel, $\mathbf{u}_{ns}(\mathbf{x})$, and the flow in a zero shear stress channel, $\mathbf{u}_s(\mathbf{x})$, such that

$$\mathbf{u}(\mathbf{x}) = \frac{\lambda}{1+\lambda}\mathbf{u}_s(\mathbf{x}) + \frac{1}{1+\lambda}\mathbf{u}_{ns}(\mathbf{x}), \tag{E.7}$$

where $\lambda = \eta/\eta_w$ [see *e.g.* Lee, Chadwick and Leal (1979)]. This linear superposition makes the simulation of particle motion in channels bounded by viscous fluids accessible as well.

Appendix F

Integrals for computing the particular solution to the global Stokes equations

The global contribution to the velocity field due to a set of particles is dictated by the particular solution to the Stokes equations subject to the body force in equation (6.38). This particular solution involves the computation of the series of integrals shown in equations (6.12)-(6.14) which are represented as

$$\mathbf{C}_1^{(k)}(x_3) = \sum_n e^{2\pi i k_\alpha x_\alpha^{(n)}} D_1^{(n)}(x_3)\mathbf{F}_n, \tag{F.1}$$

$$\mathbf{C}_2^{(k)}(x_3) = \sum_n e^{2\pi i k_\alpha x_\alpha^{(n)}} D_2^{(n)}(x_3)\mathbf{F}_n, \tag{F.2}$$

$$\mathbf{C}_3^{(k)}(x_3) = \sum_n e^{2\pi i k_\alpha x_\alpha^{(n)}} D_3^{(n)}(x_3)\mathbf{F}_n. \tag{F.3}$$

Since the notion of discrete forcing in the fluid has been introduced, the solution to the Stokes equations becomes a linear superposition of these forces and the necessary integrals simplify, *viz.*

$$
\begin{aligned}
D_1^{(n)}(x_3) = \frac{\sqrt{\alpha}}{8\pi} \Bigg\{ & 2e^{-\pi\alpha k^2 - \frac{\pi \Delta x_3^{(n)2}}{\alpha}} - e^{-\pi\alpha k^2 - \frac{\pi x_3^{(n)2}}{\alpha}} \left[\left(1 + \frac{x_3^{(n)}}{\alpha k}\right) e^{2\pi k x_3} + \left(1 - \frac{x_3^{(n)}}{\alpha k}\right) e^{-2\pi k x_3} \right] \\
& - \frac{e^{2\pi k \Delta x_3^{(n)}}}{\sqrt{\alpha} k} \left[\operatorname{erf}\left(\sqrt{\pi\alpha} k + \sqrt{\frac{\pi}{\alpha}} \Delta x_3^{(n)}\right) - \operatorname{erf}\left(\sqrt{\pi\alpha} k - \sqrt{\frac{\pi}{\alpha}} x_3^{(n)}\right) \right] \\
& - \frac{e^{-2\pi k \Delta x_3^{(n)}}}{\sqrt{\alpha} k} \left[\operatorname{erf}\left(\sqrt{\pi\alpha} k - \sqrt{\frac{\pi}{\alpha}} \Delta x_3^{(n)}\right) - \operatorname{erf}\left(\sqrt{\pi\alpha} k + \sqrt{\frac{\pi}{\alpha}} x_3^{(n)}\right) \right] \Bigg\}, \qquad \text{(F.4)}
\end{aligned}
$$

$$
\begin{aligned}
D_2^{(n)}(x_3) = \frac{\sqrt{\alpha}}{8\pi} \Bigg\{ & e^{-\pi\alpha k^2 - \frac{\pi \Delta x_3^{(n)2}}{\alpha}} - e^{-\pi\alpha k^2 - \frac{\pi x_3^{(n)2}}{\alpha}} \left[1 - 2\pi k x_3 \left(1 + \frac{x_3^{(n)}}{\alpha k}\right) \right] e^{2\pi k x_3} \\
& + \frac{2\pi \Delta x_3^{(n)}}{\sqrt{\alpha}} e^{2\pi k \Delta x_3^{(n)}} \left[\operatorname{erf}\left(\sqrt{\pi\alpha} k + \sqrt{\frac{\pi}{\alpha}} \Delta x_3^{(n)}\right) - \operatorname{erf}\left(\sqrt{\pi\alpha} k - \sqrt{\frac{\pi}{\alpha}} x_3^{(n)}\right) \right] \Bigg\}, \qquad \text{(F.5)}
\end{aligned}
$$

$$
\begin{aligned}
D_3^{(n)}(x_3) = \frac{\sqrt{\alpha}}{8\pi} \Bigg\{ & e^{-\pi\alpha k^2 - \frac{\pi \Delta x_3^{(n)2}}{\alpha}} - e^{-\pi\alpha k^2 - \frac{\pi x_3^{(n)2}}{\alpha}} \left[1 - 2\pi k x_3 \left(1 + \frac{x_3^{(n)}}{\alpha k}\right) \right] e^{-2\pi k x_3} \\
& - \frac{2\pi \Delta x_3^{(n)}}{\sqrt{\alpha}} e^{-2\pi k \Delta x_3^{(n)}} \left[\operatorname{erf}\left(\sqrt{\pi\alpha} k - \sqrt{\frac{\pi}{\alpha}} \Delta x_3^{(n)}\right) - \operatorname{erf}\left(\sqrt{\pi\alpha} k + \sqrt{\frac{\pi}{\alpha}} x_3^{(n)}\right) \right] \Bigg\}. \qquad \text{(F.6)}
\end{aligned}
$$

The functions, $\mathbf{C}_i^{(k)}(\mathbf{x_3})$, are weighted Fourier transformations of the forces in the fluid, where the weighting factors are the values of $D_i^{(n)}(x_3)$ as indicated in equations (F.1-F.3). This interpretation lends itself to direct computation via the fast Fourier transform technique.

Appendix G

Reflections of the local velocity field

For an approximation of the local contribution to the velocity field, one may treat the channel walls independently. Equation (6.33) expresses the local velocity field due to the reflection off the lower wall as a convolution of the local force density with the Stokeslet and its reflection. Integrals such as those in equation (6.34) for $\mathbf{G}(\mathbf{r}'';\alpha)$ are necessary. This is the contribution due to the Stokeslet. The contribution due to the reflected Stokeslet is broken into three pieces such that

$$\int_V \mathbf{J}_w(\mathbf{R},x_3')\left[\delta(\mathbf{r}')-\frac{1}{\alpha^{3/2}}\left(\frac{5}{2}-\frac{\pi {r'}^2}{\alpha}\right)e^{-\frac{\pi {r'}^2}{\alpha}}\right]d\mathbf{x}'=-\mathbf{G}(\mathbf{R}'';\alpha)+\mathbf{G}_w^{(1)}(\mathbf{R}'',x_3'';\alpha)+\mathbf{G}_w^{(2)}(\mathbf{R}'',x_3'';\alpha), \tag{G.1}$$

where

$$\mathbf{G}_w^{(1)}(\mathbf{R}'',x_3'';\alpha)=\nabla_x^2\int_V {x_3'}^2\mathbf{J}(\mathbf{R})\left[\delta(\mathbf{r}')-\frac{1}{\alpha^{3/2}}\left(\frac{5}{2}-\frac{\pi {r'}^2}{\alpha}\right)e^{-\frac{\pi {r'}^2}{\alpha}}\right]d\mathbf{x}'\cdot(\mathbf{I}-2\mathbf{e}_3\mathbf{e}_3)\,, \tag{G.2}$$

and

$$\mathbf{G}_w^{(2)}(\mathbf{R}'',x_3'';\alpha)=-2\left\{(\mathbf{I}-2\mathbf{e}_3\mathbf{e}_3)\cdot\nabla_x\int_V x_3'\mathbf{J}(\mathbf{R})\left[\delta(\mathbf{r}')-\frac{1}{\alpha^{3/2}}\left(\frac{5}{2}-\frac{\pi {r'}^2}{\alpha}\right)e^{-\frac{\pi {r'}^2}{\alpha}}\right]d\mathbf{x}'\cdot\mathbf{e}_3\right\}^T. \tag{G.3}$$

Again, in order to avoid computing these integrals directly one simply writes them in terms of $\mathbf{G}(\mathbf{R}''; \alpha)$. This is accomplished by taking the appropriate derivatives of $\mathbf{G}(\mathbf{R}''; \alpha)$ with respect to x_3'' such that

$$\begin{aligned} \mathbf{H}(\mathbf{R}''; \alpha) &= \int_V x_3' \mathbf{J}(\mathbf{R}) \left[\delta(\mathbf{r}') - \frac{1}{\alpha^{3/2}} \left(\frac{5}{2} - \frac{\pi {r'}^2}{\alpha} \right) e^{-\frac{\pi {r'}^2}{\alpha}} \right] d\mathbf{x}' \\ &= x_3'' \mathbf{G}(\mathbf{R}''; \alpha) + \frac{\alpha}{2\pi} \frac{\partial}{\partial x_3''} \left[\mathbf{G}(\mathbf{R}''; \alpha) + \mathbf{J}(\mathbf{R}'') \right] + \frac{1}{\alpha^{3/2}} \int_V (x_3' - x_3'') \mathbf{J}(\mathbf{R}) e^{-\frac{\pi {r'}^2}{\alpha}} d\mathbf{x}' \end{aligned} \tag{G.4}$$

and similarly

$$\begin{aligned} \int_V {x_3'}^2 \mathbf{J}(\mathbf{R}) \left[\delta(\mathbf{r}') - \frac{1}{\alpha^{3/2}} \left(\frac{5}{2} - \frac{\pi {r'}^2}{\alpha} \right) e^{-\frac{\pi {r'}^2}{\alpha}} \right] d\mathbf{x}' &= x_3'' \mathbf{H}(\mathbf{R}''; \alpha) \\ + \frac{\alpha}{2\pi} \frac{\partial}{\partial x_3''} \left[\mathbf{H}(\mathbf{R}''; \alpha) - x_3'' \mathbf{J}(\mathbf{R}''; \alpha) \right] &+ \frac{1}{\alpha^{3/2}} \int_V x_3' (x_3' - x_3'') \mathbf{J}(\mathbf{R}) e^{-\frac{\pi {r'}^2}{\alpha}} d\mathbf{x}'. \end{aligned} \tag{G.5}$$

What remains then is to convolute the reflected Stokeslet with a Gaussian and then calculate the derivatives of that integral with respect to $\mathbf{x}_3''$. This is quite difficult to compute in general, but when that integral is written more suggestively as,

$$\mathbf{v}(\mathbf{x}) = \frac{1}{\alpha^{3/2}} \left(\int_V \mathbf{J}(\mathbf{R}) e^{-\frac{\pi {r'}^2}{\alpha}} d\mathbf{x}' \right) \cdot \mathbf{F}, \tag{G.6}$$

a physical interpretation becomes rather obvious. This is the velocity field, $\mathbf{v}(\mathbf{x})$, at $\mathbf{x}$ due to a Gaussian distributed body force of magnitude $\mathbf{F}$ centered on $\mathbf{x}'' - 2x_3''\mathbf{e}_3$ and is the solution to the equations:

$$\eta \nabla_x^2 \mathbf{v}(\mathbf{x}) = \nabla p - \frac{1}{\alpha^{3/2}} e^{-\frac{\pi {R''}^2}{\alpha}} \mathbf{F}, \tag{G.7}$$

$$\nabla \cdot \mathbf{v}(\mathbf{x}) = 0. \tag{G.8}$$

This is solved using the standard Fourier transform technique [see *e.g.* Kim and Karrila (2005)] and a relatively simple expression for the integral in equation (G.6) is found:

$$\begin{aligned}\mathbf{v}(\mathbf{x}) = \frac{1}{4\pi\eta}\left(\frac{1}{4\pi\alpha^{1/2}R''^3}\right)&\Big\{\mathbf{I}\left[2\alpha^{1/2}(2\pi R''^2-\alpha)-4\pi R''^3\left(\tilde{\phi}_{-1/2}-\tilde{\phi}_{1/2}\right)\right]\\ &-\left(\mathbf{I}-\hat{\mathbf{R}}''\hat{\mathbf{R}}''\right)\left[\alpha^{1/2}(2\pi R''^2-3\alpha)+2\pi R''^3\left(\tilde{\phi}_{-1/2}-3\tilde{\phi}_{1/2}\right)\right]\Big\}\cdot\mathbf{F},\end{aligned} \tag{G.9}$$

where

$$\tilde{\phi}_k = \phi_k\left(\frac{\pi R''^2}{\alpha}\right). \tag{G.10}$$

For reference, the identities below were derived for this purpose:

$$\int_V e^{2\pi i\mathbf{x}\cdot\boldsymbol{\xi}} f(\xi)d\boldsymbol{\xi} = \frac{2}{r}\int_0^\infty \xi\sin(2\pi\xi r)f(\xi)d\xi, \tag{G.11}$$

and

$$\int_V e^{2\pi i\mathbf{x}\cdot\boldsymbol{\xi}} f(\xi)\hat{\boldsymbol{\xi}}\hat{\boldsymbol{\xi}}d\boldsymbol{\xi} = X_1\mathbf{I} + X_2\hat{\mathbf{x}}\hat{\mathbf{x}}, \tag{G.12}$$

where

$$X_1 = \int_0^\infty \left(2\pi^2 r^3\xi\right)^{-1}\left[\sin(2\pi\xi r) - 2\pi\xi r\cos(2\pi\xi r)\right]f(\xi)d\xi, \tag{G.13}$$

$$X_2 = \int_0^\infty \left(2\pi^2 r^3\xi\right)^{-1}\left[6\pi\xi r\cos(2\pi\xi r) - \left(3-(2\pi\xi r)^2\right)\sin(2\pi\xi r)\right]f(\xi)d\xi, \tag{G.14}$$

both of which are absolutely convergent for all $f(\xi) \sim o(\xi^{-2})$ as $\xi \to 0$. With this, it is straightforward to show that

$$
\begin{aligned}
\frac{1}{\alpha^{3/2}} \int_V x_3' \mathbf{J}(\mathbf{R}) e^{-\frac{\pi {r'}^2}{\alpha}} = {} & \frac{1}{4\pi\eta} \left(\frac{1}{8\pi^2 \alpha^{1/2} {R''}^7} \right) \\
& \times \Big\{ \mathbf{I} \Big[x_3'' \Big(2\pi\alpha^{1/2} {R''}^4 \Big[2\pi {R''}^2 + \alpha \Big] - 4\pi^2 {R''}^7 \Big[\tilde{\phi}_{-1/2} + \tilde{\phi}_{1/2} \Big] \Big) \\
& - R_3'' \Big(\alpha^{3/2} {R''}^2 \Big[2\pi {R''}^2 + 3\alpha \Big] - 4\pi^2 {R''}^7 \Big[\tilde{\phi}_{1/2} + \tilde{\phi}_{3/2} \Big] \Big) \Big] \\
& + (\mathbf{R}''\mathbf{e}_3 + \mathbf{e}_3\mathbf{R}'') \Big[\alpha^{3/2} {R''}^2 \Big(2\pi {R''}^2 - 3\alpha \Big) - 2\pi\alpha {R''}^5 \Big[\tilde{\phi}_{-1/2} - 3\tilde{\phi}_{1/2} \Big] \Big] \\
& + \mathbf{R}''\mathbf{R}'' \Big[x_3'' \Big(2\pi\alpha^{1/2} {R''}^2 \Big[2\pi {R''}^2 - 6\alpha \Big] - 4\pi {R''}^5 \Big[\tilde{\phi}_{-1/2} - 3\tilde{\phi}_{1/2} \Big] \Big) \\
& - R_3'' \Big(3\alpha^{3/2} \Big[2\pi {R''}^2 - 5\alpha \Big] - 4\pi {R''}^3 \Big[\alpha\tilde{\phi}_{-1/2} + \Big(\pi {R''}^2 - 3\alpha \Big) \tilde{\phi}_{1/2} - 3\pi {R''}^2 \tilde{\phi}_{3/2} \Big] \Big) \Big] \Big\} ,
\end{aligned}
\tag{G.15}
$$

and

$$
\begin{aligned}
\frac{1}{\alpha^{3/2}} \int_V x_3' (x_3' - x_3'') \mathbf{J}(\mathbf{R}) e^{-\frac{\pi {r'}^2}{\alpha}} = {} & \frac{1}{4\pi\eta} \left(\frac{1}{16\pi^3 \alpha^{1/2} {R''}^9} \right) \\
& \times \Big\{ \mathbf{I} \Big[4\alpha^{3/2} {R''}^4 \Big(\pi^2 {R''}^4 - 3\alpha^2 \Big) - 4\pi^2 {R''}^9 \Big(\tilde{\phi}_{-1/2} - \tilde{\phi}_{3/2} \Big) \\
& - x_3'' R_3'' \Big(2\pi\alpha^{3/2} {R''}^4 \Big[2\pi {R''}^2 + 3\alpha \Big] - 8\pi^3 {R''}^9 \Big[\tilde{\phi}_{1/2} + \tilde{\phi}_{3/2} \Big] \Big) \\
& + {R_3''}^2 \Big(3\alpha^{5/2} {R''}^2 \Big[2\pi {R''}^2 + 5\alpha \Big] - 8\pi^3 {R''}^9 \Big[\tilde{\phi}_{3/2} + \tilde{\phi}_{5/2} \Big] \Big) \Big] \\
& + \mathbf{e}_3\mathbf{e}_3 \Big[2\alpha^{5/2} {R''}^4 \Big(2\pi {R''}^2 - 3\alpha \Big) - 4\pi\alpha^2 {R''}^7 \Big(\tilde{\phi}_{-1/2} - 3\tilde{\phi}_{1/2} \Big) \Big] \\
& + (\mathbf{R}''\mathbf{e}_3 + \mathbf{e}_3\mathbf{R}'') \Big[x_3'' \Big(2\pi\alpha^{3/2} {R''}^4 \Big[2\pi {R''}^2 - 3\alpha \Big] - 2\pi^2\alpha {R''}^7 \Big[\tilde{\phi}_{-1/2} - 3\tilde{\phi}_{1/2} \Big] \Big) \\
& - R_3'' \Big(6\alpha^{5/2} {R''}^2 \Big[2\pi {R''}^2 - 5 \Big] - 8\pi\alpha {R''}^5 \Big[\alpha\tilde{\phi}_{-1/2} + \Big(\pi {R''}^2 - 3\alpha \Big) \tilde{\phi}_{1/2} - 3\pi {R''}^2 \tilde{\phi}_{3/2} \Big] \Big) \Big] \\
& - \mathbf{R}''\mathbf{R}'' \Big[3\alpha^{5/2} {R''}^2 \Big(2\pi {R''}^2 - 5\alpha \Big) - 2\pi\alpha^{3/2} {R''}^4 \Big(2\pi {R''}^2 - 3\alpha \Big) \\
& + 4\pi\alpha {R''}^5 \Big(\Big[\pi {R''}^2 - \alpha \Big] \tilde{\phi}_{-1/2} - \Big[4\pi {R''}^2 + 3\alpha \Big] \tilde{\phi}_{1/2} + 3\pi {R''}^2 \tilde{\phi}_{3/2} \Big) \\
& + x_3'' R_3'' \Big(6\pi\alpha^{3/2} {R''}^2 \Big[2\pi {R''}^2 - 5\alpha \Big] - 8\pi^2 {R''}^5 \Big[\alpha\tilde{\phi}_{-1/2} + \Big(\pi {R''}^2 - 3\alpha \Big) \tilde{\phi}_{1/2} - 3\pi {R''}^2 \tilde{\phi}_{3/2} \Big] \Big) \\
& - {R_3''}^2 \Big(15\alpha^{5/2} \Big[2\pi {R''}^2 - 7\alpha \Big] - 8\pi\alpha {R''}^3 \Big[2\alpha\tilde{\phi}_{-1/2} + 2\pi {R''}^2 \Big(\pi {R''}^2 - 3\alpha \Big) \tilde{\phi}_{1/2} \\
& + \Big(\pi {R''}^2 - 6\alpha \Big) \tilde{\phi}_{3/2} - 3\pi^2 {R''}^4 \tilde{\phi}_{5/2} \Big] \Big) \Big] \Big\} ,
\end{aligned}
\tag{G.16}
$$

by using the same formalism as above. After some tedious algebra during which the results from equations (G.4), (G.5) and (G.9) are combined, the reflection tensor can be computed. This is available from the publisher's office; however, a few salient details are described. The reflection tensor scales as $\exp(-\pi R^2/\alpha)$ as might be expected. However, neither the doublet or source-doublet contributions to the reflection has that same exponential scaling. This is of critical importance since it is only the sum of these two terms weighted exactly as described by Blake (1971) which has the appropriate scaling. As is usually the case with Stokes flow, there is almost no middle ground between the simplest approximations and fully developed solutions. An approximation which neglects or mis-weights either of these terms will not decay exponentially and the entire argument for splitting the disturbance velocity into two contributions becomes invalid.

$$
\begin{aligned}
\mathbf{G}_w(\mathbf{R}'', x_3''; \alpha) &= \frac{1}{4\pi\eta} \left(\frac{1}{2\pi^2 \alpha^{7/2} {R''}^{9}} \right) \qquad \text{(G.17)} \\
&\times \Big\{ \mathbf{I} \Big[2\alpha^3 {R''}^{3} \Big(\alpha^2 {R''}^{2} - \pi^2 {R''}^{6} + \alpha R_3'' \Big[2\pi x_3'' {R''}^{2} - \Big(\pi {R''}^{2} + 4\alpha \Big) R_3'' \Big] \Big) \tilde{\phi}_{-1/2} \\
&- \alpha^2 {R''}^{3} \Big(6\alpha^3 {R''}^{2} - 2\pi\alpha^2 {R''}^{4} + 9\pi^2 \alpha {R''}^{6} - 2\pi^3 {R''}^{6} \Big[{R''}^{2} - 10 {x_3''}^{2} \Big] \\
&+ 4\pi x_3'' R_3'' {R''}^{2} \Big[\pi^2 {R''}^{4} - \pi\alpha {R''}^{2} + 3\alpha^2 \Big] + 2\alpha {R_3''}^{2} \Big[\pi^2 {R''}^{4} + \pi\alpha {R''}^{2} - 12\alpha^2 \Big] \Big) \tilde{\phi}_{1/2} \\
&+ \pi\alpha {R''}^{5} \Big(-6\alpha^3 {R''}^{2} + 21\pi\alpha^2 {R''}^{4} + 16\pi^2 \alpha {R''}^{6} + 36\pi^3 {x_3''}^{2} {R''}^{6} \\
&+ 2\alpha R_3'' \Big[2\pi x_3'' {R''}^{2} \Big(23\pi {R''}^{2} - 3\alpha \Big) + R_3'' \Big(2\pi^2 {R''}^{4} + \pi\alpha {R''}^{2} + 12\alpha^2 \Big) \Big] \Big) \tilde{\phi}_{3/2} \\
&- 2\pi^2 {R''}^{7} \Big(5\alpha^3 {R''}^{2} + 12\pi\alpha^2 {R''}^{4} + 2\pi^2 \alpha {R''}^{6} + 4\pi^3 {x_3''}^{2} \\
&+ 2\alpha R_3'' \Big[\pi {R''}^{2} \Big(24\pi {R''}^{2} + 5\alpha \Big) + \alpha R_3'' \Big(20\pi {R''}^{2} - 3\alpha \Big) \Big] \Big) \tilde{\phi}_{5/2} \\
&+ 4\pi^3 {R''}^{9} \Big(\alpha {R''}^{2} \Big[\pi {R''}^{2} + \alpha \Big] + 2\pi x_3'' R_3'' {R''}^{2} \Big[2\pi {R''}^{2} + \alpha \Big] \alpha R_3'' \Big[15\pi {R''}^{2} + 7\alpha \Big] \Big) \tilde{\phi}_{7/2} \\
&- 8\pi^4 {R_3''}^{2} {R''}^{11} \Big(\pi {R''}^{2} + \alpha \Big) \tilde{\phi}_{9/2} \Big] \\
&+ \mathbf{e}_3 \mathbf{e}_3 \Big[-\alpha^4 {R''}^{3} \Big(10\alpha {R''}^{2} + \pi {R''}^{4} + 20\pi x_3'' R_3'' {R''}^{2} - 8 {R_3''}^{2} \Big[\pi {R''}^{2} + 8\alpha \Big] \Big) \tilde{\phi}_{-1/2} \\
&+ \alpha^2 {R''}^{3} \Big(30\alpha^3 {R''}^{2} - 7\pi\alpha^2 {R''}^{4} + 14\pi^2 \alpha {R''}^{6} + 40\pi^3 {R_3''}^{2} {R''}^{6} \\
&- 4\pi x_3'' R_3'' {R''}^{2} \Big[6\pi^2 {R''}^{4} + 5\pi\alpha {R''}^{2} - 16\alpha^2 \Big] + 8\alpha {R_3''}^{2} \Big[\pi^2 {R''}^{4} + 5\pi\alpha {R''}^{2} - 24\alpha^2 \Big] \Big) \tilde{\phi}_{1/2} \\
&+ 2\pi\alpha {R''}^{5} \Big(15\alpha^3 {R''}^{2} - 11\pi\alpha^2 {R''}^{4} - 14\pi^2 \alpha {R''}^{6} - 36\pi^3 R_3'' {R''}^{6} \\
&+ 2\pi {R''}^{2} x_3'' R_3'' {R''}^{2} \Big[4\pi^2 {R''}^{4} - 30\pi\alpha {R''}^{2} + 16\alpha^2 \Big] + 4\alpha {R_3''}^{2} \Big[3\pi {R''}^{4} + \pi\alpha {R''}^{2} - 24\alpha^2 \Big] \Big) \tilde{\phi}_{3/2} \\
&+ 4\pi^2 {R''}^{7} \Big(2\alpha^3 {R''}^{2} + 11\pi\alpha^2 {R''}^{4} + 2\pi^2 \alpha {R''}^{6} + 4\pi^3 x_3'' {R''}^{6} \\
&+ 4\alpha R_3'' \Big[\pi x_3'' {R''}^{2} \Big(11\pi {R''}^{2} + \alpha \Big) - R_3'' \Big(\pi^2 {R''}^{4} - 4\pi\alpha {R''}^{2} + 6\alpha^2 \Big) \Big] \Big) \tilde{\phi}_{5/2} \\
&- 8\pi^3 {R''}^{9} \Big(\alpha {R''}^{2} \Big[\pi {R''}^{2} + \alpha \Big] + 2\pi x_3'' R_3'' \Big[2\pi {R''}^{2} + \alpha \Big] + \alpha {R_3''}^{2} \Big[13\pi {R''}^{2} + \alpha \Big] \Big) \tilde{\phi}_{7/2} \\
&+ 16\pi^4 {R_3''}^{2} {R''}^{11} \Big(\pi {R''}^{2} + \alpha \Big) \tilde{\phi}_{9/2} \ ]
\end{aligned}
$$

$$
\begin{aligned}
&+ \mathbf{R}''\mathbf{e}_3 \Big[2\alpha^4 R'' \Big(-3\pi x_3'' {R''}^4 + R_3'' \Big[24\alpha {R''}^2 + \pi {R''}^4 + 24\pi x_3'' R_3'' {R''}^2 - 8{R_3''}^2 \Big(\pi {R''}^2 + 9\alpha\Big)\Big]\Big) \tilde{\phi}_{-1/2} \\
&+ 2\alpha^2 R'' \Big(\pi x_3'' {R''}^4 \Big[2\pi^2 {R''}^4 - 3\pi\alpha {R''}^2 + 9\alpha^2\Big] + \alpha R_3'' \Big[\pi {R''}^2 - 3\alpha\Big] \\
&\quad \times \Big[24\alpha {R''}^2 + \pi {R''}^4 + 24\pi x_3'' R_3'' {R''}^2 - 8R_3'' \Big(\pi {R''}^2 + 9\alpha\Big)\Big]\Big) \tilde{\phi}_{1/2} \\
&- 2\pi\alpha {R''}^3 \Big(-\pi\alpha x_3'' {R''}^4 \Big[16\pi {R''}^2 + 9\alpha\Big] + R_3'' \Big[72\alpha^3 {R''}^2 - 9\pi\alpha^2 {R''}^4 - 8\pi^2\alpha {R''}^6 - 28\pi^3 x_3'' {R''}^6 \\
&+4 x_3'' R_3'' \Big(2\pi^2 {R''}^4 - 3\pi\alpha {R''}^2 + 18\alpha^2\Big) + \alpha R_3'' \Big(\pi^2 {R''}^4 + 3\pi\alpha {R''}^2 - 54\alpha^2\Big)\Big]\Big) \tilde{\phi}_{3/2} \\
&- 4\pi {R''}^5 \Big(\pi\alpha x_3'' {R''}^4 \Big[2\pi {R''}^2 + 3\alpha\Big] + R_3'' \Big[18\alpha^3 {R''}^2 + 25\pi\alpha^2 {R''}^4 + 2\pi^2\alpha {R''}^6 + 4\pi^3 x_3'' {R''}^6 \\
&+2\alpha R_3'' \Big(\pi x_3'' \Big[20\pi {R''}^2 + 9\alpha\Big] - R_3'' \Big[2\pi^2 {R''}^4 + 27\alpha^2\Big]\Big)\Big]\Big) \tilde{\phi}_{5/2} \\
&+ 8\pi^3 R_3'' {R''}^7 \Big(2\alpha {R''}^2 \Big[\pi {R''}^2 + 3\alpha\Big] + 2\pi x_3'' R_3'' \Big[2\pi {R''}^2 + 3\alpha\Big] + \alpha R_3'' \Big[13\pi {R''}^2 + 9\alpha\Big]\Big) \tilde{\phi}_{7/2} \\
&-16\pi^4 x_3'' {R''}^9 \Big(\pi {R''}^2 + 3\alpha\Big) \tilde{\phi}_{9/2}\Big] \\
&+ \mathbf{e}_3\mathbf{R}'' \Big[2\alpha^4 {R''}^3 \Big(3\pi x_3'' {R''}^2 - R_3'' \Big[\pi {R''}^2 + 12\alpha\Big]\Big) \tilde{\phi}_{-1/2} \\
&+ 2\alpha^2 {R''}^3 \Big(\pi x_3'' {R''}^2 \Big[8\pi^2 {R''}^4 + 3\pi\alpha {R''}^2 - 9\alpha^2\Big] - \alpha R_3'' \Big[\pi {R''}^2 - 3\alpha\Big] \Big[\pi {R''}^2 + 12\alpha\Big]\Big) \tilde{\phi}_{1/2} \\
&- 2\pi\alpha {R''}^5 \Big(\pi x_3'' {R''}^2 \Big[4\pi^2 {R''}^4 + 16\pi\alpha {R''}^2 + 9\alpha^2\Big] + \alpha R_3'' \Big[8\pi^2 {R''}^4 + 3\pi\alpha {R''}^2 - 36\alpha^2\Big]\Big) \tilde{\phi}_{3/2} \\
&+ 4\pi^2\alpha {R''}^7 \Big(\pi x_3'' {R''}^2 \Big[2\pi {R''}^2 + 3\alpha\Big] + R_3'' \Big[2\pi^2 {R''}^4 + 12\pi\alpha {R''}^2 + 9\alpha^2\Big]\Big) \tilde{\phi}_{5/2} \\
&-8\pi^2\alpha {R''}^9 \Big(\pi {R''}^2 + 3\alpha\Big) \tilde{\phi}_{7/2}\Big] \\
&+ \mathbf{R}''\mathbf{R}'' \Big[-\alpha^4 R'' \Big(12\alpha {R''}^2 - \pi {R''}^4 + 8R_3'' \Big[3\pi x_3'' {R''}^2 - R_3'' \Big(\pi {R''}^2 + 9\alpha\Big)\Big]\Big) \tilde{\phi}_{-1/2} \\
&+ \alpha R'' \Big(36\alpha^3 {R''}^2 - 16\pi\alpha^2 {R''}^4 + \pi^2\alpha {R''}^6 - 2\pi^3 {R''}^8 \\
&-8\alpha R_3'' \Big[\pi {R''}^2 - 3\alpha\Big] \Big[3\pi x_3'' {R''}^2 - R_3'' \Big(\pi {R''}^2 + 9\alpha\Big)\Big]\Big) \tilde{\phi}_{1/2} \\
&+ \pi\alpha {R''}^3 \Big(36\alpha^3 {R''}^2 - 9\pi\alpha^2 {R''}^4 - 12\pi^2\alpha {R''}^6 - 28\pi^3 {x_3''}^2 {R''}^6 \\
&+4R_3'' \Big[\pi x_3'' {R''}^2 \Big(2\pi^2 {R''}^4 - 3\pi\alpha {R''}^2 + 18\alpha^2\Big) + \alpha R_3'' \Big(\pi^2 {R''}^4 + 3\pi\alpha {R''}^2 - 54\alpha^2\Big)\Big]\Big) \tilde{\phi}_{3/2} \\
&+ 2\pi^2 {R''}^5 \Big(9\alpha^3 {R''}^2 + 14\pi\alpha^2 {R''}^4 + 2\pi^2\alpha {R''}^6 + 4\pi^3 {x_3''}^2 {R''}^6 \\
&+2\alpha R_3'' \Big[\pi x_3'' {R''}^2 \Big(20\pi {R''}^2 + 9\alpha\Big) - R_3'' \Big(2\pi^2 {R''}^4 + 27\alpha^2\Big)\Big]\Big) \tilde{\phi}_{5/2} \\
&- 4\pi^3 {R''}^7 \Big(\alpha {R''}^2 \Big[\pi {R''}^2 + 3\alpha\Big] + 2\pi x_3'' R_3'' {R''}^2 \Big[2\pi {R''}^2 + 3\alpha\Big] + \alpha {R_3''}^2 \Big[13\pi {R''}^2 + 9\alpha\Big]\Big) \tilde{\phi}_{7/2} \\
&+ 8\pi^4 {R_3''}^2 {R''}^9 \Big(\pi {R''}^2 + 3\alpha\Big) \tilde{\phi}_{9/2}\Big]\Big\} .
\end{aligned}
$$

This essentially concludes the derivation of the single wall reflection of the real-space contribution to the Ewald-like force density in the fluid. It is worth noting however, that if the radius of curvature of the wall is large relative to $\sqrt{\alpha}$ it may be possible to employ this result in simulations of non-planar bounding geometries. The reason for this is obvious. Since the force density decays exponentially fast for small values of $\sqrt{\alpha}$, a wall with a sufficiently large radius of curvature appears to be locally flat. This should be rather useful for studying the motion of particles in a tube [see *e.g.* Liron (1984)] as well as particles in other curvilinear confinements.

Appendix H

Wave-space contributions to the "self" mobility tensors

Because the global disturbance velocity determined in these simulations is combined with Faxén formulas to compute the grand mobility tensor, care must be taken so that the "self" contribution is not over counted. That is, each particle must not sense its own contribution to the global disturbance flow. Therefore, this contribution is computed explicitly *a priori* and the appropriate Faxén formulas applied so that for each particle n a given fractional distance across the channel denoted (Ξ) and for a given dimensionless splitting parameter $\beta = \alpha / L_3^2$, the wave space contribution to the self mobility tensors is removed from any calculations. To simplify things, the torque and stresslet are summed into a generalized doublet denoted $\mathbf{D}$, and the rotation and rate of strain are summed into a generalized velocity gradient denoted $\nabla \mathbf{u}(\mathbf{x})$. Through symmetry arguments and fluid incompressibility it can be shown that the coupling between velocity and doublet takes the form,

$$\begin{aligned}\mathbf{M}_{UD}^{S} = \frac{1}{6\pi\eta a_n^2} \Bigg\{ & \left[f_2^{(UD)}(\Xi,\beta) \left(\frac{a_n}{L_3}\right)^2 - f_4^{(UD)}(\Xi,\beta) \left(\frac{a_n}{L_3}\right)^4 + f_6^{(UD)}(\Xi,\beta) \left(\frac{a_n}{L_3}\right)^6 \right] \mathbf{I}\mathbf{e}_3 \\ & + \left[g_2^{(UD)}(\Xi,\beta) \left(\frac{a_n}{L_3}\right)^2 - g_4^{(UD)}(\Xi,\beta) \left(\frac{a_n}{L_3}\right)^4 + g_6^{(UD)}(\Xi,\beta) \left(\frac{a_n}{L_3}\right)^6 \right] (\mathbf{e}_3\mathbf{I} - 2\mathbf{e}_3\mathbf{e}_3\mathbf{e}_3) \\ & + \left[h_2^{(UD)}(\Xi,\beta) \left(\frac{a_n}{L_3}\right)^2 - h_4^{(UD)}(\Xi,\beta) \left(\frac{a_n}{L_3}\right)^4 + h_6^{(UD)}(\Xi,\beta) \left(\frac{a_n}{L_3}\right)^6 \right] \mathbf{I}\mathbf{e}_3^T \cdot \Bigg\}, \end{aligned} \qquad \text{(H.1)}$$

while the coupling between velocity gradient and doublet can be written as

$$\begin{aligned}
\mathbf{M}_{\nabla D} = \frac{1}{6\pi\eta a_n^3} \Bigg\{ &- \left[f_3^{(ES)}(\Xi,\beta)\left(\frac{a_n}{L_3}\right)^3 - f_5^{(ES)}(\Xi,\beta)\left(\frac{a_n}{L_3}\right)^5 + f_7^{(ES)}(\Xi,\beta)\left(\frac{a_n}{L_3}\right)^7 \right] \left[(\delta_{ij} - \delta_{i3}\delta_{j3})(\delta_{kl} - \delta_{k3}\delta_{l3}) \right. \\
&\quad \left. -2(\delta_{ij} - \delta_{i3}\delta_{j3})\delta_{k3}\delta_{l3} - 2\delta_{i3}\delta_{j3}(\delta_{kl} - \delta_{k3}\delta_{l3}) + 4\delta_{i3}\delta_{j3}\delta_{k3}\delta_{l3} \right] \\
&- \left[g_3^{(ES)}(\Xi,\beta)\left(\frac{a_n}{L_3}\right)^3 - g_5^{(ES)}(\Xi,\beta)\left(\frac{a_n}{L_3}\right)^5 + g_7^{(ES)}(\Xi,\beta)\left(\frac{a_n}{L_3}\right)^7 \right] \\
&\quad \times \left[(\delta_{ik} - \delta_{i3}\delta_{k3})(\delta_{jl} - \delta_{j3}\delta_{l3}) + (\delta_{il} - \delta_{i3}\delta_{l3})(\delta_{jk} - \delta_{j3}\delta_{k3}) \right. \\
&\quad\quad \left. -2(\delta_{ij} - \delta_{i3}\delta_{j3})\delta_{k3}\delta_{l3} - 2\delta_{i3}\delta_{j3}(\delta_{kl} - \delta_{k3}\delta_{l3}) + 4\delta_{i3}\delta_{j3}\delta_{k3}\delta_{l3} \right] \\
&- \left[h_3^{(ES)}(\Xi,\beta)\left(\frac{a_n}{L_3}\right)^3 - h_5^{(ES)}(\Xi,\beta)\left(\frac{a_n}{L_3}\right)^5 + h_7^{(ES)}(\Xi,\beta)\left(\frac{a_n}{L_3}\right)^7 \right] \\
&\quad \times \left[(\delta_{ik} - \delta_{i3}\delta_{k3})\delta_{j3}\delta_{l3} + (\delta_{il} - \delta_{i3}\delta_{l3})\delta_{j3}\delta_{k3} + (\delta_{jk} - \delta_{j3}\delta_{k3})\delta_{i3}\delta_{l3} + (\delta_{jl} - \delta_{j3}\delta_{l3})\delta_{i3}\delta_{k3} \right] \Bigg\} \mathbf{e}_i\mathbf{e}_j\mathbf{e}_k\mathbf{e}_l .
\end{aligned} \tag{H.2}$$

The coupling between velocity gradient and force is simply the transpose of the velocity-doublet coupling. These are easily computed in much the same fashion as the self contribution to $\mathbf{M}_{UF}$ from the wave space disturbance flow. Plotting them is not instructive, however, and further discussion of the details and resulting tabulations may be undertaken through correspondence with the authors.

Appendix I

Tables of data from Chapter 6

I.1 Sedimentation rate of square particle lattices

S/L_3	$6\pi\eta aU_1/F_1$ ($\Xi = 1/2$)	$6\pi\eta aU_3/F_3$ ($\Xi = 1/2$)	$6\pi\eta aU_1/F_1$ ($\Xi = 1/4$)	$6\pi\eta aU_3/F_3$ ($\Xi = 1/4$)
0.41667	0.47304	0.11327	0.7149	0.10167
0.48125	0.41497	0.16863	0.60421	0.14113
0.54583	0.39398	0.22884	0.5433	0.18072
0.61042	0.39248	0.28521	0.50952	0.21453
0.675	0.4013	0.33501	0.49146	0.24115
0.73958	0.41483	0.37744	0.48236	0.26084
0.80417	0.43056	0.41285	0.47916	0.27489
0.86875	0.44691	0.44184	0.47958	0.28476
0.93333	0.463	0.46518	0.4822	0.29166
0.99792	0.47836	0.48367	0.4861	0.29648
1.0625	0.49277	0.4981	0.4907	0.29987
1.12708	0.50615	0.5092	0.49559	0.30224
1.19167	0.51848	0.5176	0.50055	0.30389
1.25625	0.5298	0.52388	0.5054	0.30503
1.32083	0.54016	0.52849	0.51005	0.30581
1.38542	0.54963	0.53182	0.51444	0.30632
1.45	0.55828	0.53418	0.51854	0.30665
1.51458	0.56618	0.53582	0.52235	0.30685
1.57917	0.5734	0.53692	0.52586	0.30695
1.64375	0.58	0.53764	0.52908	0.30698
1.70833	0.58604	0.53808	0.53204	0.30697
1.77292	0.59156	0.53833	0.53475	0.30693
1.8375	0.59663	0.53844	0.53722	0.30686
1.90208	0.60127	0.53846	0.53949	0.30678
1.96667	0.60553	0.53842	0.54156	0.30668
2.03125	0.60944	0.53835	0.54345	0.30659
2.09583	0.61304	0.53825	0.54518	0.30648
2.16042	0.61636	0.53814	0.54677	0.30637
2.225	0.61942	0.53802	0.54823	0.30626
2.28958	0.62224	0.5379	0.54956	0.30615
2.35417	0.62485	0.53778	0.55079	0.30603
2.41875	0.62726	0.53766	0.55192	0.30591
2.48333	0.62949	0.53754	0.55296	0.30579
2.54792	0.63156	0.53742	0.55392	0.30567
2.6125	0.63349	0.53731	0.5548	0.30555
2.67708	0.63527	0.53719	0.55562	0.30542
2.74167	0.63693	0.53707	0.55637	0.30529
2.80625	0.63848	0.53696	0.55706	0.30516
2.87083	0.63991	0.53684	0.55771	0.30503
2.93542	0.64126	0.53672	0.5583	0.30489
3	0.64251	0.5366	0.55886	0.30476

Table I.1: The fall speed of square lattices of varying lattice spacing S and position across the channel $\Xi = x_3/L_3$ where $L_3 = 6a$. In this case, the mean flow rate down the channel is zero (*i.e.* $Q = 0$).

S/L_3	$6\pi\eta a U_1/F_1$ ($\Xi = 1/2$)	$6\pi\eta a U_3/F_3$ ($\Xi = 1/2$)	$6\pi\eta a U_1/F_1$ ($\Xi = 1/4$)	$6\pi\eta a U_3/F_3$ ($\Xi = 1/4$)
0.41666	0.57505	0.24316	0.79425	0.22443
0.48125	0.53498	0.31836	0.70036	0.28772
0.54583	0.52292	0.38249	0.64967	0.3372
0.61041	0.52507	0.43659	0.62168	0.37434
0.675	0.53431	0.48143	0.60715	0.40126
0.73958	0.54682	0.5182	0.60058	0.42044
0.80416	0.56054	0.54804	0.5988	0.434
0.86875	0.57437	0.57196	0.5999	0.44359
0.93333	0.58772	0.59091	0.60269	0.45039
0.99791	0.60031	0.60574	0.60645	0.45523
1.0625	0.61201	0.61718	0.6107	0.45868
1.12708	0.62278	0.6259	0.61513	0.46113
1.19166	0.63267	0.63246	0.61954	0.46287
1.25625	0.6417	0.63732	0.62382	0.4641
1.32083	0.64994	0.64088	0.62789	0.46496
1.38541	0.65746	0.64344	0.63172	0.46556
1.45	0.66431	0.64526	0.63528	0.46597
1.51458	0.67057	0.64653	0.63857	0.46625
1.57916	0.67628	0.6474	0.64161	0.46643
1.64375	0.6815	0.64798	0.64439	0.46655
1.70833	0.68627	0.64835	0.64695	0.46662
1.77291	0.69064	0.64859	0.64929	0.46667
1.8375	0.69464	0.64873	0.65144	0.4667
1.90208	0.69832	0.64881	0.6534	0.46671
1.96666	0.70169	0.64885	0.65521	0.46672
2.03125	0.7048	0.64886	0.65686	0.46672
2.09583	0.70766	0.64887	0.65838	0.46673
2.16042	0.71031	0.64886	0.65978	0.46673
2.225	0.71275	0.64886	0.66108	0.46674
2.28958	0.71501	0.64886	0.66227	0.46674
2.35417	0.7171	0.64886	0.66337	0.46675
2.41875	0.71904	0.64887	0.66439	0.46676
2.48333	0.72085	0.64888	0.66534	0.46677
2.54792	0.72253	0.64889	0.66623	0.46678
2.6125	0.72409	0.64891	0.66705	0.46679
2.67708	0.72555	0.64893	0.66781	0.4668
2.74167	0.72692	0.64895	0.66853	0.46682
2.80625	0.7282	0.64898	0.6692	0.46683
2.87083	0.72939	0.649	0.66983	0.46685
2.93542	0.73052	0.64903	0.67042	0.46686
3	0.73157	0.64906	0.67097	0.46688

Table I.2: The fall speed of square lattices of varying lattice spacing S and position across the channel $\Xi = x_3/L_3$ where $L_3 = 8a$. In this case, the mean flow rate down the channel is zero (*i.e.* $Q = 0$).

S/L_3	$6\pi\eta a U_1/F_1$ ($\Xi = 1/2$)	$6\pi\eta a U_3/F_3$ ($\Xi = 1/2$)	$6\pi\eta a U_1/F_1$ ($\Xi = 1/4$)	$6\pi\eta a U_3/F_3$ ($\Xi = 1/4$)
0.41667	0.70112	0.45041	0.8601	0.43439
0.48125	0.67564	0.51615	0.79374	0.4918
0.54583	0.66937	0.56821	0.75815	0.53314
0.61042	0.67245	0.6099	0.73917	0.56256
0.675	0.68001	0.64344	0.72963	0.58335
0.73958	0.68945	0.67024	0.72552	0.59789
0.80417	0.69951	0.69167	0.7247	0.60818
0.86875	0.70947	0.70864	0.72582	0.61548
0.93333	0.71898	0.72194	0.72809	0.62067
0.99792	0.72787	0.73226	0.73097	0.62437
1.0625	0.73608	0.74017	0.73416	0.62702
1.12708	0.74361	0.74615	0.73744	0.62891
1.19167	0.75048	0.75062	0.74068	0.63025
1.25625	0.75675	0.75392	0.7438	0.6312
1.32083	0.76246	0.75631	0.74676	0.63187
1.38542	0.76765	0.75803	0.74952	0.63233
1.45	0.77238	0.75925	0.75209	0.63265
1.51458	0.77669	0.76009	0.75446	0.63286
1.57917	0.78063	0.76066	0.75664	0.63301
1.64375	0.78421	0.76104	0.75864	0.63311
1.70833	0.78749	0.76129	0.76047	0.63317
1.77292	0.7905	0.76144	0.76215	0.63321
1.8375	0.79325	0.76154	0.76369	0.63324
1.90208	0.79577	0.76159	0.76509	0.63326
1.96667	0.79809	0.76162	0.76638	0.63328
2.03125	0.80022	0.76164	0.76757	0.6333
2.09583	0.80219	0.76165	0.76866	0.63331
2.16042	0.804	0.76166	0.76966	0.63333
2.225	0.80568	0.76167	0.77058	0.63334
2.28958	0.80723	0.76168	0.77144	0.63336
2.35417	0.80867	0.76169	0.77223	0.63338
2.41875	0.81001	0.76171	0.77297	0.6334
2.48333	0.81125	0.76172	0.77365	0.63343
2.54792	0.8124	0.76175	0.77428	0.63345
2.6125	0.81348	0.76177	0.77488	0.63348
2.67708	0.81449	0.7618	0.77543	0.6335
2.74167	0.81543	0.76182	0.77595	0.63353
2.80625	0.81631	0.76185	0.77643	0.63356
2.87083	0.81714	0.76188	0.77689	0.63359
2.93542	0.81791	0.76192	0.77732	0.63362
3	0.81864	0.76195	0.77772	0.63365

Table I.3: The fall speed of square lattices of varying lattice spacing S and position across the channel $\Xi = x_3/L_3$ where $L_3 = 12a$. In this case, the mean flow rate down the channel is zero (*i.e.* $Q = 0$).

S/L_3	$6\pi\eta a U_1/F_1$ ($\Xi = 1/2$)	$6\pi\eta a U_1/F_1$ ($\Xi = 1/4$)
0.41667	3.38854	2.07168
0.48125	2.65564	1.66744
0.54583	2.14931	1.39176
0.61042	1.8032	1.20309
0.675	1.56139	1.07166
0.73958	1.38284	0.97479
0.80417	1.25114	0.90338
0.86875	1.1519	0.84967
0.93333	1.07569	0.80856
0.99792	1.01617	0.77661
1.0625	0.96897	0.75143
1.12708	0.93103	0.73134
1.19167	0.90015	0.71514
1.25625	0.87474	0.70193
1.32083	0.85361	0.69104
1.38542	0.83588	0.68199
1.45	0.82086	0.67437
1.51458	0.80804	0.66792
1.57917	0.79702	0.66239
1.64375	0.78748	0.65762
1.70833	0.77917	0.65348
1.77292	0.77188	0.64985
1.8375	0.76545	0.64664
1.90208	0.75976	0.6438
1.96667	0.75468	0.64126
2.03125	0.75014	0.63898
2.09583	0.74605	0.63693
2.16042	0.74237	0.63507
2.225	0.73902	0.63338
2.28958	0.73598	0.63183
2.35417	0.73321	0.63042
2.41875	0.73067	0.62912
2.48333	0.72834	0.62792
2.54792	0.72619	0.62682
2.6125	0.7242	0.62579
2.67708	0.72237	0.62484
2.74167	0.72066	0.62396
2.80625	0.71908	0.62314
2.87083	0.7176	0.62237
2.93542	0.71623	0.62165
3	0.71494	0.62097

Table I.4: The fall speed of square lattices of varying lattice spacing S and position across the channel $\Xi = x_3/L_3$ where $L_3 = 6a$. In this case, there is no pressure gradient applied down the channel (*i.e.* $\Delta P = 0$).

S/L_3	$6\pi\eta a U_1/F_1$ ($\Xi = 1/2$)	$6\pi\eta a U_1/F_1$ ($\Xi = 1/4$)
0.41667	2.96367	1.95952
0.48125	2.33723	1.58935
0.54583	1.93032	1.35031
0.61042	1.65047	1.18635
0.675	1.45477	1.07192
0.73958	1.31368	0.98974
0.80417	1.20933	0.92932
0.86875	1.13045	0.88402
0.93333	1.06967	0.84948
0.99792	1.02204	0.82275
1.0625	0.98416	0.80179
1.12708	0.95363	0.78513
1.19167	0.92872	0.77174
1.25625	0.90818	0.76085
1.32083	0.89107	0.7519
1.38542	0.87669	0.74445
1.45	0.8645	0.73819
1.51458	0.85409	0.73288
1.57917	0.84513	0.72833
1.64375	0.83736	0.7244
1.70833	0.83059	0.72098
1.77292	0.82464	0.71798
1.8375	0.8194	0.71533
1.90208	0.81475	0.71297
1.96667	0.8106	0.71086
2.03125	0.80689	0.70897
2.09583	0.80354	0.70725
2.16042	0.80052	0.7057
2.225	0.79779	0.70429
2.28958	0.79529	0.70299
2.35417	0.79302	0.7018
2.41875	0.79093	0.70071
2.48333	0.78901	0.6997
2.54792	0.78725	0.69877
2.6125	0.78561	0.6979
2.67708	0.7841	0.69709
2.74167	0.7827	0.69633
2.80625	0.78139	0.69562
2.87083	0.78018	0.69495
2.93542	0.77904	0.69433
3	0.77797	0.69373

Table I.5: The fall speed of square lattices of varying lattice spacing S and position across the channel $\Xi = x_3/L_3$ where $L_3 = 8a$. In this case, there is no pressure gradient applied down the channel (*i.e.* $\Delta P = 0$).

S/L_3	$6\pi\eta a U_1/F_1$ ($\Xi = 1/2$)	$6\pi\eta a U_1/F_1$ ($\Xi = 1/4$)
0.41667	2.36485	1.73685
0.48125	1.92257	1.45015
0.54583	1.6385	1.26688
0.61042	1.44718	1.14417
0.675	1.3134	1.05898
0.73958	1.21689	0.99809
0.80417	1.14548	0.95352
0.86875	1.09145	0.92026
0.93333	1.04977	0.89499
0.99792	1.01708	0.8755
1.0625	0.99105	0.86025
1.12708	0.97005	0.84815
1.19167	0.95291	0.83843
1.25625	0.93875	0.83053
1.32083	0.92695	0.82402
1.38542	0.91703	0.81861
1.45	0.9086	0.81405
1.51458	0.9014	0.81018
1.57917	0.8952	0.80685
1.64375	0.88982	0.80396
1.70833	0.88512	0.80144
1.77292	0.88099	0.79922
1.8375	0.87735	0.79724
1.90208	0.87411	0.79547
1.96667	0.87122	0.79388
2.03125	0.86863	0.79243
2.09583	0.86629	0.79111
2.16042	0.86418	0.78989
2.225	0.86227	0.78877
2.28958	0.86052	0.78772
2.35417	0.85892	0.78674
2.41875	0.85746	0.78581
2.48333	0.85611	0.78494
2.54792	0.85486	0.7841
2.6125	0.85371	0.78329
2.67708	0.85264	0.78252
2.74167	0.85165	0.78176
2.80625	0.85073	0.78102
2.87083	0.84986	0.78029
2.93542	0.84905	0.77957
3	0.84829	0.77885

Table I.6: The fall speed of square lattices of varying lattice spacing S and position across the channel $\Xi = x_3/L_3$ where $L_3 = 12a$. In this case, there is no pressure gradient applied down the channel (*i.e.* $\Delta P = 0$).

I.2 The high frequency dynamic viscosity of suspensions bound in channels and the distribution of stress across a channel

ϕ	η_∞/η $(L_3/a = 6)$	η_∞/η $(L_3/a = 8)$	η_∞/η $(L_3/a = 12)$
0.1	1.44566611356084	1.40131009053247	1.3769626715455
0.15	1.73013215628919	1.67005764179527	1.63668759347054
0.2	2.08325713725791	2.00612205342108	1.96145084144447
0.25	2.54212797601777	2.44114467660655	2.37622904678852
0.3	3.18055890379372	3.0297996490614	2.91313735800399
0.35	3.98969497434547	3.79839776229097	3.59671404304386
0.4	4.76938582829955	4.57890398838356	4.33002805576102

Table I.7: The high frequency shear viscosity of a suspension of given volume fraction varies with channel width as depicted in the above table.

$x_3/a - 1$	$S_{13}/6\pi\eta a^3\gamma$ $(\phi = 0.1)$	$S_{13}/6\pi\eta a^3\gamma$ $(\phi = 0.2)$	$S_{13}/6\pi\eta a^3\gamma$ $(\phi = 0.3)$	$S_{13}/6\pi\eta a^3\gamma$ $(\phi = 0.4)$
0	1.885334252	1.933737338	2.0400081125	2.0332964864
0.0571428571000001	1.1664391329	1.2416092718	1.3690679567	1.3714233279
0.1142857143	0.8877837753	0.9704868173	1.0926181768	1.126769004
0.1714285714	0.7502269321	0.828687015	0.9388378708	1.0035978066
0.2285714286	0.6659830164	0.7358536332	0.8363122394	0.9248166599
0.2857142857	0.5999199163	0.6719102326	0.758926813	0.8759119839
0.3428571429	0.5552700446	0.624497806	0.7045572699	0.852251276
0.4	0.5224289411	0.5803436479	0.663536846	0.8416035318
0.4571428571	0.4933399649	0.5456661295	0.6260859138	0.8390106467
0.5142857143	0.4703000251	0.5223342065	0.5986202669	0.8432067453
0.5714285714	0.4510719517	0.496900046	0.5798343766	0.8517956435
0.6285714286	0.4332306192	0.480207718	0.5664065825	0.8594529872
0.6857142857	0.417877639	0.4633829456	0.5595461773	0.8683764096
0.7428571429	0.4081563937	0.4528944863	0.5538879014	0.8752636694
0.8	0.3989192938	0.4431275139	0.5558459371	0.8869300323
0.8571428571	0.3892933231	0.4380463472	0.5481878132	0.8640055765
0.9142857143	0.3796332096	0.4281771375	0.5489733711	0.9078352928
0.9714285714	0.3734443561	0.4260286393	0.5513610664	0.9081860621
1.0285714286	0.3691786442	0.4227622363	0.5524129978	0.8903686619
1.0857142857	0.3659341811	0.4225964566	0.5608214026	0.898247473
1.1428571429	0.3631515212	0.4200944654	0.5742100615	0.9234760193
1.2	0.3586608148	0.422105642	0.5758900112	0.9410536012
1.2571428571	0.3589831311	0.4278261362	0.584593284	0.9070767503
1.3142857143	0.3539099932	0.4286892165	0.6014970627	0.9263271729
1.3714285714	0.3523236857	0.4353571768	0.6181788726	0.8841697544
1.4285714286	0.3534257695	0.442077445	0.6230138112	0.8428681962
1.4857142857	0.3526490437	0.4489157809	0.6394008193	0.893998114
1.5428571429	0.353309568	0.4478332306	0.6497937707	0.871244713
1.6	0.3558618797	0.4547068748	0.6700682092	0.870612031
1.6571428571	0.3495993078	0.4607788454	0.6720016009	0.8397477395
1.7142857143	0.35143664	0.4684828714	0.6865903181	0.8208081569
1.7714285714	0.3555566182	0.4699870519	0.6948904167	0.801986163
1.8285714286	0.3551080687	0.4800489156	0.6994097131	0.7774065666
1.8857142857	0.3520131198	0.4851941554	0.7082989479	0.766938575
1.9428571429	0.3529314783	0.48739981	0.7103289101	0.7314026166
2	0.3514255298	0.4877581557	0.7137503169	0.7280662127

Table I.8: The distribution of particle stresslet S_{13} across a channel of width $L_3 = 6a$ for varying volume fractions in an equilibrium suspension.

$x_3/a - 1$	$S_{13}/6\pi\eta a^3\gamma$ ($\phi = 0.1$)	$S_{13}/6\pi\eta a^3\gamma$ ($\phi = 0.2$)	$S_{13}/6\pi\eta a^3\gamma$ ($\phi = 0.3$)	$S_{13}/6\pi\eta a^3\gamma$ ($\phi = 0.4$)
0	1.8392348562	1.8873746704	1.9779467481	1.9488310164
0.0638297872	1.1183641073	1.2082517625	1.3305341378	1.3592205525
0.1276595745	0.8409157946	0.9402929532	1.0545213679	1.1358176336
0.1914893617	0.7106915751	0.8020535417	0.9045551974	0.9724435313
0.2553191489	0.6303112682	0.7102880155	0.812210449	0.8834105892
0.3191489362	0.5740706895	0.6551649575	0.7431017575	0.9174289825
0.3829787234	0.5304957675	0.6091682757	0.6887350052	0.8033981305
0.4468085106	0.4964941992	0.5695876069	0.6536106277	0.7871682556
0.5106382979	0.4712450487	0.5410731517	0.6249254976	0.77261993
0.5744680851	0.4498010037	0.5146205312	0.604378402	0.7570149657
0.6382978723	0.4318405883	0.4995235455	0.5954483531	0.6995005191
0.7021276596	0.4171557635	0.4828815666	0.5810338613	0.7890140303
0.7659574468	0.4063733512	0.4650543799	0.5828032274	0.769564328
0.829787234	0.3981435882	0.4592171364	0.5778825145	0.8615563994
0.8936170213	0.3904658362	0.4556953232	0.5778190822	0.8176845964
0.9574468085	0.3806375438	0.4553637568	0.5884544088	1.1348284841
1.0212765957	0.3774547661	0.4453830226	0.5991505281	0.9081802202
1.085106383	0.3718342473	0.4496996496	0.6131976588	0.9466298473
1.1489361702	0.3641100204	0.4471700698	0.61878773	1.0122628003
1.2127659574	0.360687809	0.4436798597	0.627465277	1.1660769988
1.2765957447	0.3584205321	0.4427743837	0.6425676467	1.0697651845
1.3404255319	0.3565917746	0.4463356407	0.6567673844	1.3192442231
1.4042553191	0.3544416933	0.4478681311	0.6760020479	0.9459631187
1.4680851064	0.3543986835	0.452578958	0.6726686252	0.9456838853
1.5319148936	0.3532961805	0.4542892178	0.6857567406	1.0615186589
1.5957446809	0.3528914256	0.4593881967	0.6864737367	0.93096332
1.6595744681	0.3487398552	0.4597516151	0.6965484338	1.0175560208
1.7234042553	0.3509058231	0.4632136733	0.6986681774	0.9102959353
1.7872340426	0.3512556919	0.4610080819	0.694593842	0.7882207143
1.8510638298	0.3480697673	0.4642030667	0.679464979	0.7446968546
1.914893617	0.3509867806	0.463390008	0.6673881627	0.7962203979
1.9787234043	0.3468277186	0.4603988677	0.6580653667	0.7765302057
2.0425531915	0.345224126	0.4558355637	0.6397915165	0.7004817651
2.1063829787	0.346296332	0.456022531	0.6318866456	0.7395966526
2.170212766	0.3439903269	0.448431943	0.6161402732	0.6302168217
2.2340425532	0.3417314679	0.4439441123	0.6014633284	0.7410511353
2.2978723404	0.3435465239	0.4403664536	0.591633447	0.6121016752
2.3617021277	0.3435189707	0.4382508533	0.5912485218	0.6663355438
2.4255319149	0.3439325816	0.4367975172	0.58679486	0.758503537
2.4893617021	0.3451346643	0.4375489701	0.5860492421	0.821076426
2.5531914894	0.3458102683	0.4334561204	0.5828855578	0.872104223
2.6170212766	0.34514287	0.4401429021	0.5793219677	0.4998977831
2.6808510638	0.3428843423	0.4386183185	0.5772628877	0.8756911636
2.7446808511	0.3440567823	0.4293037796	0.5757124621	0.697808221
2.8085106383	0.3441768435	0.4343285686	0.5765818815	0.9117737513
2.8723404255	0.340751768	0.4340477108	0.5736534873	0.9250433571
2.9361702128	0.3440598707	0.4318142382	0.57553052	0.5948722729
3	0.3459562267	0.4288901101	0.5705599271	0.9346426099

Table I.9: The distribution of particle stresslet S_{13} across a channel of width $L_3 = 8a$ for varying volume fractions in an equilibrium suspension.

$x_3/a - 1$	$S_{13}/6\pi\eta a^3\gamma$ ($\phi = 0.1$)	$S_{13}/6\pi\eta a^3\gamma$ ($\phi = 0.2$)	$S_{13}/6\pi\eta a^3\gamma$ ($\phi = 0.3$)	$S_{13}/6\pi\eta a^3\gamma$ ($\phi = 0.4$)
0	1.7845936995	1.8134005625	1.8230534513	1.7249103535
0.0704225352000001	1.0843798372	1.1682701753	1.2586762171	1.2347694266
0.1408450704	0.8255051894	0.9222977562	1.011288328	1.0452041256
0.2112676056	0.6997894023	0.7960459247	0.8793400559	0.952652952
0.2816901408	0.6255301511	0.713736922	0.792752837	0.8595727781
0.3521126761	0.5697828289	0.6561173258	0.7281994363	0.7979877916
0.4225352113	0.5313897548	0.6095182044	0.6841168584	0.7894029017
0.4929577465	0.5008938482	0.5800779844	0.6487157295	0.705261052
0.5633802817	0.4745659036	0.5503417596	0.6303563561	0.8286408714
0.6338028169	0.4555881415	0.5301728195	0.612965169	0.7205159721
0.7042253521	0.4375938335	0.5139584964	0.6062414921	0.7676973114
0.7746478873	0.4260318126	0.5017825325	0.608075517	0.7231406982
0.8450704225	0.4156496224	0.4950842643	0.6106419288	0.8557961667
0.9154929577	0.4074081229	0.4911569549	0.6144708643	0.9426791435
0.985915493	0.3998283876	0.486108686	0.6329218257	0.9711962284
1.0563380282	0.3963206318	0.4867328029	0.6456857156	0.9823686472
1.1267605634	0.388942862	0.4889039735	0.6572356582	1.04570644
1.1971830986	0.3872096823	0.487920438	0.673466155	1.0946828707
1.2676056338	0.3855151576	0.4923582354	0.6905894826	1.0992339838
1.338028169	0.3818340335	0.4951516167	0.7051899053	1.0643545451
1.4084507042	0.3827841	0.5020748308	0.7239415588	0.9854731076
1.4788732394	0.3821098445	0.5050709873	0.7283481815	1.1068937521
1.5492957746	0.3802508891	0.5071879131	0.7470179934	0.9874390816
1.6197183099	0.3799289176	0.5104363202	0.7527454166	1.1004598386
1.6901408451	0.3752282604	0.5125511395	0.7581330041	1.0551937431
1.7605633803	0.3782528527	0.5181944837	0.7581647926	1.0556443586
1.8309859155	0.3775376498	0.5202475944	0.7463677824	1.0501163214
1.9014084507	0.3785717769	0.5188278743	0.7392117186	0.9417635777
1.9718309859	0.37380329	0.516772547	0.7184108751	0.8333806427
2.0422535211	0.3758403874	0.5082810867	0.701131428	0.8302774087
2.1126760563	0.3741092524	0.5029004632	0.6799352174	0.767339577
2.1830985915	0.373012362	0.5013825797	0.6580510711	0.7981474234
2.2535211268	0.3684083622	0.4930666316	0.6466944047	0.7489452612
2.323943662	0.3655094819	0.4879514629	0.6375705799	0.8187016705
2.3943661972	0.3650691804	0.4782721554	0.6191184476	0.7750462039
2.4647887324	0.363086543	0.4743782949	0.6093883709	0.7746787178
2.5352112676	0.3586641679	0.465004645	0.6109053226	0.7308716405
2.6056338028	0.3595903273	0.4631490333	0.5991512699	0.750273428
2.676056338	0.3573218986	0.4563165195	0.5933711267	0.7708858442
2.7464788732	0.3553261607	0.4555069861	0.5950739951	0.7474403355
2.8169014085	0.3519297422	0.4501618494	0.5846960478	0.807702613
2.8873239437	0.3513399203	0.4448417685	0.5847691927	0.8079197723
2.9577464789	0.350971964	0.4457361021	0.5804321414	0.8705471034
3.0281690141	0.3490351967	0.4384839515	0.587161052	0.8409338443
3.0985915493	0.3457916182	0.438991044	0.5833147093	0.80965447
3.1690140845	0.3470298661	0.433496912	0.584525014	0.8555392454
3.2394366197	0.3453810457	0.4359884945	0.587452374	1.0352113839
3.3098591549	0.3450077133	0.4368183147	0.5884905639	0.8429741371
3.3802816901	0.3434414126	0.4385778453	0.5921409337	0.7450043765
3.4507042254	0.3459811148	0.4361029955	0.5942102059	0.8932301651
3.5211267606	0.3431801262	0.4383263313	0.5893438675	0.9470533711
3.5915492958	0.3458192285	0.4391521744	0.5924862939	0.8459510957
3.661971831	0.3428367384	0.4352816604	0.5992044458	0.8345181045
3.7323943662	0.342565126	0.4367578312	0.6016859989	0.9658808546
3.8028169014	0.3457629679	0.4363994547	0.6052725298	0.8253348859
3.8732394366	0.3435084241	0.4399349278	0.6084897882	0.8089412305
3.9436619718	0.3461109478	0.4414918293	0.6057910648	0.7973834089
4.014084507	0.3456212849	0.4451024204	0.6092441972	0.822910009
4.0845070423	0.3438263093	0.4390402971	0.6129448151	0.8535580886
4.1549295775	0.3446776407	0.4466417688	0.6178466192	0.8275242798
4.2253521127	0.3436222601	0.4454516973	0.6152807228	0.8198228593
4.2957746479	0.3429373773	0.4432184501	0.618745921	0.7879464339
4.3661971831	0.3430529385	0.4434434926	0.6238136757	0.9185608587
4.4366197183	0.344595722	0.4435452011	0.6178963752	0.9698928839
4.5070422535	0.3440199321	0.4457896419	0.6153273855	0.816249867
4.5774647887	0.346626678	0.4464984824	0.6260888438	1.0163895691
4.6478873239	0.3468269145	0.4461151031	0.6155534847	0.8729902319
4.7183098592	0.3436694608	0.4438724971	0.6213639917	0.8355250827
4.7887323944	0.346801887	0.447755939	0.6188743385	0.8961592416
4.8591549296	0.3460739945	0.4485554893	0.6229047437	0.9677885508
4.9295774648	0.3485421574	0.4466235726	0.6151806998	0.9355390119
5	0.3451406749	0.446038497	0.6233569108	0.8749658206

Table I.10: The distribution of particle stresslet S_{13} across a channel of width $L_3 = 12a$ for varying volume fractions in an equilibrium suspension.

I.3 The short-time self-diffusivity of a suspension bound by channel walls

		$D_0^S(x_3/a,\phi)$	(para.)			$D_0^S(x_3/a,\phi)$	(perp.)	
$x_3/a-1$	$\phi=0.1$	$\phi=0.2$	$\phi=0.3$	$\phi=0.4$	$\phi=0.1$	$\phi=0.2$	$\phi=0.3$	$\phi=0.4$
0	0.302269146	0.013521454	0.281419553	0.013851949	0.233327551	0.013764157	0.187717249	0.013120703
0.057142857	0.382023718	0.053995073	0.343761722	0.052273354	0.276036475	0.04964455	0.219533334	0.047677011
0.114285714	0.427183186	0.098802533	0.376543949	0.097665978	0.299112754	0.091429137	0.232489796	0.084736611
0.171428571	0.455002083	0.139160166	0.396322371	0.135350372	0.312276037	0.125581659	0.238701152	0.113878963
0.228571429	0.473879494	0.176367214	0.410043005	0.169028074	0.320022579	0.154594683	0.240861889	0.135033942
0.285714286	0.485629313	0.20751781	0.421589388	0.197918994	0.32614367	0.17936625	0.24202226	0.153447251
0.342857143	0.498946571	0.236872867	0.427590356	0.224608283	0.328399993	0.201734333	0.243254047	0.168447982
0.4	0.50942207	0.26078239	0.436611644	0.245608522	0.333408504	0.218586977	0.241959169	0.180066595
0.457142857	0.519902723	0.285793315	0.440674653	0.264274468	0.33353252	0.235126264	0.244403962	0.186895365
0.514285714	0.523650987	0.302106288	0.444054399	0.283035184	0.334189565	0.248407421	0.243165154	0.200074544
0.571428571	0.524989471	0.320173798	0.443982327	0.295946997	0.336896579	0.257738454	0.244107622	0.207642342
0.628571429	0.53498901	0.338331233	0.451347314	0.309606628	0.337037194	0.270684766	0.238255141	0.210658227
0.685714286	0.540228773	0.352624211	0.445837557	0.324896593	0.339639453	0.27965268	0.244760849	0.225664327
0.742857143	0.538603199	0.366913389	0.452308598	0.338213639	0.336027565	0.285627216	0.248057095	0.220850798
0.8	0.547524108	0.387234673	0.45331673	0.346570627	0.340623116	0.297690027	0.240476455	0.224240283
0.857142857	0.544204382	0.395714835	0.453387236	0.356149532	0.337157032	0.302989134	0.250462331	0.242604923
0.914285714	0.553001874	0.402859696	0.449983627	0.358944818	0.337105747	0.30660153	0.243620461	0.241587623
0.971428571	0.548801035	0.410398118	0.449906225	0.369834943	0.338347323	0.308429584	0.248127245	0.244033974
1.028571429	0.553944135	0.424220522	0.449694404	0.374445853	0.331188291	0.307935187	0.242211391	0.236798839
1.085714286	0.553035421	0.432966174	0.450318522	0.380174015	0.333236675	0.311596957	0.235614875	0.24453018
1.142857143	0.552908225	0.441068424	0.451974359	0.382430785	0.335402787	0.312882042	0.243985261	0.252296688
1.2	0.558141881	0.444220557	0.452656576	0.386428201	0.331209438	0.310876709	0.246676682	0.258174345
1.257142857	0.558045259	0.447740023	0.450602399	0.390272476	0.326917967	0.306818846	0.231698685	0.230428154
1.314285714	0.560592033	0.455764098	0.449883979	0.39358507	0.324958761	0.30579419	0.235276083	0.235226904
1.371428571	0.558042096	0.456865509	0.45079613	0.393438035	0.326744378	0.297888357	0.230739152	0.226194789
1.428571429	0.547805548	0.460684847	0.446008329	0.389962321	0.326533635	0.297270904	0.233104919	0.222090282
1.485714286	0.555937993	0.470135646	0.443351357	0.387724377	0.324119042	0.289648371	0.241495976	0.221940433
1.542857143	0.555468677	0.471249125	0.444563867	0.390931504	0.322470758	0.280871872	0.233139857	0.209681019
1.6	0.557158921	0.466600461	0.443961011	0.388831904	0.320109133	0.278540757	0.228414497	0.200264732
1.657142857	0.556165187	0.471292404	0.443345941	0.386720862	0.32012736	0.269877972	0.235207056	0.200592618
1.714285714	0.560310881	0.478020448	0.434320869	0.377203651	0.323955421	0.263473368	0.229645621	0.19128223
1.771428571	0.558873636	0.47145233	0.438704563	0.3700618	0.316509717	0.251542412	0.232677003	0.189100927
1.828571429	0.557044579	0.470764928	0.439770747	0.373465402	0.316425289	0.240987506	0.233596358	0.184554241
1.885714286	0.558322117	0.471247158	0.43787323	0.375341547	0.316325791	0.232140886	0.235347791	0.182971082
1.942857143	0.561022226	0.472480011	0.435210913	0.363406909	0.31339252	0.225644435	0.23656724	0.182211223
2	0.563582333	0.472433893	0.435766039	0.363399105	0.315283842	0.219110318	0.235104541	0.18164163

Table I.11: The short-time self-diffusivity as a function of position across the channel (x_3/a) and volume fraction for a channel of width $L_3 = 6a$.

		$D_0^S(x_3/a, \phi)$	(para.)			$D_0^S(x_3/a, \phi)$	(perp.)	
$x_3/a - 1$	$\phi = 0.1$	$\phi = 0.2$	$\phi = 0.3$	$\phi = 0.4$	$\phi = 0.1$	$\phi = 0.2$	$\phi = 0.3$	$\phi = 0.4$
0	0.324935654	0.015809927	0.300508114	0.015534094	0.263599695	0.015034512	0.214898431	0.014481967
0.063829787	0.406402909	0.059501114	0.377260799	0.059229162	0.31981691	0.057134133	0.252617631	0.054852987
0.127659575	0.458646312	0.111358285	0.418521114	0.110282057	0.348813077	0.106224865	0.26964243	0.099520977
0.191489362	0.485569686	0.156610696	0.44083227	0.155806745	0.363179461	0.148192387	0.277664195	0.134750927
0.255319149	0.503093158	0.198711476	0.458873792	0.193484232	0.372282565	0.183228973	0.281054155	0.164319039
0.319148936	0.529412175	0.233254612	0.474039825	0.227587695	0.379988318	0.21158828	0.281690383	0.185593297
0.382978723	0.54674259	0.263365239	0.484404475	0.256643673	0.386606589	0.234749802	0.283294455	0.203647936
0.446808511	0.558742012	0.292799138	0.489606986	0.279156055	0.392407821	0.256345934	0.280042247	0.215742915
0.510638298	0.563195718	0.314162471	0.494095353	0.303997986	0.397362468	0.276531787	0.285335163	0.229871837
0.574468085	0.569786446	0.338018959	0.497269083	0.322030884	0.396560838	0.291870974	0.281484479	0.236801267
0.638297872	0.582367291	0.361818812	0.50498855	0.339117894	0.392469034	0.2987152	0.283312851	0.244480277
0.70212766	0.59181948	0.378493602	0.508842057	0.353571045	0.393967602	0.313294143	0.273289886	0.253690144
0.765957447	0.585707456	0.393179783	0.506289862	0.370345888	0.395143311	0.320228643	0.280754014	0.260365971
0.829787234	0.597181017	0.406357681	0.510423208	0.382550536	0.390838559	0.337986127	0.274364536	0.260513637
0.893617021	0.600508755	0.422254573	0.511623833	0.391928354	0.395688911	0.340356178	0.272546086	0.268128314
0.957446809	0.606576829	0.436278016	0.512902121	0.400324683	0.39723684	0.347328895	0.277985317	0.264827439
1.021276596	0.609797434	0.444529363	0.516027373	0.409009588	0.391952409	0.34868207	0.278059215	0.277622275
1.085106383	0.609805576	0.46294369	0.517970766	0.424150899	0.395255906	0.352315093	0.264110972	0.264666451
1.14893617	0.605866445	0.471849749	0.515466673	0.425671945	0.39179074	0.359483088	0.274687874	0.265372768
1.212765957	0.616926568	0.480197287	0.515865908	0.431092216	0.386413886	0.358418792	0.262675339	0.269169687
1.276595745	0.618683912	0.492795114	0.514707311	0.441382727	0.389485518	0.361394988	0.273160058	0.262149419
1.340425532	0.623103576	0.505750365	0.520965249	0.443548798	0.389311346	0.360778802	0.285826328	0.276278418
1.404255319	0.620444514	0.503847444	0.518387395	0.450537326	0.388052139	0.354558856	0.274621309	0.255747654
1.468085106	0.62014591	0.510402514	0.516924939	0.452556352	0.385494737	0.352403692	0.26960904	0.251567956
1.531914894	0.621934446	0.516820828	0.523947004	0.453544098	0.387250424	0.347334251	0.266719246	0.242565923
1.595744681	0.622306051	0.530729643	0.513664564	0.453794488	0.382724186	0.345823641	0.269187545	0.234795841
1.659574468	0.621944158	0.526668046	0.520800089	0.460193241	0.384492401	0.331600846	0.266058634	0.227870229
1.723404255	0.622884927	0.530432161	0.516145548	0.458883106	0.382026558	0.330185736	0.272161951	0.223542688
1.787234043	0.626033988	0.538331325	0.516075021	0.458086453	0.381132562	0.323035305	0.27040341	0.21672021
1.85106383	0.630294377	0.54380291	0.510165921	0.451301546	0.379523872	0.31627497	0.273708032	0.218893179
1.914893617	0.631236948	0.539602123	0.520502882	0.458762184	0.384306076	0.316248673	0.27850159	0.228470427
1.978723404	0.622392437	0.541060029	0.513305768	0.451832079	0.38305	0.319530902	0.279054257	0.229159535
2.042553192	0.62919903	0.547193049	0.518349533	0.45358095	0.386550466	0.313349906	0.28220718	0.237495582
2.106382979	0.626741286	0.545515618	0.517481323	0.45542993	0.391402602	0.325807528	0.281615912	0.245042444
2.170212766	0.631519322	0.562574305	0.520678949	0.455372396	0.393567868	0.332937445	0.28221069	0.252036186
2.234042553	0.624485198	0.558066711	0.520319902	0.468713284	0.396971323	0.340244812	0.286312426	0.257159526
2.29787234	0.631427859	0.55426652	0.515937191	0.468173771	0.393777743	0.354465809	0.284549257	0.262341785
2.361702128	0.632230655	0.560076518	0.523725694	0.470158889	0.396012652	0.361350592	0.282261249	0.267248826
2.425531915	0.63352422	0.563395911	0.523919614	0.469558933	0.395642313	0.364262153	0.28231719	0.274396899
2.489361702	0.64107115	0.563654575	0.526109306	0.480813417	0.405195997	0.374823759	0.282302428	0.275140756
2.553191489	0.638796881	0.568149363	0.524276139	0.480287526	0.39946437	0.379287178	0.286835629	0.287252857
2.617021277	0.632463231	0.569744419	0.524637908	0.47974986	0.402754353	0.377094183	0.279051145	0.277644704
2.680851064	0.637639129	0.574438871	0.52697427	0.485580126	0.400802774	0.382381195	0.281631539	0.277924882
2.744680851	0.633030955	0.568121591	0.523561727	0.484133894	0.402749494	0.389850911	0.28173193	0.288033747
2.808510638	0.636850871	0.565278549	0.527248362	0.491641052	0.403391258	0.385874252	0.277324454	0.278968863
2.872340426	0.632663155	0.567377884	0.524225092	0.486723143	0.399994075	0.384175844	0.273025991	0.276463951
2.936170213	0.638450587	0.580832854	0.528596302	0.485069634	0.401424238	0.3888035	0.284344396	0.282741866
3	0.63989709	0.578675026	0.525976894	0.481096261	0.403490661	0.387939623	0.29012874	0.28955083

Table I.12: The short-time self-diffusivity as a function of position across the channel (x_3/a) and volume fraction for a channel of width $L_3 = 8a$.

		$D_0^S(x_3/a, \phi)$	(para.)			$D_0^S(x_3/a, \phi)$	(perp.)	
$x_3/a - 1$	$\phi = 0.1$	$\phi = 0.2$	$\phi = 0.3$	$\phi = 0.4$	$\phi = 0.1$	$\phi = 0.2$	$\phi = 0.3$	$\phi = 0.4$
0.01	0.322965568	0.017041022	0.311686623	0.017084123	0.276917425	0.017054859	0.223822468	0.016458447
0.070422535	0.412557631	0.062214652	0.392627416	0.064198285	0.335307933	0.062845726	0.265260892	0.059160854
0.14084507	0.457476762	0.117297347	0.435338162	0.120407419	0.368144881	0.116125034	0.282339451	0.10770269
0.211267606	0.498730025	0.168918341	0.459986884	0.169769852	0.382849979	0.161373606	0.28903125	0.147226852
0.281690141	0.520653555	0.210510025	0.480516594	0.21045434	0.391229232	0.195328922	0.295315509	0.178114953
0.352112676	0.531432603	0.239924145	0.489591272	0.243873291	0.403707912	0.226362945	0.297441623	0.20104677
0.422535211	0.54827291	0.270512814	0.501066638	0.275609853	0.405308306	0.251145421	0.294232257	0.220791521
0.492957747	0.551507321	0.2953325	0.510355002	0.29897329	0.410635498	0.274574143	0.295006207	0.228772991
0.563380282	0.556318731	0.314572798	0.519873401	0.323660242	0.41341367	0.293484519	0.300771071	0.249051275
0.633802817	0.582398254	0.355886635	0.521597973	0.34291573	0.41410887	0.30862231	0.285043466	0.257517409
0.704225352	0.578842338	0.373138601	0.525571988	0.35993368	0.418201216	0.322959451	0.294105763	0.265864343
0.774647887	0.588825869	0.380693637	0.527305878	0.374123075	0.414711028	0.336358907	0.280709637	0.263319384
0.845070423	0.591350414	0.402364831	0.53011975	0.391915912	0.415579204	0.344239571	0.291772803	0.272829382
0.915492958	0.589030693	0.41029578	0.536922863	0.406597884	0.413413229	0.356104097	0.288176106	0.282398726
0.985915493	0.592544797	0.437716059	0.536542872	0.416904078	0.418490365	0.360858447	0.284478468	0.26831946
1.056338028	0.61762415	0.4443041	0.536155535	0.42786568	0.416518635	0.364090858	0.282195661	0.265315061
1.126760563	0.611366096	0.468541728	0.541114621	0.43601545	0.417761943	0.369567468	0.279753666	0.269610509
1.197183099	0.619062557	0.481765082	0.537738512	0.44440368	0.41121235	0.370745503	0.271264538	0.267220425
1.267605634	0.623575567	0.474957867	0.541595527	0.455380132	0.414400864	0.375243195	0.291901702	0.272896886
1.338028169	0.614381394	0.494823285	0.540328871	0.461203507	0.414865235	0.375833606	0.276422578	0.260069291
1.408450704	0.63300362	0.504811738	0.541443021	0.461595158	0.41627734	0.379051953	0.277153451	0.258253927
1.478873239	0.623335095	0.509560983	0.541712552	0.465581902	0.409838958	0.373273226	0.281117973	0.240301893
1.549295775	0.628712756	0.518702192	0.547160189	0.472334212	0.417483047	0.372212953	0.285051807	0.256882766
1.61971831	0.632042492	0.528800634	0.53715728	0.475157519	0.407226411	0.362776678	0.278874349	0.239148435
1.690140845	0.627190433	0.527032317	0.540458396	0.479428525	0.407259642	0.356167097	0.28429257	0.239642437
1.76056338	0.63015233	0.530965194	0.542742579	0.475646346	0.411716364	0.355791504	0.286851639	0.235528819
1.830985916	0.640066111	0.535651378	0.547094257	0.477575694	0.412772222	0.347457917	0.289531072	0.236456646
1.901408451	0.626750451	0.533657734	0.547672038	0.480141923	0.414807192	0.343113097	0.289839595	0.237217776
1.971830986	0.640416464	0.534086965	0.544143932	0.473568654	0.41759912	0.342858938	0.293409039	0.245855612
2.042253521	0.633776374	0.571752742	0.55045487	0.473155624	0.416480873	0.343129004	0.298778885	0.250019736
2.112676056	0.634045101	0.562551436	0.547826944	0.47588361	0.415561265	0.35352266	0.299010418	0.265564464
2.183098592	0.634364167	0.542841644	0.551851833	0.485962286	0.41774398	0.354923605	0.30043788	0.280811132
2.253521127	0.642756042	0.546311316	0.55112258	0.48155203	0.423305421	0.372035364	0.304376498	0.285012943
2.323943662	0.633691508	0.560414532	0.557203925	0.497148397	0.418474667	0.371654372	0.302946341	0.294782612
2.394366197	0.643376064	0.560703277	0.554926323	0.49560809	0.41981106	0.392132192	0.295828847	0.294637895
2.464788732	0.634027327	0.575492857	0.55042848	0.501203008	0.423089423	0.38839944	0.30047591	0.30120374
2.535211268	0.651077969	0.566896074	0.554140302	0.506350405	0.426973301	0.398936531	0.296031991	0.296842584
2.605633803	0.64373611	0.574302632	0.558619063	0.509228724	0.426789131	0.39638588	0.297060241	0.299357942
2.676056338	0.651319166	0.584787778	0.559320842	0.517805145	0.429387905	0.406161783	0.298686964	0.303620307
2.746478873	0.63612833	0.57731763	0.558361608	0.514181381	0.429800563	0.409669457	0.299552647	0.30157658
2.816901409	0.652544118	0.604014384	0.556696505	0.521502889	0.42836024	0.41237004	0.30008284	0.300132991
2.887323944	0.644064856	0.591733846	0.559883231	0.528078728	0.432803669	0.413353714	0.29683559	0.29667901
2.957746479	0.65362652	0.609491528	0.558598159	0.52315554	0.427355674	0.413199332	0.29344472	0.305864901
3.028169014	0.639475513	0.597847188	0.560532949	0.52283083	0.430418379	0.419737684	0.288542564	0.290495103
3.098591549	0.636420947	0.60630548	0.558632601	0.523901219	0.431567654	0.412228884	0.29955822	0.295329779
3.169014085	0.646958665	0.611980122	0.562383141	0.534389501	0.423969657	0.419281965	0.301198909	0.290970193
3.23943662	0.645499522	0.613973243	0.562639962	0.530075148	0.431905373	0.41702069	0.293932259	0.298503216
3.309859155	0.655839532	0.619476844	0.563616874	0.536773472	0.430587313	0.413732935	0.297058638	0.28645899
3.38028169	0.653570537	0.610392149	0.567400208	0.534711242	0.436499914	0.420395123	0.304465372	0.29082205
3.450704225	0.646681479	0.604473308	0.560533728	0.53534622	0.431483833	0.414229452	0.304135406	0.286327005
3.521126761	0.655569562	0.611504727	0.566273994	0.547743211	0.423744374	0.419094139	0.299622904	0.287242486
3.591549296	0.669015265	0.599757731	0.564490311	0.541640403	0.432795958	0.417405919	0.298201965	0.287872331
3.661971831	0.670152201	0.623246811	0.567597542	0.537975577	0.435797887	0.415410695	0.301455493	0.286608986
3.732394366	0.656585562	0.605918789	0.565498995	0.536661146	0.431391125	0.408649245	0.30176403	0.280545887
3.802816901	0.645529956	0.61702728	0.561227214	0.540217892	0.423835951	0.410013567	0.307388291	0.280004605
3.873239437	0.649435399	0.607281053	0.554308734	0.534418389	0.427833794	0.417425808	0.303740833	0.29076874
3.943661972	0.643053142	0.644658516	0.564676752	0.540825323	0.430950261	0.414421988	0.30426614	0.285116319
4.014084507	0.669732717	0.624368263	0.56412044	0.547857106	0.435039363	0.419425214	0.299001042	0.28611334
4.084507042	0.663775369	0.63843311	0.565247286	0.537095782	0.432087567	0.417965472	0.30727129	0.296230318
4.154929578	0.678589854	0.647389782	0.569237619	0.537142127	0.431359772	0.409462797	0.303731396	0.29146719
4.225352113	0.655611351	0.621860321	0.568917915	0.550666039	0.429003631	0.413114292	0.306762851	0.301044605
4.295774648	0.659027467	0.640436658	0.561549755	0.546460811	0.432702241	0.426705576	0.300699132	0.297011458
4.366197183	0.667226982	0.644166964	0.565659441	0.544950837	0.428917452	0.416821764	0.301860395	0.297040401
4.436619718	0.662550087	0.616672555	0.563888558	0.542605851	0.427523039	0.418461279	0.301138174	0.300767954
4.507042254	0.651796946	0.618427702	0.568352389	0.546002706	0.429759823	0.414032025	0.303383254	0.294478313
4.577464789	0.653881142	0.636014738	0.56619302	0.54653096	0.433176581	0.415674777	0.295390365	0.294320184
4.647887324	0.661759352	0.62996218	0.565738987	0.548873543	0.431169454	0.422057443	0.300105197	0.303958598
4.718309859	0.648618212	0.615422585	0.567868553	0.543427036	0.43178539	0.418638925	0.298006605	0.299606566
4.788732394	0.650654316	0.629856067	0.567079885	0.553208147	0.430590606	0.414772216	0.304873362	0.300039463
4.85915493	0.666615325	0.618268055	0.563871496	0.549460766	0.426914191	0.420943568	0.303128297	0.321574381
4.929577465	0.672148556	0.634664637	0.564483838	0.554069431	0.429436595	0.415383301	0.304811717	0.302290273
5	0.670440435	0.635175212	0.56442203	0.544052811	0.43268084	0.422179556	0.308896603	0.300008825

Table I.13: The short-time self-diffusivity as a function of position across the channel (x_3/a) and volume

I.4 The sedimentation rate of random equilibrium suspensions bound in channels

		$6\pi\eta aU(x_3/a,\phi)/F$	(para.)			$6\pi\eta aU(x_3/a,\phi)/F$	(perp.)	
$x_3/a-1$	$\phi=0.1$	$\phi=0.2$	$\phi=0.3$	$\phi=0.4$	$\phi=0.1$	$\phi=0.2$	$\phi=0.3$	$\phi=0.4$
0	0.1925124	0.0119557	0.1305089	0.0097579	0.1143697	0.0097968	0.0815824	0.0104490
0.057142857	0.2403364	0.0438260	0.1576075	0.0358211	0.1316745	0.0344236	0.0921535	0.0373307
0.114285714	0.2675590	0.0792809	0.1736565	0.0634211	0.1389726	0.0598677	0.0979540	0.0660785
0.171428571	0.2928232	0.1096958	0.1851399	0.0866186	0.1410569	0.0791771	0.1010787	0.0879662
0.228571429	0.3027247	0.1362595	0.1912285	0.1059856	0.1438866	0.0945907	0.1030778	0.1051048
0.285714286	0.3143852	0.1605319	0.1985079	0.1223055	0.1437094	0.1084956	0.1044746	0.1193955
0.342857143	0.3314419	0.1947583	0.2059704	0.1495350	0.1466136	0.1291725	0.1069898	0.1381824
0.4	0.3328041	0.2077120	0.2083959	0.1583418	0.1432789	0.1338673	0.1026215	0.1428934
0.457142857	0.3379508	0.2191907	0.2070457	0.1643908	0.1397523	0.1373645	0.0998300	0.1468328
0.514285714	0.3479430	0.2314241	0.2085691	0.1712355	0.1394720	0.1412284	0.0988272	0.1497977
0.571428571	0.3467518	0.2430894	0.2075401	0.1765895	0.1367765	0.1440795	0.0981987	0.1523909
0.628571429	0.3549845	0.2549005	0.2144574	0.1835863	0.1393742	0.1473711	0.0985445	0.1541973
0.685714286	0.3594279	0.2689914	0.2203742	0.1925340	0.1408618	0.1545084	0.0994205	0.1581248
0.742857143	0.3654354	0.2797549	0.2191997	0.1983621	0.1398033	0.1569939	0.0992104	0.1584011
0.8	0.3640233	0.2847061	0.2218431	0.1998873	0.1377152	0.1559222	0.0984805	0.1559984
0.857142857	0.3676312	0.2869015	0.2185608	0.2000869	0.1361017	0.1527067	0.0946714	0.1527319
0.914285714	0.3720631	0.2931179	0.2215790	0.2017096	0.1356667	0.1528861	0.0958372	0.1523813
0.971428571	0.3735627	0.2987051	0.2229373	0.2032052	0.1385777	0.1535301	0.0971895	0.1482588
1.028571429	0.3789998	0.3018113	0.2306619	0.2019697	0.1409339	0.1530120	0.0966127	0.1467350
1.085714286	0.3862256	0.3109471	0.2354074	0.2083269	0.1457327	0.1560231	0.1008762	0.1462428
1.142857143	0.3887928	0.3126184	0.2338922	0.2073690	0.1447041	0.1525922	0.1014214	0.1399987
1.2	0.3863137	0.3104458	0.2327259	0.2042979	0.1455654	0.1506975	0.1010354	0.1364115
1.257142857	0.3807674	0.3139616	0.2340567	0.2010070	0.1469102	0.1478598	0.1034953	0.1327726
1.314285714	0.3840457	0.3123042	0.2415620	0.2016783	0.1481272	0.1477539	0.1011378	0.1287623
1.371428571	0.3920067	0.3157314	0.2414716	0.2005858	0.1542299	0.1487704	0.1059338	0.1259949
1.428571429	0.3905035	0.3182601	0.2496797	0.2021967	0.1576352	0.1497402	0.1101560	0.1243530
1.485714286	0.3932068	0.3159439	0.2491816	0.1991237	0.1600719	0.1470978	0.1130791	0.1200682
1.542857143	0.3944410	0.3170016	0.2528066	0.1987985	0.1624413	0.1457026	0.1137196	0.1167205
1.6	0.4000538	0.3153452	0.2534787	0.1957754	0.1639888	0.1432686	0.1157717	0.1141183
1.657142857	0.3955710	0.3154223	0.2567085	0.1931829	0.1657658	0.1421420	0.1182239	0.1119832
1.714285714	0.4011663	0.3149355	0.2597130	0.1920540	0.1685126	0.1424701	0.1223129	0.1114843
1.771428571	0.4042483	0.3166444	0.2627357	0.1929706	0.1741933	0.1414855	0.1268219	0.1117492
1.828571429	0.4067993	0.3183406	0.2640726	0.1895699	0.1767834	0.1393863	0.1304076	0.1114898
1.885714286	0.3943851	0.3107344	0.2640408	0.1869231	0.1767171	0.1352540	0.1306667	0.1108663
1.942857143	0.3937814	0.3094466	0.2601252	0.1820725	0.1772400	0.1322173	0.1294643	0.1098279
2	0.3986538	0.3080650	0.2574003	0.1801617	0.1761646	0.1300095	0.1292642	0.1093669

Table I.14: The sedimentation rate as a function of position across the channel (x_3/a) and volume fraction for a channel of width $L_3 = 6a$. In this case, there is no mean flow down the channel (*i.e* $Q = 0$).

		$6\pi\eta aU(x_3/a,\phi)/F$	(para.)			$6\pi\eta aU(x_3/a,\phi)/F$	(perp.)	
$x_3/a-1$	$\phi=0.1$	$\phi=0.2$	$\phi=0.3$	$\phi=0.4$	$\phi=0.1$	$\phi=0.2$	$\phi=0.3$	$\phi=0.4$
0	0.1891857	0.0129217	0.1241922	0.0108881	0.1002197	0.0105026	0.0739939	0.0116732
0.063829787	0.2391492	0.0491303	0.1517546	0.0395696	0.1208836	0.0377863	0.0892423	0.0419707
0.127659575	0.2739898	0.0892015	0.1720978	0.0726853	0.1325155	0.0674632	0.0998498	0.0749465
0.191489362	0.2931381	0.1248651	0.1799663	0.0998655	0.1375026	0.0915684	0.1059175	0.0993709
0.255319149	0.3070342	0.1571820	0.1883712	0.1261814	0.1410592	0.1118512	0.1128868	0.1193516
0.319148936	0.3241367	0.1853607	0.1949082	0.1464697	0.1417056	0.1272900	0.1156123	0.1330239
0.382978723	0.3276629	0.2091393	0.1993086	0.1622647	0.1428342	0.1380769	0.1183764	0.1435820
0.446808511	0.3455692	0.2301920	0.2030205	0.1754642	0.1420278	0.1478132	0.1185365	0.1511333
0.510638298	0.3411153	0.2445965	0.2058542	0.1867560	0.1420661	0.1546010	0.1189817	0.1557986
0.574468085	0.3477698	0.2603525	0.2076536	0.1940997	0.1424978	0.1597115	0.1186081	0.1596967
0.638297872	0.3572114	0.2708942	0.2083940	0.2006402	0.1405701	0.1621045	0.1156487	0.1607433
0.70212766	0.3623647	0.2816806	0.2085723	0.2057446	0.1387283	0.1637435	0.1157807	0.1624438
0.765957447	0.3616506	0.2943015	0.2097548	0.2136039	0.1404784	0.1684745	0.1158569	0.1626142
0.829787234	0.3736430	0.3046957	0.2127520	0.2164902	0.1401846	0.1694035	0.1160281	0.1619602
0.893617021	0.3748999	0.3132875	0.2132789	0.2206970	0.1403586	0.1692638	0.1139271	0.1582626
0.957446809	0.3731517	0.3204271	0.2182492	0.2227209	0.1410285	0.1693688	0.1124888	0.1548294
1.021276596	0.3788081	0.3226820	0.2217873	0.2245701	0.1400936	0.1687882	0.1118238	0.1515783
1.085106383	0.3779792	0.3308208	0.2199581	0.2218746	0.1423077	0.1660560	0.1067107	0.1476290
1.14893617	0.3891517	0.3317928	0.2248871	0.2229350	0.1413591	0.1637167	0.1102160	0.1421103
1.212765957	0.3869992	0.3337097	0.2248513	0.2211024	0.1422622	0.1620093	0.1076498	0.1383202
1.276595745	0.3932713	0.3406798	0.2294172	0.2221982	0.1436063	0.1603985	0.1105798	0.1354200
1.340425532	0.3963630	0.3424872	0.2273818	0.2225501	0.1458255	0.1599772	0.1067291	0.1304987
1.404255319	0.4014809	0.3488239	0.2333475	0.2208320	0.1479969	0.1576526	0.1074532	0.1270674
1.468085106	0.4059945	0.3525421	0.2349601	0.2190599	0.1473804	0.1546434	0.1050402	0.1205869
1.531914894	0.4054705	0.3496973	0.2396870	0.2152076	0.1506123	0.1529504	0.1073157	0.1168818
1.595744681	0.4109386	0.3505395	0.2401508	0.2159248	0.1530874	0.1507969	0.1076139	0.1146762
1.659574468	0.4143890	0.3522337	0.2417227	0.2107836	0.1541745	0.1480264	0.1087421	0.1095875
1.723404255	0.4151768	0.3465159	0.2448301	0.2103057	0.1561271	0.1466052	0.1068020	0.1093953
1.787234043	0.4209766	0.3536496	0.2494345	0.2092218	0.1575841	0.1467831	0.1048074	0.1086114
1.85106383	0.4289473	0.3554131	0.2516757	0.2124274	0.1610465	0.1455965	0.1032974	0.1099142
1.914893617	0.4204610	0.3526112	0.2533519	0.2093552	0.1635722	0.1429255	0.1021738	0.1106896
1.978723404	0.4236877	0.3529082	0.2598430	0.2101939	0.1622042	0.1426212	0.1011138	0.1133527
2.042553192	0.4319124	0.3542653	0.2639698	0.2094747	0.1631366	0.1450787	0.0994350	0.1151225
2.106382979	0.4290211	0.3573501	0.2652400	0.2106059	0.1641082	0.1464307	0.0972426	0.1173240
2.170212766	0.4405933	0.3551180	0.2647644	0.2100732	0.1643595	0.1509202	0.0989707	0.1202211
2.234042553	0.4407441	0.3573256	0.2699450	0.2132357	0.1650356	0.1517767	0.0977713	0.1208905
2.29787234	0.4478768	0.3631775	0.2700687	0.2163067	0.1637522	0.1527086	0.0987289	0.1213015
2.361702128	0.4436617	0.3597516	0.2746968	0.2188839	0.1669001	0.1540942	0.0991025	0.1218684
2.425531915	0.4518620	0.3659765	0.2782238	0.2198038	0.1670644	0.1548644	0.1000003	0.1192351
2.489361702	0.4423489	0.3631789	0.2822010	0.2229932	0.1675760	0.1548738	0.1010045	0.1177639
2.553191489	0.4562207	0.3687971	0.2817159	0.2224798	0.1676127	0.1533929	0.1005608	0.1160940
2.617021277	0.4520479	0.3656159	0.2825693	0.2239760	0.1697100	0.1534806	0.1022634	0.1163955
2.680851064	0.4549302	0.3642402	0.2822270	0.2218439	0.1679950	0.1514244	0.1011373	0.1152575
2.744680851	0.4505408	0.3649866	0.2852953	0.2257034	0.1679811	0.1513640	0.1009654	0.1115058
2.808510638	0.4573506	0.3654786	0.2859814	0.2234329	0.1669084	0.1492806	0.1023443	0.1131404
2.872340426	0.4585903	0.3650478	0.2862756	0.2279913	0.1686996	0.1496315	0.1053831	0.1123739
2.936170213	0.4665101	0.3707489	0.2872676	0.2260790	0.1710427	0.1506474	0.1039031	0.1112125
3	0.4599572	0.3655672	0.2806387	0.2227325	0.1700423	0.1504827	0.1058948	0.1132205

Table I.15: The sedimentation rate as a function of position across the channel (x_3/a) and volume fraction for a channel of width $L_3 = 8a$. In this case, there is no mean flow down the channel (*i.e* $Q = 0$).

		$6\pi\eta aU(x_3/a,\phi)/F$	(para.)			$6\pi\eta aU(x_3/a,\phi)/F$	(perp.)	
$x_3/a-1$	$\phi=0.1$	$\phi=0.2$	$\phi=0.3$	$\phi=0.4$	$\phi=0.1$	$\phi=0.2$	$\phi=0.3$	$\phi=0.4$
0	0.1938153	0.0140174	0.1260489	0.0125287	0.0990865	0.0124547	0.0670996	0.0149778
0.070422535	0.2434097	0.0532030	0.1577254	0.0461054	0.1190034	0.0461224	0.0813497	0.0552550
0.14084507	0.2785518	0.0993030	0.1809552	0.0860881	0.1314736	0.0853058	0.0931374	0.0996159
0.211267606	0.3029872	0.1420436	0.1829411	0.1198306	0.1396642	0.1164347	0.1012171	0.1327595
0.281690141	0.3159712	0.1775247	0.1958941	0.1500107	0.1444835	0.1405027	0.1078637	0.1569716
0.352112676	0.3202814	0.2064297	0.2035721	0.1753371	0.1472652	0.1611083	0.1152521	0.1748592
0.422535211	0.3383250	0.2325000	0.2005086	0.1935922	0.1510666	0.1767651	0.1181789	0.1868922
0.492957747	0.3357387	0.2567128	0.2048024	0.2118331	0.1528606	0.1872673	0.1222586	0.1939018
0.563380282	0.3439926	0.2772845	0.2026327	0.2248082	0.1538421	0.1953482	0.1258093	0.1998594
0.633802817	0.3474916	0.2927190	0.2093044	0.2356306	0.1534509	0.2027305	0.1284249	0.2028535
0.704225352	0.3479006	0.3084141	0.2117064	0.2447082	0.1545438	0.2059638	0.1303532	0.2032883
0.774647887	0.3570416	0.3231228	0.2095257	0.2548848	0.1549238	0.2096835	0.1326898	0.2027961
0.845070423	0.3655403	0.3350500	0.2117251	0.2560200	0.1557994	0.2102655	0.1342918	0.2018008
0.915492958	0.3674675	0.3473183	0.2085388	0.2601631	0.1596713	0.2102408	0.1339120	0.1982577
0.985915493	0.3678127	0.3511369	0.2103296	0.2624568	0.1586275	0.2096704	0.1356241	0.1930788
1.056338028	0.3692182	0.3574595	0.2124831	0.2648665	0.1605900	0.2070231	0.1358053	0.1882937
1.126760563	0.3730474	0.3710031	0.2132053	0.2687223	0.1645963	0.2053111	0.1372159	0.1838055
1.197183099	0.3851447	0.3715945	0.2159055	0.2665005	0.1607925	0.1988641	0.1367259	0.1771148
1.267605634	0.3759131	0.3765670	0.2164599	0.2670027	0.1644993	0.1975909	0.1344909	0.1689628
1.338028169	0.3754460	0.3817855	0.2133752	0.2629150	0.1682709	0.1920238	0.1354454	0.1618158
1.408450704	0.3918474	0.3841466	0.2157869	0.2621093	0.1602017	0.1862486	0.1330725	0.1526886
1.478873239	0.3985998	0.3874041	0.2246631	0.2644571	0.1654782	0.1836113	0.1336506	0.1445056
1.549295775	0.3979848	0.3933596	0.2233793	0.2585929	0.1660235	0.1770274	0.1314345	0.1383380
1.61971831	0.3918319	0.3886508	0.2232134	0.2502709	0.1705754	0.1759409	0.1303927	0.1309120
1.690140845	0.4005265	0.3947714	0.2237325	0.2525125	0.1706287	0.1720265	0.1296489	0.1250441
1.76056338	0.4027971	0.3947696	0.2334985	0.2492428	0.1684645	0.1642697	0.1281759	0.1207062
1.830985916	0.3945006	0.3873593	0.2300120	0.2477628	0.1705876	0.1614507	0.1240310	0.1173550
1.901408451	0.4110203	0.3932077	0.2357013	0.2463922	0.1705937	0.1578324	0.1199024	0.1168013
1.971830986	0.4204778	0.4071696	0.2344557	0.2449867	0.1681343	0.1568098	0.1150219	0.1170772
2.042253521	0.4145923	0.3949252	0.2375679	0.2410903	0.1659829	0.1553798	0.1093993	0.1186044
2.112676056	0.4165271	0.3933662	0.2361060	0.2399365	0.1603522	0.1591002	0.1043303	0.1219729
2.183098592	0.4171666	0.3956128	0.2393279	0.2416278	0.1566407	0.1607535	0.0999789	0.1240074
2.253521127	0.4200731	0.3976923	0.2384089	0.2444931	0.1518774	0.1617410	0.0963784	0.1251838
2.323943662	0.4277918	0.4003793	0.2415520	0.2429616	0.1487701	0.1652041	0.0928539	0.1252058
2.394366197	0.4401857	0.4050803	0.2383491	0.2469576	0.1442755	0.1670626	0.0915496	0.1253514
2.464788732	0.4341324	0.4034881	0.2389402	0.2488995	0.1403099	0.1670979	0.0894631	0.1258670
2.535211268	0.4448625	0.4098756	0.2403435	0.2482225	0.1376631	0.1686117	0.0906599	0.1255578
2.605633803	0.4479092	0.4144199	0.2416600	0.2548112	0.1355301	0.1688493	0.0913987	0.1245941
2.676056338	0.4409332	0.4137167	0.2385141	0.2502996	0.1349976	0.1686833	0.0907244	0.1241653
2.746478873	0.4461002	0.4185791	0.2408552	0.2449959	0.1360668	0.1674079	0.0932098	0.1247259
2.816901409	0.4438257	0.4132376	0.2455905	0.2555753	0.1351064	0.1672780	0.0953696	0.1235635
2.887323944	0.4574015	0.4211005	0.2485535	0.2509492	0.1353145	0.1659767	0.0980140	0.1243591
2.957746479	0.4657357	0.4228760	0.2506082	0.2537333	0.1340215	0.1646086	0.0982393	0.1228442
3.028169014	0.4564558	0.4127131	0.2514264	0.2528723	0.1385935	0.1651475	0.1016590	0.1228344
3.098591549	0.4684946	0.4254418	0.2559152	0.2516289	0.1419852	0.1660844	0.1075103	0.1241990
3.169014085	0.4711617	0.4201918	0.2600734	0.2514218	0.1430948	0.1627258	0.1065785	0.1232493
3.23943662	0.4731153	0.4152142	0.2627416	0.2518143	0.1458071	0.1673065	0.1084080	0.1241741
3.309859155	0.4857051	0.4306351	0.2687752	0.2527232	0.1487275	0.1644938	0.1094107	0.1241226
3.38028169	0.4924928	0.4213767	0.2766888	0.2580966	0.1501783	0.1640837	0.1087659	0.1233949
3.450704225	0.4884553	0.4315726	0.2760757	0.2514163	0.1524505	0.1643582	0.1111479	0.1251767
3.521126761	0.4931287	0.4213234	0.2803286	0.2540557	0.1540546	0.1648455	0.1110596	0.1262550
3.591549296	0.5007699	0.4284535	0.2831036	0.2518956	0.1572704	0.1656693	0.1097334	0.1264548
3.661971831	0.4966832	0.4244341	0.2809651	0.2477950	0.1561685	0.1616917	0.1091016	0.1270082
3.732394366	0.5017343	0.4254737	0.2899447	0.2521637	0.1591412	0.1651859	0.1082519	0.1284692
3.802816901	0.5032084	0.4241814	0.2968543	0.2546613	0.1617029	0.1650361	0.1061219	0.1283755
3.873239437	0.5057203	0.4324186	0.3027245	0.2553017	0.1647004	0.1666848	0.1031316	0.1279631
3.943661972	0.5126672	0.4296076	0.3017849	0.2545311	0.1652883	0.1674388	0.1005753	0.1288513
4.014084507	0.5116630	0.4283282	0.2988582	0.2523728	0.1653867	0.1660492	0.0980421	0.1289573
4.084507042	0.5253092	0.4346090	0.3061263	0.2541338	0.1682271	0.1688173	0.0956068	0.1285189
4.154929578	0.5346388	0.4395821	0.3087629	0.2554365	0.1683721	0.1671708	0.0935473	0.1285602
4.225352113	0.5314409	0.4262961	0.3100905	0.2550358	0.1683101	0.1699011	0.0918882	0.1284178
4.295774648	0.5278977	0.4358234	0.3101530	0.2566182	0.1699330	0.1693841	0.0890208	0.1288671
4.366197183	0.5214204	0.4254487	0.3153631	0.2552727	0.1703344	0.1700906	0.0890290	0.1280383
4.436619718	0.5309274	0.4342712	0.3121386	0.2515741	0.1686734	0.1701567	0.0871453	0.1274876
4.507042254	0.5267708	0.4283387	0.3219988	0.2604555	0.1705105	0.1687322	0.0842686	0.1258833
4.577464789	0.5309997	0.4301051	0.3130382	0.2488441	0.1702058	0.1706649	0.0844870	0.1255843
4.647887324	0.5197900	0.4262429	0.3158717	0.2517714	0.1687378	0.1671211	0.0851476	0.1251513
4.718309859	0.5328123	0.4311857	0.3147613	0.2526234	0.1709022	0.1697850	0.0831037	0.1237195
4.788732394	0.5265679	0.4264227	0.3213416	0.2587577	0.1720960	0.1703010	0.0835378	0.1248740
4.85915493	0.5221453	0.4186387	0.3222510	0.2598531	0.1711689	0.1686549	0.0812919	0.1237333
4.929577465	0.5407118	0.4384154	0.3238052	0.2604705	0.1712618	0.1696320	0.0813759	0.1209411
5	0.5440601	0.4484957	0.3238532	0.2536512	0.1680934	0.1687477	0.0830681	0.1235601

Table I.16: The sedimentation rate as a function of position across the channel (x_3/a) and volume fraction

		$6\pi\eta aU(x_3/a,\phi)/F$	(para.)	
$x_3/a-1$	$\phi=0.1$	$\phi=0.2$	$\phi=0.3$	$\phi=0.4$
0	0.8339672811	1.2495145485	1.4881378991	1.3986624208
0.0571428571000001	1.0650304118	1.5568597374	1.7664793113	1.6075855448
0.1142857143	1.2134837938	1.7369941589	1.9143565522	1.7095007856
0.1714285714	1.3122136389	1.8581860662	2.0034171145	1.769209121
0.2285714286	1.3907541853	1.950776099	2.0655241999	1.8085382113
0.2857142857	1.4676491657	2.0335913145	2.1204350544	1.8367063641
0.3428571429	1.5389365466	2.1255740842	2.1825619904	1.8702991958
0.4	1.5904375337	2.1763578818	2.2131346914	1.8817088477
0.4571428571	1.6380939978	2.2275740613	2.2372632207	1.8887470296
0.5142857143	1.6836815521	2.27199698	2.2615606261	1.8894365866
0.5714285714	1.7223447625	2.3158898738	2.2814961307	1.8990389995
0.6285714286	1.7605331281	2.3522536879	2.2994073105	1.9009298956
0.6857142857	1.8067602586	2.3920966489	2.3157346705	1.9006574782
0.7428571429	1.8461226125	2.4343102201	2.3322359944	1.9123914687
0.8	1.8628554142	2.4583458906	2.3441421685	1.9130610126
0.8571428571	1.8901130987	2.4833274551	2.3479067181	1.8995349838
0.9142857143	1.9183265188	2.50579098	2.3522360481	1.893159012
0.9714285714	1.9458830484	2.5212396409	2.3585781556	1.8882980072
1.0285714286	1.9669999653	2.544422299	2.3614691548	1.8782828542
1.0857142857	1.9972575007	2.5747111725	2.36720219	1.8797192078
1.1428571429	2.0112962823	2.5882717142	2.372362263	1.8945534834
1.2	2.0279574078	2.5905872704	2.3683230231	1.8959363033
1.2571428571	2.0411970627	2.6067773021	2.3708193147	1.8807099213
1.3142857143	2.0545334877	2.6141995354	2.36882359	1.881132768
1.3714285714	2.0666308041	2.6173806752	2.3660441127	1.8767745778
1.4285714286	2.0865908258	2.6281223149	2.3754504891	1.8769311969
1.4857142857	2.0963545395	2.6295387043	2.3732619667	1.8803590829
1.5428571429	2.0946612924	2.6361563581	2.367194006	1.881883818
1.6	2.1067502029	2.6365322133	2.3627705783	1.8912607682
1.6571428571	2.1059200824	2.6341844767	2.3544791591	1.891776425
1.7142857143	2.1112814872	2.6300573152	2.3539269493	1.8929208837
1.7714285714	2.1200301358	2.6270923751	2.350935595	1.9035522185
1.8285714286	2.1262414345	2.6275230576	2.3471337328	1.9157394619
1.8857142857	2.1215262392	2.626146182	2.3394287628	1.9177704333
1.9428571429	2.1152327096	2.6265759884	2.3281302169	1.9211004231
2	2.1215128476	2.614444106	2.3269471858	1.9240089069

Table I.17: The sedimentation rate as a function of position across the channel (x_3/a) and volume fraction for a channel of width $L_3 = 6a$. In this case, there is no applied pressure gradient down the channel (*i.e* $\Delta P = 0$).

		$6\pi\eta aU(x_3/a,\phi)/F$	(para.)	
$x_3/a-1$	$\phi=0.1$	$\phi=0.2$	$\phi=0.3$	$\phi=0.4$
0	1.0892740121	1.685947803	2.0312140193	1.9867050649
0.0638297872	1.409089547	2.1224187306	2.4461878515	2.2942157815
0.1276595745	1.6205594883	2.3898320639	2.676768776	2.4486845294
0.1914893617	1.7616528456	2.5740108446	2.8212870732	2.5392829508
0.2553191489	1.8822384626	2.7101927525	2.9194970049	2.5970272748
0.3191489362	1.9837941321	2.8231351925	2.998023411	2.6387719496
0.3829787234	2.0790858039	2.9385363334	3.0713012585	2.6737317708
0.4468085106	2.1683502107	3.0350699626	3.129916602	2.6965075076
0.5106382979	2.2566507088	3.1257420553	3.1796344578	2.7171798077
0.5744680851	2.3303352599	3.2040509054	3.2231689411	2.7327845332
0.6382978723	2.3972591977	3.2794996539	3.2593334175	2.7381488921
0.7021276596	2.4607032332	3.3386469006	3.2869892544	2.745311923
0.7659574468	2.5139962981	3.391290348	3.3060757696	2.7502274154
0.829787234	2.5674964668	3.4505723314	3.3312609856	2.7451959954
0.8936170213	2.6280182246	3.501304329	3.3498450269	2.7637153851
0.9574468085	2.6809866652	3.5514797813	3.366917566	2.7397862893
1.0212765957	2.7409201505	3.6007425733	3.3849298116	2.7491343284
1.085106383	2.7772457312	3.636560755	3.3937398061	2.74346611
1.1489361702	2.8216269273	3.675786353	3.4016594615	2.7455509622
1.2127659574	2.866899143	3.7119393195	3.4148453339	2.741902474
1.2765957447	2.8945317447	3.7270168759	3.4124438251	2.7315916778
1.3404255319	2.9451066347	3.7636295947	3.4224772569	2.7268321034
1.4042553191	2.9706882436	3.7940291715	3.4262886341	2.7317482617
1.4680851064	3.0124022714	3.8190483195	3.4333869605	2.7226917366
1.5319148936	3.0369177701	3.8473438919	3.4384181719	2.7219884142
1.5957446809	3.0719519077	3.8641995954	3.4426729055	2.7266320994
1.6595744681	3.1014731747	3.8873104103	3.4503752464	2.735586696
1.7234042553	3.1264525297	3.9042781039	3.4684317756	2.7471626889
1.7872340426	3.156253591	3.9289817335	3.4730931934	2.7666227217
1.8510638298	3.184056731	3.9390616448	3.4891446227	2.7931580421
1.914893617	3.1993765858	3.9604814524	3.50716824	2.82777507
1.9787234043	3.2260191097	3.9895330727	3.5353217616	2.8647176666
2.0425531915	3.2447038685	4.0079754813	3.5696355111	2.8993072745
2.1063829787	3.2736379302	4.038675526	3.6116199813	2.9325065753
2.170212766	3.2896203608	4.0636465377	3.6512338959	2.9619667095
2.2340425532	3.3092604344	4.0918617181	3.691119175	2.9913069306
2.2978723404	3.3269144503	4.1238045838	3.732654119	3.0177452998
2.3617021277	3.344765017	4.1622263607	3.7646209202	3.0413143879
2.4255319149	3.3576911229	4.1819654105	3.791690743	3.0559018101
2.4893617021	3.3805866408	4.2054538109	3.8206753059	3.0748109532
2.5531914894	3.3943139142	4.2246393421	3.8405714581	3.0871069178
2.6170212766	3.4013980015	4.2488826727	3.8594493898	3.0995125205
2.6808510638	3.4148129298	4.2615425556	3.8778214109	3.1095192613
2.7446808511	3.4216931357	4.2810995343	3.885530409	3.1140015379
2.8085106383	3.4346446411	4.285106309	3.8940446248	3.1258708928
2.8723404255	3.4273224053	4.2899557548	3.9077748976	3.1237096531
2.9361702128	3.4361143441	4.2989011313	3.9093230216	3.1319806107
3	3.4337620523	4.2958378877	3.9105768021	3.1303860878

Table I.18: The sedimentation rate as a function of position across the channel (x_3/a) and volume fraction for a channel of width $L_3 = 8a$. In this case, there is no applied pressure gradient down the channel (*i.e* $\Delta P = 0$).

		$6\pi\eta aU(x_3/a, \phi)/F$	(para.)	
$x_3/a - 1$	$\phi = 0.1$	$\phi = 0.2$	$\phi = 0.3$	$\phi = 0.4$
0	1.6450826378	2.6709434538	3.3975312098	3.4963397196
0.0704225352000001	2.1050496746	3.3780121328	4.1208042921	4.0308709387
0.1408450704	2.4316306667	3.813875219	4.5241611251	4.333097646
0.2112676056	2.6747232871	4.1091825629	4.7725017229	4.5137536111
0.2816901408	2.8566959413	4.355101217	4.9605717105	4.6109699418
0.3521126761	3.0366318799	4.5606099313	5.1092034589	4.7298510844
0.4225352113	3.1992813059	4.7396655165	5.2311837588	4.7723021809
0.4929577465	3.334028547	4.8906609411	5.3330018155	4.869169578
0.5633802817	3.4782626913	5.0395324121	5.4204598163	4.854255292
0.6338028169	3.613488332	5.1744008562	5.4973185254	4.8951406671
0.7042253521	3.7113691338	5.2958233126	5.5568663205	4.9236465324
0.7746478873	3.8361295147	5.3963638992	5.6093559381	4.917052816
0.8450704225	3.9337171437	5.5110534983	5.654667948	4.9165470397
0.9154929577	4.0483455352	5.6015354334	5.710521919	4.9598708506
0.985915493	4.1484844162	5.6950325186	5.7374968482	4.9793006808
1.0563380282	4.2401614462	5.7724368394	5.777845939	4.9764140146
1.1267605634	4.3497956452	5.8484456427	5.7931571854	4.9318270036
1.1971830986	4.4356640296	5.9125306326	5.8169522068	4.9942345516
1.2676056338	4.5055852888	5.9920837665	5.8351674643	4.9644479163
1.338028169	4.5867185815	6.0600913684	5.8513640537	4.9852232615
1.4084507042	4.6624706093	6.1073905498	5.8698913151	4.9755856117
1.4788732394	4.735349141	6.1720224642	5.8838725898	5.0083506623
1.5492957746	4.8136679118	6.2165364136	5.8865883168	4.9924046601
1.6197183099	4.8939789814	6.2752920375	5.9021185693	4.9854261047
1.6901408451	4.9636880938	6.3255679322	5.9220854948	4.9630169157
1.7605633803	5.0440840671	6.3862600756	5.9255604881	4.9975808501
1.8309859155	5.1007959904	6.4187143315	5.9387561717	4.9709560944
1.9014084507	5.1594008064	6.4655314621	5.9587092442	5.0139068705
1.9718309859	5.2404489331	6.5143116737	5.9737414743	5.0356077883
2.0422535211	5.2822268057	6.5771275856	6.0143144488	5.0416427472
2.1126760563	5.3438195308	6.610282714	6.0536133013	5.0452401438
2.1830985915	5.4201602629	6.6743603954	6.0949325484	5.0609675313
2.2535211268	5.4821740787	6.7251730543	6.1230859706	5.0678275569
2.323943662	5.5366915502	6.7843074362	6.1645996962	5.0517961053
2.3943661972	5.584940616	6.8368731911	6.201289754	5.0559799005
2.4647887324	5.6486765918	6.9037345849	6.2346443347	5.0673985909
2.5352112676	5.7055554443	6.9514703736	6.2643760367	5.0481564028
2.6056338028	5.7638657799	7.0100830209	6.3072493355	5.065884587
2.676056338	5.824437894	7.065012122	6.3380195936	5.0710410474
2.7464788732	5.879695447	7.1289034975	6.3744552782	5.0735266412
2.8169014085	5.9322236306	7.1942769182	6.409502899	5.0625291362
2.8873239437	5.9778817541	7.2443728219	6.449620641	5.0717144351
2.9577464789	6.0417309041	7.3024986165	6.4868798268	5.0893511246
3.0281690141	6.0900500741	7.3613747861	6.5311224083	5.135596687
3.0985915493	6.1313065384	7.4224406093	6.578614815	5.145397102
3.1690140845	6.1810153096	7.478993967	6.6121493746	5.1460661108
3.2394366197	6.2342823894	7.5317246528	6.6562365988	5.1428957912
3.3098591549	6.2591984335	7.5801474067	6.6987103076	5.1910673174
3.3802816901	6.3125394792	7.6467902148	6.7374118334	5.2053439738
3.4507042254	6.3663842101	7.6932357196	6.7811432757	5.2527258833
3.5211267606	6.3948738115	7.7436862451	6.825776973	5.284306139
3.5915492958	6.4431651803	7.7886074128	6.8623925193	5.3135532246
3.661971831	6.4800629159	7.8462462839	6.9132192454	5.3621878026
3.7323943662	6.5025446272	7.8893626271	6.9472278383	5.4117902058
3.8028169014	6.5514904312	7.9323413506	7.0016311637	5.4462634066
3.8732394366	6.5858536037	7.9743508372	7.0379948722	5.4719090465
3.9436619718	6.6161442049	8.0264584627	7.0826745946	5.5244536252
4.014084507	6.6510663556	8.0644288846	7.1237666567	5.5548519271
4.0845070423	6.6721837239	8.0945201108	7.1677080761	5.6012669886
4.1549295775	6.6992078501	8.1416293567	7.2010707248	5.6469685982
4.2253521127	6.7207844186	8.1579123824	7.2391097493	5.6648773001
4.2957746479	6.7339828515	8.1989157298	7.2685334925	5.6904572239
4.3661971831	6.7653179348	8.2231660734	7.3083158725	5.7196939872
4.4366197183	6.7744156997	8.245484419	7.3357550954	5.7426223231
4.5070422535	6.7885832987	8.2697707482	7.3591465249	5.7692360663
4.5774647887	6.8054201866	8.280519343	7.3831578729	5.7836158331
4.6478873239	6.8115030142	8.3100788739	7.4022265864	5.7805027943
4.7183098592	6.8244987364	8.3128472729	7.4138760064	5.7961408022
4.7887323944	6.8296150682	8.3303819692	7.4258365602	5.8081979392
4.8591549296	6.837231184	8.3405007983	7.4349425199	5.8214085175
4.9295774648	6.8440156998	8.3418667307	7.4443578708	5.8261943178
5	6.8517128684	8.3372897655	7.4462979588	5.8211612377

Table I.19: The sedimentation rate as a function of position across the channel (x_3/a) and volume fraction

Appendix J

Tables of data from Chapter 7

J.1 The evanescent wave short-time self-diffusivity

κa	$\phi = 0.1$	$\phi = 0.15$	$\phi = 0.2$	$\phi = 0.25$	$\phi = 0.3$	$\phi = 0.35$	$\phi = 0.4$
0.25	0.60095328	0.57081199	0.52377301	0.46636039	0.40446922	0.33984515	0.28604075
0.586206913	0.57640404	0.55004209	0.50650275	0.45292428	0.39412794	0.33150646	0.28045189
0.922413766	0.55490428	0.53198093	0.49176034	0.44170234	0.38575077	0.32514682	0.27640051
1.258620739	0.53738469	0.51724839	0.47986346	0.43278024	0.37926435	0.32055566	0.27360427
1.594827533	0.52316874	0.50519109	0.47014746	0.42554146	0.37409344	0.31712046	0.27157709
1.931034446	0.51139194	0.49507505	0.46196377	0.41944733	0.36977971	0.3143838	0.26998714
2.267241478	0.50139582	0.48637047	0.45487162	0.41415003	0.36604142	0.31207493	0.26864839
2.603448391	0.49272913	0.47872615	0.44859099	0.40943655	0.36271289	0.31004149	0.26746085
2.939655066	0.48508349	0.47190696	0.44294056	0.40517282	0.35969356	0.30819699	0.26637048
3.275861979	0.47824335	0.46574971	0.43779752	0.40127003	0.35691914	0.30649069	0.26534733
3.612068892	0.47205377	0.46013632	0.43307459	0.39766583	0.35434592	0.30489162	0.26437426
3.948275805	0.46640018	0.45497864	0.42870685	0.39431483	0.35194248	0.30337989	0.26344112
4.284482956	0.46119583	0.4502086	0.42464462	0.39118201	0.34968534	0.30194217	0.26254168
4.620689869	0.45637381	0.4457728	0.42084831	0.38823989	0.34755608	0.30056888	0.26167178
4.956896782	0.45188126	0.44162819	0.4172861	0.38546625	0.34554002	0.29925305	0.26082861
5.293103218	0.447676	0.43773967	0.4139317	0.38284272	0.34362504	0.29798916	0.26001015
5.629310131	0.44372362	0.43407834	0.41076314	0.38035399	0.34180114	0.29677272	0.25921467
5.965517044	0.43999574	0.43061996	0.4077619	0.37798697	0.34005976	0.29560018	0.25844085
6.301723957	0.43646872	0.42734411	0.40491208	0.37573054	0.33839351	0.29446834	0.2576876
6.63793087	0.43312263	0.42423338	0.40220004	0.37357506	0.33679622	0.29337451	0.25695392
6.974137783	0.42994043	0.42127275	0.39961392	0.37151206	0.33526227	0.29231632	0.25623891
7.310344696	0.42690757	0.41844934	0.3971433	0.36953413	0.33378688	0.29129162	0.25554177
7.646551609	0.42401129	0.41575179	0.39477912	0.36763492	0.33236581	0.29029858	0.25486174
7.982758522	0.42124063	0.41317013	0.3925133	0.36580858	0.33099532	0.28933546	0.25419825
8.318965912	0.41858581	0.41069579	0.39033875	0.36404997	0.32967198	0.28840071	0.25355056
8.655172348	0.41603824	0.40832093	0.38824901	0.36235464	0.32839286	0.2874929	0.25291812
8.991379738	0.41359034	0.40603861	0.38623843	0.36071831	0.32715523	0.28661078	0.25230041
9.327586174	0.4112353	0.40384272	0.38430184	0.35913742	0.32595667	0.2857531	0.25169688
9.663793564	0.40896693	0.40172762	0.38243464	0.35760853	0.32479495	0.28491879	0.2511071

Table J.1: The evanescent wave short-time self-diffusivity PARALLEL to the channel walls is a function of the evanescent penetration depth κ and the suspension volume fraction ϕ. These results are for a channel of width $L_3 = 12a$

κa	$\phi = 0.1$	$\phi = 0.15$	$\phi = 0.2$	$\phi = 0.25$	$\phi = 0.3$	$\phi = 0.35$	$\phi = 0.4$
0.25	0.4591891	0.4401068	0.4002996	0.3554013	0.3055577	0.2464062	0.205473
0.586206913	0.3935683	0.3780301	0.3445019	0.3057826	0.2623481	0.2062643	0.1713678
0.922413766	0.3389978	0.3271022	0.2993045	0.2662737	0.228523	0.1765402	0.1464876
1.258620739	0.2970104	0.2882107	0.2649891	0.2367374	0.203612	0.1561709	0.1297728
1.594827533	0.2648734	0.2584622	0.2387176	0.2143641	0.1849361	0.1419795	0.118384
1.931034446	0.2397031	0.2350608	0.2179509	0.1967815	0.1703474	0.1315608	0.1101978
2.267241478	0.2194335	0.2160802	0.2009992	0.1824587	0.1584989	0.1234676	0.1039447
2.603448391	0.2027001	0.2002804	0.1867953	0.1704518	0.148577	0.1168693	0.0989014
2.939655066	0.1885985	0.1868537	0.1746515	0.1601641	0.1400755	0.1112834	0.0946533
3.275861979	0.1765126	0.1752553	0.1641052	0.1512014	0.1326641	0.1064203	0.0909565
3.612068892	0.1660087	0.1651033	0.154832	0.143291	0.126116	0.102099	0.0876623
3.948275805	0.1567726	0.1561206	0.1465955	0.1362364	0.1202691	0.0982014	0.0846769
4.284482956	0.1485709	0.1481005	0.1392184	0.1298912	0.1150027	0.094647	0.0819381
4.620689869	0.1412264	0.1408846	0.1325637	0.1241432	0.1102247	0.0913785	0.0794033
4.956896782	0.1346015	0.1343493	0.126524	0.1189044	0.105863	0.0883533	0.0770417
5.293103218	0.1285881	0.1283964	0.1210131	0.1141045	0.10186	0.085539	0.0748303
5.629310131	0.1230995	0.1229468	0.1159611	0.1096863	0.0981688	0.08291	0.0727513
5.965517044	0.1180654	0.1179357	0.1113103	0.1056029	0.0947511	0.0804453	0.0707904
6.301723957	0.1134283	0.1133096	0.1070129	0.101815	0.0915748	0.0781278	0.0689359
6.63793087	0.1091401	0.1090238	0.1030286	0.0982897	0.0886129	0.075943	0.067178
6.974137783	0.1051609	0.1050408	0.0993232	0.0949991	0.0858427	0.0738786	0.0655083
7.310344696	0.1014567	0.1013285	0.0958677	0.0919191	0.0832446	0.0719239	0.0639197
7.646551609	0.0979987	0.0978593	0.0926369	0.0890292	0.0808018	0.0700697	0.0624058
7.982758522	0.094762	0.0946098	0.0896091	0.0863116	0.0784998	0.0683078	0.0609611
8.318965912	0.0917253	0.0915592	0.0867655	0.0837505	0.0763259	0.066631	0.0595806
8.655172348	0.0888698	0.0886897	0.0840895	0.0813323	0.074269	0.065033	0.0582599
8.991379738	0.0861795	0.0859853	0.0815665	0.079045	0.0723192	0.0635079	0.0569952
9.327586174	0.0836398	0.0834323	0.0791837	0.0768778	0.0704679	0.0620508	0.0557828
9.663793564	0.0812383	0.0810183	0.0769296	0.0748213	0.0687075	0.060657	0.0546194

Table J.2: The evanescent wave short-time self-diffusivity PERPENDICULAR to the channel walls is a function of the evanescent penetration depth κ and the suspension volume fraction ϕ. These results are for a channel of width $L_3 = 12a$

J.2 The evanescent wave collective diffusivity

κa	$\phi = 0.1$	$\phi = 0.15$	$\phi = 0.2$	$\phi = 0.25$	$\phi = 0.3$	$\phi = 0.35$	$\phi = 0.4$
0.25	6.6230003	9.3199586	11.1669829	12.5859261	14.1821071	14.6245688	15.5336847
0.586206897	1.6586359	2.3439009	2.8805183	3.3350421	3.8427521	3.9941354	4.4956156
0.922413793	0.9425529	1.3265017	1.6333420	1.9258200	2.2181119	2.3818129	2.8498705
1.25862069	0.6770587	0.9456510	1.1489938	1.3683100	1.5597391	1.7340673	2.1841116
1.594827586	0.5353120	0.7418579	0.8842234	1.0581620	1.1917506	1.3640365	1.7853894
1.931034483	0.4450153	0.6122614	0.7151882	0.8572956	0.9546378	1.1174465	1.5030721
2.267241379	0.3816054	0.5215354	0.5977977	0.7161988	0.7893700	0.9395423	1.2880353
2.603448276	0.3342924	0.4540866	0.5118085	0.6119293	0.6681696	0.8048984	1.1183126
2.939655172	0.2974936	0.4018263	0.4463943	0.5320737	0.5759973	0.6996605	0.9815102
3.275862069	0.2679854	0.3600855	0.3951725	0.4692336	0.5039228	0.6154590	0.8695702
3.612068966	0.2437605	0.3259496	0.3541190	0.4186942	0.4462944	0.5468662	0.7768391
3.948275862	0.2234966	0.2975030	0.3205765	0.3773060	0.3993585	0.4901743	0.6991792
4.284482759	0.2062859	0.2734276	0.2927190	0.3428895	0.3605293	0.4427449	0.6335045
4.620689655	0.1914819	0.2527868	0.2692544	0.3138888	0.3279711	0.4026496	0.5774555
4.956896552	0.1786104	0.2348958	0.2492474	0.2891659	0.3003444	0.3684388	0.5292270
5.293103448	0.1673171	0.2192423	0.2320035	0.2678722	0.2766571	0.3390068	0.4874052
5.629310345	0.1573297	0.2054342	0.2169991	0.2493648	0.2561592	0.3134939	0.4508833
5.965517241	0.1484359	0.1931668	0.2038325	0.2331464	0.2382744	0.2912243	0.4187848
6.301724138	0.1404674	0.1821994	0.1921899	0.2188288	0.2225522	0.2716619	0.3904054
6.637931034	0.1332889	0.1723391	0.1818247	0.2061041	0.2086390	0.2543757	0.3651722
6.974137931	0.1267904	0.1634294	0.1725393	0.1947264	0.1962514	0.2390154	0.3426260
7.310344828	0.1208815	0.1553420	0.1641744	0.1844966	0.1851614	0.2252960	0.3223852
7.646551724	0.1154868	0.1479706	0.1566002	0.1752521	0.1751833	0.2129838	0.3041358
7.982758621	0.1105436	0.1412262	0.1497089	0.1668595	0.1661638	0.2018847	0.2876138
8.318965517	0.1059987	0.1350342	0.1434122	0.1592074	0.1579764	0.1918369	0.2726007
8.655172414	0.1018071	0.1293308	0.1376357	0.1522028	0.1505152	0.1827045	0.2589108
8.99137931	0.0979299	0.1240622	0.1323167	0.1457679	0.1436919	0.1743735	0.2463874
9.327586207	0.0943339	0.1191815	0.1274023	0.1398365	0.1374307	0.1667473	0.2348956
9.663793103	0.0909905	0.1146486	0.1228470	0.1343520	0.1316676	0.1597430	0.2243209
10	0.0878745	0.1104288	0.1186121	0.1292661	0.1263478	0.1532906	0.2145635

Table J.3: The evanescent wave collective diffusivity PERPENDICULAR to the channel walls is a function of the evanescent penetration depth κ and the suspension volume fraction ϕ. These results are for a channel of width $L_3 = 12a$